

Marco Fanciulli
Editor

TOPICS IN APPLIED PHYSICS 115

Electron Spin Resonance and Related Phenomena in Low-Dimensional Structures

 Springer

Topics in Applied Physics

Volume 115

Available **online** at
SpringerLink.com

Topics in Applied Physics is part of the SpringerLink service. For all customers with standing orders for Topics in Applied Physics we offer the full text in electronic form via SpringerLink free of charge. Please contact your librarian who can receive a password for free access to the full articles by registration at:

springerlink.com → Orders

If you do not have a standing order you can nevertheless browse through the table of contents of the volumes and the abstracts of each article at:

springerlink.com → Browse Publications

Topics in Applied Physics

Topics in Applied Physics is a well-established series of review books, each of which presents a comprehensive survey of a selected topic within the broad area of applied physics. Edited and written by leading research scientists in the field concerned, each volume contains review contributions covering the various aspects of the topic. Together these provide an overview of the state of the art in the respective field, extending from an introduction to the subject right up to the frontiers of contemporary research.

Topics in Applied Physics is addressed to all scientists at universities and in industry who wish to obtain an overview and to keep abreast of advances in applied physics. The series also provides easy but comprehensive access to the fields for newcomers starting research.

Contributions are specially commissioned. The Managing Editors are open to any suggestions for topics coming from the community of applied physicists no matter what the field and encourage prospective editors to approach them with ideas.

Managing Editor

Dr. Claus E. Ascheron

Springer-Verlag GmbH
Tiergartenstr. 17
69121 Heidelberg
Germany
Email: claus.ascheron@springer.com

Assistant Editor

Adelheid H. Duhm

Springer-Verlag GmbH
Tiergartenstr. 17
69121 Heidelberg
Germany
Email: adelheid.duhm@springer.com

Marco Fanciulli (Ed.)

Electron Spin Resonance and Related Phenomena in Low-Dimensional Structures

With 97 Figures

 Springer

Prof. Dr. Marco Fanciulli
University of Milano-Bicocca
Department of Material Science
20125 Milano, Italy
and
CNR-INFM MDM National Laboratory
Via C. Olivetti, 2
20041 Agrate Brianza MI, Italy
E-mail: marco.fanciulli@mdm.infm.it

Topics in Applied Physics

ISSN 0303-4216

ISBN 978-3-540-79364-9

e-ISBN 978-3-540-79365-6

DOI 10.1007/978-3-540-79365-6

Library of Congress Control Number: 2008944295

© Springer-Verlag Berlin Heidelberg 2009

This work is subject to copyright. All rights are reserved, whether the whole or part of the material is concerned, specifically the rights of translation, reprinting, reuse of illustrations, recitation, broadcasting, reproduction on microfilm or in any other way, and storage in data banks. Duplication of this publication or parts thereof is permitted only under the provisions of the German Copyright Law of September 9, 1965, in its current version, and permission for use must always be obtained from Springer-Verlag. Violations are liable to prosecution under the German Copyright Law.

The use of general descriptive names, registered names, trademarks, etc. in this publication does not imply, even in the absence of a specific statement, that such names are exempt from the relevant protective laws and regulations and therefore free for general use.

Production: VTEX

Cover concept: eStudio Calamar Steinen

Cover design: SPI Publisher Services

SPIN: 12216970 57/3180/VTEX

Printed on acid-free paper

9 8 7 6 5 4 3 2 1

springer.com

Foreword

The spin degree-of-freedom is offering a wide range of intriguing opportunities both in fundamental as well as in applied solid-state physics. When combined with the rich and fertile physics of low-dimensional semiconducting structures and with the possibility to change, for example, carrier density, electric fields or coupling to other quantum systems in a controlled way, an extremely exciting and interesting research field is opened. Most commercial electronic devices are based on spin-independent charge transport. In the last two decades, however, scientists have been focusing on the ambitious objective of exploiting the spin degree-of-freedom of the electron to achieve novel functionalities. Ferromagnetic semiconductors, spin transistors, single-spin manipulations or spin-torque MRAMs (magnetoresistive random access memories) are some of the hot topics. The importance of spin phenomena for new applications was recognized by the Royal Swedish Academy of Sciences by awarding the 2007 Nobel Prize in Physics jointly to Albert Fert and Peter Grünberg “for the discovery of giant magnetoresistance”. This effect originates from spin-dependent scattering phenomena in a two-terminal ferromagnetic–paramagnetic–ferromagnetic junction leading to a new type of magnetic memory. The Hall effect and its applications remain fertile research areas. The spin Hall effect, in analogy with the conventional Hall effect, occurs in paramagnetic systems as a result of spin-orbit interaction. The predicted generation of a pure spin current transverse to an applied electric field even in the absence of applied magnetic fields has been observed in semiconductors more than 30 years after its prediction, providing an important method to produce spin-polarized currents in nanoelectronic devices. After the Nobel Prize discoveries of the quantum Hall effect (QHE) and of the fractional quantum Hall effect (FQHE), electron-spin resonance or other spin-related phenomena, like skyrmion excitations and spontaneous spin polarization, have been observed in low-dimensional structures both in the QHE regimes and in 1- and 0-dimensional structures. In particular, the interaction of the electron spin with nuclear spins has been studied in a systematic way. Many of the theoretical ideas in spin physics are used for the interpretation of new phenomena in interacting double layers where a pseudospin characterizes the two layers. Since the pioneering works on quantum electronic transport, the importance of disorder and correlation in low-dimensional sys-

tems has been deeply investigated and understood. Two phenomena due to the breaking of symmetry in semiconductor heterostructures and correlation in spin-polarized systems have been observed. The first one is related to the dependence of the spin-coherence length on the direction of polarization (parallel or perpendicular to the semiconductor interfaces) in a quantum-well structure. The other one is the observation of a positive magnetoresistance when a magnetic field is applied parallel to the plane of a purely 2D electron gas, a result attributed to correlation in low-dimensional spin-polarized systems. The advances in nanotechnology led also to the possibility of detecting and manipulating a single spin embedded in quantum dots with phenomena like spin-blockade and Kondo physics. Spin-dependent electronic transport in ultrascaled electronics devices is also an important means to exploit further the ingenuities of modern microelectronics. Single-atom electronics has been already observed and charge-transport manipulation using the spin degree of freedom is being actively pursued by different research teams. The electron spin also provides the ideal two-level system necessary for quantum bits (qubits), the building blocks of quantum information processors (QIP). Electron and nuclear spins in low-dimensional semiconductor structures in which detection and manipulation are feasible, are key elements for the development of a QIP. This is an ambitious objective that requires significant advances in nanotechnology as well as a deep understanding of other important parameters related to the spin such as coherence. This book collects a series of review articles written by experts in the field dedicated to most of the intriguing and exciting topics outlined above.

Stuttgart,
January 2009

Klaus von Klitzing

Index

fractional quantum Hall effect, v	quantum Hall effect, v
Kondo physics, vi	quantum information processor, vi
QHE, v	skyrmion excitations, v
QIP, vi	spin Hall effect, v

Preface

The idea of this book was formulated during an exciting and stimulating workshop on “Electron spin resonance and related phenomena in low dimensional structures” that I organized in Sanremo (Italy) in the spring of 2006. During three days, we had the pleasure to listen to the key-note lecture by Nobel Laureate Klaus von Klitzing and to eighteen talks from leading experts in the field from Europe, the United States, Canada, Japan, and Australia. Young researchers also had the opportunity to present their work during a poster session. The main topics addressed during the workshop were electron spin resonance in III–V heterostructures and quantum dots, spin detection and manipulation in silicon and silicon–germanium nanostructures, spin coherence, and spin in semiconducting nanostructures for quantum information processing.

In this book, some of the contributions given at the workshop as well as some additional reviews provided by other experts have been collected into three sections dealing with III–V heterostructures, quantum dots and quantum wires, silicon-based nanostructures, and quantum information processing. Theoretical as well as experimental aspects are presented and discussed for each topic. The fundamental aspects as well as the implications for applications of spin detection and manipulation in low dimensional structures represent an intriguing and exciting research area in contemporary condensed matter physics.

In summary, this volume reflects the most important contributions given at the International Workshop on “Electron spin resonance and related phenomena in low dimensional structures”, which took place at the Villa Nobel in Sanremo (IM), Italy, from March 6 to March 8, 2006, and additional review articles from leading experts in the field. It is a pleasure to acknowledge and gratefully thank all the people and the institutions that supported the Workshop, on one hand, and, on the other, those who contributed to this volume. The Workshop was funded by the Provincia di Imperia which also made available the beautiful and inspirational Villa Nobel, and by Fondazione Carige, Comune di Sanremo, Casinò di Sanremo, and Sanremo Promotion. The staff of Villa Nobel and of the Sanremo Promotion Agency was very helpful in handling the logistics related to the Workshop. I shall also thank

the staff of the CNR-INFN MDM National Laboratory for their help in the workshop organization.

Agrate Brianza (Milano),
May 2009

Marco Fanciulli

Contents

Foreword	V
Preface	VII
Resistively Detected ESR and ENDOR Experiments in Narrow and Wide Quantum Wells: A Comparative Study	
Joshua D. Caldwell, Clifford R. Bowers, Guennadii M. Gusev	1
1 Introduction	1
2 Theory	2
3 Experiment	4
4 Results	4
5 Conclusions	11
References	12
Index	13
Electron-Spin Manipulation in Quantum Dot Systems	
Yasuhiro Tokura, Toshiaki Obata, Tsuyoshi Hatano, Seigo Tarucha	15
1 Introduction	15
2 Single-Spin Manipulation	16
2.1 Oscillating Magnetic Field	17
2.2 Slanting Zeeman Field	19
3 Two-Spin Interaction	23
3.1 Formulation	23
3.2 Hybrid Double Dots	27
3.3 Double QD with Slanting Zeeman Field	30
4 Conclusion	31
References	31
Index	34
Resistively Detected NMR in GaAs/AlGaAs	
Guillaume Gervais	35
1 Nuclear Magnetic Resonances with ‘Too Few Spins’	36

1.1	The ‘Too Few Spins’ Problem	36
1.2	Electrons as an In-Situ Detector of the NMR	37
2	Recent Advances in GaAs/AlGaAs Semiconductor Quantum Wells	40
2.1	Resistively Detected NMR Lineshapes in GaAs/AlGaAs	40
2.2	Spin-Lattice Relaxation-Time Measurements	43
3	Towards a Complete NMR Probe of Quantum Structures	46
3.1	NMR in Quantum Electronic Structures of GaAs/AlGaAs	46
3.2	NMR on a Chip: Quantum Coherent Control of the Nuclear Spins at the Nanoscale	47
4	Concluding Remarks	48
	References	48
	Index	49

Electron-Spin Dynamics in Self-Assembled (In,Ga)As/GaAs Quantum Dots

A.	Greilich, D.R. Yakovlev, M. Bayer, A. Shabaev, Al.L. Efros	51
1	Introduction	51
2	Experiment	53
3	Electron g-Factor	54
4	Creation of Spin Coherence by Spin Initialization	56
5	Electron-Spin Coherence	65
6	Summary	77
	References	78
	Index	80

Single-Electron-Spin Measurements in Si-Based Semiconductor Nanostructures

H.W.	Jiang, E. Yablonovitch, M. Xiao, M. Sakr, G. Scott, E.T. Croke	81
1	Introduction	81
2	Measurements of a Single Spin in the SiO ₂ of a Submicrometer Si Field Effect Transistor	83
2.1	Statistical Measurements	84
2.2	Detection of Electron-Spin Resonance (ESR) of a Single Spin	88
2.3	Single-Shot Measurement	91
3	Fabrication and Characterization of Electrostatically Confined Quantum-Dot Structures in Si/SiGe Heterostructures	91
3.1	Demonstration of a One-Electron Quantum Dot	92
3.2	Characterization of the Spin-Transition Sequence	95
3.3	Single-Shot Measurement	96
4	Concluding Remarks	98
	References	98
	Index	100

Si/SiGe Quantum Devices, Quantum Wells, and Electron-Spin Coherence

J.L. Truitt, K.A. Slinker, K.L.M. Lewis, D.E. Savage, Charles Tahan, L.J. Klein, J.O. Chu, P.M. Mooney, A.M. Tyryshkin, D.W. van der Weide, Robert Joynt, S.N. Coppersmith, Mark Friesen, M.A. Eriksson	101
1 Introduction	102
2 Silicon Quantum Devices	103
3 Spins and Valleys	106
4 ESR in Silicon Quantum Wells	107
5 Samples	109
6 ESR Measurements	110
7 Decoherence Analysis	111
8 Results	113
9 Conclusions	115
References	115
Index	126

Electrical Detection of Electron-Spin Resonance in Two-Dimensional Systems

Junya Matsunami, Tohru Okamoto	129
1 Mechanism of Electrical Detection	129
2 Determination of Spin-Relaxation Times	133
References	138
Index	140

Quantitative Treatment of Decoherence

Leonid Fedichkin, Vladimir Privman	141
1 Introduction	141
2 Measures of Decoherence	142
2.1 Relaxation Timescales	142
2.2 Quantum Entropy	143
2.3 Fidelity	143
2.4 Norm of Deviation	145
2.5 Arbitrary Initial States	145
3 Decoherence of Double Quantum-Dot Charge Qubits	146
3.1 Model	147
3.2 Piezoelectric Interaction	148
3.3 Deformation Interaction	150
3.4 Error Estimates During Gate Functions	151
3.5 Relaxation During the NOT Gate	151
3.6 Dephasing During a Phase Gate	154
3.7 Qubit Error Estimates	155

4 Additivity of Decoherence Measures 157
 4.1 The Maximal Deviation Norm 158
 4.2 Upper Bound for Measure of Decoherence 160
 References 162
 Index 167

Measuring the Charge and Spin States of Electrons on Individual Dopant Atoms in Silicon

Søren E.S. Andresen, Dane R. McCamey, Rolf Brenner,
 Marc A. Ahrens, Mladen Mitic, Victor C. Chan, Eric Gauja,
 Fay E. Hudson, Andrew J. Ferguson, Tilo M. Buehler, David J. Reilly,
 Robert G. Clark, Andrew S. Dzurak, Alex R. Hamilton,
 Cameron J. Wellard, Changyi Yang, Toby Hopf, Jeff McCallum,
 David N. Jamieson, Lloyd C. L. Hollenberg, Wayne D. Hutchison,
 Hans Huebl, Martin S. Brandt 169
 1 Quantum Computing with Phosphorus in Silicon 170
 1.1 Electronic Donor States of Phosphorus in Silicon 171
 1.2 Coupled Pairs of Phosphorus Donors as Charge Qubits 171
 2 Controlled Single-Ion Implantation 173
 2.1 Single-Ion Detection with Integrated p-i-n Diodes 173
 3 Charge Sensing with Superconducting RF-SETs 174
 3.1 Layout and Performance of RF-SET Measurements 175
 4 Initialization and Readout with Schottky Contacts 177
 4.1 Contacting Atomically Doped Devices 177
 5 Magnetic Resonance in Nanoscale Implanted Devices 178
 References 181
 Index 182

Electron Spin as a Spectrometer of Nuclear-Spin Noise and Other Fluctuations

Rogerio de Sousa 183
 1 Introduction 183
 2 Noise, Relaxation, and Decoherence 186
 2.1 The Bloch–Wangsness–Redfield Master Equation 186
 2.2 Finite Frequency Phase Fluctuations and Coherence Decay
 in the Semiclassical-Gaussian Approximation 188
 2.3 Single-Spin Measurement Versus Ensemble Experiments:
 Different Coherence Times? 194
 3 Electron-Spin Evolution Due to Nuclear Spins: Isotropic and
 Anisotropic Hyperfine Interactions, Internuclear Couplings and
 the Secular Approximation 196
 3.1 The Electron–Nuclear Spin Hamiltonian 196

3.2	Electron–Nuclear-Spin Evolution in the Secular Approximation	198
3.3	Beyond the Secular Approximation: Nuclear–Nuclear Interactions Mediated by the Electron Spin Hyperfine Interaction	200
4	Microscopic Calculation of the Nuclear-Spin Noise Spectrum and Electron-Spin Decoherence	202
4.1	Nuclear-Spin Noise	203
4.2	Mean Field Theory of Noise Broadening: Quasiparticle Lifetimes	206
5	Electron Spin-Echo Decay of a Phosphorus Impurity in Silicon: Comparison with Experiment	209
5.1	Effective-Mass Model for a Phosphorus Impurity in Silicon	209
5.2	Explicit Calculations of the Nuclear-Spin Noise Spectrum and Electron Spin-Echo Decay of a Phosphorus Impurity in Silicon	210
6	Conclusions and Outlook for the Future	215
	References	218
	Index	220

A Robust and Fast Method to Compute Shallow States without Adjustable Parameters: Simulations for a Silicon-Based Qubit

	Alberto Debernardi, Marco Fanciulli	221
1	Shallow Impurities in an External Field	223
1.1	Envelope Function Approximation	224
1.2	The Central-Cell Correction	225
1.3	Numerical Basis Set	226
2	Phosphorous Impurity in Silicon	226
2.1	Bulk Ingredients	227
3	Theoretical Results: Si:P	227
3.1	The Core-Correction Contribution	228
3.2	Stark Effect	229
3.3	Electric-Field Dependence of Superhyperfine Constants	232
4	Confinement Effects	234
5	Conclusions	237
	References	238
	Index	239

Photon-Assisted Tunneling in Quantum Dots

	Enrico Prati, Rossella Latempa, Marco Fanciulli	241
1	Introduction	241
2	Theory of Photon-Assisted Tunneling in Quantum Dots	242

	Hamiltonian Formalism of Tunneling under Microwave Irradiation	243
	Tunneling in Quantum Dots under Microwave Irradiation	244
	Typical Regimes of Operation	246
3	Experimental Results in III–V Heterostructure Quantum Dots	247
4	Group IV Heterostructure Quantum Dots	250
5	Si/SiO ₂ nanoFET Quantum Dots	252
6	Conclusions	256
	References	257
	Index	258
	Index	259

Resistively Detected ESR and ENDOR Experiments in Narrow and Wide Quantum Wells: A Comparative Study

Joshua D. Caldwell¹, Clifford R. Bowers¹, and Guennadii M. Gusev²

¹ Department of Chemistry and National High Magnetic Field Lab, University of Florida, Gainesville, FL 32611-7200, USA
russ@ufl.edu

² Instituto de Física, Universidade de São Paulo, Caixa Postal 66318, 05315-970, São Paulo, SP, Brazil

Abstract. Resistively detected electron-spin resonance and electron nuclear double resonance spectra have been acquired in the lowest electronic subband of a remotely Si-doped 400-nm wide GaAs/AlAs digital parabolic quantum well in high parallel and perpendicular magnetic fields at temperatures in the 0.5–10 K range. The temperature dependences of the g -factor, ESR linewidth, line amplitude and nuclear-spin relaxation times, acquired in the two different orientations, are compared to data obtained previously in a 30-nm GaAs quantum well with similar electron density and mobility.

1 Introduction

In a parabolic quantum well (PQW) formed by an AlAs/GaAs digital superlattice, the aluminum fraction in the center of the well is zero but increases along the growth direction toward each barrier, yielding a parabolic conduction electron potential $V(z) = (az)^2$. Such quantum structures have several interesting properties that might prove advantageous for spin-based devices. For example, it has been shown that the electron density in the PQW can be shifted substantially at relatively modest gate voltage [1]. Because the Landé g -factors in GaAs and AlAs are -0.44 and 1.99 , respectively [2, 3], the g -factor in the electron system is gate controllable over a wide range [1]. The g -factor is also tunable by varying the electron density, temperature, or well-width [4, 5]. Furthermore, g is expected to depend on the angle θ between the growth direction (z) and applied magnetic field (B). A $\theta = 0^\circ \rightarrow 90^\circ$ rotation in a sufficiently strong magnetic field causes the two-dimensional electron system (2DES) of the wide PQW to evolve into a quasi-3DES.

Here, we employ resistively detected ESR (RDESR) and electron nuclear double resonance (RDENDOR) to study a remotely Si-doped 400-nm wide GaAs/AlAs digital PQW in high parallel ($\theta = 90^\circ$) and perpendicular ($\theta = 0^\circ$) fields. The temperature dependences of the g -factor, linewidth

and amplitude are compared to those measured in a 30-nm GaAs QW with similar density and mobility. Furthermore, the possibility to achieve dynamic nuclear polarization (DNP) by simultaneously saturating the electron-spin resonance line while slowly ramping down the applied magnetic field will be demonstrated in the two orientations. The subsequent decay of the Overhauser shift following the DNP downsweep provides a means to determine the overall nuclear-spin relaxation time. The temperature dependence of the nuclear-spin relaxation time is reported for a strong parallel field as well as two different values of θ at the Landau level filling factor $\nu = 1$.

2 Theory

In a PQW with $V(z) = (az)^2$, application of a strong B field along the z -axis yields the energy spectrum of a 2DES, where

$$E_{i,n}(\theta = 0^\circ) = E_i + (n + 1/2)\hbar\omega_c \quad (1)$$

is the energy of the n th Landau level of the i th subband, $\omega_c = eB/m$ and m is the effective mass. When a high inplane field is applied such that $\omega_c \gg a(2/m)^{1/2}$, the spectrum becomes equivalent to that of a 3DES:

$$E_n(\theta = 90^\circ) = (n + 1/2)\hbar\omega_c + \hbar^2 k_x^2 / 2m. \quad (2)$$

The evolution of the system eigenstates, as the sample is rotated in the high magnetic field, should be reflected in the electronic g-factor and hyperfine contact interaction [6]. In the perpendicular field, electrons in each subband of the 2DES sample different g-factors across the entire PQW structure on a timescale much shorter than one electron Larmor period. According to a basic tenet of quantum mechanics, the g-factor of an electron in the i th subband can be calculated from

$$g_i = \int_{-W_e/2}^{+W_e/2} g(z) |\phi_i(z)|^2 dz, \quad (3)$$

where W_e is the effective well width and $\phi_i(z)$ is the subband wavefunction. As in the simple particle-in-a-box, higher i subbands will have increased probability density away from the center of the PQW where the Al fraction is higher. Thus, due to the dependence of the g-factor on the Al fraction, [1] the magnitude of g is expected to decrease with increasing i . Figure 1a presents a calculation of g for the first seven subbands of the parabolic well shown in Fig. 1b. The g-factor, resonance linewidth, and nuclear-spin relaxation time are all expected to vary with tilt angle due to changes in the electronic quantum states and hyperfine couplings as the systems evolves from a 2DES to a quasi-3DES.

The following expression for the nuclear spin-lattice relaxation time in the vicinity of the 2DES at odd-integer filling factors has appeared in the literature [7].

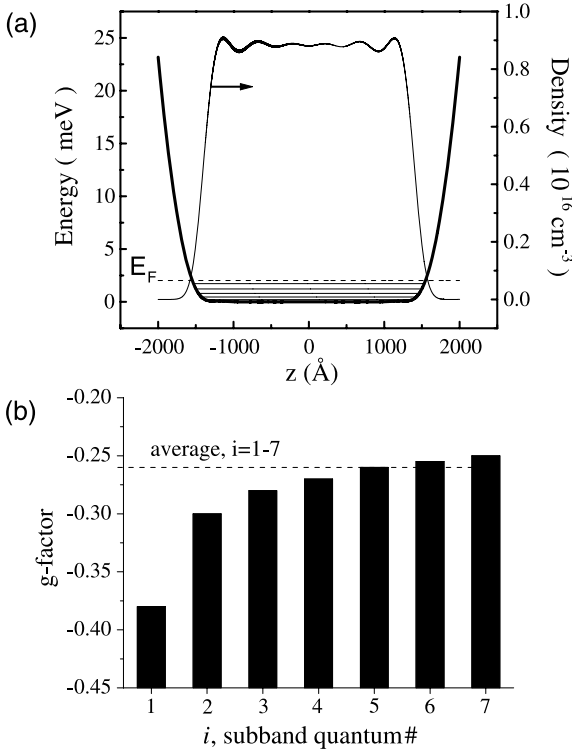


Fig. 1. (a) Potential energy and electronic energies in the 400-nm PQW studied here, and the total electron density of the 7 filled subbands at zero field. (b) Calculation of the g-factor for the $i = 1 \rightarrow 7$ subbands and the average (dashed line)

$$\frac{1}{T_{1n}} = \gamma_n^2 \gamma_e^2 \eta^2 |\phi(z)|^4 D^\uparrow D^\downarrow, \quad (4)$$

where D^\uparrow (D^\downarrow) are the density of spin-up (-down) states at the Fermi level and η is the Bloch correction factor. The equation is an adaptation of the Korringa formula for metals [8] in the limit where kT is much less than the Landau level broadening. The relaxation rate exhibits the familiar $1/T_{1n} \propto T$ dependence observed in normal metals. The dependence of the relaxation rate on the electronic wavefunction and density of states at the Fermi level suggests that the spin relaxation should also be highly sensitive to the tilt angle and filling factor. In principle, the nuclear-spin relaxation could be affected by many-body interactions in the electron system. Measurements of T_{1n} by resistively detected nuclear magnetic resonance (RDNMR) in ultrahigh-mobility GaAs quantum wells at filling factors $0.895 \leq \nu \leq 0.84$ deviated strongly from Korringa-like $T_{1n} \propto T^{-1}$ behavior in the 25–100 mK range [9], possibly due to fluctuations associated with the Goldstone mode of the skyrmion crystal [10]. However, in another study of the temperature dependence of T_{1n} under similar conditions and similar high sample mobility [11], qualitative agreement with (4) was observed. Thus, the role of many-body effects in the nuclear-spin relaxation remains unclear. It should be noted that the

wide parabolic well studied here has significantly lower mobility than in the narrow GaAs quantum wells studied by RDNMR.

3 Experiment

Resistively detected ESR experiments were performed on a 400-nm wide AlAs/GaAs digital PQW, where the average Al mole fraction is 0.0 at the center and 0.29 in the layers adjacent to the $\text{Al}_{0.31}\text{Ga}_{0.69}\text{As}$ barriers. Electrons were introduced by remote silicon δ -doping. A detailed experimental characterization and theoretical analysis of the transport properties in this particular sample has been previously published (sample AG662) [6]. The density and mobility prior to optical illumination with an LED was measured to be $1.5 \times 10^{11} \text{ cm}^{-2}$ and $1.2 \times 10^5 \text{ cm}^2/\text{V s}$, respectively. Illumination at $\approx 1.6 \text{ K}$ for 60 s by an LED 1 cm from the sample increased these values to $3.5 \times 10^{11} \text{ cm}^{-2}$ and $2.4 \times 10^5 \text{ cm}^2/\text{V s}$. The resistance activation energy at high perpendicular field was found to be $1.9 \pm 0.1 \text{ K}$ at $\nu = 1$. For comparison purposes, we will also present data acquired previously in a 30-nm wide GaAs multiple QW sample (consisting of 24 wells) with $\text{Al}_{0.1}\text{Ga}_{0.9}\text{As}$ barriers. The mobility and density of this sample are $0.44 \times 10^6 \text{ cm}^2/\text{V s}$ and $6.9 \times 10^{10} \text{ cm}^{-2}$ per layer. Both samples were patterned by photolithography into a standard Hall bar geometry. The ESR spectra were acquired via the resonant microwave-induced resistance change, ΔR_{xx} . The details of the instrumentation and measurement procedure are described in [12]. NMR spectra were acquired indirectly via radio-frequency swept RDENDOR, where the perturbation of the steady-state RDES signal at constant B field is measured as the radio-frequency field is swept through NMR resonance. Additional details of this technique are presented in [13].

4 Results

The field dependence of R_{xx} in the parallel and perpendicular orientations of the 400-nm wide PQW is shown in Fig. 2. In the parallel field, the transition to a quasi-3DES can be observed as the magnetic length l_0 becomes comparable to the well width, W_e . This is observed as the final oscillation of R_{xx} at $B \approx 1 \text{ T}$. When $W_e \gg l_0$, magnetic confinement dominates and the density of states approximates to that of a 3DES at high field. Under these conditions the electron Zeeman energy is expected to be broadened due to the spatial variation of g . In the perpendicular orientation, $R_{xx}(B)$ resembles that of an ordinary 2DES in which resistance minima are observed as the Fermi energy is swept through the minima in the density of states. The experimental studies in this orientation will focus on $\nu = 1$ where the lower-energy spin state of the lowest Landau level is completely filled, while the upper spin state is empty.

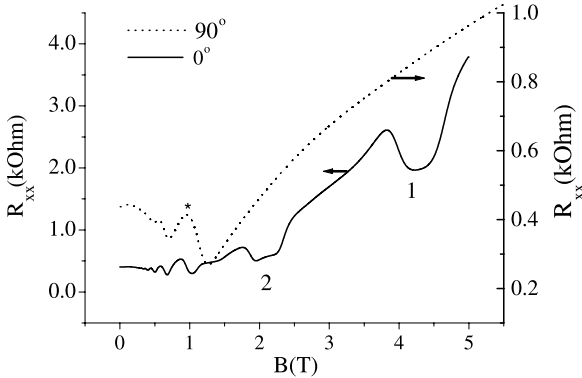


Fig. 2. Longitudinal resistance traces at 1.5 K in the two orthogonal field orientations of the 400-nm PQW. The *asterisk* marks the onset of depopulation of the lowest Landau level with increasing field

In our previous work [14] we reported the g -factor anisotropy in the 400-nm PQW (sample AG662). The g -factor is close to that of bulk GaAs, indicating that the ESR signal arises mainly from $i = 1$ electrons localized near the center of the PQW where the Al fraction is small. A -5% monotonic decrease in g was observed when the sample was rotated from $\theta = 0 \rightarrow 90^\circ$. The $g(\theta)$ dependence in the 400-nm PQW is distinctly different than in the two previous experimental reports of g anisotropy in narrow GaAs/Al $_x$ Ga $_{x-1}$ As QWs [15, 16]. As explained in [15], the observed g anisotropy reflects two opposing terms: the nonparabolicity of the bulk GaAs conduction band and the diamagnetic correction in the parallel field. Our data suggest that the diamagnetic correction to the g -factor, $\Delta g \propto -\Delta z^2 \sin^2 \theta$, where Δz is the spatial extent of the wavefunction, dominates the change in the g anisotropy in the wide PQW. While the anisotropy due to the spin-orbit Bychkov–Rashba field cannot be completely ruled out, in principle it should be absent in the GaAs/AlAs PQW due to the bulk inversion symmetry and mirror-plane symmetry of the structure [17]. The time-resolved photoluminescence polarization measurements of [16] showed no g anisotropy for $W_e > 12$ -nm, while in an electrically detected ESR study of a 15-nm wide QW [15], g slightly decreased with increasing θ at $\nu = 1$ for small tilt angles. The latter is similar to the behavior exhibited in our 400-nm PQW. However, with increasing θ , the tilt-angle dependences of the two samples are quite different. For all Landau levels of the 15-nm QW, g increases sharply with increasing θ , an effect attributed to nonparabolicity of the bulk GaAs conduction band, while in the 400-nm PQW, g decreases monotonically over the $0 \rightarrow 90^\circ$ range.

As is evident in Fig. 3, the temperature dependence of g in the 400-nm PQW in the parallel field is opposite to that of the 2DES in the 30-nm QW at $\nu = 1$. In addition, a slight broadening of the ESR line was observed with increasing θ in the PQW. These observations, taken together with the fact that g in the PQW is close to that of bulk GaAs, suggest that the thickness of the detected layer of electrons within the wide PQW increases slightly with temperature, probably due to population of the $i > 1$ subbands. In the

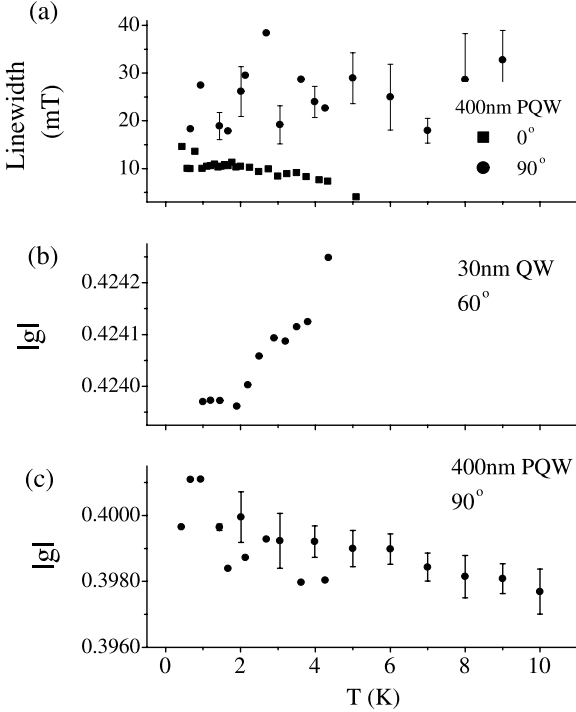


Fig. 3. (a, c) Temperature dependences of the RDESr linewidth and g-factor in the 400-nm GaAs/AlAs PQW in a 6.5 T parallel ($\theta = 90^\circ$) field. (b) Temperature dependence of g in the 30-nm GaAs QW at 5.5 T ($\theta = 60^\circ$)

narrow QW, the opposite trend is observed: g increases while the linewidth decreases (data not shown).

In Fig. 4 we present the temperature dependence of the RDESr signal amplitudes in the $\theta = 0^\circ$ and 90° (with $\nu = 1$) orientations. The temperature dependence at $\nu = 1$ in the 30-nm GaAs QW is also presented for comparison. The appearance of a sharp maximum, with the signal vanishing as $T \rightarrow 0$, is consistent with the simple resonance heating model proposed in [12]. The temperature dependence of ΔR_{xx} in the PQW is much more pronounced in the perpendicular orientation, resembling the temperature dependence in the 30-nm square QW. In the parallel orientation of the PQW, the signal was only weakly temperature dependent, and could be detected at temperatures as high as 10 K. These results suggest a qualitatively different mechanism for the RDESr in the quasi-3DES state.

In GaAs quantum wells, it is well known that the RDESr lineshape may be strongly affected by the effects of DNP; the enhancement of the nuclear polarization ($\langle \hat{I}_z \rangle / I$) due to the combined effects of electron-spin resonance saturation and electron-nuclear crossrelaxation via the flip-flop terms in the Fermi contact interaction (i.e. $\hat{I}_- \hat{S}_+ + \hat{I}_+ \hat{S}_-$). For electrons in a conduction band described by s-type Bloch functions, the secular part of the Hamiltonian due to the coupling with a large number of nuclei can be expressed as:

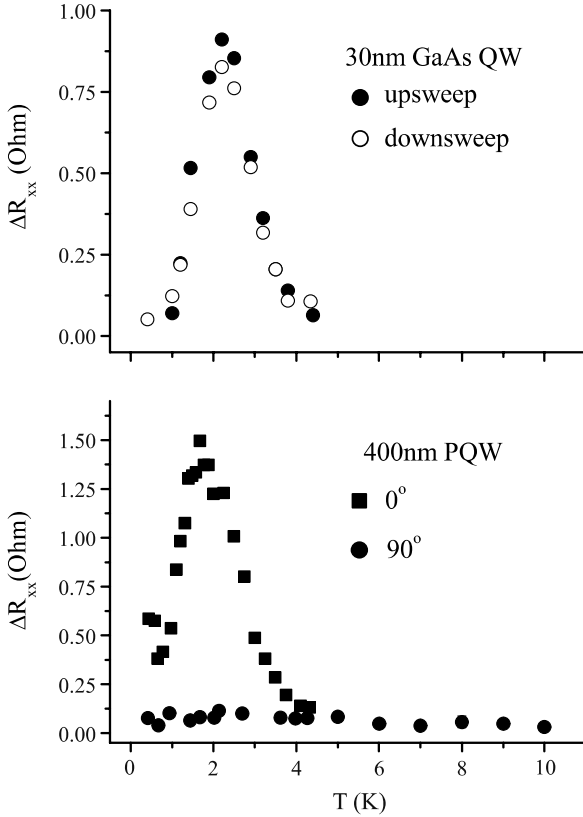


Fig. 4. Temperature dependence of the RDES amplitude in the 400-nm GaAs/AlAs PQW (*bottom*) and 30-nm GaAs square QW at 5.5 T (*top*)

$$\hat{H} = g_e \mu_B B_n \hat{S}_z, \quad (5)$$

where

$$B_n = b_n \int_{W_e/2}^{+W_e/2} \langle \hat{I}_z \rangle |\phi(z)|^2 dz \quad (6)$$

is the local nuclear hyperfine field associated with the enhanced Zeeman order on each isotope within the well and b_n is the hyperfine coupling constant of the given isotope. The total B_n field experienced by the electrons is the sum of the fields due to each isotope: $B_n^{\text{tot}} = B_n^{75} + B_n^{71} + B_n^{69}$. Due to the relative signs of g_e and γ_n (the nuclear gyromagnetic ratio) for all three isotopes in GaAs (as well as ^{27}Al), B_n^{tot} adds constructively to the applied field, thereby increasing the Zeeman splitting of the electron-spin system. Thus, the application of resonant microwaves yields a DNP enhancement of B_n which shifts the ESR line out of resonance and reduces the electron spin saturation. A steady state is reached wherein the rate of polarization is balanced by the rate of nuclear-spin relaxation. A sufficiently slow magnetic field downsweep starting on the high-field side of the resonance line, while

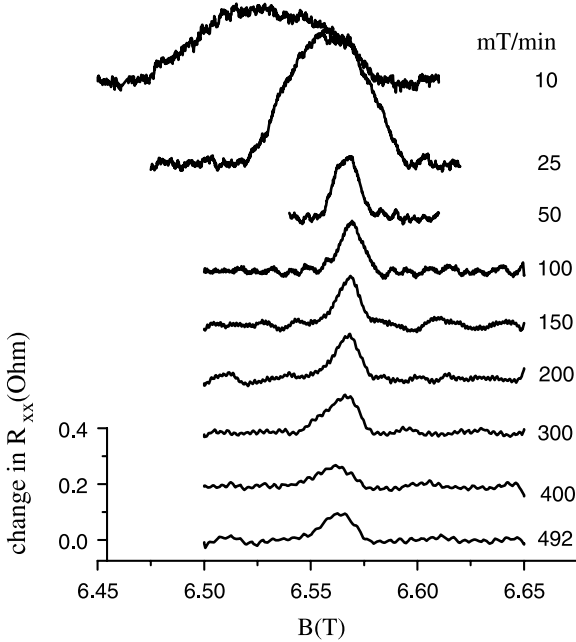


Fig. 5. Dynamic nuclear polarization in the 400-nm PQW in a high parallel field as a function of the field downswEEP rate, as indicated

applying the CW microwave field will produce a continuous increase in B_n , thereby “pinning” the ESR to the applied field [7, 12, 18]. However, if the field sweep is too rapid, the pinning condition cannot be sustained. The pinning effect can be used to enhance the nuclear field in contact with the 2DES appreciably, but it has not been previously demonstrated in a quasi-3DES.

Figure 5 demonstrates the pinning effect in the 400-nm PQW in a parallel field as a function of the downswEEP rate. Note that as the sweep rate is decreased from 490 to 50 mT/min, the amplitude of the RDESr peak increases, but does not broaden significantly. This same phenomenon, for which there is currently no explanation, was also noted in the 30-nm GaAs QW (at $\nu = 1$) [13]. Only at the two lowest sweep rates is any appreciable pinning observed. The ability to pin the ESR resonance to the applied field requires the rate of increase in B_n due to dynamic nuclear polarization, which is determined by the electron–nuclear crossrelaxation rate, to keep up with the rate of reduction of the applied field. The observation that the ESR can be pinned only at the reduced sweep rates, compared to the pinning effect observed in perpendicular field, is a strong indication that the electron–nuclear crossrelaxation rate is reduced in the parallel field, either due to a reduction in the contact interaction or change in the spectral density of the fluctuations in the hyperfine coupling. Such a conclusion is supported by the nuclear-spin relaxation time measurements shown in Fig. 6a.

The ability to spin polarize the nuclei in the QW by field-pinned DNP provides a convenient method for measuring the time constant τ_n for the

decay of B_n [7]. Following a DNP downsweep to initially polarize the nuclei, the microwaves are switched off, and the decay of the ESR line position is followed by successive rapid upsweeps of the field. Although the observed decay appears to be monoexponential, it should be recognized that τ_n does not correspond to the nuclear spin-lattice relaxation time of a single isotope. Neglecting spin diffusion, the B_n is expected to have the following functional form:

$$B_n(t) = \int |\phi(z)|^2 \sum_i b_n^i [\langle \hat{I}_z^i \rangle^{\text{eq}} (1 - e^{-t/T_1^i}) + \langle \hat{I}_z^i \rangle^\circ e^{-t/T_1^i}] dz, \quad (7)$$

where the summation extends over each isotope, and T_1^i and $\langle \hat{I}_z^i \rangle^\circ$ (the initial DNP-enhanced Zeeman order) both depend on the distance z from the center of the well. As shown in Fig. 6a, adherence to the Korringa law is observed at $\nu = 1$ for both $\theta = 0^\circ$ and 44° , but the slope with respect to $1/T$ is reduced upon tilting the sample. However, in the parallel orientation, the decay rate was temperature independent in the 1.5–5.0 K range, suggesting that one or more other background mechanisms for nuclear-spin relaxation (e.g., dipole–dipole, quadrupolar, spin-diffusion) dominate the relaxation in the quasi-3DES. One could speculate that this is due to the reduction in the

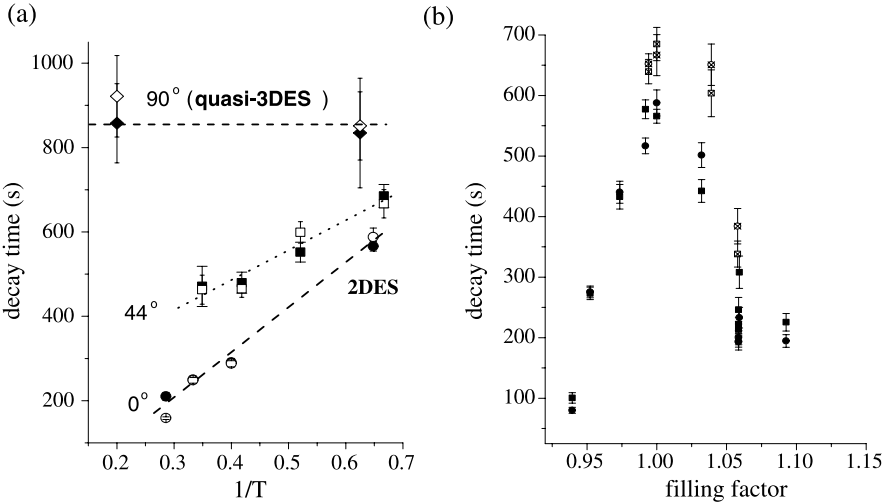


Fig. 6. (a) Temperature dependence of T_{1n} at 0° (circles), 44° (squares) and 90° (diamonds). The data at 0° and 44° were acquired at a filling factor $\nu = 1$ using microwave frequencies of 27.14 and 35.59 GHz, respectively. The data acquired at 90° was recorded at 36.65 GHz, a frequency that was selected to maximize the sensitivity. (b) Landau level filling factor dependence of the B_n decay constant, τ_n , at $T = 1.5$ K, and two different tilt angles: $\theta = 0^\circ$ (circles) and 44° (squares). Data acquired in the down- and upsweeps are displayed as open and filled symbols, respectively

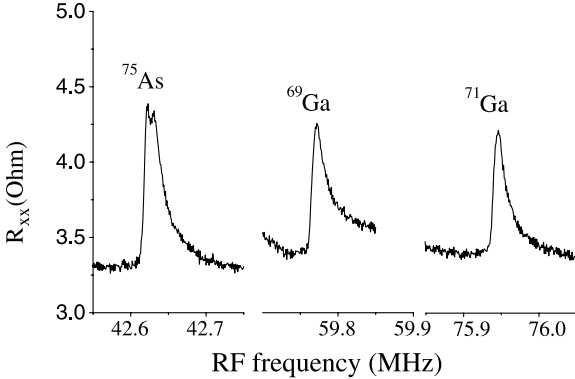


Fig. 7. RF swept RDENDOR transitions observed at filling factor $\nu = 1$ in the 400-nm wide GaAs/AlAs digital parabolic QW sample at $\theta = 16^\circ$ by continuous-wave microwave excitation of ESR at a steady-state nuclear field of 38 mT while sweeping the RF field at a rate of kHz/s with a frequency step size of 1 kHz

extent of the wavefunction, Δz , such that fewer nuclei are contacted in the high parallel field. In any case, the relaxation data are consistent with Fig. 5 where pinning is observed at only the lowest sweep rates.

Figure 6b presents the filling factor dependence of τ_n around $\nu = 1$ at two different orientations. The filling-factor dependence closely resembles that observed around $\nu = 1$ and $\nu = 3$ in narrow GaAs quantum wells [7, 12] and is consistent with Korringa-like relaxation.

Finally, we note that in principle the relative amplitude of the ^{27}Al RDENDOR signal (with respect to ^{75}As , for example) could be used to evaluate the extent of the electronic delocalization in a GaAs/AlAs PQW superlattice, since the variation of the Al content across the well is known. Figure 7 presents the ^{69}Ga , ^{71}Ga , and ^{75}As RDENDOR spectra recorded at the $\nu = 1$ resistance minimum by sweeping the radio frequency through each resonance line while the ESR transition is irradiated at fixed B . In this variation of the RDENDOR method, the steady-state B_n field is perturbed as the RF field is swept through the nuclear-spin resonance condition, resulting in a sudden increase in microwave absorption that is registered as a sharp increase in R_{xx} . Following passage through NMR resonance, DNP resumes, B_n is restored, and R_{xx} returns to its preresonant value [13]. The RDENDOR linewidths of the three isotopes were found to be 21, 22, and 30 kHz, respectively. The substantial line broadening is most likely a consequence of inhomogeneous electric quadrupole interactions associated with the residual strain in the digital AlAs/GaAs superlattice and/or band-bending effects. The relative signal amplitudes reflect differences in the local nuclear field associated with each isotope. In the case of the ^{75}As resonance, the onset of a splitting is apparent. Repeated attempts to observe a ^{27}Al were unsuccessful, even after

averaging 16 scans, despite the $>20:1$ signal-to-noise ratio obtained on the other three isotopes after only one scan.

5 Conclusions

To summarize, we have detected the ESR of conduction electrons in a PQW in both the perpendicular and parallel high magnetic fields. The amplitude of the ESR signal was much smaller in the parallel orientation and the linewidth was greater by about a factor of 2. The temperature dependence of the resistance change due to ESR at $\nu = 1$ was much more pronounced in the perpendicular orientation, resembling the temperature dependence observed in a 30-nm square quantum well at $\nu = 1$. In the parallel orientation, the signal was only weakly temperature dependent, and could be detected at temperatures as high as 10 K. The g -factor was found to be nearly independent of temperature in both orientations, indicating that the charge distribution does not change much in the 0.5–10 K range. A monotonic decrease in g by 5% could be induced by rotating the sample from $0^\circ \rightarrow 90^\circ$ as the system evolves from a 2DES to the equivalent of a 3DES at high field. The $g(\theta)$ dependence in the 400-nm PQW is distinctly different from the two previous experimental reports of g anisotropy in narrow GaAs/Al_{*x*}Ga_{*x-1*}As QWs. However, at all angles, the observed g -factor is close to that of bulk GaAs, indicating that the ESR signal arises mainly from electrons localized near the center of the PQW where the Al fraction is small. At zero field, seven subbands are occupied, but at high field, only the lowest subband is occupied. Thus, only this subband, which is resolved energetically from the higher subbands, contributes to the resonant microwave photoresistance signal. The observed g -factor is close to the $i = 1$ g -factor predicted by (3).

The 2DES and quasi-3DES are perhaps most clearly distinguished on the basis of the temperature dependence of the nuclear spin-lattice relaxation times. In the 3DES, a temperature independent decay constant of 900 s was observed, while in the 2DES, the relaxation time was substantially shorter (150–200 s) over the temperature range studied, and in addition, the Korringa law was observed. Differences in the nuclear-spin relaxation behavior are attributed to differences in the energy spectrum, density of states, electron–electron interactions, and hyperfine contact couplings.

The absence of an ^{27}Al RDENDOR signal, despite high signal-to-noise ratios for detection of the other isotopes, is consistent with the g -factor data. A likely explanation for these observations is as follows: in the wide PQW, the detected signal is derived primarily from the central part of the PQW structure where the mobility of the conduction channel is highest. Thus, the $g(\theta)$ dependence in the wide PQW appears to be dominated by the transport characteristics of the 3DES in this sample rather than nonparabolicity effects. The increased broadening of the ESR line observed in the parallel field is

consistent with an inhomogeneous distribution of g factors along the z -axis of the wide PQW.

Acknowledgements

This work was supported by NSF grant DMR-0106058, CNP/q-NSF U.S.-Brazil Cooperative Research Grant 0334573. J.D.C. received financial support from a University of Florida Aschoff Dissertation Fellowship. Technical support was provided by G. Labbe and J. Graham of the UF Physics Department. Provision of the digital parabolic quantum well sample by A.I. Toropov and A.K. Bakarov of the Institute of Semiconductor Physics, Novosibirsk, Russia, is gratefully acknowledged.

References

1. A. Poggio et al., Phys. Rev. Lett. **91**, 207602 (2001) 1, 2
2. C. Weisbuch, C. Hermann, Phys. Rev. B **15**, 816 (1977) 1
3. M. Schulte, J.G.S. Lok, G. Denninger, W. Dietsche, Phys. Rev. Lett. **94**, 137601 (2005) 1
4. H.W. van Kesteren et al., Phys. Rev. B **61**, 426 (1989) 1
5. R. Bottcher et al., Phys. Status Solidi B **58**, K23 (1973) 1
6. S. Sergio et al., Phys. Rev. B **64**, 115314 (2001) 2, 4
7. A. Berg, M. Dobers, R.R. Gerhardtts, K. v. Klitzing, Phys. Rev. Lett. **64**, 2563 (1990) 2, 8, 9, 10
8. C.P. Slichter, *Principles of Magnetic Resonance*, 3rd edn. (Springer, New York, 1990) 3
9. G. Gervais et al., Phys. Rev. Lett. **94**, 196803 (2005) 3
10. H.A. Fertig et al., Phys. Rev. B **55**, 10671 (1997) 3
11. L.A. Tracy et al., Phys. Rev. B **73**, 121306 (2006) 3
12. E. Olshanetsky et al., Phys. Rev. B **67**, 165325 (2003) 4, 6, 8, 10
13. E. Olshanetsky et al., Physica B **373**, 182–193 (2006) 4, 8, 10
14. J.D. Caldwell, C.R. Bowers, G.M. Gusev, Phys. Rev. B **72**, 115339 (2005) 5
15. M. Dobers, K. v. Klitzing, G. Weimann, Solid State Commun. **70**, 41–44 (1989) 5
16. P. Le Jeune et al., Semicond. Sci. Technol. **12**, 380 (1997) 5
17. Z. Wilamowski, W. Jantsch, Phys. Rev. B **69**, 035328 (2004) 5
18. C. Hillman, H.W. Jiang, Phys. Rev. B **64**, 201308 (2001) 8

Index

AlAs/GaAs, 1

DNP, 6

dynamic nuclear polarization, 2, 8

ESR, 1

GaAs/AlAs, 1

local nuclear field, 10

nuclear-spin relaxation time, 8

parabolic quantum well, 1

resistively detected ESR, 1

resistively detected nuclear magnetic
resonance, 3

“This page left intentionally blank.”

Electron-Spin Manipulation in Quantum Dot Systems

Yasuhiro Tokura^{1,2}, Toshiaki Obata¹, Tsuyoshi Hatano¹, and
Seigo Tarucha^{1,3}

¹ Quantum Spin Information Project, ICORP, JST, Atsugi-shi,
Kanagawa 243-0198, Japan
tokura@nttbl.jp

² NTT Basic Research Laboratories, NTT Corporation, Atsugi-shi,
Kanagawa 243-0198, Japan

³ Department of Applied Physics, University of Tokyo, Hongo, Bunkyo-ku,
Tokyo 113-8656, Japan

Abstract. Recent experimental and theoretical progress as regards the full manipulation of electron spins in quantum dot systems is reviewed. In order to realize coherent single-spin manipulation, we propose quantum-dot devices with an integrated high-frequency line designed to generate an ac magnetic field. We also discuss in detail the electric dipole spin resonance realized with a slanting Zeeman field. After discussions of the exchange coupling between the two electron spins in a double quantum-dot system, we present current spectra of a hybrid vertical-lateral double quantum-dot device.

1 Introduction

The rapidly developing young fields of spin electronics (or spintronics) and quantum information science have led to a strong interest in the ability to probe and coherently manipulate electron spins. In particular, a single electron spin $1/2$ confined in a solid-state environment such as a quantum dot, has been put forward as a natural quantum two-level system for implementing quantum bits (qubits).

Semiconductor quantum dots (QDs) are man-made structures that can confine conduction electrons in semiconductors with a nanometer-size volume. We can precisely control various QD parameters, for example, dot size, potential barrier height/width, and potential symmetry, by designing the device layout using advanced nanofabrication techniques or by controlling the gate voltages statically and dynamically. The electrons can be controlled and monitored individually, starting from zero [1, 2]. The potentially long spin-coherence time in quantum dots [3] is another driving force behind the study of spin qubits. Of the numerous proposals for systems that realize “qubit” assemblies, the Loss and DiVincenzo proposal [4] has stimulated continuing experimental efforts to realize universal unitary gate operations, which comprise single-qubit rotation and a two-qubit CNOT gate, using electron spins.

This chapter reviews our recent experimental and theoretical progress as regards the full manipulation of electron spins in quantum-dot systems. For related recent reviews, please see [5, 6]. In Sect. 2, we discuss single-spin manipulation. Electron-spin resonance (ESR) is an established method for controlling electron spins. However, in the context of quantum computing, we need individual access to single spins. For that purpose, we discuss quantum-dot devices with an integrated high-frequency line designed to generate an ac magnetic field near the quantum dot. An electron spin is generally very weakly coupled to its environment compared with an electron charge. The result is that the coherence time for electron spins is much longer than those for electron charges. On the other hand, electron-spin- (especially single electron-spin) based systems are much harder to control than charge-based systems. Therefore, we suggest an alternative method, namely electric-dipole spin resonance, and we detail our proposal, which uses a slanting Zeeman field.

In Sect. 3, we discuss the exchange coupling between the two electron spins in a double quantum-dot system. Using the Hund–Mulliken approximation, we derived a general expression for the exchange coupling constant J for (asymmetric) double quantum dots. We also present current spectra of a hybrid vertical-lateral double quantum dot device. The electron number in each dot and the tunnel coupling can be controlled precisely. Section 4 provides our conclusions and the future outlook.

2 Single-Spin Manipulation

Single electron-spin resonance (SESR) plays a key role in realizing electron-spin-qubit rotation. It must be time controlled and selective for each spin. The SESR Hamiltonian is

$$H_{\text{ESR}} = g\mu_{\text{B}}(B_0 S_z + B_{\text{ESR}} \sin(2\pi\nu t) S_x) \quad (1)$$

$$= \frac{1}{2}\epsilon_z \sigma_z + \frac{1}{2}\epsilon_x \sin(2\pi\nu t) \sigma_x, \quad (2)$$

where $S_{x,z} = \frac{1}{2}\sigma_{x,z}$ are electron-spin operators, which are expressed with the Pauli electron-spin matrices. $\epsilon_z = g\mu_{\text{B}}B_0$ is the Zeeman energy induced by a uniform magnetic field B_0 with g the effective g-factor and $\mu_{\text{B}} = \frac{e\hbar}{2m}$ the Bohr magneton. $\hbar = \frac{h}{2\pi}$, e and m are a reduced Planck's constant, the elementary charge, and the mass of an electron, respectively. In the following, we focus on arguing the manipulation of electron spins in a semiconductor material, GaAs. Although the bulk g-factor of GaAs is $g = -0.44$, the value is different when the electrons are confined in quantum wells or QDs [7]. The experimentally evaluated $|g|$ value has reported values of 0.37 [8], 0.27–0.29 [9, 10], and 0.16 [11] for two-dimensional QDs confined with surface gates, and 0.25 [12] for a vertical QD. Here, we use a representative value for the effective g-factor $|g|$ of 0.3. The oscillating magnetic field, B_{ESR} determines

$\epsilon_x \equiv g\mu_B B_{\text{ESR}}$. When the microwave (mw) frequency ν is chosen to be in resonance with the Zeeman energy; $\epsilon_z = h\nu$, the dynamics of the spin becomes the rotation around the x -axis with the frequency $f_x \equiv \epsilon_x/(2\hbar)$ [13]. The time necessary for the electron spin, initially in the spin-up state, and being driven to the spin-down state (π operation), is $T_\pi = 1/(2f_x) = \hbar/\epsilon_x$, which is $T_\pi \sim 240 \text{ ns}/B_{\text{ESR}}$ (mT) for GaAs QD. When such an electron spin, initially in the spin-up state, is influenced by B_{ESR} for a period $T_\pi/2$ ($\pi/2$ operation), the final state is a linear superposition state of spin up and spin down. The characteristic time for the decay of such a coherent superposition is T_2 , which is a crucial parameter for quantum computing. Although the electron-spin coherence time T_2 of GaAs is still a big issue, a coherence time for two-electron spin states in coupled quantum dots exceeding $1 \mu\text{s}$ was recently observed using spin-echo techniques on a two-electron system [14]. Therefore, a B_{ESR} of more than 1 mT seems desirable for coherent SESR.

SESR has not yet been detected in semiconductor QDs. (Recently, an ESR scheme for one of the two electrons in a coupled QD system has been demonstrated [15].) With SESR it is difficult to introduce a high-frequency ($\sim 10 \text{ GHz}$) selective magnetic field at a QD in a cryogenic (100 mK) setup. It is also difficult to apply an ESR field with a conventional method using waveguides and microwave cavities because of high-frequency radiation, which heats the spin qubit limiting the operating temperature to 1 K. One viable approach consists of producing a local ESR field using an onchip mw coil or resonator. A second viable approach is to rotate spin that is coupled to an electric dipole driven with an ac electric field (electric dipole spin resonance).

2.1 Oscillating Magnetic Field

Here, we review an onchip mw coil and resonator designed to generate a local ac magnetic field B_{ESR} ($\sim \text{mT}$) in order to realize SESR in GaAs quantum-dot devices. The ac magnetic field is induced by an ac current driven through a metal line in the vicinity of the dot as shown in Fig. 1a [16]. A current of several mA is required to generate a magnetic field at the dot. We use semirigid and flexible coaxial cables to bring the microwave signal (10 MHz–50 GHz) to the sample. The coaxial line is connected to the onchip ac line via

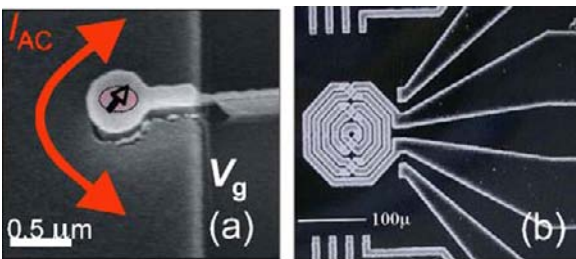


Fig. 1. Scanning electron microscope (SEM) pictures of (a) ac magnetic field generator around a vertical QD [16] and (b) one design of an onchip coil

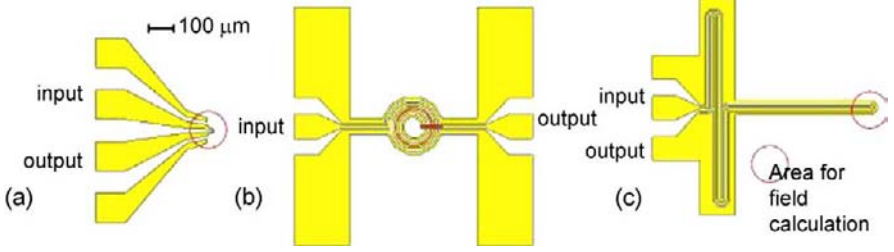


Fig. 2. Three designs for onchip mw circuits: (a) single line, (b) onchip coil, (c) onchip resonator. The *dark regions* are metallic pads and the *circles* indicate the areas where the electric and magnetic fields are calculated

a 50- Ω impedance-matched coplanar waveguide and Au bonding wires. We measure the electron transport through the dot for various ac currents and find evidence for the presence of an ac electric field in the form of photon-assisted tunneling (PAT) and current rectification [12]. We have been unable to detect any effect of the ac magnetic field on SESR, probably because the ac magnetic field at the spin position is too weak due to impedance mismatch.

We now propose a new design for a metal line to generate an ac magnetic field of more than 1 mT [17]. The onchip high-frequency line designs are shown in Fig. 2. All the patterns are designed to produce a magnetic field perpendicular to the surface and to have QDs very near the surface. (a) is the first trial of a single line pattern (half-turn coil), where impedance matching is taken into account. (b) is the onchip coil. A different design for a coil fabricated on GaAs is shown in Fig. 1b. (c) is a previously proposed onchip resonator [18, 19] that we modified so that it had a node at the edge. The resonance frequency was adjusted to around 20 GHz.

We performed high-frequency (20 GHz) electromagnetic simulations using the three device designs shown in Fig. 2. The thickness of the pattern was set at 1 μm . The inplane component of the ac electric field and the perpendicular component of the ac magnetic field are shown in Fig. 3 as a function of the distance from a QD located at the center of the circles in Fig. 2. The electric field induces PAT and the magnetic field causes ESR. The excitation is 1 V at the input port and the output port is ideally grounded. The other metallic pads shown in the design are also grounded. The inplane component of the ac magnetic field is negligible. The onchip resonator can produce the largest magnetic field and it produces a larger electric field than the onchip coil pattern. The single line pattern produces the largest electric field.

Can we maintain a low temperature if a mA current causes Joule heating? The resonant frequency of 20 GHz corresponds to a magnetic field of about 4.8 T and energy equivalent to 1 K. The electron temperature should be less than 1 K to detect the electron spin imparted by the tunneling current to the lead [9]. The dilution refrigerator that we use has a cooling power of 1 mW at 300 mK, which is equal to the total power dissipated by an impedance-

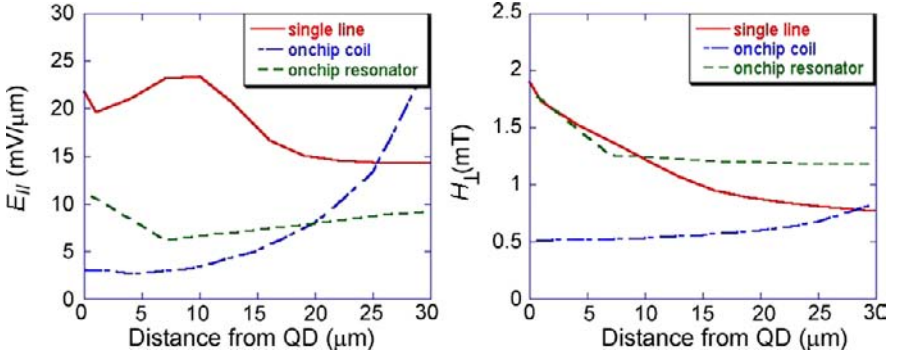


Fig. 3. Evaluation of electric and magnetic fields from onchip mw circuits. *Left*: in-plane component of ac electric field, *right*: perpendicular component of ac magnetic field at 20 GHz

matched (50Ω) oscillating current of about 4 mA. A coaxial cable from the source at room temperature is thermally contacted at 4 K and is connected to a superconducting coaxial cable and then a short copper cable to the sample. The corresponding input power to the sample is 0 dBm ($= 1\text{ mW}$) and the input voltage is 220 mV. Since the estimated cable loss is 4 dB, the necessary input power from the source is +4 dBm. Assuming a mw line resistance of 15Ω at 20 GHz, which is estimated from a typical value of DC residual resistance and a surface skin depth, the power dissipated in the sample is about $240\mu\text{W}$. From Fig. 3, we expect $B_{\text{ESR}} \sim \frac{220\text{ mV}}{1\text{ V}} \times 1.8 \sim 0.4\text{ mT}$ for an onchip resonator. Koppens and coworkers [15] reports that $B_{\text{ESR}} = 0.59\text{ mT}$ at 1 mA, while the coil (stripline) design is different and the frequency (200 MHz) is much smaller.

2.2 Slanting Zeeman Field

Although the electric field does not usually affect the spin states, it couples strongly to the orbital states (electric dipole). Therefore, if we can “mix” the spin and orbital degrees of freedom in a controlled way, we can manipulate the spin caused by the electric field effectively. Spin-orbit (SO) coupling is one of the candidates for mixing the spin and orbital states. Electrical control of the effective g-factor has been demonstrated in an $\text{Al}_x\text{Ga}_{1-x}\text{As}$ parabolic quantum well, where a parabolic spatial change in the Al concentration introduces an inhomogeneous g-factor [20]. This method is useful for addressing individual spins caused by fine electric gates with a uniform magnetic field, however, the system itself does not mix the spin and orbital states in the lowest approximation. By exploiting strong anisotropies in the effective g-factor tensor \hat{g} , the electron spins at a GaAs/AlGaAs semiconductor heterostructure can be manipulated by GHz-frequency control of the gate voltage (g-tensor modulation resonance g-TMR) [21]. The

Hamiltonian is expressed by $H_{g\text{-TMR}} = \mu_B \mathbf{S} \cdot \hat{\mathbf{g}}(V(t)) \cdot \mathbf{B}$. Recently, electric dipole spin resonance (EDSR) caused by various SO coupling mechanisms was argued for the electrons in a parabolic quantum well [22, 23]. The SO interaction Hamiltonian for a two-dimensional electron system is $H_{\text{SO}} = H_{\text{D}} + H_{\text{R}}$, where the Dresselhaus term $H_{\text{D}} = \alpha_{\text{D}}(\sigma_x k_x - \sigma_y k_y)$ and the Rashba term $H_{\text{R}} = \alpha_{\text{R}}(\sigma_x k_y - \sigma_y k_x)$, where α_{D} , α_{R} characterize the SO interactions and $k_{x/y}$ indicates two-dimensional kinetic momenta. The in-plane (time-dependent) electric field has finite coupling to the electron spin, subject to a magnetic field. Another EDSR scheme consists of a QD containing a single electron facilitated with two gates to create an alternating electric field [24]. The estimated effective oscillating field is 1 mT for an electric field of 10^2 V/cm for GaAs quantum dots. The strained semiconductor film enables spin manipulation even without a magnetic field [25].

An alternative method recently proposed by our group, is to modulate a QD electric field in a nonuniform magnetic field [26]. This scheme eliminates the need for SO coupling, as opposed to earlier work on electron-spin control based on g-tensor modulation [21], and on electric fields [22–24]. Instead, ESR is achieved by applying microwave gate voltage pulses, and letting the electron position in a QD oscillate in a static slanting Zeeman field. Note the analogy with the Stern–Gerlach experiment, where the spin and orbital degrees of freedom are coupled by employing an inhomogeneous magnetic field. The spatial oscillation of the electron within the QD involves the hybridization of orbital states, as depicted schematically in Fig. 4a for the two lowest orbital states, $n = 1, 2$. This effectively provides the electron spin with the necessary time-dependent transverse magnetic field. We find that we can achieve an effective ESR magnetic field of 1.5 mT per millivolt of gate voltage modulation and a slanting magnetic field of the order of $1 \text{ T}/\mu\text{m}$.

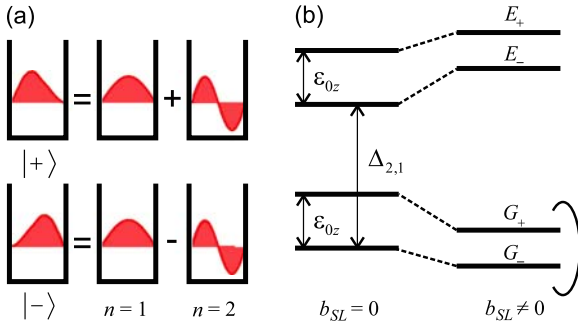


Fig. 4. (a) Schematic representation of how a spatial oscillation between wavefunctions $|+\rangle$ and $|-\rangle$ involves the hybridization of multiple orbital states. (b) Energy spectrum of a quantum dot (QD) with two orbital levels (level spacing $\Delta_{2,1}$) and constant Zeeman energy ε_{0z} with/without a magnetic field gradient b_{SL} . The lowest levels, $|G_{\pm}\rangle$, constitute a qubit. $|E_{\pm}\rangle$ are excited states, which are energetically separated from $|G_{\pm}\rangle$ and are neglected in the qubit dynamics

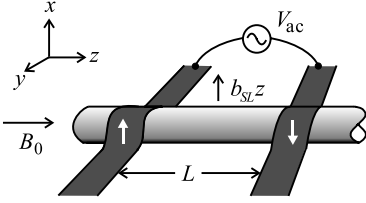


Fig. 5. Model of a one-dimensional (1D) QD in a slanting Zeeman field. Ferromagnetic gate electrodes (*dark gray*) are located at either end of the dot and are magnetically polarized in the plus/minus x -direction, creating a magnetic-field gradient b_{SL} . A uniform magnetic field B_0 is applied in the z -direction. The spin in the dot is controlled by applying an oscillating voltage V_{ac} between the two gates

A possible realization of the system is presented in Fig. 5. A quasi-1D conductor such as a carbon nanotube, [27] semiconductor nanowire, or gate-defined quantum wire, is gated by ferromagnetic electrodes that define both the tunnel barriers of the QD and the slanting magnetic field. In this configuration, the magnetic field is given by $\mathbf{B} = b_{SL}z\mathbf{i}_x + (B_0 + b_{SL}x)\mathbf{i}_z$, where B_0 is the external uniform magnetic field parallel to the z -axis and b_{SL} is the z -direction gradient of the field parallel to the x -axis. The middle point of the QD corresponds to $z = 0$. We assume a true 1D system or two-dimensional (2D) QD formed at a heterostructure with an electron strongly confined in the x -direction. Therefore, the inhomogeneous term along the z -axis, $b_{SL}x\mathbf{i}_z$, can be eliminated (which was present so that \mathbf{B} obeyed Maxwell's equations). A magnetic field gradient b_{SL} of more than $1 \text{ T}/\mu\text{m}$ can be obtained with a standard micromagnet material [28, 29].⁴

We now derive the effective Hamiltonian of the hybrid spin qubit, taking into account the corrections to the slanting form. To that end, we start with a time-independent Hamiltonian that describes the dynamics of a single electron confined in a 2D QD in the absence of a high-frequency electric field

$$H = H_0 + W\sigma_x, \quad (3)$$

$$H_0 = E_0 - \frac{\hbar^2}{2m^*}(\partial_y^2 + \partial_z^2) + V(y, z) - \frac{g\mu_B}{2}B_0\sigma_z, \quad (4)$$

$$W = -\frac{g\mu_B}{2}b_{SL}z, \quad (5)$$

where m^* is the electron effective mass and $\boldsymbol{\sigma} = (\sigma_x, \sigma_y, \sigma_z)$ the Pauli spin matrices. In general, the vector potential originating from the slanting field may couple to the orbital motion and modify the QD wavefunctions (a uniform inplane field B_0 does not couple). Here, this effect can be neglected if we assume relatively strong lateral confinement $V(y, z)$. The eigenvalues of H_0 are $\epsilon_{pn\sigma} = \epsilon_{pn} + \frac{1}{2}g\mu_B B_0\sigma$ with eigenfunctions $\langle y, z | p, n, \sigma \rangle = \phi_{pn}(y, z)\psi_\sigma$,

⁴ Very recently, EDSR signals had been observed in a series double QD with slanting field by a Co micromagnet [30].

where $n = 1, 2, \dots$, $\sigma = \pm 1$ and ψ_σ is the spinor. We only consider the symmetric confinement potential: $V(y, z) = V(y, -z)$ and the index $p = e$ (o) implies the even (odd) parity of the wavefunction $\phi_{pn}(y, z)$ with respect to the change of the sign z . The ground-state wavefunction has even parity, $\phi_{e1}(y, z)$. The Hamiltonian matrix (3) expanded with the eigenvalues of H_0 can be block-diagonalized with the two subsets of the eigenstates: $[|e, n, +1\rangle, |o, n, -1\rangle]$ and $[|e, n, -1\rangle, |o, n, +1\rangle]$. The ground states of these blocks constitute our “qubit”,

$$H|G\sigma\rangle = \mathcal{E}_{G\sigma}|G\sigma\rangle, \quad (6)$$

$$|G\sigma\rangle = C_{e,1,\sigma}|e, 1, \sigma\rangle + \sum_{p=e/o, k} C_{p,k,\sigma_p}|p, k, \sigma_p\rangle, \quad (7)$$

where $\sigma_p = \sigma$ for $p = e$ and $\sigma_p = -\sigma$ for $p = o$. We assumed that the spin excitation energy (Zeeman energy $\varepsilon_{0z} \equiv g\mu_B B_0$) is smaller than the orbital excitation energy: $\varepsilon_{0z} < \min\{\varepsilon_{o1}, \varepsilon_{e2}\} - \varepsilon_{e1}$. The eigenenergy $\mathcal{E}_{G\sigma}$ and coefficients of eigenfunctions C_{p,n,σ_p} are obtained by perturbation theory. For a weak perturbation of W , $|C_{e,1,\sigma}| \sim 1$ and the obtained qubit is nearly the same as a “pure” spin qubit $|e, 1, \sigma\rangle$. The “qubit” energy levels are separated by $\varepsilon_z \equiv \mathcal{E}_{G+1} - \mathcal{E}_{G-1}$, which is slightly smaller than the raw Zeeman energy, ε_{0z} as shown in Fig. 4b.

The inplane electric field, $e\mathbf{E}(t) \cdot \mathbf{z}$, couples the states $|G+1\rangle$ and $|G-1\rangle$, but has no effect on the diagonal part $\langle G\sigma|z|G\sigma\rangle = 0$. The leading ESR component is obtained by

$$\begin{aligned} \varepsilon_x \sin(2\pi\nu t) &\equiv 2\langle G+1|e\mathbf{E}(t) \cdot \mathbf{z}|G-1\rangle \\ &= 2e \frac{V_{\text{ac}}}{L} \sin(2\pi\nu t) \langle e1|z|o1\rangle (C_{o,1,\sigma} + C_{o,1,-\sigma}), \end{aligned} \quad (8)$$

where V_{ac} is the applied high-frequency voltage between the gate electrodes, L is the gate separation shown in Fig. 5 and ν is the mw frequency. In the lowest-order perturbation, $C_{o,1,\sigma} = \frac{\langle e1|W|o1\rangle}{\varepsilon_{e1} - \varepsilon_{o1} + \varepsilon_{0z}\sigma}$. Thus, the effective ESR Hamiltonian (1) is obtained. It should be noted that addressing an individual qubit is easy since the ESR field is very local and can be reproduced for each dot. In the analysis, we used the material parameters of GaAs and a confinement energy of the order of 1 meV, which corresponds to $\langle e1|z|o1\rangle \sim 24 \text{ nm}$ [26]. The corresponding ESR magnetic field is about 1.5 mT at a 1 mV modulation amplitude, $L = 0.8 \mu\text{m}$, hence an electric field of 12.5 V/cm, and $b_{\text{SL}} \sim 1 \text{ T}/\mu\text{m}$. The electric field required to achieve a 1-mT oscillating field using micromagnets is about ten times smaller than that using the SO interaction [24].

Acoustic phonon scattering can cause orbital relaxation between the “qubit” states, since we hybridize the spin and orbital degrees of freedom. The timescale characterizing the electron spin, initially in the up state, to decay into the down state is T_1 [3, 9]. We estimated $T_1 \sim 2.1 \text{ ms}$ at $B_0 = 2 \text{ T}$, which is dominated by transverse piezoelectric scattering [26]. Since the dephasing effect without relaxation is negligible, the coherence time T_2 is $2T_1$.

The quality factor Q is estimated by dividing T_2 by the time required for π operation: T_π , which is of the order of 10^4 .

3 Two-Spin Interaction

To realize the necessary unitary operations for the quantum computation algorithm, controlled-NOT (CNOT) or a swap operation is essential for the two qubits. Following the original proposal of [4], we rely on the exchange interaction allowed from the finite tunnel coupling between two quantum dots. The low-energy spin dynamics is described by an isotropic Heisenberg interaction

$$\mathcal{H}_S = J\mathbf{S}_R \cdot \mathbf{S}_L + g\mu_B\mathbf{B}_0 \cdot (\mathbf{S}_R + \mathbf{S}_L), \quad (9)$$

where \mathbf{S}_ν ($\nu = R/L$) represents a localized electron spin in the left (L) or right (R) quantum dot. Therefore, an estimation of the exchange coupling J is vital to the two-spin qubit operation. There have been several reports on the estimation of J [6, 31–33]. The estimation of J in symmetric double dots with a Gaussian confinement potential and a magnetic field was done in [31, 32] and was generalized to an asymmetric system in [33]. More detailed evaluation of J with various tunneling barrier shapes was done in [6]. We discuss the general low-energy properties of the double quantum-dot system using a Hund–Mulliken approximation with the notations of Burkard et al. [33]. We focused particularly on the situation when the two dots are not equivalent [33] or when there is a finite energy offset between the two dots [34]. We fabricated a hybrid vertical-lateral double-dot device, consisting of laterally coupled vertical quantum dots in a few-electron regime and measured its electric properties.

3.1 Formulation

We study two electron states in closely located quantum dots (L) and (R). When there is no tunneling between these two dots, the two-electron ground state consists either of each dot being occupied by one electron with spin up or down or one of the two dots being occupied by two electrons in the spin singlet state (if the magnetic field is not very strong). If the tunneling is turned on but is not very strong compared with the single-particle energy-level spacing of each dot, only the ground-state wavefunctions are relevant and are weakly perturbed. Starting from the approximate ground-state wavefunctions localized to two local minima $\nu = L$ and R , we obtain two orthonormalized wavefunctions $\phi_\nu(r)$ using the overlap integral S [34]. In the following discussions, we consider a zero magnetic field ($B_0 = 0$) or an inplane magnetic field and these wavefunctions are real.⁵ With these wavefunctions, the Hamiltonian $\mathcal{H} = T + C$ can be formulated as in the Hubbard model.

⁵ The effect of a magnetic field perpendicular to the tunneling direction has been studied in detail in [6, 31–33] using various model potentials.

The kinetic term is $T = \sum_{\sigma} \sum_{\nu} \epsilon_{\nu} a_{\nu\sigma}^{\dagger} a_{\nu\sigma} + \sum_{\sigma} (t a_{L\sigma}^{\dagger} a_{R\sigma} + \text{H.C.})$, where $\epsilon_{\nu} \equiv \langle \nu | h | \nu \rangle$ and $t \equiv \langle \nu | h | \bar{\nu} \rangle$ using a single-particle Hamiltonian h . The interaction term is $C = \frac{1}{2} \sum_{\sigma\sigma'} \sum_{\nu,\nu',\nu'',\nu'''} \langle \nu\nu' | V | \nu''\nu''' \rangle a_{\nu\sigma}^{\dagger} a_{\nu'\sigma'}^{\dagger} a_{\nu''\sigma''} a_{\nu'''\sigma'}$, where the Coulomb matrix elements are

$$\begin{aligned} \langle \nu\nu' | V | \nu''\nu''' \rangle &= \int d\mathbf{r} d\mathbf{r}' \phi_{\nu}(r) \phi_{\nu'}(r') V(r, r') \phi_{\nu''}(r) \phi_{\nu'''}(r') \\ &= \langle \nu'\bar{\nu} | V | \nu''\bar{\nu} \rangle \\ &= \langle \nu\nu''' | V | \nu''\nu' \rangle. \end{aligned} \quad (10)$$

We used the symmetry of the (screened) Coulomb interaction kernel $V(r, r') = V(r', r)$ and the realness of the wavefunctions for the last two equations. We name several Coulomb matrix elements to clarify the following discussions, the intradot Coulomb interaction energies: $\langle \nu\nu | V | \nu\nu \rangle \equiv U_{\nu}$, the interdot Coulomb interaction energy: $\langle \nu\bar{\nu} | V | \nu\bar{\nu} \rangle \equiv V_{\text{inter}}$, the exchange energy in the tunnel barrier $\langle \nu\bar{\nu} | V | \bar{\nu}\nu \rangle \equiv V_x$, and the remaining energies $\langle \nu\nu | V | \nu\bar{\nu} \rangle \equiv W_{\nu}$ [35]. The naming of the intradot/interdot Coulomb interaction is physically accurate solely for the limit of the vanishing overlap integral S . In general, $U_{\nu} > V_{\text{inter}} > V_x$, $W_{\nu} > 0$, and for the two equivalent dots, $U_L = U_R$ and $W_L = W_R$.

We then construct a six-dimensional two-particle Hilbert space with

$$\begin{aligned} |S_a\rangle &= \frac{1}{\sqrt{2}} (a_{L\uparrow}^{\dagger} a_{R\downarrow}^{\dagger} - a_{L\downarrow}^{\dagger} a_{R\uparrow}^{\dagger}) |0\rangle, \\ |S_b\rangle &= \frac{1}{\sqrt{2}} (a_{L\uparrow}^{\dagger} a_{L\downarrow}^{\dagger} + a_{R\uparrow}^{\dagger} a_{R\downarrow}^{\dagger}) |0\rangle, \\ |S_c\rangle &= \frac{1}{\sqrt{2}} (a_{L\uparrow}^{\dagger} a_{L\downarrow}^{\dagger} - a_{R\uparrow}^{\dagger} a_{R\downarrow}^{\dagger}) |0\rangle, \\ |T^1\rangle &= a_{L\uparrow}^{\dagger} a_{R\uparrow}^{\dagger} |0\rangle, \\ |T^0\rangle &= \frac{1}{\sqrt{2}} (a_{L\uparrow}^{\dagger} a_{R\downarrow}^{\dagger} + a_{L\downarrow}^{\dagger} a_{R\uparrow}^{\dagger}) |0\rangle, \\ |T^{-1}\rangle &= a_{L\downarrow}^{\dagger} a_{R\downarrow}^{\dagger} |0\rangle, \end{aligned}$$

where the vacuum $|0\rangle$ is two empty dots. If the Coulomb interaction is not very strong and the degeneracy of the lowest empty levels is lifted, two dots with filled shells could be assumed as $|0\rangle$. We took account of a single level (for example, s-orbital) in each dot and neglected excited levels (p-orbitals). The above six-dimensional Hilbert space is not sufficient when the offset $|\epsilon_L - \epsilon_R|$ is comparable to single-dot singlet-triplet energy separation, $V_{\text{intra},s-p} - V_{x,s-p}$, where $V_{\text{intra},s-p}$ and $V_{x,s-p}$ are the intradot Coulomb energy and the exchange energy between s- and p-orbitals, respectively. We obtain the matrix elements of the Hamiltonian \mathcal{H} with these states. For example, $\langle S_a | C | S_a \rangle = V_{\text{inter}} + V_x > \langle T^0 | C | T^0 \rangle = V_{\text{inter}} - V_x$, where the inequality can be understood by noting that electrons with parallel spin avoid each other and gain Coulomb energy $2V_x$ (exchange energy) because of the Pauli exclusion principle. The

eigenenergies of the triplet states $|T^{\pm 1,0}\rangle$ are degenerate when there is no magnetic field, given by

$$E_T = \epsilon_L + \epsilon_R + V_{\text{inter}} - V_x. \quad (11)$$

The eigenenergies of singlet states, $E_{S0} < E_{S1} < E_{S2}$, are obtained from the Hamiltonian matrix,

$$H_s = E_T + \frac{1}{2}U_H + 2V_x + \begin{pmatrix} -\frac{1}{2}U_H & 2t_H & \delta W \\ 2t_H & \frac{1}{2}U_H & F \\ \delta W & F & \frac{1}{2}U_H - 2V_x \end{pmatrix}, \quad (12)$$

where we defined $F \equiv \epsilon_L - \epsilon_R + (U_L - U_R)/2$, $t_H \equiv t + (W_L + W_R)/2$, $\delta W \equiv W_L - W_R$, $U_H \equiv (U_L + U_R)/2 - V_{\text{inter}}$. An example of the numerical results is shown in Fig. 6.

First, we consider $F = 0$ when the singlet ground state is the largest. Please note that for the asymmetric dot, the condition of $F = 0$ deviates from the one-electron zero-offset condition $\epsilon_L = \epsilon_R$. We have $E_{S0} = E_T + 2V_x + \frac{1}{2}(U_H - \sqrt{U_H^2 + (4t_H)^2}) + b\delta W^2$, to the lowest order in δW , where the small parameter b is positive for $t_H \ll U_H$. The exchange coupling energy J is defined by the energy difference between the triplet and the singlet ground states:

$$J|_{F=0} \equiv E_T - E_{S0} = \frac{1}{2}(\sqrt{U_H^2 + (4t_H)^2} - U_H) - 2V_x - b\delta W^2, \quad (13)$$

which reduces to a familiar form $J = 4t_H^2/U_H - 2V_x$ with $t_H \ll U_H$ and for symmetric dots [31, 33]. If $\delta W = 0$, the wavefunction of the singlet ground state is

$$|\Psi_{S0}\rangle = \frac{1}{\sqrt{1 + \phi^2}}(|S_a\rangle - \phi|S_b\rangle), \quad (14)$$

where $\phi \equiv J|_{F=0}/2t_H$. With increasing $|F|$, the ground-state energy of the singlet state decreases monotonically. When $|F| \sim U_H$, the lowest two-spin

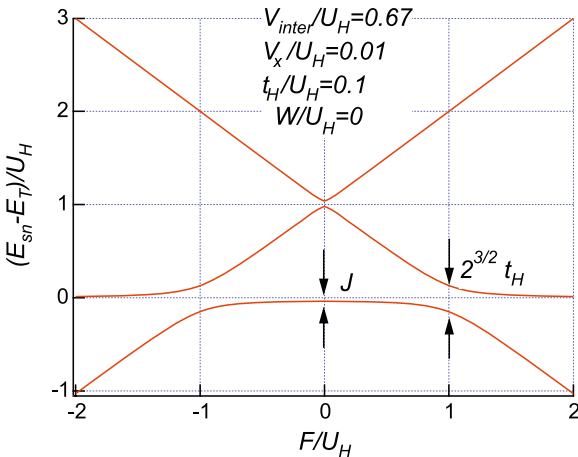


Fig. 6. Solution of (12) evaluated numerically, for $V_{\text{inter}}/U_H = 0.67$, $V_x/U_H = 0.01$, $T_H/U_H = 0.1$, $\delta W/U_H = 0$. The energies of the spin singlet states are measured from that of the spin triplet state

singlet states S_0 and S_1 anticross with a separation of $\sim 2\sqrt{2}t_H$, as shown in Fig. 6. We can have a simple expression in the limit of large energy offsets, $F \rightarrow \infty$. The energy of the ground state is $E_{S_0} \sim 2\epsilon_R + U_R$ and that of the first excited singlet is $E_{S_1} = E_T + 2V_x - 4t_H\delta W/F + \{4t_H^2(U_H - \delta W) + U_H\delta W^2\}/F^2$. Therefore, the energy difference between the excited singlet and the ground triplet states is

$$J_{S_1-T} \equiv E_{S_1} - E_T = 2V_x - \frac{4t_H\delta W}{F} + \frac{4t_H^2(U_H - \delta W) + U_H\delta W^2}{F^2}. \quad (15)$$

The exchange energy $2V_x$ can be obtained by measuring J_{S_1-T} in the limit of large $|F|$ unless the other two electron states originating from the single-particle excited states of each dot cross over [36]. When the asymmetry is absent ($\delta W = 0$), the energy splitting J_{S_1-T} reduces to $2V_x$ with F^{-2} . We suggest that J_{S_1-T} is related to the critical magnetic field as regards the sudden increase in leakage current in spin-blockaded quantum dots [36–38]. The inplane magnetic field dominantly lifts the triplet-state degeneracy, and when one of the triplet levels crosses over the S_1 level, nuclear-spin-mediated spin-transition (flip-flop type) is allowed and the current starts to flow. In this system, the source–drain voltage controls the offset F , and we may determine δW or other parameters.

We can use the local two electron spin-singlet basis instead of $|S_2\rangle, |S_3\rangle$,

$$\begin{aligned} |S_R\rangle &= a_{R\uparrow}^\dagger a_{R\downarrow}^\dagger |0\rangle, \\ |S_L\rangle &= a_{L\uparrow}^\dagger a_{L\downarrow}^\dagger |0\rangle. \end{aligned}$$

Then, using the basis ($|S_1\rangle, |S_R\rangle, |S_L\rangle$), the Hamiltonian (12) becomes,

$$H_s = E_T + \frac{1}{2}U_H + 2V_x + \begin{pmatrix} -\frac{1}{2}U_H & \frac{2t_H + \delta W}{\sqrt{2}} & \frac{2t_H - \delta W}{\sqrt{2}} \\ \frac{2t_H + \delta W}{\sqrt{2}} & \frac{1}{2}U_H - F - V_x & V_x \\ \frac{2t_H - \delta W}{\sqrt{2}} & V_x & \frac{1}{2}U_H + F - V_x \end{pmatrix}. \quad (16)$$

The two-spin singlet states $|S_1\rangle$ and $|S_R\rangle$ come into resonance when $F = U_H - V_x$ (see the first and the second diagonal elements). Therefore, near this value of F , we can neglect the effect of $|S_L\rangle$ and we obtain the two lowest eigenenergies simply by using the upper 2×2 matrix of (16). The result is $E_{0,1} = E_T + 2V_x - \frac{1}{2}(\epsilon \pm \sqrt{\epsilon^2 + 2(2t_H - \delta W)^2})$, where we defined the energy offset from the resonance $\epsilon \equiv F - (U_H - V_x)$ [38]. This result is not accurate for the asymptotic regime, namely for ϵ or $F \rightarrow \infty$. In this approximation, the energy split between the first excited spin singlet state and the spin triplet state is

$$E_{S_1} - E_T = 2V_x + \frac{1}{2F}(2t_H - \delta W)^2, \quad (17)$$

where, in contrast to (15), the F^{-1} term persists even for the symmetric case ($\delta W = 0$). The difference between these two approaches is depicted in Fig. 7 in a log–log plot. As can be seen, the $1/F^2$ dependence is missing for the approximation curve.

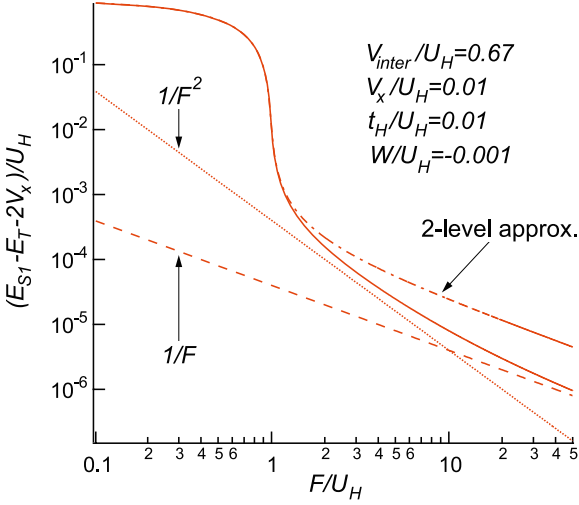


Fig. 7. Log-log plot of the eigenenergies evaluated numerically, for $V_{inter}/U_H = 0.67$, $V_x/U_H = 0.01$, $t_H/U_H = 0.01$, $\delta W/U_H = -0.001$. The energies of the spin singlet states are measured from that of the spin triplet state $+2V_x$

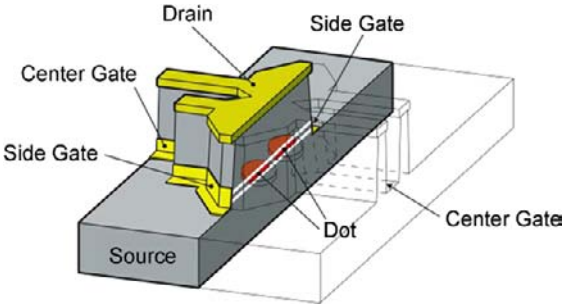


Fig. 8. Schematic of the hybrid vertical-lateral double-dot device

3.2 Hybrid Double Dots

The value of the exchange coupling J was determined in an ellipsoidal quantum dot [39] by measuring the cotunneling current for various magnetic fields and in lateral double dots with various offset energies in the very weak tunneling regime [14]. The latter utilizes the pulse sequence to the gates and finite inhomogeneous nuclear fields. The measurement of J in the sequential tunneling and cotunneling regimes in series double quantum dots has been proposed [40]. However, there are two difficulties with the series dot configurations. The first is that except for the ‘triple point’ where the energies of three states (N_L, N_R) , $(N_L + 1, N_R)$, $(N_L, N_R + 1)$, are the same, the current is strongly suppressed. Here, (N_L, N_R) represents the occupancy of N_L (N_R) electrons in the left (right) dot. The second is that the finite source–drain voltage may affect the energy offset $\epsilon_L - \epsilon_R$, and nonlinear spectroscopy as discussed in [40] cannot determine J accurately.

As shown in Fig. 8, we measured Coulomb oscillations in a unique hybrid vertical-lateral double-dot device, which consists of two laterally coupled ver-

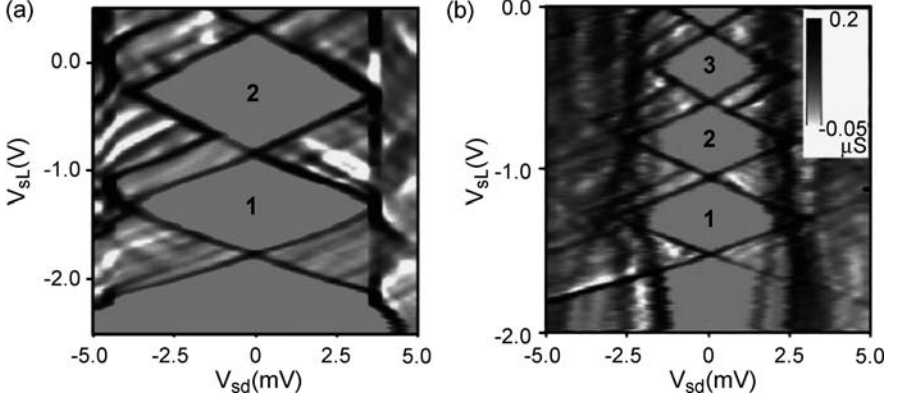


Fig. 9. Differential conductance dI_{sd}/dV_{sd} vs. V_{sd} and V_{sL} (V_{sR}) measured for the left dot with $V_{sR} = -1.4$ V and center gate voltage $V_c = -1.3$ V (a) and the right dot with $V_{sR} = -2.4$ V and $V_c = -0.6$ V (b)

tical dots with four split gates [41, 42]. Two of the gates (side gates) are used to tune the electron number in each dot independently, and the remaining two gates (center gates) are used to tune the interdot tunnel coupling. Current I_{sd} flows in the vertical direction through the two dots connected in parallel when source–drain voltage V_{sd} is applied. The measurements were performed in a dilution refrigerator at a base temperature of 20 mK employing a dc measurement system. The electron temperature is about 110 mK estimated from the width of the Coulomb oscillation peaks. The maximum applied voltage is 5 mV and the current is about 5 nA. The power dissipated into the device, ~ 25 pW, is much smaller than the cooling power of our refrigerator. We measured the nonlinear I – V characteristics of the left and right dots. Figure 9a (b) shows grayscale plots of the differential conductance dI_{sd}/dV_{sd} of the left (right) dot as a function of V_{sd} and the left (right) side gate voltages V_{sL} (V_{sR}) at the right (left) side gate voltage V_{sR} (V_{sL}) = -1.4 (-2.4) V and the center gate voltage $V_c = -1.3$ (-0.6) V. Several Coulomb diamonds are clearly observed. When the left and right side gate voltages became smaller than ~ -2 V, we were no longer able to observe Coulomb diamond, and confirmed that the electron numbers in the two dots are counted one by one starting from zero.

A grayscale plot of the Coulomb oscillations as a function of V_{sL} and V_{sR} at $V_c = -1.2$ (-0.5) V and $V_{sd} = 8$ μ V is shown in Fig. 10a (b). As shown in Fig. 10a, the Coulomb oscillation peaks changing the number of electrons in the left dot (vertical lines) and those changing electrons in the right dot (horizontal lines) cross perpendicularly. Thus, the two dots do not couple when there are few electrons in each dot. When V_c increases to -0.5 V, diagonal gaps, or “anticrossings” appear at the Coulomb oscillation vertices resulting in a hexagonal stability diagram [43] as shown in Fig. 10b. These

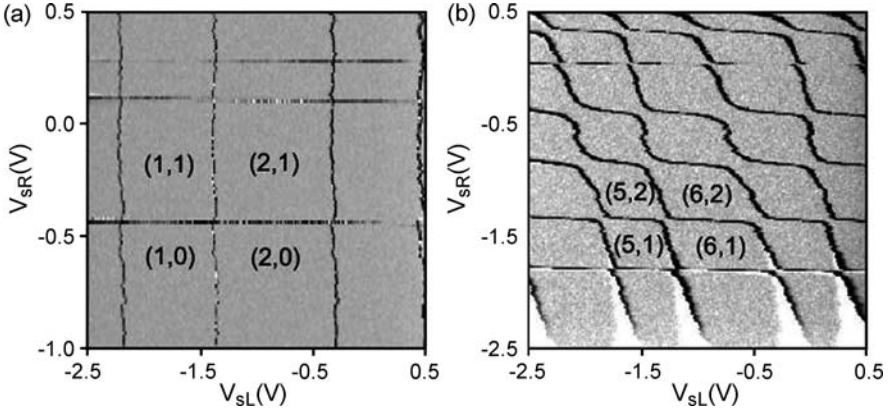


Fig. 10. Linear conductance vs. V_{sL} and V_{sR} measured for $V_c = -1.2$ V (a) and -0.5 V (b)

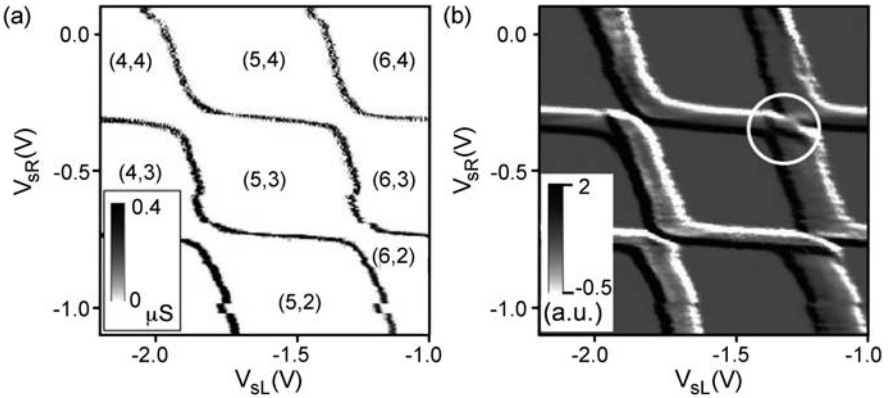


Fig. 11. Charging diagram at a fixed center gate voltage $V_c = -0.55$ V and $V_{sd} = 8$ μ V (a) and $V_{sd} = -300$ μ V (b). The line of the excited molecular state is observed in the band region of finite conductance from the (5, 3) state to the (6, 4) state

anticrossings result from both quantum-mechanical tunnel coupling and the interdot Coulomb interaction.

When the offset between the levels of the two dots changes, the molecular levels anticross with the minimum energy separation $2t$ between the two levels. A grayscale plot of the differential conductance $(dI_{sd}/dV_{sL} + dI_{sd}/dV_{sR})/\sqrt{2}$ at $V_c = -0.55$ V and $V_{sd} = 8$ μ V (-300 μ V) is shown in Fig. 11a (b). In this region, where (N_L, N_R) transits from (5, 3) to (6, 4), the line of the excited state clearly shows the antibonding states. The estimated tunnel coupling energy is 120 μ eV. This tunnel coupling energy can be controlled by controlling V_c and the magnetic field.

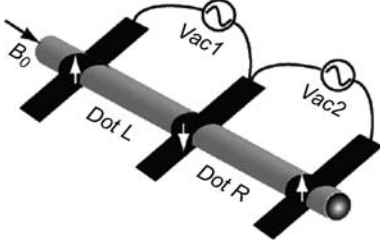


Fig. 12. Schematic of coupled 1D dots with ferromagnetic electrodes magnetized in antiparallel configuration. A uniform magnetic field is applied in parallel to the wire

3.3 Double QD with Slanting Zeeman Field

Here, we present a realization of a two-qubit gate based on the two coupled dots discussed in Sect. 2.2 in series with an alternately magnetized electrode as shown in Fig. 12. Although it has been pointed out that an inhomogeneous magnetic field introduces swap errors [44, 45], we show that correct swap operation is possible in our system. The two-qubit Hamiltonian is $\mathcal{H} = \sum_{\nu=L,R} \mathcal{H}_{0\nu} + \mathcal{H}_T + \mathcal{H}_V$, where $\mathcal{H}_{0\nu}$ is the single-dot Hamiltonian (see (1)) $\nu = L, R$ (ac field is off, $\epsilon_x = 0$ and with intradot Coulomb interaction U), \mathcal{H}_T represents the tunneling between the dots, and \mathcal{H}_V represents the interdot interaction V_{inter} . We assume that the two dots are nominally the same and there are no offsets and we disregard the other Coulomb matrix elements, V_x and W_ν . By projecting the Hamiltonian onto the qubits, we find

$$\mathcal{H}_{0\nu} = \frac{\epsilon_z}{2} \sum_{\sigma} \sigma c_{\nu\sigma}^{\dagger} c_{\nu\sigma} + U n_{\nu\uparrow} n_{\nu\downarrow}, \quad (18)$$

$$\mathcal{H}_T = \sum_{\sigma} [t_{\sigma} c_{L\sigma}^{\dagger} c_{R\sigma} + s_{\sigma} c_{L\sigma}^{\dagger} c_{R-\sigma} + \text{H.C.}], \quad (19)$$

$$\mathcal{H}_V = V_{\text{inter}} \sum_{\sigma\sigma'} n_{L\sigma} n_{R\sigma'}, \quad (20)$$

where $c_{\nu\sigma}$ annihilates an electron of pseudospin σ in dot ν . A spin-dependent tunneling term t_{σ} and a tunneling term with spin-flip s_{σ} emerge, which are defined by $t_{\sigma} = C_{e,1,\sigma}^2 t_{e1,e1} - C_{o,1,-\sigma} C_{o,1,-\sigma} t_{o1,o1} + 2C_{e,2,\sigma} t_{e1,e2}$, $s_{\sigma} = (C_{o,1,\sigma} - C_{o,1,-\sigma}) t_{e1,o1}$, where $t_{pn,p'n'}$ represents the tunneling amplitude from level (pn) in dot L to level $(p'n')$ in dot R. We used the symmetry of the coefficients $C_{o,n,\sigma}^L = -C_{o,n,\sigma}^R$ since the magnetization of the magnets is staggered (Fig. 12), and we neglected the index L/R. The relevant lowest four eigenenergies and their eigenfunctions are obtained by the effective exchange Hamiltonian using local spin operators:

$$\mathcal{H}_S = J_{\parallel} S_{Lz} S_{Rz} + J_{\perp} (S_{Lx} S_{Rx} + S_{Ly} S_{Ry}) + \varepsilon_z (S_{Lz} + S_{Rz}), \quad (21)$$

where $J_{\parallel} = \frac{2(t_{\uparrow}^2 + t_{\downarrow}^2)}{U_H} - \frac{4s_{\sigma}^2 U_H}{U_H^2 - \epsilon_z^2}$, $J_{\perp} = \frac{4t_{\uparrow} t_{\downarrow}}{U_H}$, $\varepsilon_z = \epsilon_z (1 - \frac{2s_{\sigma}^2}{U_H^2 - \epsilon_z^2})$, and $U_H \equiv U - V_{\text{inter}}$. In contrast to the isotropic Heisenberg coupling of spins

(see (9)), the exchange-coupling energy becomes anisotropic. It is well known that the SO interaction makes the exchange Hamiltonian anisotropic [46]. Unlike the SO case, where the antisymmetric term ($\mathbf{S}_L \times \mathbf{S}_R$) dominates, the dominant anisotropic correction of \mathcal{H}_S in a slanting field is the symmetric term. Nevertheless, CNOT operation can be accomplished by this anisotropic exchange Hamiltonian simply by replacing the J of the Heisenberg Hamiltonian with J_{\parallel} , and single-qubit operation (SESR) can be achieved by replacing ϵ_z with ε_z , as shown in [45, 46].

4 Conclusion

In this chapter we reviewed our progress on spin manipulation in semiconductor quantum dots. A high-frequency local ac magnetic field can be obtained by using an onchip resonator. As seen in Fig. 2, the design cannot address individual qubits because it is still very large and in practice, two or more quantum dots could be accommodated. The proposed single ESR scheme with a slanting Zeeman field can realize an ESR field up to 1.5 mT per millivolt gate modulation. Addressing individual qubits is easy since the ESR field is very local and can be reproduced for each dot. Combining the onchip resonator with a magnetic field gradient generated by a micromagnet in each dot would be another way to obtain individual access to an ensemble of qubits.

The exchange interaction between two electrons is estimated for an asymmetric double dot in a zero magnetic field. The contribution of exchange energy in the tunnel barrier V_x can be estimated by the energy difference between the excited singlet and triplet ground states under large energy offset conditions. The hybrid vertical-lateral double-dot device can accommodate electrons one by one by controlling the side gates, and the tunnel coupling is precisely controlled by the center gates. Hence, the exchange coupling parameter J between the two electron spins in the two dots can be temporally controlled, enabling two spins to be swapped [4].

Acknowledgments

We thank W.G. van der Wiel, M. Pioro-Ladrière, T. Kodera, and T. Kubo for useful discussions.

References

1. S. Tarucha, D.G. Austing, T. Honda, R.J. van der Hage, L.P. Kouwenhoven, *Phys. Rev. Lett.* **77**, 3613 (1996) 15
2. M. Ciorga, A.S. Sachrajda, P. Hawrylak, C. Gould, P. Zawadzki, S. Juliano, Y. Feng, Z. Wasilewski, *Phys. Rev. B* **61**, R16315 (2000) 15

3. T. Fujisawa, D.G. Austing, Y. Tokura, Y. Hirayama, S. Tarucha, *Nature* **419**, 278 (2002) 15, 22
4. D. Loss, D.P. DiVincenzo, *Phys. Rev. A* **57**, 120 (1998) 15, 23, 31
5. V. Cerletti, W.A. Coish, O. Gywat, D. Loss, *Nanotechnology* **16**, R27–R49 (2005) 16
6. W.G. van der Wiel, M. Stopa, T. Kodera, T. Hatano, S. Tarucha, *New J. Phys.* **8**, 28 (2006) 16, 23
7. E.L. Ivchenko, A.A. Kiselev, *Pis'ma Zh. Éksp. Teor. Fiz.* **67**, 41 (1998) (*JETP Lett.* **67**, 43 (1998)) 16
8. R.M. Potok, J.A. Folk, C.M. Marcus, V. Umansky, M. Hanson, A.C. Gossard, *Phys. Rev. Lett.* **91**, 016802 (2003) 16
9. R. Hanson, B. Witkamp, L.M.K. Vandersypen, L.H. Willems van Beveren, J.M. Elzerman, L.P. Kouwenhoven, *Phys. Rev. Lett.* **91**, 196802 (2003) 16, 18, 22
10. L.H. Willems van Beveren, R. Hanson, I.T. Vink, F.H.L. Koppens, L.P. Kouwenhoven, L.M.K. Vandersypen, *New J. Phys.* **7**, 182 (2005) 16
11. A. Kogan, S. Amasha, D. Goldhaber-Gordon, G. Granger, M.A. Kastner, H. Shtrikman, *Phys. Rev. Lett.* **93**, 166602 (2004) 16
12. T. Kodera, W.G. van der Wiel, T. Maruyama, S. Tarucha, in *Proc. Int. Symp. on Mesoscopic Superconductivity and Spintronics 2004 (MS+S2004)* (World Scientific, Singapore, 2005) 16, 18
13. C.P. Slichter, *Principles of Magnetic Resonance* (Springer, Berlin, 1990) 17
14. J.R. Petta, A.C. Johnson, J.M. Taylor, E.A. Laird, A. Yacoby, M.D. Lukin, C.M. Marcus, M.P. Hanson, A.C. Gossard, *Science* **309**, 2180 (2005) 17, 27
15. F.H.L. Koppens, C. Buizert, K.J. Tielrooij, I.T. Vink, K.C. Nowack, T. Meunier, L.P. Kouwenhoven, L.M.K. Vandersypen, *Nature* **442**, 766 (2006) 17, 19
16. T. Kodera, W.G. van der Wiel, K. Ono, S. Sasaki, T. Fujisawa, S. Tarucha, *Physica E* **22**, 518 (2004) 17
17. T. Obata, Y. Tokura, S. Tarucha, *Rev. Sci. Instrum.* **78**, 104704 (2007) 18
18. A. Blais, R.-S. Huang, A. Wallraff, S.M. Girvin, R.J. Schoelkopf, *Phys. Rev. A* **69**, 062320 (2004) 18
19. A. Wallraff, D.I. Schuster, A. Blais, L. Frunzio, R.-S. Huang, J. Majer, S. Kumar, S.M. Girvin, R.J. Schoelkopf, *Nature* **431**, 162 (2004) 18
20. G. Salis, Y. Kato, K. Ensslin, D.C. Driscoll, A.C. Gossard, D.D. Awschalom, *Nature* **414**, 619 (2001) 19
21. Y. Kato, R.C. Myers, D.C. Driscoll, A.C. Gossard, J. Levy, D.D. Awschalom, *Science* **299**, 1201 (2003) 19, 20
22. A.L. Efros, E.I. Rashba, *Phys. Rev. B* **73**, 165325 (2006) 20
23. E.I. Rashba, A.L. Efros, *Phys. Rev. Lett.* **91**, 126405 (2003) 20

24. V.N. Golovach, M. Borhani, D. Loss, Phys. Rev. B **74**, 165319 (2006) 20, 22
25. Y. Kato, R.C. Myers, A.C. Gossard, D.D. Awschalom, Nature **427**, 50 (2004) 20
26. Y. Tokura, W.G. van der Wiel, T. Obata, S. Tarucha, Phys. Rev. Lett. **96**, 047202 (2006) 20, 22
27. M.J. Biercuk, S. Garaj, N. Mason, J.M. Chow, C.M. Marcus, Nano Lett. **5**, 1267 (2005) 21
28. J. Wròbel, T. Dietl, A. Lusakowski, G. Grabecki, K. Fronc, R. Hey, K.H. Ploog, H. Shtrikman, Phys. Rev. Lett. **93**, 246601 (2004) 21
29. M. Pioro-Ladrière, Y. Tokura, T. Obata, T. Kubo, S. Tarucha, Appl. Phys. Lett. **90**, 024105 (2007) 21
30. M. Pioro-Ladrière, T. Obata, Y. Tokura, Y.-S. Shin, T. Kubo, K. Yoshida, T. Taniyama, S. Tarucha, Nat. Phys. **4**, 776 (2008) 21
31. G. Burkard, D. Loss, D.P. DiVincenzo, Phys. Rev. B **59**, 2070 (1999) 23, 25
32. X. Hu, S. Das Sarma, Phys. Rev. A **61**, 062301 (2000) 23
33. G. Burkard, G. Seelig, D. Loss, Phys. Rev. B **62**, 2581 (2000) 23, 25
34. J. Schliemann, D. Loss, A.H. MacDonald, Phys. Rev. B **63**, 085311 (2001) 23
35. Y. Tokura, D.G. Austing, S. Tarucha, J. Phys. Condens. Matter **11**, 6023 (1999). In the analysis of Coulomb matrix elements, V_x and W_V were neglected, since they are very small in a vertical quantum dot 24
36. K. Ono, D.G. Austing, Y. Tokura, S. Tarucha, Science **297**, 1313 (2002) 26
37. K. Ono, S. Tarucha, Phys. Rev. Lett. **92**, 256803 (2004) 26
38. F.H.L. Koppens, J.A. Folk, J.M. Elzerman, R. Hanson, L.H. Willems van Beveren, I.T. Vink, H.P. Tranitz, W. Wegscheider, L.P. Kouwenhoven, L.M.K. Vandersypen, Science **309**, 1346 (2005) 26
39. D.M. Zumbühl, C.M. Marcus, M.P. Hanson, A.C. Gossard, Phys. Rev. Lett. **93**, 256801 (2004) 27
40. V.N. Golovach, D. Loss, Phys. Rev. B **69**, 245327 (2004) 27
41. T. Hatano, M. Stopa, T. Yamaguchi, T. Ota, K. Yamada, S. Tarucha, Phys. Rev. Lett. **93**, 066806 (2004) 28
42. T. Hatano, M. Stopa, S. Tarucha, Science **309**, 268 (2005) 28
43. W.G. van der Wiel, S. De Franceschi, J.M. Elzerman, T. Fujisawa, S. Tarucha, L.P. Kouwenhoven, Rev. Mod. Phys. **75**, 1 (2003) 28
44. R. de Sousa, X. Hu, S. Das Sarma, Phys. Rev. A **64**, 042307 (2001) 30
45. X. Hu, R. de Sousa, S. Das Sarma, Phys. Rev. Lett. **86**, 918 (2001) 30, 31
46. G. Burkard, D. Loss, Phys. Rev. Lett. **88**, 047903 (2002) 31

Index

coherent single-spin manipulation, 15

Coulomb oscillations, 27

electric-dipole spin resonance, 16

hybrid double dots, 27

single-spin manipulation, 16

slanting Zeeman field, 15, 16, 19

spin manipulation, 19, 20, 31

vertical-lateral double quantum dot,
15, 16

Resistively Detected NMR in GaAs/AlGaAs

Guillaume Gervais

Physics Department, McGill University, 3600 rue Université, Montréal,
Qc H3A 2T8 Canada
gervais@physics.mcgill.ca

Abstract. Since its development in the late 1940s, nuclear magnetic resonance (NMR) has emerged as a powerful technique for probing the local field distribution in liquid and solid matter as well as providing important information on spin and vortex dynamics. While significant progress has been achieved in NMR spectroscopy, conventional *inductively detected* NMR remains essentially a *bulk* technique that proves to be extremely difficult to scale down to systems of very small sizes. For the most part, NMR remains limited to systems with a total number of nuclear spins present in the sample exceeding $\sim 10^{16}$, hence prohibiting the NMR detection in a wide variety of systems. Recent advances in the engineering, design and fabrication of meso- and nanoscaled materials have resulted in an experimental measurement gap where conventional NMR techniques cannot be utilized because of the “too few spins” problem. For example, a GaAs/AlGaAs semiconductor heterostructure interface ~ 30 nm wide has less than 10^{15} nuclear spins, a quantum dot $\sim 10^6$ – 10^{10} spins and a single carbon nanotube 10^3 spins. The very few nuclei available in these systems makes traditional NMR measurements extremely difficult, if not totally impossible, unless the NMR detection scheme could be redefined in an entirely new way.

One appealing alternative to the conventional inductive NMR exists and makes it possible to obtain the nucleus’ point-of-view in GaAs-based semiconductors through a resistive detection. This approach seems promising to tackle a broader class of problems in systems of small sizes such as mesoscopic quantum dots and other nanostructures. We shall review here the state-of-the-art in the field of resistively detected NMR, and discuss recent advances such as the relaxation-time experiments and the development of pulsed techniques. Finally, we discuss how resistively detected NMR might be pushed towards the bottom so as to obtain a complete nucleus’ point-of-view of the nanoscale with “very little spins”.

1 Nuclear Magnetic Resonances with ‘Too Few Spins’

1.1 The ‘Too Few Spins’ Problem

The Conventional NMR of Bloch and Purcell

Since its development in the late 1940s independently by Bloch [1] and Purcell [2], nuclear magnetic resonance (NMR) has emerged as a complete spectroscopic tool that uses the nuclear spin to probe the local field distribution in liquid and solid matter as well as providing important information on spin and vortex dynamics. In fact, NMR has by now become so routine that it is used to tackle problems ranging from protein folding to the vortices in high- T_c materials, as well as brain imaging and quantum computing. The rapid development of the NMR technique in the 1950s to its wide range of known applications has crowned NMR as a true champion technique with seemingly endless possibilities, for as long as one can find matter with nonzero nuclear spins. Still, all the way at the bottom of the scale, where materials are currently being engineered and patterned into systems and devices with micro- and nanoscopic size, the opposite could not be more true, for the ‘too few spins’ problem must first be overcome before NMR can reveal any useful information.

In conventional NMR, an antenna is used to resonantly drive the nuclei at the Larmor frequency of the nuclear species under investigation. The nuclear magnetic resonance is then detected in the same electromagnetic device through its effect on the quality factor of the resonant circuit driving the nuclear system. Modern techniques use pulse sequences to detect the resonance in a similar way through the induction of a macroscopic current in the antenna after having disturbed the nuclei from equilibrium with a train-of-pulse. The energy involved here between the state of the nuclei in equilibrium *before* the disturbance, and that created *after* the pulse is, nevertheless, extremely small, and can be estimated to $\sim 10^{10}$ eV for the $\sim 10^{22}$ protons contained in a 1 cc volume of water, for example. As a consequence, the voltage induced across the antenna by the buildup of these $\sim 10^{22}$ protons is approximately ~ 0.1 volt. While this is clearly macroscopic and in the observable range, the technique of nuclear detection by an electromagnetic device remains unfortunately extremely hard to scale down to systems with far fewer nuclear spins owing to the detection limits of the very small voltage induced in the NMR coil, typically in the μV range. As a general guideline, with today’s available state-of-the-art radio-frequency (RF) electronics, conventional NMR remains limited to measuring bulk systems containing more than $\sim 10^{16}$ nuclear spins and has little hope to be improved over the several orders of magnitudes needed to reach the meso- or nanoscopic limit.

NMR for Nanostructured Materials

The recent advances in the design of nanostructured materials and devices have created an experimental measurement gap where conventional NMR is most often impossible because of the ‘too few spin’ problem. As examples, a typical GaAs/AlGaAs single semiconductor heterostructure ~ 30 nm wide has less than $\sim 10^{15}$ nuclear spins available to NMR, a quantum dot $\sim 10^6$ to 10^{10} , and a single carbon nanotube less than $\sim 10^3$ nuclear spins (for ^{13}C). Several techniques have been devised throughout the years to obtain NMR information on smaller systems, yet they often require narrow constraints in the chosen system, or temperature region where the experiments can be performed. For instance, the physics of the fractional quantum Hall regime where many-body quantum phenomena such as fractionalized charge excitations and quantum statistics occur, and the physics of coherent manipulation and detection of quantum states, all call for a noninvasive way to obtain NMR information at temperatures very near the absolute zero, $T \sim 50$ mK or less. Furthermore, since the NMR sensitivity of an electromagnetic device cannot be improved by the several orders of magnitudes needed for nanostructures, the NMR detection scheme has to be redefined altogether; one possible solution to the problem might come from the hyperfine interaction that exists between the electronic and nuclear spin degree-of-freedom.

1.2 Electrons as an In-Situ Detector of the NMR

Electrical Detection of the NMR in GaAs/AlGaAs in 1988

In the last section, we discussed how an extremely large number of nuclei are required for detecting the NMR inductively in an electromagnetic device. Despite this, several other schemes have been employed in the past that to some degree have gone around the problem and allow the probing of much smaller samples. These include, for example, the recent advances in magnetic resonance force microscopy [3], dynamical nuclear pumping of the nuclei via optical techniques [4], the all-optical NMR techniques [5], and the so-called resistively detected NMR [6] that make use of the particularly strong hyperfine coupling existing at GaAs/AlGaAs semiconductor interfaces to obtain a signal. While all of these techniques can extend the reach of NMR to systems with smaller number of spins, the latter technique is particularly appealing for a wide variety of problems involving nanostructures in GaAs, for it makes use of the electrons as an in-situ detector of the NMR.

Historically, electrical detection of the NMR was clearly demonstrated in 1988 in a seminal experiment conducted by a team led by K. von Klitzing [6]. In this experiment, the nuclear magnetic resonance of a GaAs/AlGaAs heterostructure was electrically detected for the first time. In their experiment, depicted in Fig. 1, the magnetoresistivity of the two-dimensional electron gas confined at the interface, ρ_{xx} , was recorded at low temperatures

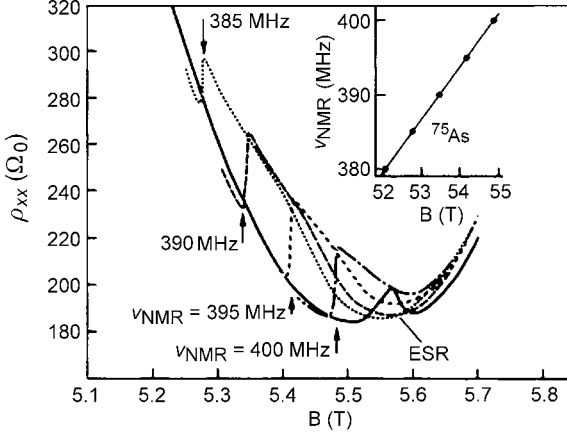


Fig. 1. First electrical detection of the NMR in a GaAs/AlGaAs heterostructure. The magnetoresistivity, ρ_{xx} , is shown at near-complete filling of the third Landau level by electrons under continuous microwave radiation (GHz) and radio-frequency (MHz) radiation. The *solid trace* is for an upsweep in magnetic field, and the other traces for a downsweep. The measurements for the NMR signal of the ^{75}As nucleus are shown at four different radio-frequencies ranging from 38 to 40 MHz, with the *inset* showing the linear dependance in field, as expected from the Larmor frequency. After Dobers et al. [6]

($T \sim 300$ mK) under continuous microwave (\sim GHz) and radio-frequency radiation (\sim MHz) while the magnetic field was slowly swept across the NMR resonance of frequency $\nu_{nmr} = \gamma H_0$, where $\gamma = 7.29$ MHz/T for the $I = \frac{3}{2}$ nuclei of ^{75}As . Here, the suffix xx in ρ_{xx} refers to the longitudinal element of the resistivity tensor ρ_{ij} (for a two-dimensional electron sheet) as opposed to ρ_{xy} , the Hall resistivity (or Hall voltage divided by the current). At the magnetic field corresponding to the NMR frequency, ν_{NMR} , a small but sizable change in magnetoresistivity $\delta\rho_{xx}$ was observed, which demonstrated unambiguously that the nuclear resonance can be detected by means of resistivity only. In this scheme, the newly redefined NMR “detector” is the electrons in situ and it does not rely on the total number of nuclear spins of the sample, but rather on the subtle hyperfine interaction $\mathcal{A} \cdot S$ that exists between the electron (S) and the nuclear spin (I).

The Strong Overhauser Field of GaAs/AlGaAs

In GaAs, the hyperfine interaction that couples the electronic and nuclear spins is particularly strong, and is at the origin of the electrical detection of the NMR signal. In the case of a two-dimensional electron gas confined at a semiconductor interface and in the presence of an applied magnetic field, H_0 , the electronic Zeeman energy can be written as $E_z = g^* \mu_B (H_0 + B_N) S_z$, where

$B_N = \mathcal{A}\langle I_z \rangle / g^* \mu_B$ is known as the Overhauser shift, \mathcal{A} the hyperfine constant and $\langle I_z \rangle$ is the z -component of the nuclear-spin polarization, and g^* the effective electronic g -factor. If the nuclear spins were to be fully polarized, the Overhauser B_N in bulk GaAs would be as high as ~ 10 T, which is exceedingly large. At the ultralow temperatures, $T \sim 10$ mK, where experiments can be performed by using commercially available dilution refrigerators, the thermal nuclear-spin polarization, which obeys Boltzmann statistics, is approximately $\sim 6\%$ in a 10 T magnetic field. Hence, at these temperatures, the hyperfine interaction represents a significant fraction of the total Zeeman energy of the electron gas and can be tuned by modifying the nuclear spin polarization by means of a small resonant radio-frequency field.

In resistive NMR, an RF field is applied at a frequency matching the NMR frequency, which has the effect of depolarizing the nuclear spins, or in NMR jargon, to saturate the nuclear magnetization. This results in a decrease of B_N , thus modifying the electronic Zeeman energy by δE_z . Provided that this small change in Zeeman energy provokes a modification of the transport properties of the in-situ electrons, the resonance can then be picked up resistively. This has been shown to be the case for the electrons confined at GaAs semiconductor interfaces in the integer and fractional quantum Hall regime [6, 7], in quantum point contacts [8], in the Wigner crystal regime at very high magnetic fields [9] and recently in vertical quantum dots as well [10].

Nuclear-Spin-Dependent Transport in the Quantum Hall Regime

Much of the success of resistively detected NMR lies deep in the physics of the integer and fractional quantum Hall regime. When the temperature of a two-dimensional electron gas is lowered such that $k_B T \ll \Delta$, with Δ being the relevant energy gap of a fractional quantum Hall state and of order of a few degrees kelvin, and when a strong magnetic field is applied, the electronic system can exhibit new quantum properties where a fermion can be transformed into bosons, quantum numbers can take exact fractional values, and the quantum statistics upon adiabatic exchange of these particles can be fractional (anyons). These phenomena arise as a consequence of the electronic orbital degree-of-freedom being quantized into a discrete ladder of energy levels, the so-called Landau levels, and of electron–electron interaction. When the Fermi energy of the two-dimensional electron gas (which can be tuned by the magnetic field and/or a gate voltage) lies at, or very near an odd number of Landau levels, the transport properties are sensitive to small change in the spin-flip energy since in the so-called ‘thermally activated regime’ the resistance is given by an exponential function of the quantum Hall energy gap, $R_{xx} \sim e^{\frac{-\Delta}{2k_B T}}$, where the energy gap $\Delta = E_z + E_{\text{exch}}$ is the sum of Zeeman energy, which depends on B_N the Overhauser field, and of the exchange energy E_{exch} arising from electron–electron interaction. Figure 2 shows an example of a resistively detected NMR signal for an experiment performed

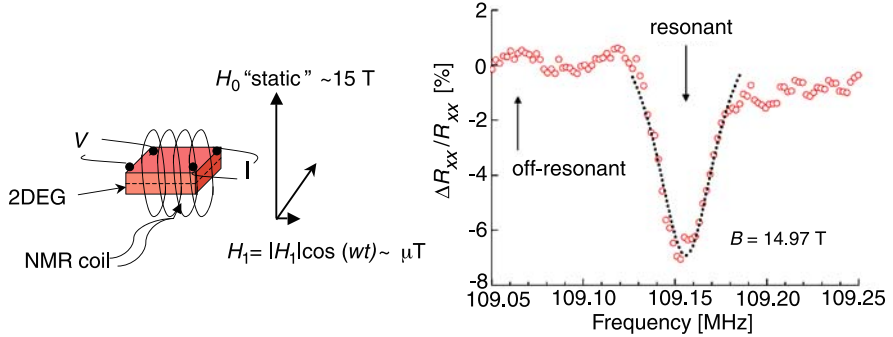


Fig. 2. *Left:* Cartoon depicting a resistively detected NMR experiment. An NMR coil is wrapped around a GaAs/AlGaAs sample contacted electrically with current (I) and voltage leads (V). A radio-frequency field, $H_1 \cos(\omega t) \sim \mu\text{T}$, is radiated on the sample through a coil matching the NMR frequency, and a large static magnetic field H_0 is applied perpendicularly to the two-dimensional electron gas (2DEG). *Right:* the data show an example of resistively detected NMR for a single quantum well. The experiment is performed by measuring extremely accurately the resistance, R_{xx} , and sweeping the frequency of the RF field continuously. Data after Gervais et al. (unpublished)

at $\sim 15\text{ T}$ and at temperatures $T \sim 35\text{ mK}$ corresponding to a Fermi level lying at near-complete filling of the first Landau level. The resistively detected lineshape can be well fitted by a Lorentzian, although various deviations from this standard form have been observed previously. The signal strength is typically in the few per cent range, $\delta R_{xx}/R_{xx} \sim 5\%$, but often much smaller [7]. A cartoon of the experiment is also depicted in Fig. 2. An NMR coil is wrapped around the sample and a RF field H_1 is applied in the plane of the 2DEG, while a strong static field H_0 is applied perpendicularly to it. In this continuous-wave version, the experiment is in fact quite simple: the resistance is monitored very accurately through a four-terminal measurement using a quasi-dc lockin technique with proper preamplification at room temperature while the frequency of the RF field is slowly swept across the resonance.

2 Recent Advances in GaAs/AlGaAs Semiconductor Quantum Wells

2.1 Resistively Detected NMR Lineshapes in GaAs/AlGaAs

Resistive NMR Lineshapes

Understanding the lineshape requires knowledge of the electronic transport upon a change in nuclear field δB_N at the specific filling factors investigated. The conventional wisdom of resistive NMR states that a change in the nuclear Overhauser field δB_N will incur a change in the electronic resistance

δR_{xx} owing to a change in the electronic Zeeman gap in odd Landau levels. One would therefore expect, upon complete or partial saturation of the nuclear magnetization, a Lorentzian lineshape very similar to those observed in previous works (see [7] for example, or Fig. 2). This lineshape can be understood by a change in resistance $\delta R_{xx} \propto \frac{g^* \mu_B \delta B_N}{2k_B T}$ in the regime where $g^* \mu_B \delta B_N \ll 2k_B T$ (true in most cases) where $R_{xx} \sim e \frac{-\Delta}{2k_B T}$ can be linearized, and from homogeneous broadening of the line. With the exception of the first Landau level, and to our knowledge, all resistively detected NMR experiments in GaAs/AlGaAs have produced Lorentzian lineshapes when the nuclear magnetization was slowly saturated by a RF field, i.e., with an exposure time τ_{exp} at a given frequency of order or greater than T_1 , the nuclear spin-lattice relaxation time.

This conventional wisdom is, nevertheless, being challenged in the first Landau level by the puzzling observation of a ‘dispersive-like’ lineshape near $\nu \sim 1$ by the Grenoble group [7]. This has since been observed by the Caltech group [13] and recently in the high-field electron solid phase [12]. The data from these experiments are shown in Fig. 3, panels A, B, C, and D.

The dispersive-like nature of the lineshape is, nonetheless, puzzling, and its underlying nature is not understood. Desrat et al. [7] speculated that the dispersive-like lineshape may originate from the localization of skyrmions into a crystal [14] predicted to occur near $\nu \sim 1$. While appealing, this ad hoc explanation is, nevertheless, hard to reconcile with the observation of

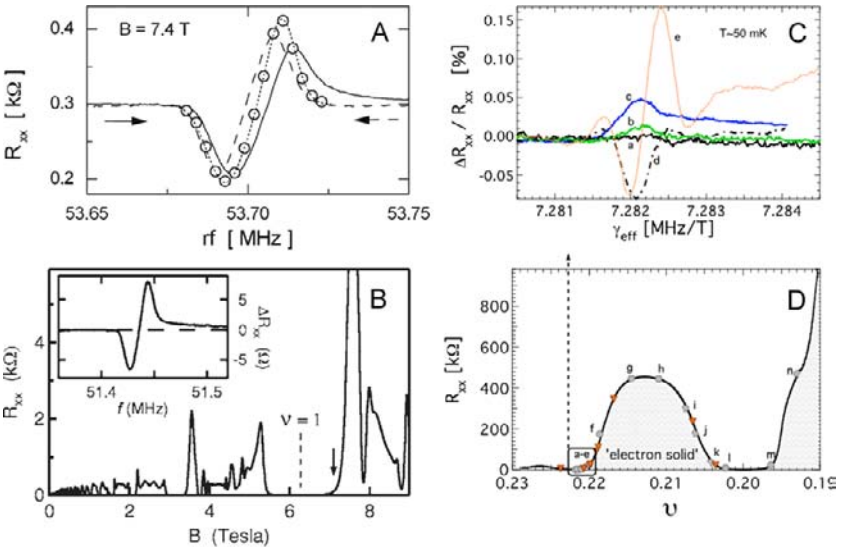


Fig. 3. Dispersive-like lineshape observed near filling factor $\nu \sim 1$ by the Grenoble (panel A) [7] and Caltech groups (panel B) [13], and in the high-field electron solid phases, where $\nu \simeq \frac{2}{9}$ or $\nu < \frac{1}{5}$ (panels C and D) [12]

similar lineshapes in the high-field electron solid regime [12], $\nu < \frac{2}{9}$ and $B \simeq 30$ T, where skyrmionic excitations seem most unlikely. Recently, Tracy et al. [13] suggested that the lineshape may originate from an interesting interplay between nuclear spin and thermal properties [13], yet it does remain unclear why this lineshape would appear only at certain filling factor regions, and only in the first Landau level. It is worthwhile mentioning that the typical signal of dispersive-like lineshapes is very strong, and often observed to be as large as $\frac{\Delta R_{xx}}{R_{xx}} > 40\%$, while typical Lorentzian signals away from $\nu = 1$ are typically of less than a per cent. This certainly suggests that the intricate relationship between nuclear spins and transport is not totally understood, and that two mechanisms may be at play here to generate this unusual lineshape. Future work is certainly needed to elucidate this phenomenon.

Skyrmions in the Ground State of Quantum Hall

The resistively detected NMR technique has opened up a new door to probe the two-dimensional electrons confined in GaAs-based structures where the hyperfine field is particularly strong. In a recent new development, this technique has been employed to perform NMR relaxation-time experiments in pristine, ultrahigh-quality single-layer quantum wells, where there are predictions for nontrivial skyrmionic spin excitations [15]. This picture is consistent with previous NMR experiments performed on a “stack” of quantum wells grown by molecular beam epitaxy [4], and with tilted transport measurements [16]. In particular, the new NMR relaxation time data [12] may have provided evidence for the formation of the so-called skyrmion crystal [14, 17].

In his seminal work on nuclear matter more than forty years ago, Skyrme showed that baryons emerge mathematically as a static solution of a meson field described by the so-called Skyrme Lagrangian [18]. His work provided the foundation for the quantum theory of solitons, and more recently found an interesting and a priori surprising connection to the physics of electrons confined to a two-dimensional plane. When only the lowest of Landau levels is almost completely occupied, the elementary excitations of the system become large topologically stable spin textures known as skyrmions [15]. It was further proposed that at $T = 0$ skyrmions would localize on a square lattice [14]. This ground state represents a new type of magnetic ordering that possesses long-range orientation and positional order, and is the solid-state analog of the skyrmion crystal state that is used to describe dense nuclear matter using Skyrme’s topological excitation model. At filling factor $\nu = 1$, where ν is defined by the ratio of the electronic density n to the magnetic flux density, $\nu = \frac{n}{B/\Phi} = \frac{nh}{eB}$, the quantized Hall state is ferromagnetic. For sufficiently small Zeeman-to-Coulomb energy ratio $\eta = E_z/E_c = \frac{g^* \mu_B B}{e^2 l_B}$, where g^* is the electronic g-factor and $l_B = \sqrt{\hbar/eB}$ is the magnetic length, Sondhi et al. showed that the low-lying excitations are not single spin-flips,

but rather a smooth distortion of the spin field in which several spins (4–30) participate [15]. These skyrmions are topologically stable, charged $\pm e$, and gapped excitations that are the result of an energy tradeoff where a higher Zeeman cost is paid for the profit of lowering the exchange energy between neighboring spins. The inset of the right panel of Fig. 3 shows the topology of a quantum Hall skyrmion, with the surface indicating the localized charge density with respect to the quantum Hall liquid state. One hallmark of the Skyrme crystal state, i.e., a lattice state of localized skyrmions, is the possible existence of a spin-wave gapless Goldstone mode that would efficiently and collectively couple the crystalline skyrmionic state to the nuclear-spin degree-of-freedom. In fact, earlier predictions by Côté et al. [17] estimated that the formation of a Skyrme crystal state would generate a three-fold enhancement of the nuclear-spin relaxation rate when compared to similar relaxation process from a spin-polarized two-dimensional Fermi gas. This three-fold enhancement in the relaxation rate of the nuclear spin can be directly tested by measuring the spin-lattice relaxation time T_1 by means of resistively detected NMR in single, ultrahigh-quality, and pristine quantum wells.

2.2 Spin-Lattice Relaxation-Time Measurements

The spin-lattice relaxation time T_1 can also be extracted using resistively detected NMR. Our technique has been designed to keep constant throughout the measurement the RF heating of the electrons as it arises from the RF field $H_1 \cos(\omega t)$. This ensures that the resistance is modified only by the hyperfine-coupled nuclei, and not the sample temperature. To achieve this, we monitor the time dependence of the resistance of the 2DEG at constant field H_0 and temperature T under a zero and nonzero effective RF field for the nuclei. Figure 4 shows an example of such a measurement. An RF field with frequency f_1 is applied onresonance and R_{xx} is monitored until a steady state is reached, and where the nuclear magnetization is partially saturated. This is shown in Fig. 4, right panel, at time $t < 0$. At the time $t \sim 1000$ s, the frequency is moved offresonance from f_2 to f_1 so that the nuclei effectively do not ‘see’ an H_1 field. As a result, the resistance undergoes a free decay to its original state as the nuclear magnetization \mathcal{M} relaxes in a time T_1 to its thermal equilibrium value, \mathcal{M}_0 . The time dependence of $R_{xx}(t)$ is found to fit very well a single exponential of the form $R_{xx}(t) = \alpha + \beta e^{-t/T'_1}$ (solid line in Fig. 4). We define T'_1 as the characteristic relaxation time of R_{xx} and α, β are coefficients that determine the on- and offresonance resistance values. In the case where the resistance is given by $R_{xx} \sim e^{\frac{-A}{2k_B T}}$, and for which the resistance can be linearized with $\delta R_{xx} \propto \frac{g^* \mu_B \delta B_N}{2k_B T}$, which is valid when $T > 30$ mK, and when the nuclei are only partially saturated, i.e., $g^* \mu_B \delta B_N \ll 2k_B T$. In this case, $T'_1 \simeq T_1$ to a very good approximation since $B_N \propto \mathcal{M}$.

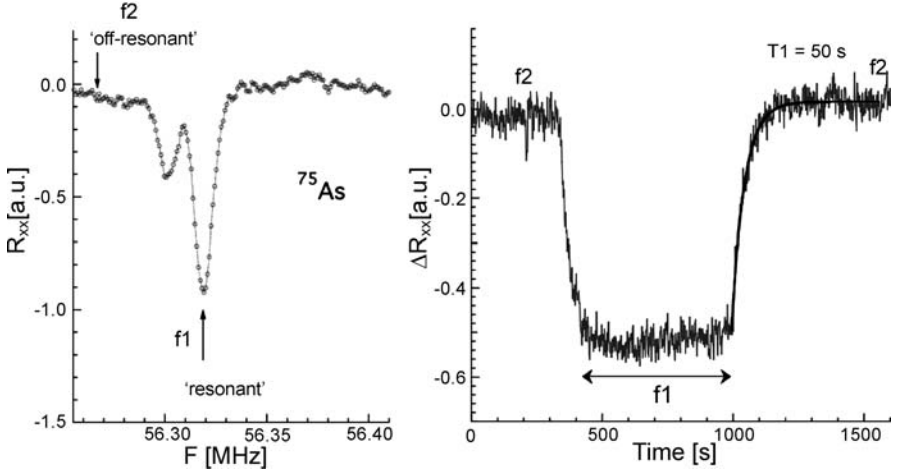


Fig. 4. *Left:* Resistively detected NMR spectrum for ^{75}As near $\nu \sim 1$ at $T \sim 30$ mK. The arrows indicate the “onresonance” (f_1) and “offresonance” (f_2) frequencies used to determine T_1 . *Right:* resistance versus time at frequencies f_2 and f_1 . The *solid line* is a fit to an exponential recovery with a single relaxation time. After Gervais et al. [12]

T_1 and the Evidence for a Skyrmion Crystal

The extracted rates $1/T_1$ measured by the Grenoble group [7] in a single GaAs/AlGaAs heterostructure are shown in the left panel of Fig. 5 at various magnetic fields, together with the corresponding magnetoresistance (solid line). The data show a clear enhancement of the nuclear-spin relaxation rates $1/T_1$ when the first Landau level is almost completely filled, i.e., near $\nu \sim 1$. Subsequent experiments in even higher quality samples have revealed similar behavior, showing that the nuclear spin-lattice relaxation rate is maximal whenever $R_{xx} \rightarrow 0$ [12]. This is particularly interesting since in the quantum Hall regime the vanishing of the resistance is a consequence of the two-dimensional properties of the electron gases and of the localization of electronic states. So, the data here suggest the nuclear-spin relaxation induced predominantly by these localized states, rather than by those remaining electronic states contributing to the conductivity. At a more quantitative level, the relaxation rates also show a $\sim 10^2$ enhancement, which is consistent with the three-fold increase estimated by Côté et al. [17]. Overall, this data provides experimental evidence for the formation of a magnetic phase of localized skyrmions in the first Landau level, and relaxing the nuclear spins through the a spin-wave collective mode of the Skyrme crystal.

T_1 in the Electron Solid Phases of GaAs/AlGaAs

At sufficiently high magnetic fields, the series composite fermions fractional quantum Hall states emanating from $\nu = \frac{1}{4}$ eventually yields to an electron solid phase interrupted by fractional quantum Hall liquid at $\nu = \frac{1}{5}$ (see Fig. 3 panel D). This electron solid is thought to be a Wigner crystal state with large quantum correlation. We expect, in this regime where the applied magnetic field is ~ 30 T or more for an electronic density $\sim 1.5 \times 10^{11} \text{ cm}^{-2}$ (as for the sample used in Fig. 5) the electrons to be fully polarized, and hence being a weak mechanism for nuclear-spin relaxation.

The spin-lattice relaxation rate ($1/T_1$) in this regime is given in the right panel of Fig. 6 versus the filling factor. The relaxation time associated with these rates are found to be long, ranging from ~ 350 s to 1000 s, and approximately a factor of 10^2 longer than near $\nu \sim 1$ in the same sample. Performing the T_1 measurements at a minimum or maximum of the dispersive-like line-shape yields no dramatic differences in the relaxation time, showing that the nuclei at different frequencies are indeed subjected to similar magnetic fluctuations and relaxation mechanism. No systematic dependence of the spin-lattice relaxation rate is observed on the filling factor in the range investigated

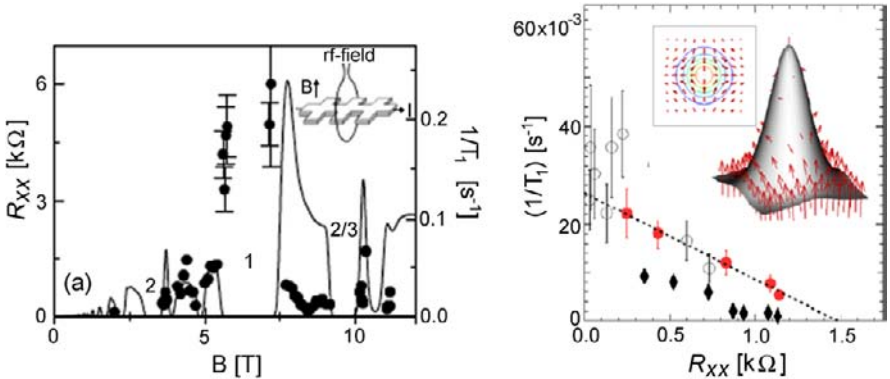


Fig. 5. *Left:* Magnetoresistance R_{xx} versus the magnetic field at $T \sim 50$ mK of a GaAs/AlGaAs heterostructure (*solid line*). The numbers on the plot indicate some filling factors ν of interest (in terms of Landau levels). The *solid dots* are nuclear spin-lattice relaxation rate $1/T_1$ measurements that shows a strong enhancement near $\nu \sim 1$. Data after Desrat et al. [7]. *Right:* Spin-lattice relaxation rate at filling factor $\nu = 0.84$ (*diamond*), 0.86 (*filled circles*) and 0.895 (*empty circles*) and plotted as a function of the electronic resistance, R_{xx} , and T ranging from ~ 20 to 100 mK. The data suggest maximal relaxation of the nuclei when $R_{xx} \rightarrow 0$, i.e., when the electronic states are fully localized. The *inset* shows the spin topology of a two-dimensional quantum Hall skyrmion that might be at the origin of the nuclear-spin relaxation observed near $\nu \sim 1$. Data after Gervais et al. [7, 12] and skyrmion topology courtesy of René Côté

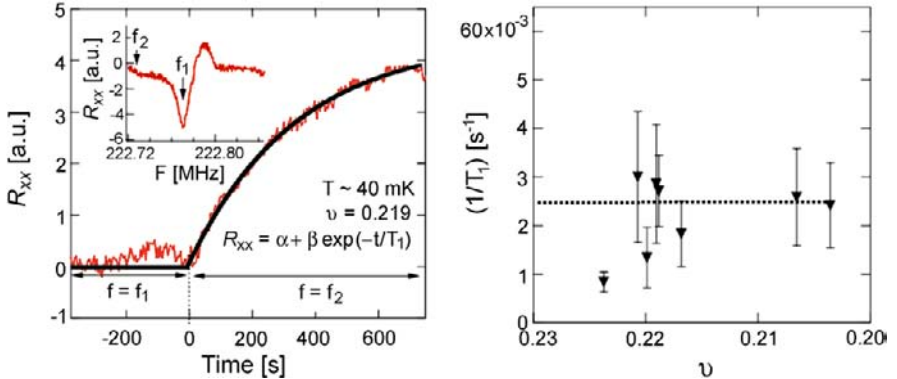


Fig. 6. *Left:* resistively detected nuclear-spin relaxation time in the electron solid phases of GaAs/AlGaAs. *Right:* nuclear-spin relaxation rates as a function of the filling factor in between $\nu = \frac{2}{9}$ and $\nu = \frac{1}{5}$. After Gervais et al. [12]

between $\nu = \frac{2}{9}$ and $\nu = \frac{1}{5}$, and hence no dependence on R_{xx} , which ranged from 0.75 k Ω to 100s of k Ω . This suggests that the nuclear-spin relaxation is entirely independent of the two-dimensional electron gas in this regime. The lack of sensitivity of $(1/T_1)$ to R_{xx} and ν in the high-field electron solid phase is in sharp contrast with our result near $\nu \sim 1$ where a linear dependence of $(1/T_1)$ with decreasing R_{xx} was found [12]. In particular, the much faster rates observed in the limit $R_{xx} \rightarrow 0$ when a well-developed quantum Hall state occurred is not observed in the electron solid regime.

3 Towards a Complete NMR Probe of Quantum Structures

3.1 NMR in Quantum Electronic Structures of GaAs/AlGaAs

The two examples discussed above show that the hyperfine coupling can be efficiently exploited in GaAs-based semiconductors to gain new knowledge on the fundamental properties of electronic matter at low temperatures, and also has a high potential of application in the field of quantum information processing. Of particular interest is that the “all-electrical” NMR technique allows us to probe systems with small sizes, and that it might be possible to bring it down even further. But are there limitations to the technique and how far down can we reach?

The prospects of reaching the nanoscale in several devices with resistive NMR seems good. In fact, for GaAs-based devices, resistive NMR is primarily limited by the electrical contacts so that NMR information can be recorded electrically. While small Hall bar geometry can be patterned and contacted to a size of about ~ 100 nm, smaller contacted devices, nevertheless, remain

difficult to fabricate. Still, the challenges imposed by the requirements of the contacts might be overcome by fabricating smaller gated devices patterned by e-beam techniques, where the device itself is effectively smaller than the source–drain contacts used to flow the electrical current. To this end, a team in Japan led by Tarucha has recently demonstrated the first electrical detection of the NMR in quantum dots [10], so it appears within the realm of the possible to scale it down even further and to make it a complete analytical tool of nanostructures. The development of highly sensitive readout and noise-reduction techniques might also allow for the probing of other systems where the hyperfine field is not as strong. In fact, for as long as a structure can be electrically contacted, and for which there is a hyperfine field, it is *in principle* possible to resistively detect the NMR, although the signal strength is highly dependent on the strength of the hyperfine interaction itself.

3.2 NMR on a Chip:

Quantum Coherent Control of the Nuclear Spins at the Nanoscale

The recent advances in quantum information processing have generated a high level of interest for the experimental realization of a scalable quantum computer capable of tasks impossible by classical physics, or in a much more efficient algorithm that exploits the powerful nature of quantum mechanics. Yet, one of the greatest challenges of quantum computation in a solid-state device remains the ability to gain coherent control over the quantum states of the device for a time sufficiently long so that logic operation can be performed. The modern challenge is therefore to ‘quantum engineer’ new technologically relevant materials and devices relying on basic principles totally distinct from modern electronics. Several candidates have been proposed for quantum computing or storage such as, for example, the charge and spin qubits of coupled semiconductor quantum dots (see [19], for example) or the quantum box [20]. Yet, in spite of the high level of excitement and recent progress made in the study of these new-generation devices, there remain significant difficulties in keeping the system quantum-mechanically coherent over times long enough to implement realistic computational algorithms. For instance, the coherence times have been determined to range from $\sim \mu\text{s}$ for the “quantonium device” [20] to $\sim \text{ns}$ for coupled quantum dots [19]. One interesting alternative to electrons as an information carrier is the nuclear spin of GaAs [21], which is much more resilient to its environment, and for which the quantum coherence between spins is in the ms range. Recently, a team in Japan has taken this approach one step further, and has succeeded in the detection and control of multiple quantum coherences of the nuclear spins in GaAs by using a newly developed pulsed resistive NMR technique ‘on the chip’ [11]. This result could pave the way toward the implementation of the Grover quantum search engine [22] in a semiconductor device.

4 Concluding Remarks

Since its beginning, NMR has provided a powerful analytical tool to study a wide range of systems and problems from biology, chemistry or solid-state physics. While the conventional NMR approach has proven to be very successful for bulk matter, it remains, nevertheless, extremely difficult to scale it down to systems of nanoscopic size. As a relatively new and exciting development, the GaAs-based nanostructures and their parent heterostructures are now providing us with a template to study NMR on systems with as few as $\sim 10^7$ nuclear spins, about ten orders of magnitude smaller than with conventional detection schemes. The technique itself has already shed some light on the fundamental aspects of many-body quantum physics and shows high promise in its application to quantum devices and computing. An important question, however, remains: is resistive NMR simply a special case mostly applicable to GaAs-based semiconductors, or a completely new tool to tackle nanoscience and nanotechnologies from the nucleus' point-of-view? The answer, which only future studies will reveal, is most likely lying in the middle. Should resistive NMR be applicable to a much broader class of materials and compounds, it would certainly extend its reach toward the nanoscale where most bulk magnetic resonance techniques do not apply, yet the progress achieved so far in the GaAs-based materials certainly warrants further investigations aimed at elucidating quantum phenomena at the limits of the nanoscale, ultralow temperatures, and with 'too few spins'.

Acknowledgements

The author would like to thank H.L. Stormer, D.C. Tsui, K.W. West, L.N. Pfeiffer, and L.W. Engel for their contributions to data and coauthorship of published works presented in this review, and the hospitality of the National High-magnetic field Laboratory (NHMFL) in Tallahassee, Florida, where much of the work took place. The author would also like to thank the National Science Foundation, the National Sciences and Engineering Council of Canada (NSERC), the Fond Québécois de Nature et Technologies (FQRNT) and the Alfred P. Sloan Foundation for their financial support.

References

1. F. Bloch, W.W. Hansen, M. Packard, Phys. Rev. **70**, 474 (1946) 36
2. E.M. Purcell, H.C. Torrey, R.V. Pound, Phys. Rev. **69**, 37 (1946) 36
3. D. Rugar, R. Budakian, H.J. Mamin, B.W. Chui, Nature **430**, 329 (2004) 37
4. S.E. Barrett, R. Tycko, L.N. Pfeiffer, K.W. West, Phys. Rev. Lett. **72**, 1368 (1994) 37, 42

5. G. Salis, D.T. Fuchs, J.M. Kikkawa, D.D. Awschalom, Y. Ohno, H. Ohno, *Phys. Rev. Lett.* **86**, 2677 (2001) 37
6. M. Dobers, K. v. Klitzing, J. Schneider, G. Weimann, K. Ploog, *Phys. Rev. Lett.* **61**, 1650 (1988) 37, 38, 39
7. W. Desrat, D.K. Maude, M. Potemski, J.C. Portal, Z.R. Wasilewski, G. Hill, *Phys. Rev. Lett.* **88**, 256807 (2002) 39, 40, 41, 44, 45
8. K.R. Wald, L.P. Kouwenhoven, P.L. McEuen, N.C. van der Vaart, C.T. Foxon, *Phys. Rev. Lett.* **73**, 1011 (1994) 39
9. G. Gervais, H.L. Stormer, D.C. Tsui, P.L. Kuhns, W.H. Moulton, A.P. Reyes, L.N. Pfeiffer, K.W. West, *Phys. Rev. B* **72**, R041310 (2005) 39
10. K. Ono, S. Tarucha, *Phys. Rev. Lett.* **92**, 256803 (2004) 39, 47
11. G. Yusa, K. Muraki, K. Takashina, K. Hashimoto, Y. Hirayama, *Nature* **434**, 1001 (2005) 47
12. G. Gervais, H.L. Stormer, D.C. Tsui, P.L. Kuhns, W.H. Moulton, A.P. Reyes, L.N. Pfeiffer, K.W. West, *Phys. Rev. Lett.* **94**, 196803 (2005) 41, 42, 44, 45, 46
13. L.A. Tracy, J.P. Eisenstein, L.N. Pfeiffer, K.W. West, *Phys. Rev. B* **73**, 121306 (2006) 41, 42
14. L. Brey, H.A. Fertig, R. Côté, A.H. MacDonald, *Phys. Rev. Lett.* **75**, 2562 (1995) 41, 42
15. S.L. Sondhi, A. Karlhede, S.A. Kivelson, E.H. Rezayi, *Phys. Rev. B* **47**, 16419 (1993) 42, 43
16. A. Schmeller, J.P. Eisenstein, L.N. Pfeiffer, K.W. West, *Phys. Rev. Lett.* **75**, 4290 (1995) 42
17. R. Côté, A.H. MacDonald, L. Brey, H.A. Fertig, S.M. Girvin, H.T.C. Stoof, *Phys. Rev. Lett.* **78**, 4825 (1997) 42, 43, 44
18. T.H.R. Skyrme, *Nucl. Phys.* **31**, 556 (1962), and references therein 42
19. J.R. Petta, A.C. Johnson, C.M. Marcus, M.P. Hanson, A.C. Gossard, *Phys. Rev. Lett.* **93**, 1868702 (2004) 47
20. D. Vion, A. Aassime, A. Cottet, P. Joyez, J.H. Pothier, C. Urbina, D. Esteve, M.H. Devoret, *Science* **296**, 5569 (2002) 47
21. M.N. Leuenberger, D. Loss, M. Poggio, D.D. Awschalom, *Phys. Rev. Lett.* **89**, 207601 (2002) 47
22. L.K. Grover, *Phys. Rev. Lett.* **79**, 4709 (1997) 47

Index

- | | |
|------------------------------|------------------------------------|
| GaAs, 38 | NMR, 37, 38, 40, 47 |
| GaAs/AlGaAs, 35 | quantronium device, 47 |
| inductively detected NMR, 35 | quantum information processing, 47 |
| Landau levels, 42 | quantum wells, 40 |
| | semiconductor quantum dots, 47 |

semiconductor quantum wells, 40
Skyrme crystal, 44
Skyrme Lagrangian, 42

skyrmions, 42
spin-lattice relaxation time T_1 , 43
strong Overhauser field, 38

Electron-Spin Dynamics in Self-Assembled (In,Ga)As/GaAs Quantum Dots

A. Greilich¹, D.R. Yakovlev¹, M. Bayer¹, A. Shabaev², and A.I.L. Efros²

¹ Experimentelle Physik II, Technische Universität Dortmund, 44221 Dortmund, Germany

² Naval Research Laboratory, Washington, DC 20375, USA

Abstract. Electron spins in semiconductor quantum dots are considered as elementary building blocks for a new class of devices. Here, we address both static and dynamic properties of such electron spins that are confined in singly charged (In,Ga)As/GaAs self-assembled quantum dots. In particular, we discuss first the g-factor tensor and then turn to the creation of spin coherence. We also discuss how long this spin coherence is maintained against scattering resulting in spin relaxation.

1 Introduction

Recently, the coherent dynamics of elementary excitations in semiconductor heterostructures has attracted considerable interest for applications in quantum information processing such as cryptography or computing. This field has been originally worked on in atomic quantum optics and nuclear magnetic resonance, for which it is easy to identify well-defined two-level systems that can be used as carriers of quantum information (the so-called quantum bits or, in short, qubits) that are well separated from the environment. Therefore, it was a natural development that the quantum information activities started to flourish in these fields due to the superior coherence properties of the elementary excitations such as atomic levels or nuclear spins. Quite a few proof-of-principle activities have been done, such as demonstration of few qubit entanglement, quantum-gate operation and design of simple quantum processors. However, currently these approaches appear to be limited due to the lack of scalability towards large numbers of involved qubits.

The potential to reach this goal has been attributed to semiconductor physics, due to the proven level of system integration in conventional electronics. Therefore, the underlying ideas and concepts have been transferred to semiconductors, even though it was clear, for example, that it is much more complicated to identify well-isolated two-level systems, by which coherence and therefore quantum information can be retained for long enough times. This has consequently directed interest toward semiconductor quantum dots because of their discrete energy-level structure, due to which they bear some

resemblance to atoms found in nature. The limitations of this analogy have been, however, clearly worked out in the meantime.

This ‘artificial atom’ analogy has been studied a lot by optical spectroscopy, for which self-assembled quantum-dots structures are very well suited due to their high quantum efficiency. For example, at cryogenic temperatures the linewidth of the radiative decay of electron–hole pairs (excitons) confined in quantum dots is limited by the radiative decay time T_1^X , corresponding to widths of a few μeV . But at elevated temperatures the interaction with higher-lying confined states in the dots and with continuum states of the dot environment becomes so important that the linewidth reaches a few meV. Further, recent studies have also shown that the simple exponential decay laws that give a perfect description of radiative decays in atomic physics can typically not be applied for quantum dots. Only for strictly resonant excitation of the transition between the valence and conduction band ground states at low temperatures may a two-level scheme be used.

On the other hand, from ultrafast optical spectroscopy it has been well established that the coherent manipulation of the excitons that are created by this type of excitation can in principle be done on a subpicosecond timescale, and therefore attraction was caught first by charge excitations. This has to be compared to the coherence time T_2^X . Long coherence times are required for performing a sufficient number of quantum manipulations before destruction of coherence occurs. The decoherence of charges such as electrons and holes typically occurs very fast in semiconductors, but charge-neutral complexes such as excitons show longer coherence. Nonlinear optical studies on quantum-dot excitons have rendered T_2^X -values in the ns range, which are ultimately limited by the radiative lifetime. This time might be extended, for example, by suppression of spontaneous emission that would require a tailoring of the photonic environment in which the quantum dots are located by a photonic crystal, for example, requiring sophisticated nanopatterning technology. This patterning itself could be, however, a source of decoherence. Alternately, by application of electric fields the electron and hole overlap may be reduced, but it is not clear yet whether the field variation can be done adiabatically. In any case it seems hard to increase the T_1^X and T_2^X times by more than an order of magnitude. The coherence time span might therefore be too short for quantum computing but could turn out to be sufficient for application in quantum communication, requiring a rather limited number of involved qubits. Further, when quantum dots are coupled to molecules, as required for quantum-gate application, the coherence time may be reduced as compared to the quantum-dot case, setting further limitations on their use.

Therefore, the interest has moved to spin excitations in semiconductors [1–3], in particular, because already for bulk semiconductors very long electron-spin coherence times T_2^S have been determined [4]. Further, it has been shown that the spin-relaxation mechanisms that are effective in higher-dimensional systems are strongly suppressed in quantum dots. For electrons,

for example, only the spin-orbit coupling and the interaction with the background of nuclei is effective, while for holes the interaction with the nuclei is also suppressed.

The interest in quantum-dot spins was enhanced further by the demonstration of very long electron spin-relaxation lifetimes, T_1^S , in the milliseconds range [5, 6]. This has raised hopes that T_2 , which may theoretically last as long as $2T_1$ [7], could be similarly long, with encouraging indications to that effect found lately [8].

In this chapter we give some insight into the current status of coherent optical manipulation of electron spins in self-assembled (In,Ga)As/GaAs quantum dots. In Sect. 2 we describe the samples as well as the experimental techniques used for studying them. Section 3 addresses the electron g-factor. In Sect. 4 we describe how the spins can be oriented efficiently by coherent optical excitation, and in Sect. 5 we describe measurements of the spin coherence and all-optical manipulation of the spins. The chapter is concluded by a summary and an outlook on future work.

2 Experiment

The experiments were performed on self-assembled (In,Ga)As/GaAs QDs, which for our studies were fabricated by molecular beam epitaxy on a (001)-oriented GaAs substrate. Here, we use the generic term (In,Ga)As for the quantum-dot material as the precise composition is unknown. To obtain strong enough light-matter interaction, the sample contained 20 quantum-dot layers separated by 60-nm wide barriers. The layer dot density is about 10^{10} cm^{-2} . For an average occupation by a single electron per dot, the structures were n -modulation doped 20 nm below each layer with a Si-dopant density roughly equal to the dot density. The as-grown sample shows ground-state emission at wavelengths around $1.2 \mu\text{m}$, which is outside of the sensitivity range of silicon detectors. Therefore, it was thermally annealed for 30 s at 945°C so that its emission occurs around 1.396 eV , as seen from the luminescence spectrum in Fig. 1. This range is easily accessible for Si detectors. The full width at half-maximum of the emission is about 10 meV, demonstrating a rather good homogeneity, achieved through the annealing step. Further optical properties of these dots can be found in [9, 10].

Most of the experiments reported here were performed with the sample immersed in liquid helium at a temperature $T = 2 \text{ K}$. The sample chamber was placed between the coils of an optical split-coil magneto-cryostat for fields up to $B = 10 \text{ T}$. For reference, we define the sample growth direction as the z -axis. The orientation of the sample could be varied relative to the magnetic-field direction. Experiments were performed for longitudinal (Faraday geometry) or transverse (Voigt geometry) magnetic-field orientation relative to the sample growth direction. In addition, the sample could be rotated about the growth axis.

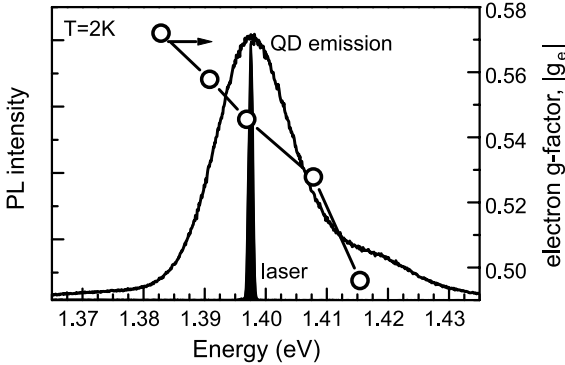


Fig. 1. Photoluminescence spectrum of the studied (In,Ga)As/GaAs quantum-dot sample. The filled trace gives the spectrum of the excitation laser used in the Faraday-rotation experiments, which could be tuned across the inhomogeneously broadened emission band. The symbols give the electron g-factor across this band, for which the right scale is relevant

For optical excitation, a Ti-sapphire laser emitting pulses with a duration of ~ 1.5 ps (full width at half-maximum of ~ 1 meV) was used, striking the sample along the z -axis. The laser repetition rate was 75.6 MHz, corresponding to a period $T_R = 13.2$ ns between the pulses. The laser pulse separation could be increased to multiples of T_R by a pulse-picker system. The emission energy was tuned to be in resonance with the ground-state transition of the charged quantum dots (see Fig. 1).

This laser system was used for implementation of two different optical techniques for studying the electron-spin dynamics, both based on time-resolved pump-probe Faraday-rotation methods [11, 12]. The first technique exploits an intense circularly polarized pump pulse for inducing circular dichroism of the quantum dots by optical orientation of carrier spins. The second technique, optically induced linear dichroism, exploits a linearly polarized pump beam that results in optical alignment of excitons in the quantum dots. In both cases, the optical anisotropies due to the pump pulses were analyzed by measuring the rotation angle of the polarization plane of a linearly polarized probe pulse of rather weak intensity. For detecting the rotation angle of the linearly polarized probe beam, a homodyne technique based on phase-sensitive balanced detection was used. The pump beam hits the sample at time zero, and the probe beam could be delayed relative to the pump beam by a delay line.

3 Electron g-Factor

The open circles in Fig. 1 show the variation of the electron g-factor across the inhomogeneously broadened emission of the quantum-dot ensemble. To

measure it, the energy of the exciting laser was shifted across the emission band with details of the g-factor determination to be found below. The magnetic field was oriented perpendicular to the heterostructure growth direction [001] along the [1-10] crystal direction (the y -direction). The g-factor modulus decreases with increasing emission energy from 0.57 on the low-energy side to less than 0.50 on the high-energy side, and therefore shows a variation of about 7.5% about its mean value.

The g-factor of conduction-band electrons typically differs considerably from its value of $g_0 = 2$ for free electrons or for electrons in atoms. The reason is the strong spin-orbit interaction in semiconductors, leading to a strong mixing of bands. If one makes the assumption that the main effect of the confinement in quantum dots is an increase of the bandgap E_g between conduction and valence band, but neglects all other effects such as changes of crystal anisotropies, of spin-orbit splittings, etc., the deviation from the free-electron g-factor, as determined from $\mathbf{k} \cdot \mathbf{p}$ theory, can be estimated by using the form for the g-factor in bulk [13]:

$$g_e = g_0 - \frac{4m_0P^2}{3\hbar^2} \frac{\Delta}{E_g(E_g + \Delta)}. \quad (1)$$

Here, m_0 is the free-electron mass, and P is the matrix element describing the coupling between valence and conduction band. Δ is the spin-orbit splitting of the valence-band ground state. For GaAs- or InAs-based semiconductors the coupling matrix element and the splitting are so large that the g-factor even becomes negative, for example -0.44 in GaAs bulk at cryogenic temperatures.

From our measurements we do not obtain direct access to the sign of the g-factor, but the systematic variation across the emission band allows us to determine it indirectly. Increasing emission energy corresponds to an increase of the bandgap, leading to a reduction of the right-hand side of (1). The decrease of the g-factor modulus with increasing emission energy can then be only explained if the g-factor is negative.

There is another striking difference between the g-factors of a free electron and a crystal electron. Due to the crystallographic anisotropy it is no longer a scalar quantity in general, but has to be described by a tensor of second order. In crystals with cubic symmetry this tensor can be reduced to a scalar, but for nanostructures this cannot be done in any case. Still, for GaAs-based quantum wells, for example, the conduction-band g-factor can often be taken as isotropic as the carrier orbitals are formed from s-type atomic orbitals. For self-assembled quantum dots this approximation can no longer be used.

An example of this behavior is shown in Fig. 2, for which the magnetic-field orientation was varied in the quantum-dot plane. The full circles give the electron g-factor at $B = 5$ T. For comparison also the g-factor of the exciton is shown there by the full triangles. For both, a remarkable anisotropy is seen, even though the quantum dots appear to be rather well circularly shaped in electron-microscopy images.

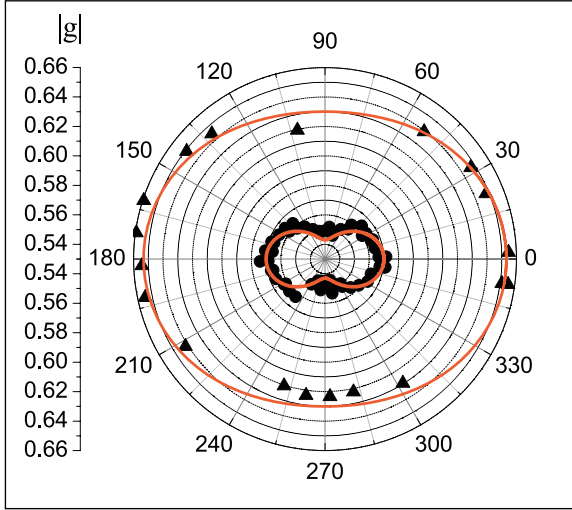


Fig. 2. (Color online) Inplane angular dependence of the electron (circles) and exciton (triangles) g-factors obtained from the circular dichroism experiments. Red lines are fits to data as described in text. $B = 5$ T. Angle zero corresponds to field orientation along the x -axis that is defined by the $[110]$ crystal axis

The anisotropy can be well described by a pattern with two-fold symmetry axis. Therefore, for an arbitrary direction, characterized by the angle α relative to the x -axis, the electron g-factor can be written as

$$\sqrt{g_{e,x}^2 \cos^2 \alpha + g_{e,y}^2 \sin^2 \alpha} = g_{e\perp}, \quad (2)$$

where $g_{e,x}$ and $g_{e,y}$ are the g-factors along the x - and y -axes, $[110]$ and $[1-10]$, respectively. The solid lines in Fig. 2 are fits to the data using (2). From these fits we obtain $g_{e,x} = 0.57$ and $g_{e,y} = 0.54$ for the electron. This corresponds to a relative variation of 2.7% around the mean value.

We have also done measurements of the electron g-factor with the magnetic field aligned along the heterostructure growth direction, exploiting linear dichroism in the Faraday-rotation measurements. From these studies (not shown here) we obtain a g-factor of the electron along z of -0.61 , which is about 10% larger than the average g-factor in the dot plane.

4 Creation of Spin Coherence by Spin Initialization

For addressing the electron-spin coherence, the quantum-dot sample was studied by Faraday-rotation spectroscopy. The pump beam was circularly polarized and directed along the heterostructure growth direction. Since it was resonant with the ground state, it can inject an electron and a hole into the conduction- and valence-band ground states of the quantum dots. These carriers will have a well-defined spin orientation due to the optical selection rules. For example, for σ^+ (σ^-)-excitation the electron will have a spin projection along z , $S_z = -1/2$ ($S_z = +1/2$), while the total angular momentum of the hole (being the sum of the orbital moment and the spin) will be

$J_z = +3/2$ ($J_z = -3/2$). Injection of such an electron–hole combination will of course only be possible if it is in accord with the Pauli principle, since there is already an electron in the quantum dot due to the doping whose spin orientation has to be opposite to that of the optically injected electron.

The resulting spin imbalance leads to a net spin polarization along z . If one assumes a spin polarization in the ensemble, such that for example, the quantum dots contain more electrons with spin-up ($S_z = +1/2$ in state $|\uparrow\rangle$) than with spin-down ($S_z = -1/2$ in state $|\downarrow\rangle$) this will be reflected by the transmitted probe beam (propagating under a slight angle relative to z , to avoid interference with the pump). Its linear polarization can be decomposed into two countercircularly polarized components of equal weight. Due to the spin imbalance, the interaction of the σ^+ -polarized part will be smaller than that of the σ^- -polarized part, leading to different propagation speeds. Combining the two components behind the sample again will therefore result again in linear polarization, but due to the different propagation times a phase shift has occurred, reflected by a rotation of the polarization angle.

This is the description for a static situation. In the following case the carrier spins are injected in a transient fashion, as after some time the electron–hole pair will recombine radiatively. In addition, a static magnetic field is applied normal to the spin orientation so that the carrier spins precess about this field, which is oriented along x . Due to the spin precession the spin polarization also oscillates, which can be mapped through the oscillating rotation angle of the probe beam’s polarization. An example of the experimental data that can be obtained in this way is given in Fig. 3a showing the Faraday-rotation signal of the (In,Ga)As/GaAs quantum dots versus the delay between pump and probe for different magnetic fields. Pronounced electron-spin quantum beats are observed with some additional modulation at high B .

In quantum-mechanical language the precession corresponds to a quantum beating between two spin-split levels. For the electron, for example, the two Zeeman-split spin eigenstates in transverse magnetic field are spin parallel and spin antiparallel to the magnetic field, i.e., the spin points either along the $+x$ or the $-x$ direction. Using the S_z states as basis, these states can be written as: $|\pm x\rangle = (|\uparrow\rangle \pm |\downarrow\rangle)/\sqrt{2}$, reflecting the zero spin polarization along z . Illuminating with a laser pulse that is short enough so that its spectral width covers the energy separation between the split states, can excite a superposition of the two split states. The time evolution of this superposition shows oscillations with a frequency corresponding to the splitting.

The modulations of the beats at strong applied fields is seen only at short delay times not exceeding 400 ps. This time corresponds to the lifetime of electron–hole pairs, as determined from time-resolved photoluminescence. As can be seen from the signal at weak fields, for longer delays the Faraday-rotation signal contains oscillations with only a single frequency component,

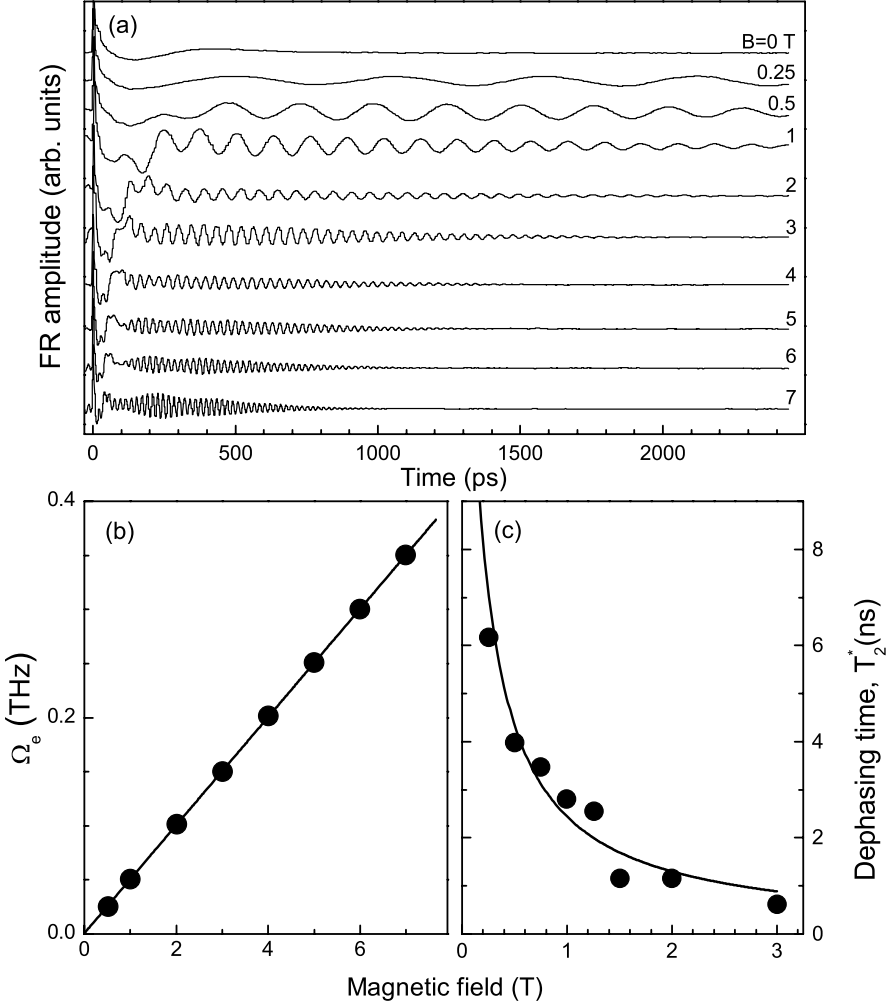


Fig. 3. (a) Faraday-rotation traces of n -doped (In,Ga)As/GaAs quantum dots vs. delay between pump and probe at different magnetic fields. The pump power was ~ 10 mW. (b) Field dependencies of the electron precession frequency. (c) Spin dephasing time T_2^* versus B . The line is a $1/B$ -fit to the data

which are exponentially damped. The lifetime of these beats is as long as 4 ns at $B = 0.5$ T, for example, exceeding essentially the lifetime of optically excited carriers. Therefore, these long-lived oscillations can be attributed to residual electrons in the dots. The modulation at early delays apparently arises from interference of the long-lived oscillation with an oscillation related to optically excited carriers, and the two oscillation frequencies lie close to each other, so that the observed beating behavior occurs.

Three features are to be noted for the appearance of the oscillations:

- We have first analyzed the long-lived precession component by the form:

$$\exp\left(-\frac{t}{T_2^*}\right) \cos(\Omega_e t), \quad (3)$$

where T_2^* is the dephasing time and Ω_e is the electron precession frequency given by the spin-splitting $\Omega_e = g_{e,x}\mu_B B/\hbar$ with the Bohr magneton μ_B . $g_{e,x}$ is the electron g-factor along the field. From the field dependence of the precession frequency the g-factor can therefore be determined, and this was the technique that was applied to gain the data shown in Sect. 2. Figure 3b shows the field dependence of the precession frequency Ω_e obtained from fitting our data (the circles), which are in agreement with a linear dependence on B , as expected from the equation above. Note that in general deviations from such a linear behavior might also occur if the magnetic field is able to modify the band structure, leading to a change of the g-factor. This might be the case in particular for holes, but less so for electrons. From a B -linear fit (the black solid line in Fig. 3b) we obtain $|g_{e\perp}| = 0.57$.

- The spin beats become increasingly damped with increasing magnetic field, corresponding to a reduction of the ensemble spin dephasing time T_2^* , plotted in Fig. 3c. The damping arises from variations Δg_e of the electron g-factor within the quantum dot ensemble, which are translated into a spread of the precession frequency: $\delta\Omega_e = \Delta g_e \mu_B B/\hbar$. The electron spins become oriented at the moment of pump pulse arrival, after which they start to precess about the field. Due to the varying frequency the precession of the electrons runs out of phase with increasing delay, so that the coherent signal is reduced. Note, however, that this is a destructive-interference effect from the ensemble, but does not mean that the coherence of each individual spin in a QD is lost.

Obviously this frequency spread increases linearly with increasing magnetic field, which in the time domain (as measured by T_2^*) leads to a dependence inversely proportional to the magnetic field. Therefore the dephasing can be described by $[T_2^*(B)]^{-1} = [T_2^*(0)]^{-1} + \Delta g_e \mu_B B/\sqrt{2}\hbar$. The solid line in Fig. 3c shows a $1/B$ -fit to the T_2^* data, by which a g-factor variation $\Delta g_e = 0.004$ is extracted, which is only about 0.7% of the mean value. This variation appears to be surprisingly small given the fact that we address an inhomogeneously broadened ensemble consisting of millions of dots. However, one has to keep in mind that we select by our laser pulse a rather narrow energy range of about 1 meV of quantum-dot exciton energies.

From the data one can also conclude that $T_2^*(0)$ exceeds 6 ns in the limit of zero magnetic field, for which the g-factor variations no longer play a role. The zero-field dephasing is mainly caused by electron-spin precession about the frozen magnetic field of the nuclei [14]. The net nuclear

orientation varies from dot to dot, and it is these variations that lead to ensemble spin dephasing.

- The additional modulation of the quantum beats at high fields is observable only during about 400 ps. Therefore, it can be assigned to photoexcited carriers, which show a precession with a frequency close to that of the electron. This results in the beating from interference of the two signals. From the data in Fig. 2 we know that the exciton has a similar g -factor as the electron, and therefore we attribute these short-lived beats to the exciton spin precession in quantum dots that do not contain a resident electron. This precession persists only during the radiative decay of the excitons, which is in good accord with the beat lifetime (see above). From the ratio of the amplitudes of the electron and exciton beats we can estimate the ratio of charge-neutral and single-charged quantum dots. In this way, we find that out of the dots containing fewer than 2 electrons about 75% contain a single electron, while 25% contain no residual charge. Dots with more than 2 electrons do not show a considerable spectroscopic response in resonant Faraday rotation due to Pauli blocking.

Next, after this analysis of the static g -factor properties, we want to address why spin precession is observed at all. At least in high magnetic fields, for which the spin splitting is quite large compared to the thermal energy, the system should be in equilibrium before photoexcitation. This means that the spin is either parallel or antiparallel to the magnetic field. Through the optical excitation we are apparently able to rotate the electron spin by 90° , so that precession can occur. To obtain some insight into the underlying mechanism, additional information is needed:

Figure 4a shows FR signals at $B = 1$ T for different pump powers. The corresponding FR amplitudes are plotted in Fig. 4b versus the laser pulse area Θ , which is defined as $\Theta = 2 \int [d\mathbf{E}(t)] dt/\hbar$ in dimensionless units with the dipole matrix element d for the transition from the valence to the conduction band. For pulses of constant duration, but varying power, as used here, Θ is proportional to the square root of excitation power, and it is given in arbitrary units in Fig. 4b. The Faraday-rotation amplitude shows a nonmonotonic behavior with increasing pulse area. It rises first to reach a maximum, then drops to about 60%. Thereafter, it shows another strongly damped oscillation.

This behavior is similar to the one known from Rabi oscillations of the Bloch vector, whose z -component describes the electron-hole population [15, 16]. The laser pulse drives coherently this population, leading to coherent oscillations as function of the pulse area Θ . For $\Theta = 0$ (no pulse) it does not change the population, while for $\Theta = \pi$ the system is inverted, leading to electron-hole pair population in an undoped quantum dot. For $\Theta = 2\pi$ the Bloch vector is rotated by 360° and so on. To observe periodic oscillations, damping has to be suppressed, that is, the system has to be homogeneous and the driving laser pulse has to be shorter than any decoherence times. In our

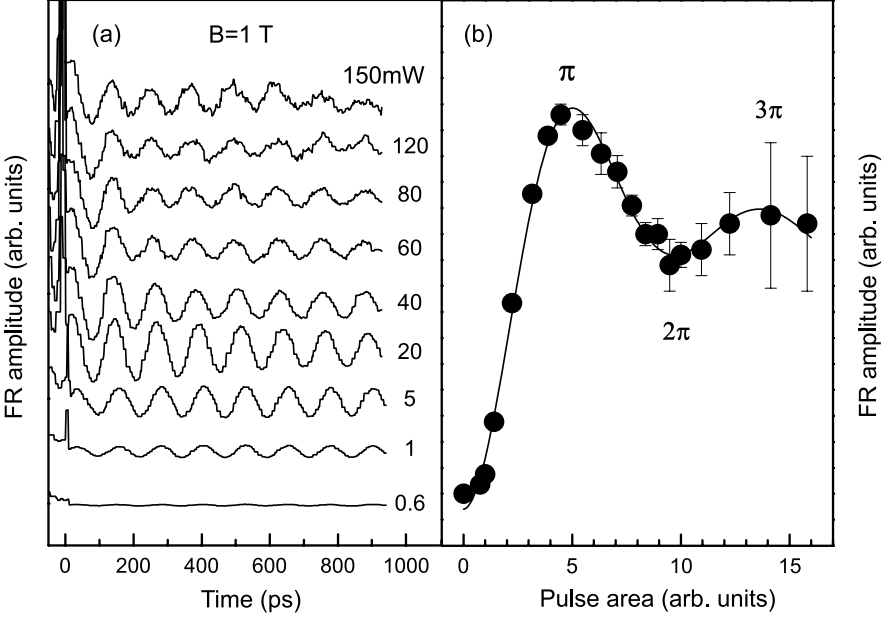


Fig. 4. (a) Short-delay closeup of the Faraday-rotation signal at $B = 1$ T for different pump powers. (b) Faraday-rotation amplitude versus laser pulse area θ . The line is a guide to the eye

case, the Faraday-rotation amplitude becomes maximum when applying a π -pulse as pump, and it becomes minimum for a 2π -pulse. The damping of the oscillations most likely is due to ensemble inhomogeneities of quantum-dot properties such as the dipole moment \mathbf{d} [17].

With these observations at hand we can understand the origin of the observed spin coherence. For that purpose we first discuss charge-neutral dots. Resonant optical pulses with σ^- polarization create a superposition state of vacuum and exciton:

$$\cos\left(\frac{\Theta}{2}\right)|0\rangle - i\sin\left(\frac{\Theta}{2}\right)|\uparrow\downarrow\rangle, \quad (4)$$

where $|0\rangle$ describes the de-excited semiconductor. The hole-spin orientations $J_{h,z} = \pm 3/2$ are symbolized by the arrows \uparrow and \downarrow , respectively. The electron and spins are reversed in the exciton for σ^+ -excitation. The exciton component precesses in magnetic field for a time, which cannot last longer than the exciton lifetime. In the ensemble, the precession might be visible only for shorter times, if the coherence of the states is destroyed by spin scattering of either electron or hole. The strength of the contribution to the ensemble Faraday-rotation signal is given by the square of the exciton coefficient $\sin^2(\Theta/2)$.

Let us turn now to singly charged quantum dots, for which the resonant excitation can lead to the excitation of trions. Let us assume that the de-excited quantum-dot state is given by an electron with arbitrary spin orientation:

$$\alpha|\uparrow\rangle + \beta|\downarrow\rangle, \quad (5)$$

with $|\alpha|^2 + |\beta|^2 = 1$. As seen above, a σ^- -polarized laser pulse ‘tries to place’ an exciton with spin configuration $|\uparrow\downarrow\rangle$ in the quantum dot. This action is, however, restricted by the Pauli principle, due to which the optically excited electron must have a spin orientation opposite to the resident one. Therefore, the pulse excites only the second component of the initial electron state.

In consequence, a coherent superposition state of an electron and trion is created:

$$\alpha|\uparrow\rangle + \beta \cos\left(\frac{\Theta}{2}\right)|\downarrow\rangle - i\beta \sin\left(\frac{\Theta}{2}\right)|\downarrow\uparrow\downarrow\rangle, \quad (6)$$

which consist of two electrons forming a spin singlet and a hole in state $|\downarrow\rangle$. Here, we assume again that decoherence does not occur, i.e., the pulse length is much shorter than the radiative decay and the carrier spin-relaxation times. One sees that the electron–hole population oscillates with the pulse area Θ . The excitation is most efficient for $\Theta = \pi$, for example, and for simplicity we restrict ourselves to this case, which then gives the superposition state:

$$\alpha|\uparrow\rangle - i\beta|\downarrow\uparrow\downarrow\rangle. \quad (7)$$

After some time the electron–hole pair will relax, leaving the resident electron in the quantum dot. This occurs on the mean timescale given by the radiative lifetime. Taking the ensemble average will wipe out any contribution from the last summand to the Faraday rotation signal. If before recombination hole spin-relaxation occurs, the situation will not be changed, as the ensemble average will again nullify the contribution from the second part.

The efficiency of this protocol is obviously determined by the quality of the suppression of the pure $|\downarrow\rangle$ -component that in effect reduces the electron-spin polarization along z . The probability to excite it is given by $\cos^2(\Theta/2)$, or vice versa, the probability of avoiding it is $1 - \cos^2(\Theta/2) = \sin^2(\Theta/2)$. Since the Faraday-rotation signal is proportional to the electron-spin polarization, we expect a dependence proportional to $\sin^2(\Theta/2)$, neglecting any damping. This is reflected by the observed Rabi oscillations in Fig. 4.

Let us consider the problem more quantitatively: By variation of the area Θ not only the electron and trion state populations are changed periodically with period $\Theta = 2\pi$, but also the orientation of electron and trion spins \mathbf{S} and \mathbf{J} are controlled. The electron-spin polarization is described by a spin vector $\mathbf{S} = (S_x, S_y, S_z)$ defined by: $S_x = \text{Re}(\alpha\beta^*)$, $S_y = -\text{Im}(\alpha\beta^*)$, $S_z = (1/2)(|\alpha|^2 - |\beta|^2)$. Similarly, one can introduce the spin vector, $\mathbf{J} = (J_x, J_y, J_z)$, which represents the polarization of the trion, $|\psi\rangle = \bar{\alpha}|\uparrow\downarrow\uparrow\rangle + \bar{\beta}|\uparrow\downarrow\downarrow\rangle$. The spin vectors \mathbf{S} and \mathbf{J} represent 6 of the 16 components

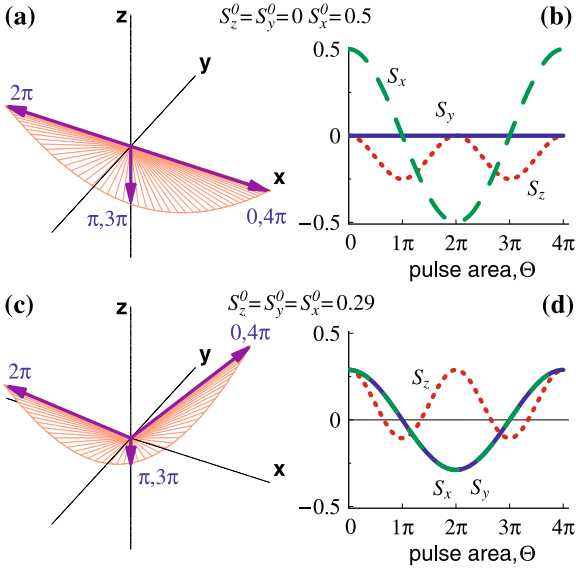


Fig. 5. (a) and (c): Reorientation of the electron-spin polarization by application of a resonant optical pulse of varying area as denoted. Calculations have been done for two different initial values of spin polarization, S_x^0 and S_z^0 . (b) and (d): Electron-spin polarization components versus pulse area Θ

of the four-level density matrix, and their dynamics is given by density matrix equations of motion [18].

The electron-spin vector evolution as a function of Θ is shown in Fig. 5 for two initial orientations: one is parallel to the magnetic field and the other exemplifies an arbitrary direction. A short σ^+ -polarized pulse excites the initial electron-spin state, $\alpha|\uparrow\rangle + \beta|\downarrow\rangle$, into an electron-trion superposition state $\alpha \cos(\Theta/2)|\uparrow\rangle + \beta|\downarrow\rangle - i\alpha \sin(\Theta/2)|\uparrow\downarrow\rangle$. The light-induced change of the S_z component, $|S_z - S_z^0| = |\alpha|^2 \sin^2(\Theta/2)$ varies with the $|\uparrow\rangle$ state population, and independently of the initial conditions it reaches a maximum for $\Theta = (2n + 1)\pi$ -pulses, for which the S_x and S_y components vanish. In particular, $S_z([2n + 1]\pi) = -0.25$ for $S_z^0 = 0$ [25]. Unlike the S_z component, the electron spin swings between its initial direction (S_x^0, S_y^0, S_z^0) and the direction $(-S_x^0, -S_y^0, S_z^0)$ with a period of 4π . This is because the $S_{x,y}$ components that are proportional to $\cos(\Theta/2)$ components describe the coherence of the electron-spin state and vary both with the phase of the spin wave function.

The control of spin dynamics by an optical pulse allows for a fast spin alignment. In a quantum-dot ensemble, a small-area pulse, $\Theta \ll 1$, induces a coherent spin polarization proportional to Θ [19]. With increasing Θ , the total spin polarization oscillates with a period 2π , as does the S_z component of each individual spin in the ensemble, explaining the Faraday-rotation amplitude oscillations in Fig. 4. The long trion lifetimes in our quantum dots could enable realization of a regime in which a pulse of rather low power, but long duration can be used to reach a large pulse area without decoherence due to radiative decay. Further, the S_x and S_y components change sign

with period 2π . This implies that $2n\pi$ -pulses can be used for refocusing the precessing spins, similar to spin-echo techniques [20].

Let us turn now to the spin dynamics after initialization by a short pulse. Then the offdiagonal component of the density matrix, describing electron-trion coherence, is decoupled from the electron and trion spin vectors, which are governed independently by two vector equations [9]:

$$\begin{aligned}\frac{d\mathbf{J}}{dt} &= [\boldsymbol{\Omega}_h \times \mathbf{J}] - \frac{\mathbf{J}}{\tau_s^h} - \frac{\mathbf{J}}{\tau_r}, \\ \frac{d\mathbf{S}}{dt} &= [(\boldsymbol{\Omega}_e + \boldsymbol{\Omega}_N) \times \mathbf{S}] + \frac{(\hat{\mathbf{J}}\hat{\mathbf{z}})\hat{\mathbf{z}}}{\tau_r},\end{aligned}\tag{8}$$

where $\boldsymbol{\Omega}_{e,h} \parallel \mathbf{e}_x$ and $\boldsymbol{\Omega}_N = g_e\mu_B\mathbf{B}_N/\hbar$ is the electron precession frequency in an effective nuclear magnetic field, \mathbf{B}_N . In the second equation we do not include the electron spin-relaxation time, τ_s^e , explicitly. At low temperatures, τ_s^e is of the order of μs and is mainly determined by fluctuations of the nuclear field $\boldsymbol{\Omega}_N$ in a single quantum dot [5, 6, 10, 14, 21]. This timescale is irrelevant to our problem. The spin relaxation of the hole in the trion, τ_s^h , is caused by phonon-assisted processes and at low temperatures may be as long as τ_s^e [22, 23].

Solving (8) we obtain the time evolution of the spin vectors \mathbf{S} and \mathbf{J} . After trion recombination ($t \gg \tau_r$), the amplitude of the long-lived electron-spin polarization excited by a $(2n+1)\pi$ -pulse is given by

$$S_z(t) = \text{Re} \left\{ \left(S_z(0) + \frac{0.5J_z(0)/\tau_r}{\gamma_T + i(\omega_e + \Omega_h)} + \frac{0.5J_z(0)/\tau_r}{\gamma_T + i(\omega_e - \Omega_h)} \right) \exp(i\omega_e t) \right\},\tag{9}$$

where $S_z(0)$ and $J_z(0)$ are the electron and trion spin polarizations created by the pulse. $\omega_e = \Omega_e + \Omega_{N,x}$. $\gamma_T = 1/\tau_r + 1/\tau_s^h$ is the total trion decoherence rate. If the radiative relaxation is fast $\tau_r \ll \tau_s^h$, $\Omega_{e,h}^{-1}$, the induced spin polarization $S_z(t)$ is nullified on average by trion relaxation, as $S_z(0) = -J_z(0)$. In contrast, if the spin precession is fast, $\Omega_{e,h} \gg \tau_r^{-1}$, the electron-spin polarization is maintained after trion decay [24, 25]. This is the situation in our experiment.

For an ensemble of quantum dots, the electron-spin polarization is obtained by averaging (8) over the distribution of g-factors and nuclear configurations. At low B , the random nuclear magnetic field becomes more important for the electron-spin dephasing than for g-factor dispersion, leading to dephasing during several nanoseconds [14]. As discussed, the rotation of the linear probe polarization is due to the difference in scattering of its σ^+ and σ^- polarized components by one of the transitions $|\uparrow\rangle \rightarrow |\uparrow\downarrow\uparrow\rangle$ and $|\downarrow\rangle \rightarrow |\uparrow\downarrow\downarrow\rangle$. The scattering efficiency is proportional to the population difference of the states involved in these transitions $\Delta n_+ = n_{\uparrow} - n_{\uparrow\downarrow}$ or $\Delta n_- = n_{\downarrow} - n_{\downarrow\downarrow}$. The Faraday-rotation angle is $\phi(t) \sim (\Delta n_+ - \Delta n_-)/2 = S_z(t) - J_z(t)$. Figure 6 shows the Faraday-rotation signal after a σ^+ -polarized excitation pulse, cal-

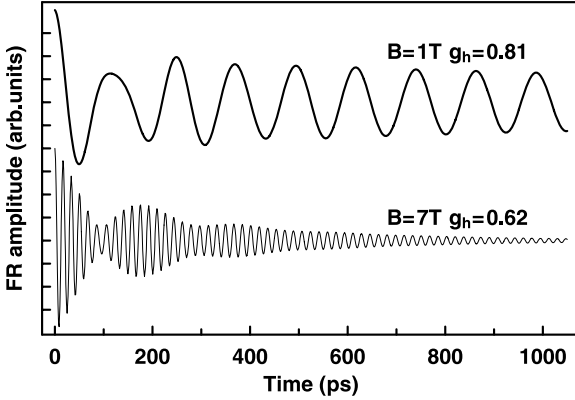


Fig. 6. Calculated time dependence of pump-probe Faraday-rotation signal of n -doped quantum dots excited by a σ^+ polarized pulse. $\tau_r = 400$ ps, $\tau_s^h = 170$ ps, $|g_e| = 0.57$, and $\Delta g_e = 0.004$

culated with input parameters corresponding to the experimental situation. At $B = 7$ T, the Faraday rotation shows modulated beats resulting from interference of the electron and exciton precessions.

5 Electron-Spin Coherence

For quantum information applications, the details of the electron-spin dynamics need to be understood. In particular, the timescales during which the coherence of a spin state is retained have to be addressed. Phenomenologically, the spin dynamics can be described by two times, the longitudinal spin relaxation time T_1 and the transverse spin relaxation time T_2 . In a simple picture these timescales can be understood in the following way. A “longitudinal” magnetic field leads to a spin splitting. The T_1 time then describes the timescale on which the relaxation of a spin from the upper into the lower state occurs. If the spin is, on the other hand, oriented normal to the magnetic field, it precesses about this field. In this case, the T_2 time describes the time during which the precession is going on in a unperturbed way until the first scattering followed by a phase-change precession occurs. It is this latter timescale that is the relevant quantity for quantum information processing.

In the previous section we had introduced an additional time constant T_2^* to describe the decay of the ensemble coherent signal, called dephasing. As we had pointed out, the origin of this fast decay in the ns range may lie in ensemble inhomogeneities that lead to a strong variation of the precession frequency. These variations are dominant at strong enough fields. Toward zero field the spin-coherence lifetime is limited by dot-to-dot variations of the nuclear fluctuation fields about which each electron precesses. Besides such momentary inhomogeneities, T_2^* might in general also be limited by variations of the experimental conditions during the measurement time, such as signal integration times that are much longer than the time during which

the conditions can be kept stable. This is the typical case for single quantum-dot measurements, for which one has to perform an experiment many times in order to get a statistically significant result.

Generally, the dephasing time is much shorter than T_2 . Note, however, that dephasing does not lead to a destruction of the coherence of an individual spin. But it does mask the duration of the single-spin coherence due to the rapid loss of coherence among the phases of the spins. Theoretically, the single-spin coherence time may be as long as twice the spin-relaxation time, which is on the scale of milliseconds [5], as recent experiments have demonstrated. The true spin-coherence time may be obtained by sophisticated spin-echo techniques [26], which typically are quite laborious. In general, a less complicated and robust measurements scheme would be highly desirable, by which also the spin coherence could be preserved so that ultimately many of the operations critical to the processing of quantum information, including initialization, manipulation, and readout of a coherent spin state, would become possible.

To address this point, we look again at Faraday-rotation traces, recorded similar to the ones presented before. Before we had shown the traces only for positive delays between probe and pump. Now we take a look also at negative delays. This is done for three different magnetic fields in Fig. 7, lower panel. At $B = 0$ T a strongly damped oscillation is seen at positive delays that occurs solely after the pump pulse arrival at $t = 0$. This signal arises from the exciton contribution of the charge-neutral quantum dots in the ensemble. In magnetic fields of 1 and 6 T, long-lived electron-spin quantum beats appear at positive delays, as discussed before. Surprisingly, under these conditions strong spin beats with a frequency corresponding to the electron precession are observed also at negative delays in nonzero magnetic field. The amplitude of these quantum beats increases when approaching zero delay $t = 0$. Spin beats at negative delay have been reported for experimental situations in which the decay time exceeds the time interval between the pump pulses: $T_2^* \geq T_R$ [3]. This is clearly not the case here, where the Faraday-rotation signal has fully vanished after 1.2 ns at $B = 6$ T, so that $T_2^* < T_R$. The rise time of the signal at the negative-delay side is the same as the decay time on the positive-delay side, suggesting that the negative-delay signal also can be traced to electron-spin precession.

The upper panel shows the signal when scanning the delay over a larger range in time, in which four pump pulses, separated by 13.2 ns from each other, are located. At each pump arrival electron-spin coherence is created, which after a few ns is quickly dephased. Before each pump arrival the coherent signal from electrons appears again. This negative-delay precession can occur only if the coherence of the electron spin in each single dot prevails for much longer times than the time interval T_R between the laser pump pulses, in contrast to the ensemble spin dephasing. Leaving the origin of the coherent signal appearance aside for a moment, this opens a pathway towards

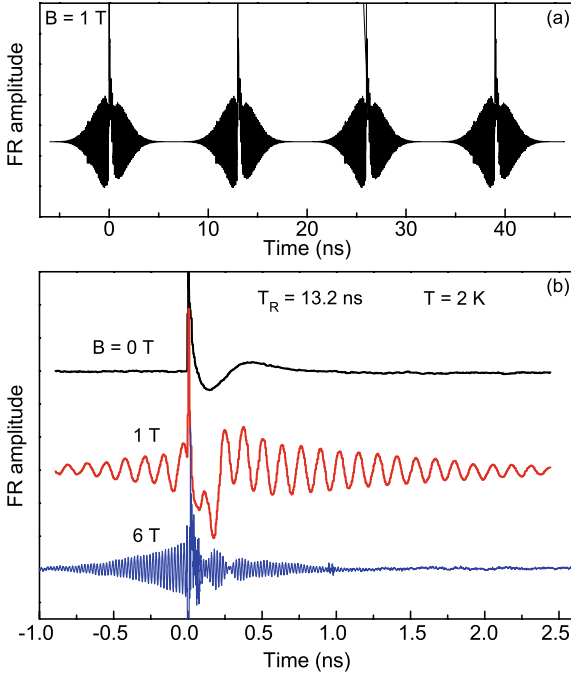


Fig. 7. *Lower panel:* Pump-probe Faraday-rotation signal versus delay measured at different magnetic fields on singly charged (In,Ga)As/GaAs quantum dots. The pump power density is 60 W/cm^2 , the probe density is 20 W/cm^2 . *Upper panel:* Faraday-rotation signal recorded for a longer delay range in which four pump pulses were located

measuring the spin-coherence time T_2 : When increasing the pump pulse separation continuously, we end up in a range comparable to the T_2 times in which coherence is continuously reduced, which should reduce the amplitude of the signal on the negative-delay side. Finally, if the pump-pulse separation is increased far above the average coherence time, this signal should vanish completely.

Corresponding data at $B = 6 \text{ T}$ measured for two pump densities differing by a factor of two are given in Fig. 8, showing the Faraday-rotation amplitude on the negative-delay side shortly before the next pump arrival as a function of T_R . The repetition period, T_R , was increased from 13.2 up to 990 ns by means of a laser pulse picker. A significant Faraday-rotation signal can be measured even for the longest pulse interval of a μs . Technically it would be possible to go to even larger T_R , but the repetition rate of the experiment is also strongly reduced in the measurement, leading to weak signal strength and therefore complicating the experiment. From the data we see, however, that a drop of Faraday-rotation amplitude occurs, meaning that we scan a range that must be comparable with T_2 .

In order to understand why the single quantum-dot coherence time can be seen at all in an ensemble measurement, let us consider excitation of a single quantum dot by a periodic π -pulse train of circularly polarized light. The first impact of the pulse train is a synchronization of electron-spin precession. To discuss this effect we define the degree of spin syn-

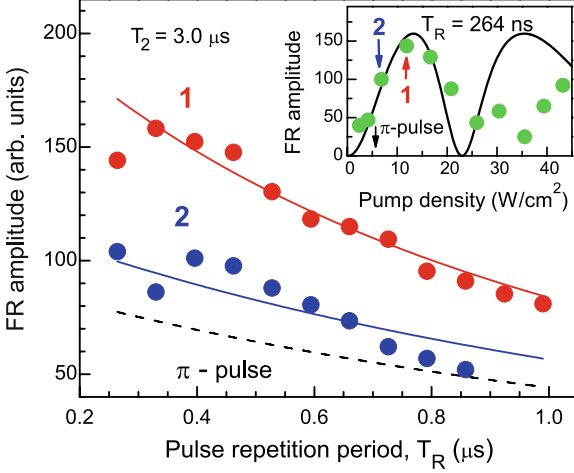


Fig. 8. Faraday-rotation amplitude at negative delay as function of time interval between pump pulses. The experimental data were measured at $B = 6 \text{ T}$ for two pump densities of 12 and 6 W/cm^2 shown in the *inset* by the *red* and *blue* arrows. $T = 6 \text{ K}$. The *solid lines* show the theoretical dependencies described by (22), which contained as a single fit parameter $T_2 = 3.0 \mu\text{s}$. In the *inset* the Faraday-rotation amplitude measured at $T_R = 264 \text{ ns}$ is shown as a function of pump density. The *solid line* shows the theoretical dependence described by (22). The comparison of experiment and theory allows us to determine the pump density, which corresponds to the π -pulse (shown by the *black arrow*). The theoretical dependence of the Faraday-rotation amplitude on T_R calculated for π -pulse excitation is shown by the *dashed line*

chronization by $P(\omega_e) = 2|S_z(\omega_e)|$. Here, $S_z(\omega_e)$ is the z -projection of the electron spin at the moment of pulse arrival. If the pulse period, T_R , is equal to an integer number, N , times the electron-spin precession period in a transverse magnetic field, $2\pi/\omega_e$, such a train of π -pulses leads to almost complete electron-spin alignment along the light-propagation direction [25] (as above). The degree of spin synchronization reaches its largest value $P_\pi = \exp(-T_R/T_2)/[2 - \exp(-T_R/T_2)]$, corresponding to almost 100% synchronization, because for excitation with a high repetition rate (as in experiments) $T_R \ll T_2$ so that $\exp(-T_R/T_2) \approx 1$.

An ensemble contains quantum dots whose precession frequencies fulfill the following relation that we term the phase-synchronization condition:

$$\omega_e = 2\pi N/T_R \equiv N\Omega. \quad (10)$$

Since the electron-spin precession frequency is typically much larger than the laser repetition rate for not too small magnetic fields, multiple quantum-dot subsets satisfy the condition (10) for different N within the whole ensemble, as in addition the precession frequencies are widely distributed. This is illustrated by Fig. 9, where panel A sketches the precession for $N = K$ and $K + 1$,

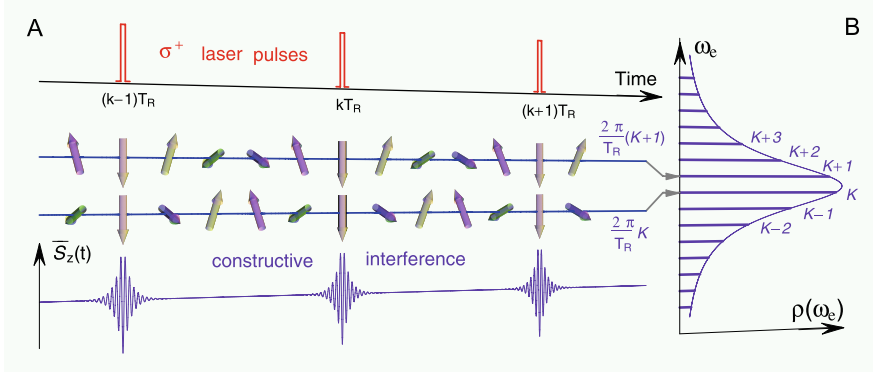


Fig. 9. Phase synchronization of electron-spin precession by a train of π -pulses of circularly polarized light. The top panel shows the train of σ^+ -polarized laser pulses with repetition period T_R . The train synchronizes the electron-spin precession in quantum dots where the precession frequency is a multiple of $(2\pi/T_R)$: $\omega_e = N(2\pi/T_R)$. In these quantum dots, the spins are aligned at the moment of the pulse arrival: each spin is opposite to the light-propagation direction. The two *middle panels* show the phase synchronization for two spins with precession frequencies differing by $2\pi/T_R$: $N = K$ and $N = K + 1$ (K is a large integer). The *bottom panel* shows a time evolution of the average spin polarization $\overline{S}_z(t)$, resulting from a constructive interference of the phase-synchronized quantum-dot subsets. **(B)** Spectrum of phase-synchronized electron-spin precession modes enveloped by the density of precession frequencies $\rho(\omega_e)$ in a quantum-dot ensemble. Only those electron spins that are synchronized by the pulse train give a contribution to the spectrum, consisting of sharp peaks at the frequencies $\omega_e = N(2\pi/T_R)$ ($N = \dots, K - 1, K, K + 1, \dots$) which satisfy the phase-synchronization condition (10)

and panel B gives the spectrum of phase-synchronized precession modes. The number of synchronized subsets, ΔN , can be estimated from the broadening of the electron-spin precession frequencies by: $\Delta N \sim \gamma/\Omega$. It increases linearly with magnetic field, B , and pulse period, T_R . The spins in each subset precess between the pump pulses with frequency $N\Omega$, starting with an initial phase that is the same for all subsets. Their contribution to the spin polarization of the ensemble at a time t after the pulse is given by $-0.5 \cos(N\Omega \cdot t)$. As sketched in Fig. 9, the sum of oscillating terms from all subsets leads to a constructive interference of their contributions when the next pulse arrives. The rest of the quantum dots do not contribute to the average electron-spin polarization $\overline{S}_z(t)$ at times $t \gg T_2^*$, due to dephasing. The synchronized spins therefore move on a background of dephased electrons, which, however, also still precess individually.

The average spin polarization can be written as $\overline{S}_z(t) = -0.5\Omega \times \sum_{N=-\infty}^{\infty} \cos(N\Omega \cdot t)\rho(N\Omega)$, where $\rho(\omega_e)$ is the density of the quantum-dot precession frequencies within the laser excitation profile. Assuming that this

density has a Lorentzian shape³ $\rho(\omega_e) = (\gamma/\pi)(1/[(\omega_e - \bar{\omega}_e)^2 + \gamma^2])$, centered around the average frequency $\bar{\omega}_e$, we obtain:

$$\bar{S}_z(t) \approx \frac{\beta \cosh\{\beta[1 - 2 \operatorname{mod}(t, T_R)]\} - \sinh \beta}{\beta \sinh \beta} \cos(\bar{\omega}_e t), \quad (11)$$

where $\beta = \gamma T_R/2$ and $\operatorname{mod}(x, y) = x - y[x/y]$ is the modul function, with $[x/y]$ defined as integer division. The resulting time dependence of $\bar{S}_z(t)$ (Fig. 9A) explains the appearance of Faraday-rotation signal at negative delays.

Obviously, π -pulse excitation is not critical for the electron-spin phase synchronization by the circularly polarized light pulse train. Resonant pulses of arbitrary intensity create a coherent superposition of the trion and electron state in a quantum dot, leading to a long-lived coherence of resident electron spins, because the coherence is not affected by the radiative decay of the trion component. Each pulse of σ^+ -polarized light changes the electron-spin projection along the light-propagation direction by $\Delta S_z = -(1 - 2|S_z(t \rightarrow t_n)|)W/2$, where $t_n = nT_R$ is the time of the n th pulse arrival, and $W = \sin^2(\Theta/2)$ with Θ being the pulse area [9, 27]. Consequently, a train of these pulses orients the electron spin opposite to the light-propagation direction, and it also increases the degree of electron-spin synchronization P . Application of $\Theta = \pi$ -pulses (corresponding to $W = 1$) leads to a 99% degree of electron-spin synchronization already after a dozen of pulses. However, if the electron-spin coherence time is long enough ($T_2 \gg T_R$), an extended train of pulses leads to a high degree of spin synchronization even for $\Theta \ll 1$ ($W \approx \Theta^2/4$).

Let us consider the problem in more detail: An infinite train of circularly polarized light pulses propagating along the z -direction in a transverse magnetic field parallel to the x -axis, leads to a periodic time-dependent distribution of electron-spin polarization, $S_{z,y}(t + T_R) = S_{z,y}(t)$, in a single quantum dot. If the pulse duration Δt is much shorter than the trion radiative decay time, the electron and hole spin relaxation times and the electron and hole precession times, the creation of spin polarization can be separated in two well-defined processes, as discussed in the previous section [9]. The first one is the electron excitation into a coherent superposition state of electron and trion. The second one describes the radiative decay of the trion component in this superposition into the electron precessing in the transverse magnetic field [9, 25, 27]. As a result, the electron-spin polarization in high magnetic fields, $\omega_e \tau_T \gg 1$, is controlled by the electron-spin generation during the pump pulse and its later precession with a slow decay. This leads to the following time dependence of the electron-spin polarization after the

³ We chose a Lorentzian profile for the quantum-dot precession frequencies in the consideration because it leads to the closed form for $\bar{S}_z(t)$ in (11). Generally, our numerical calculations do not show any of qualitative or quantitative differences for the both Gaussian or Lorentzian profiles as long as the distribution $\rho(\omega_e)$ is smoothly going to zero on the scale of its width.

initialization pulse:

$$\begin{aligned} S_z(t) &= [S_z^0(t_n) \cos(\omega_e t) + S_y^0(t_n) \sin(\omega_e t)] \exp(-t/T_2), \\ S_y(t) &= [S_y^0(t_n) \cos(\omega_e t) - S_z^0(t_n) \sin(\omega_e t)] \exp(-t/T_2), \end{aligned} \quad (12)$$

where $S_{z,y}^0(t_n)$ are the electron-spin polarizations created in the quantum dot by the n th pulse. A pulse of σ^+ circular helicity creates the following polarization components:

$$\begin{aligned} S_z^0(t_n) &= S_z^- [1 - \sin^2(\Theta/2)/2] - \sin^2(\Theta/2)/4, \\ S_y^0(t_n) &= S_y^- \cos(\Theta/2), \end{aligned} \quad (13)$$

where Θ is the pulse area and $S_{z,y}^- = S_{z,y}(t \rightarrow t_n)$ are the z - and y -projections of the electron-spin polarization shortly before the pulse arrival. Equations (12) and (13) allow us to connect the spin polarizations before the n th and the $(n+1)$ th pulses. These relationships can be written as:

$$\begin{aligned} S_z^-(t_{n+1}) &= \left\{ \left[-\frac{W}{4} + S_z^-(t_n) \left(1 - \frac{W}{2} \right) \right] \cos(\omega_e T_R) \right. \\ &\quad \left. + \nu \sqrt{1-W} S_y^-(t_n) \sin(\omega_e T_R) \right\} e^{-T_R/T_2}, \\ S_y^-(t_{n+1}) &= \left\{ \left[\frac{W}{4} - S_z^-(t_n) \left(1 - \frac{W}{2} \right) \right] \sin(\omega_e T_R) \right. \\ &\quad \left. + \nu \sqrt{1-W} S_y^-(t_n) \cos(\omega_e T_R) \right\} e^{-T_R/T_2}, \end{aligned} \quad (14)$$

where $W = \sin^2(\Theta/2)$ and $\nu = \text{sign}[\cos(\Theta/2)]$. The steady-state value of these amplitudes, $S_{z,y}(\omega_e)$, is found by the transition $n \rightarrow \infty$:

$$\begin{aligned} S_z(\omega_e) &= -W e^{-T_R/T_2} \frac{\cos(\omega_e T_R) - C_W^\nu}{2\Delta(\omega_e)}, \\ S_y(\omega_e) &= W e^{-T_R/T_2} \frac{\sin(\omega_e T_R)}{2\Delta(\omega_e)}, \end{aligned} \quad (15)$$

where $C_W^\nu = \nu \sqrt{1-W} e^{-T_R/T_2}$ and the denominator $\Delta(\omega_e)$ is given by

$$\begin{aligned} \Delta(\omega_e) &= 2 - e^{-T_R/T_2} (2 - W) \cos(\omega_e T_R) \\ &\quad + C_W^\nu [(2 - W) e^{-T_R/T_2} - 2 \cos(\omega_e T_R)]. \end{aligned} \quad (16)$$

$\Delta(\omega_e)$ almost vanishes at the frequencies satisfying the phase-synchronization condition of (10). As a result, the distribution of spin polarization synchronized by the train of pulses, $S_z(\omega_e)$, consists of sharp peaks at frequencies $\omega_e = N\Omega$. Near the peaks, at small T_R/T_2 and Θ , the spectrum is given by

$$S_z(\omega_e) = -\frac{1}{2} \frac{(W/2T_R)(W/2T_R + 1/T_2)}{(W/2T_R + 1/T_2)^2 + (\omega_e - N\Omega)^2}. \quad (17)$$

In the case of π -pulse excitation ($W = 1$) the distribution of spin polarization takes the form:

$$S_z(\omega_e) = \frac{1}{2} \cdot \frac{e^{-T_R/T_2} \cos(2\pi\omega_e/\Omega)}{e^{-T_R/T_2} \cos(2\pi\omega_e/\Omega) - 2}. \quad (18)$$

One can see that in this case $S_z(\omega_e)$ has maxima, each with a width equal to the separation between them.

It is convenient to introduce the time-dependent electron-spin polarization vector in a single quantum dot as $\mathbf{S}_{\omega_e}(t) = S_z(t) + iS_y(t)$. Substituting (15) into (12), we obtain the time dependence of $\mathbf{S}_{\omega_e}(t)$ in the time interval $t_n \leq t < t_{n+1}$:

$$\mathbf{S}_{\omega_e}(t) = -W e^{-t/T_2} \frac{e^{-i\omega_e t} - C_W^\nu e^{-i\omega_e(t-T_R)}}{2\Delta(\omega_e)}. \quad (19)$$

The electron-spin polarization for an ensemble of QDs is obtained by averaging over the density of electron-spin precession frequencies $\rho(\omega_e)$. In this case the average electron-spin polarization are $\overline{S}_z(t) = \text{Re}[\overline{\mathbf{S}}(t)]$ and $\overline{S}_y(t) = \text{Im}[\overline{\mathbf{S}}(t)]$, where $\overline{\mathbf{S}}(t) = \int d\omega_e \rho(\omega_e) \mathbf{S}_{\omega_e}(t)$. The integral can be written as

$$\overline{\mathbf{S}}(t) = A_W^\nu(t) \mathcal{M}(t), \quad (20)$$

and can be expressed by the Faraday-rotation amplitude $A_W^\nu(t)$ and the sum of poles in the complex plane:

$$\mathcal{M}(t) = -\frac{\Omega}{2} \sum_{N=-\infty}^{\infty} \rho(N\Omega t) e^{-iN\Omega t}. \quad (21)$$

The sum over the quantum-dot subsets for which the electron-spin precession is phase synchronized in (21) leads to the constructive interference in the Faraday rotation signal at negative delay. It is remarkable that this interference does not depend on the excitation intensity. The simplified expression for the average electron-spin polarization in (11), which is equal to $\text{Re}[\mathcal{M}(t)]$, can be obtained using $S_z(\omega_e) = -0.5\Omega \sum_N \delta(\omega_e - N\Omega)$. The Faraday-rotation amplitude $A_W^\nu(t)$ is given by:

$$A_W^\nu(t) = W \frac{e^{-t/T_2} e^{-\Gamma t} [1 - C_W^\nu e^{\Gamma(2t-T_R)}]}{\sqrt{[4 - (W-2)^2 e^{-2T_R/T_2}][1 - (C_W^\nu)^2]}}, \quad (22)$$

with an additional dephasing rate that is connected to the broadening of the phase-synchronized spectrum by

$$\Gamma = \frac{1}{T_2} + \frac{1}{T_R} \ln \frac{2 - C_W^\nu (W-2) e^{-T_R/T_2} \sqrt{[4 - (W-2)^2 e^{-2T_R/T_2}][1 - (C_W^\nu)^2]}}{2 + 2\nu\sqrt{1-W} - W}. \quad (23)$$

Equation (22) shows that the excitation intensity controls the time dependence of the Faraday-rotation amplitude. Let us use these results to analyze the data further.

The dependence of the Faraday-rotation amplitude at negative delay time on the laser pulse repetition period T_R , does not generally allow for a direct measurement of the single quantum-dot coherence time. An increase of T_R also modifies the steady-state value of the electron-spin polarization at the moment of the pulse arrival, as one can see from (15). In particular, at small W it will strongly reduce the Faraday-rotation amplitude. The Faraday-rotation amplitude dependence on the pump density measured for $T_R = 264$ ns shows a nonmonotonic behavior (inset of Fig. 8 in manuscript), which is connected to the complex dependence of the Faraday-rotation amplitude on the pulse area. Additional decoherence mechanisms decrease the Faraday-rotation amplitude in experiment at high pump densities beyond a 2π -pulse, as one can see in the inset of Fig. 8. It is worthwhile to note here that in the case of π -pulse excitation, the Faraday-rotation amplitude can be approximated by: $\exp[-(2 + \frac{1}{2\sqrt{3+3}})\frac{T_R}{T_2}]$ for $T_R < T_2$, and it is described by a simple exponential form $\exp(-2T_R/T_2)$ at $T_R \gg T_2$.

Therefore, the degree of synchronization is given by $P(\omega_e) = 2|S_z(\omega_e)|$:

$$P(\omega_e) = \frac{(W/2T_R)(W/2T_R + 1/T_2)}{(W/2T_R + 1/T_2)^2 + (\omega_e - N\Omega)^2}. \quad (24)$$

One sees that: (i) a train of pulses synchronizes the spin precession of quantum-dot electrons with precession frequencies in a narrow range of width $W/2T_R + 1/T_2$ around the phase-synchronization condition, (ii) the electron-spin synchronization still reaches 100% if $W/2T_R \gg 1/T_2$.

When $\Theta = \pi$, (18) gives the degree of the electron-spin synchronization as:

$$P_\pi(\omega_e) = \frac{e^{-T_R/T_2} |\cos(2\pi\omega_e/\Omega)|}{2 - e^{-T_R/T_2} \cos(2\pi\omega_e/\Omega)}, \quad (25)$$

corresponding to the maximum degree of spin synchronization, P_π , for electrons matching the phase-synchronization condition. Obviously, π -pulses synchronize the electron-spin precession in a broad range of frequencies with width $\sim \Omega$, which is about the gap between neighboring phase-synchronization condition frequencies.

The effect of the pump density (namely of the pump area) on the distribution of the spin-polarization synchronized by and with the pulse train at the moment of the pulse arrival ($t = t_n$) for $\Theta = 0.4\pi$, π and 1.6π , is shown in Figs. 10A–C. Calculations were done for $T_R = 13.2$ ns (red) and 52.8 ns (blue). The density of the electron-spin precession modes is shown by the black line, which gives the envelop of the spin-polarization distribution. The quasidiscrete structure of the distribution created by the pulse train is the most important feature, which allows us to measure the long spin-coherence

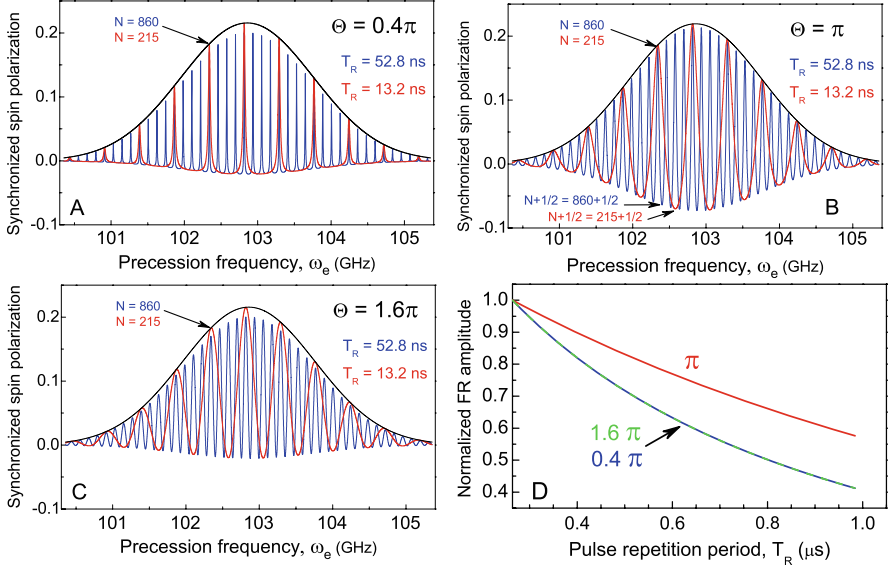


Fig. 10. Spectra of phase-synchronized electron-spin precession modes created by a train of circularly polarized pulses, $-\bar{S}_z(t_n)$, calculated for the pulse area $\Theta = 0.4\pi$, π , and 1.6π , respectively. The spectra have been calculated for two pump-pulse repetition periods: $T_R = 13.2$ ns (red) and 52.8 ns (blue). At low pumping intensity (panel **A**) the pulse train synchronizes electron-spin precession in a very narrow frequency range near the phase-synchronization condition: $\omega_e = N(2\pi/T_R)$. The π -pulses (panel **B**) widen the range of synchronized precession frequencies. In addition, the electron spins with opposite polarization at frequencies between the phase-synchronization condition become significantly synchronized. The degree of synchronization for these spins decreases at $\Theta > \pi$ (panel **C**). (**D**) Negative-delay Faraday-rotation amplitude dependence on pump-pulse repetition period T_R calculated for the same three pulse areas. The amplitude is normalized to its value at $T_R = 264$ ns. All calculations have been done for a magnetic field of $B = 2$ T with $g_e = |0.57|$, $\Delta g_e = 0.005$ and $T_2 = 3.0$ μ s

time of a single quantum dot on an ensemble: A continuous density of spin-precession modes would always cause fast dephasing with a time inversely proportional to the total width of the frequency distribution: $T_2^* = \hbar/\gamma$. Only the gaps in the density of precession modes facilitate the constructive interference at negative delay times in Fig. 7. These gaps are created by mode locking of the electron spins with the periodic laser emission.

The broadening of the quasidiscrete spectra around the phase-synchronization condition is significantly smaller than γ . Nevertheless, it leads to dephasing. The calculations show that the dephasing rate of the quantum-dot ensemble can be written as $\Gamma_{\text{pump}} + 1/T_2$, where the additional dephasing rate Γ depends on T_2 , W , and T_R as seen from (23). In the present limit of $T_R \ll T_2$, (23) gives $\Gamma \approx W/2T_R + 1/T_2$ and $\Gamma \approx \ln(2 + \sqrt{3})/T_R + 1/T_2$ for $W \ll 1$

and $W = 1$, respectively. T is obviously smaller for weak excitation pulses. These results are consistent with the fact that the dephasing is inversely proportional to the broadening of the phase-matched precession modes.

Figure 10D shows the decay of the normalized Faraday-rotation amplitudes as a function of pulse repetition time T_R , calculated using (22). The decay depends on the pulse area and is minimized for a π -pulse. The decay rate for pulses with areas deviating from π are equal for $\Theta = \pi - \alpha$ and $\pi + \alpha$. We have fitted the experimental dependence of the Faraday-rotation amplitude on T_R (Fig. 8) and its dependence on pump density (inset in Fig. 8) by (22). The factor two difference in pumping intensities used for recording the data labeled 1 and 2 leads to a significant restriction of the T_2 value in Fig. 8. The fit allows us to determine a pump density corresponding to the π -pulse and a single quantum-dot coherence time $T_2 = 3.0 \pm 0.3 \mu\text{s}$, which is four orders of magnitude longer than the ensemble dephasing time $T_2^* = 0.4 \text{ ns}$ at 6 T.

The Faraday-rotation amplitude does not reach its largest value at π -pulse pumping (see inset of Fig. 8). This is because the train of π -pulses synchronizes the spin precession for a broad distribution of precession frequencies and not only for the ω_e satisfying the phase-synchronization condition. For example, in the quantum dots with $\omega_e = (N + 1/2)\Omega$ the spin-synchronization degree is $1/3$. However, the S_z projection of electron spin in these quantum dots is opposite to that for quantum dots that satisfy the phase-synchronization condition ($\omega_e = N\Omega$), as seen in Fig. 10B. This leads to cancellation effects in the total Faraday-rotation amplitude of the quantum-dot ensemble. In contrast, one can see in Fig. 10C that pulses with an area $\Theta > \pi$ are not so efficient in synchronizing the electron-spin precession in quantum dots that do not satisfy the phase-synchronization condition. This diminishes the “negative” contribution of such quantum dots to the electron-spin polarization and increases the Faraday-rotation amplitude. Generally, the rise of the excitation intensity from zero to π -pulses increases the number of quantum dots contributing to the Faraday-rotation signal at negative delays.

After having shown that a specific protocol for a laser pulse sequence can be used for selecting a subset of synchronized quantum dots with the single-dot dephasing time, we turn to testing the degree of control that can be achieved by such sequences. For that purpose each pump is split into two pulses with a fixed delay $T_D < T_R$ between them. The results of measurements for $T_D = 1.84 \text{ ns}$ are plotted in Fig. 11A. Both pumps were circularly copolarized and had the same intensities. When the quantum dots are exposed to only one of the two pumps (the two upper traces), the Faraday-rotation signals are identical except for a shift by T_D . The signal changes drastically under excitation by the two pulse train (the lower trace): Around the arrival of pump 1 the same Faraday-rotation response is observed as before in the one-pump experiment. Also, around the pump 2 qualitatively

the same Faraday-rotation pattern is observed with considerably larger amplitude. Therefore, the coherent response of the synchronized quantum-dot ensemble can be amplified by the second laser pulse. Even more remarkable are the echo-like responses showing up in the Faraday-rotation signal before the first and after the second pump pulse. They have a symmetric shape with the same decay and rise times T_2^* . The temporal separation between them is a multiple of T_D . Note that these Faraday-rotation bursts show no additional modulation of the Faraday-rotation traces as seen at positive delay times when the pump is applied. This is in agreement with the assignment of the modulation to the photogenerated carriers [9].

Apparently, the electron spins in the quantum-dot subensemble, which is synchronized with the laser repetition rate, have been clocked by introducing a second frequency that is determined by the laser-pulse separation. The clocking results in multiple bursts in the Faraday-rotation response. This behavior can be explained by our theoretical model: The echo-like signal has the same origin as the Faraday-rotation revival in the single-pump experiment, which is constructive interference of the Faraday-rotation amplitudes from quantum-dot subsets with phase-synchronized electron-spin precession. We have calculated the distribution of electron-spin polarization created by a train of π -pulses in the two-pump experiment, using a technique similar to the one described above for the single-pump experiment. The resultant time dependence of the Faraday-rotation signal reproduces well the experimental burst signals (Fig. 11B).

Considering the above mode-locking mechanism in an ensemble of quantum dots with inhomogeneously broadened precession frequencies raises the question as to what properties should a quantum-dot ensemble have for their use in various quantum coherent devices. In general, quantum-dot ensembles in which spin states are only homogeneously broadened would be optimal for quantum information processing. Moreover, precise tailoring of properties such as the electron g-factor should be possible. However, fabrication of such ensembles cannot be foreseen based on current state-of-the-art techniques, which always lead to sizeable inhomogeneities. Under these circumstances, a sizable distribution of the electron g-factor is good for mode locking, as the phase-synchronization condition is fulfilled by many quantum-dot subsets, leading to strong spectroscopic response. Further, it gives some flexibility when changing, for example, the laser protocol (e.g., wavelength, pulse duration and repetition rate) by which the quantum dots are addressed, and therefore changing the phase-synchronization condition, as the ensemble involves other quantum-dot subsets for which the single-dot coherency can be recovered. However, a very broad distribution of electron g-factors would lead to a very fast dephasing in the ensemble, making it difficult to observe the Faraday rotation both after and before pulse arrival. In this case, the phase synchronization can be exploited only during a very short period of time.

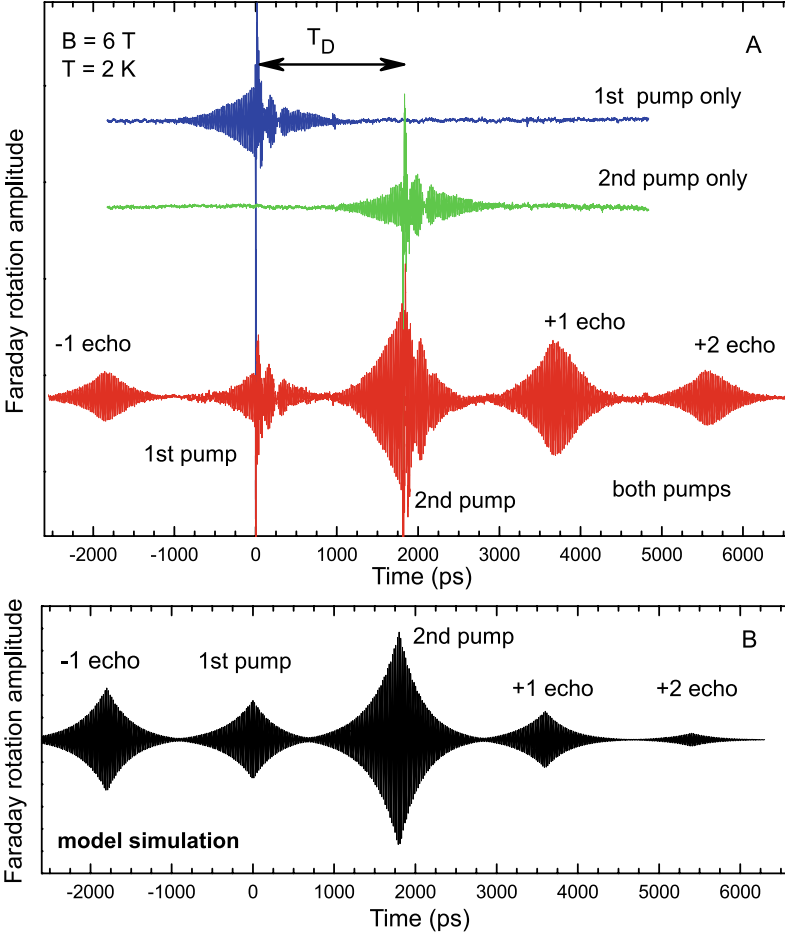


Fig. 11. Control of the electron-spin synchronization by two trains of pump pulses with $T_R = 13.2$ ns shifted in time by $T_D = 1.84$ ns. **(A)** Experimental Faraday-rotation signal measured for separate action of the first or the second pump (the two *upper curves*) and for joint action of both pumps (the *bottom curve*). The pumps were copolarized (σ^+). **(B)** Theoretical modeling of the spin-echo-like signals in the two-pulse experiment with the parameters: $\Theta = \pi$ and $\gamma = 3.2$ GHz

6 Summary

In summary, we have performed detailed studies of the electron g-factor in quantum dots. The spin is described by a complex g-factor tensor with pronounced anisotropies. With this knowledge we have addressed the coherent manipulation of the spin. We have shown first a very efficient technique by which the spin can be oriented (initialized) by circularly polarized laser pulses. By such pulses the spin orientation can be controlled. We have then shown

that the electron can be phase synchronized with the periodic laser protocol. As a first tradeoff this technique allowed an electron-spin coherence time of 3 μs at cryogenic temperatures. We have then succeeded with a first demonstration that this method also allows a far-reaching coherent control of the spins: A two-pulse protocol allowed us to clock the electron spin such that periodic bursts appear in the Faraday-rotation signal.

This result shows that the deficits that are typically attributed to quantum-dot spin ensembles may be overcome when combining them with elaborated laser excitation protocols, with all the related advantages due to the robustness of the phase synchronization of the quantum-dot ensemble: (i) a strong detection signal with relatively small noise; (ii) changes of external parameters like repetition rate and magnetic field strength can be accommodated for in the phase-synchronization condition due to the broad distribution of electron-spin precession frequencies in the ensemble and the large number of involved quantum dots. This should be elaborated further in future studies.

Acknowledgements

This work was supported by the Bundesministerium für Bildung und Forschung (program ‘nanoquit’), the Defense Advanced Research Program Agency (program ‘QuIST’), the Office of Naval Research, and the Deutsche Forschungsgemeinschaft (Forschergruppe ‘Quantum Optics in Semiconductor Nanostructures’). R.O. thanks the Alexander von Humboldt foundation. Parts of this work were done in collaboration with R. Oulton, E.A. Zhukov, I.A. Yugova. We additionally thank I.A. Merkulov for the fruitful discussions. Samples on which the described work was done were grown in Bochum University by V. Stavarache, D. Reuter, and A.D. Wieck.

References

1. D. Loss, D.P. DiVincenzo, *Phys. Rev. A* **57**, 120 (1998) 52
2. A. Imamoglu, D.D. Awschalom, G. Burkard, D.P. DiVincenzo, D. Loss, M. Sherwin, A. Small, *Phys. Rev. Lett.* **83**, 4204 (1999) 52
3. D.D. Awschalom, D. Loss, N. Samarth (eds.), *Semiconductor Spintronics and Quantum Computation* (Springer, Heidelberg, 2002) 52, 66
4. J.M. Kikkawa, D.D. Awschalom, *Science* **287**, 473 (2000) 52
5. J.M. Elzerman, R. Hanson, L.H. Willems Van Beveren, B. Witkamp, L.M.K. Vandersypen, L.P. Kouwenhoven, *Nature* **430**, 431 (2004) 53, 64, 66
6. M. Kroutvar, Y. Ducommun, D. Heiss, M. Bichler, D. Schuh, G. Abstreiter, J.J. Finley, *Nature* **432**, 81 (2004) 53, 64
7. W.A. Coish, D. Loss, *Phys. Rev. B* **70**, 195340 (2004) 53

8. J.R. Petta, A.C. Johnson, J.M. Taylor, E.A. Laird, A. Yacoby, M.D. Lukin, C.M. Marcus, M.P. Hanson, A.C. Gossard, *Science* **309**, 2180 (2005) 53
9. A. Greilich, R. Oulton, E.A. Zhukov, I.A. Yugova, D.R. Yakovlev, M. Bayer, A. Shabaev, A.L. Efros, I.A. Merkulov, V. Stavarache, D. Reuter, A. Wieck, *Phys. Rev. Lett.* **96**, 227401 (2006) 53, 64, 70, 76
10. R. Oulton, A. Greilich, S.Yu. Verbin, R.V. Cherbunin, T. Auer, D.R. Yakovlev, M. Bayer, V. Stavarache, D. Reuter, A. Wieck, *cond-mat/0505446* 53, 64
11. S.A. Crooker, D.D. Awschalom, J.J. Baumberg, F. Flack, N. Samarth, *Phys. Rev. B* **56**, 7574 (1997) 54
12. R.E. Worsley, N.J. Trainor, T. Grevatt, R.T. Harley, *Phys. Rev. Lett.* **76**, 3224 (1996) 54
13. P.Y. Yu, M. Cordona, *Fundamentals of Semiconductors* (Springer, Berlin, 1996) 55
14. I.A. Merkulov, A.L. Efros, M. Rosen, *Phys. Rev. B* **65**, 205309 (2002) 59, 64
15. T.H. Stievater, X. Li, D.G. Steel, D.S. Katzer, D. Park, C. Piermarocchi, L. Sham, *Phys. Rev. Lett.* **87**, 133603 (2001) 60
16. A. Zrenner, E. Beham, S. Stuffer, F. Findeis, M. Bichler, G. Abstreiter, *Nature* **418**, 612 (2002) 60
17. P. Borri, W. Langbein, S. Schneider, U. Woggon, R.L. Sellin, D. Ouyang, D. Bimberg, *Phys. Rev. B* **66**, 081306(R) (2002) 61
18. A. Shabaev, A.L. Efros, unpublished 63
19. M.V. Gurudev Dutt, J. Cheng, B. Li, X. Xu, X. Li, P.R. Berman, D.G. Steel, A.S. Bracker, D. Gammon, S.E. Economou, R.-B. Liu, L.J. Sham, *Phys. Rev. Lett.* **94**, 227403 (2005) 63
20. G. Morigi, E. Solano, B.-G. Englert, H. Walther, *Phys. Rev. A* **65**, 040102(R) (2002) 64
21. A.V. Khaetskii, D. Loss, L. Glazman, *Phys. Rev. Lett.* **88**, 186802 (2002) 64
22. D.V. Bulaev, D. Loss, *Phys. Rev. Lett.* **95**, 076805 (2005) 64
23. T. Flissikowski, I.A. Akimov, A. Hundt, F. Henneberger, *Phys. Rev. B* **68**, 161309(R) (2003) 64
24. S.E. Economou, R.-B. Liu, L.J. Sham, D.G. Steel, *Phys. Rev. B* **71**, 195327 (2005) 64
25. A. Shabaev, A.L. Efros, D. Gammon, I.A. Merkulov, *Phys. Rev. B* **68**, 201305 (2003) 63, 64, 68, 70
26. C.P. Slichter, *Principles of Magnetic Resonance* (Springer, Berlin, 1996) 66
27. T.A. Kennedy, A. Shabaev, M. Scheibner, A.L. Efros, A.S. Bracker, D. Gammon, *Phys. Rev. B* **73**, 045307 (2006) 70

Index

coherent optical manipulation, 53

decoherence mechanisms, 73

electron g-factor, 54

electron-spin coherence, 56, 78

ensemble spin dephasing time, 59

Faraday-rotation spectroscopy, 56

g-factor tensor, 51, 77

Pauli blocking, 60

phase-synchronization condition, 68

quantum information processing, 76

Rabi oscillations, 60

self-assembled (In,Ga)As/GaAs
quantum dots, 53

self-assembled quantum dots, 51, 52, 55

singly charged quantum dots, 62

spin coherence, 51, 61

spin coherence times, 52

spin synchronization, 68

time-resolved pump-probe Faraday-
rotation methods, 54

two-level systems, 51

Single-Electron-Spin Measurements in Si-Based Semiconductor Nanostructures

H.W. Jiang¹, E. Yablonovitch¹, M. Xiao¹, M. Sakr¹, G. Scott¹, and
E.T. Croke²

¹ University of California, Los Angeles, CA 90095, USA

² HRL Laboratories, LLC, Malibu, CA 90265, USA

Abstract. In this chapter, we review the experimental efforts that focus on the measurement of single-electron spins in two particular Si-based semiconductor nanostructure systems. First, we describe experiments in a real transistor structure (i.e., a submicrometer commercial Si field effect transistor) in which the source/drain channel is used to electrically detect the spin states of an adjacent single paramagnetic spin center. This transistor structure is similar to a number of proposed spin-based qubit architectures that can be used as a potential quantum information processor. Second, we describe the effort to fabricate similar devices in specially designed semiconductor structures that promise greater control over electron spin, the ability to entangle two spins, and to eventually build a scalable quantum processor. In these engineered structures, quantum dots are created by metallic gates patterned over a 2D electron gas in a strained silicon-germanium heterostructure. In addition to the discussion of fabrication issues, we also show examples of single-electron-spin measurements in the few-electron regime of quantum dots.

1 Introduction

Isolated electron spins in low-temperature semiconductors are now recognized to have considerable potential for storing and manipulating quantum information. One of the attractions of a spin in a semiconductor is its very long decoherence time. The tunable spin-orbital coupling and the ability to control the electron wavefunctions in semiconductors allow gate operations on the spins. Another advantage is that they can be embedded into transistor structures, a premise that lends itself to the large-scale integration necessary for a quantum information processor. The extensive collection of chipmaking techniques, accumulated over decades, is expected to be extremely invaluable for building such a scalable processor. Possible applications of the quantum information processing devices including encryption and secure communications are recognized to be important to a modern society. While a fully functional factorization engine needs at least 1000 quantum logic bits, communication devices such as a quantum repeater require only 3 quantum logic gates [1].

Amongst various semiconductor materials, silicon is recognized to be a leading candidate for this purpose [2]. Electron spins in Si are endowed with the particular properties that would make them useful as qubits. The most important property is the safe preservation of quantum-mechanical phase information. It has been demonstrated experimentally that isotopically pure Si materials can have extremely long phase-coherence times, many orders of magnitude longer than that for group III–V semiconductors [3]. The primary mechanism for electron-spin decoherence of electron-spin states is their interaction with nuclear spins. If the nuclear spins sense, in any way, the relative up and down orientation of the electron spin, they become entangled with the electron-spin Zeeman levels, destroying the quantum coherence. It is fortunate that silicon is 95 per cent nuclear-spin free, and that germanium is 92 per cent nuclear-spin free. They are both subject to additional isotopic purification. Isotopically pure epitaxial Si²⁸ is 99.9 per cent nuclear-spin free, and is commercially available, while the III–V semiconductors have no spin-zero nuclei. In addition, Si can be embedded in strained silicon-germanium heterostructures. In strained SiGe structures, spin-orbital coupling is tunable, which makes gate operations on an individual spin possible [4].

Several schemes for measuring the electron spin in compound semiconductor structures have been proposed for quantum information processing [4–6]. In order to physically implement any of the proposals, it is essential to measure the state of a single spin. Diverse ideas for electrical detection of the state of an isolated spin have been discussed, however, all of them present significant experimental challenges.

In this chapter, we review the experimental efforts that focus on the measurement of single-electron spins in two particular Si-based semiconductor nanostructure systems. First, we will describe experiments in a real transistor structure (i.e., a submicrometer commercial Si field effect transistor) in which the source/drain channel is used to electrically detect the spin states of an adjacent single paramagnetic spin center. This transistor structure is similar to a number of proposed spin-based qubit architectures that can be used as a potential quantum information processor. Secondly, we will describe the effort to fabricate similar devices in specially designed semiconductor structures that promise greater control over electron spin, the ability to entangle two spins, and to eventually build a scalable quantum processor. In these engineered structures, quantum dots are created by metallic gates patterned over a 2D electron gas in a strained silicon-germanium heterostructure. As has been mentioned, SiGe is expected to be a superior material compared to III–V semiconductors for scalable quantum information processors. In addition to the discussion of fabrication issues, we will also show examples of single-electron-spin measurements in the few-electron regime of quantum dots.

2 Measurements of a Single Spin in the SiO₂ of a Submicrometer Si Field Effect Transistor

For the single-spin measurements, a sequence of submicrometer n-channel Si field effect transistors (FETs) have been used. It is well known from the extensive literature of magnetic-resonance studies that there exist structural paramagnetic defects near the Si/SiO₂ interface. For a small device, it is possible that there is only one isolated trap state that is both within the tunneling distance of the channel, and with an energy that is close to the Fermi level.

Figure 1a shows a microscope picture of a typical Si FET sample used for the single-spin measurements. It shows a line of devices on the left, and a magnified view of a single device on the right. The device has a channel size of length 300 nm by width 270 nm. Figures 1b and c sketch a simplified version of such a device that represents the two charged states of the trap in the experimental system. In a FET, the conductivity of a “channel” from the drain to the source is controlled by a voltage applied to the gate.

For the FET device, the signature of a single trap state is the current switching between two discrete states, known as the random telegraph signal (RTS). Over the years, observations of RTS, have been reported in a variety of mesoscopic electronic systems. It has now been commonly accepted that the RTS is an unequivocal signature of capture and emission of one electron

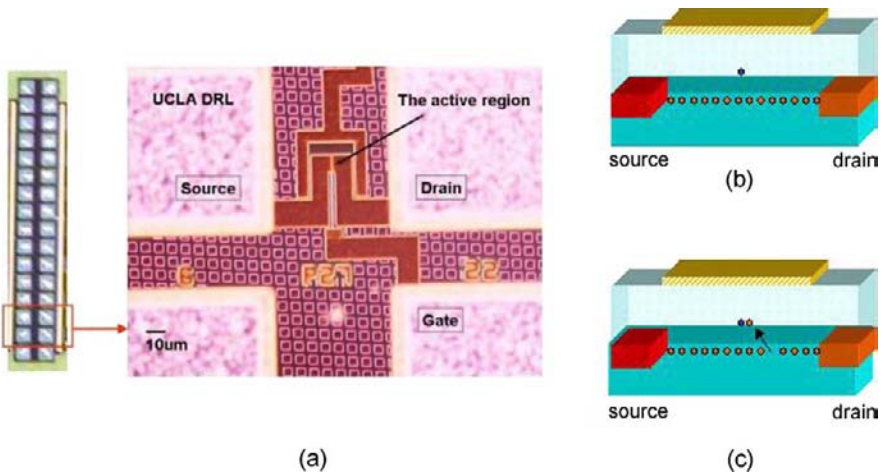


Fig. 1. (a) Microscope picture of a typical Si field effect transistor device used for the single-spin measurements. It shows a line of devices on the *left*, and a magnified view of one device on the *right*. The *light squares* are the contact surfaces. The device has a channel length of 300 nm and a channel width of 270 nm. (b) The two charge states of a trap in the SiO₂ of the device located in the close proximity of the channel

by a single trap state.¹ In particular, the pioneering work of Ralls et al. [8] demonstrated that, for a MOSFET, when the Fermi level of the conducting channel is in the proximity of the trap energy level, the electron from the channel can tunnel on and off the trap. Changes in the trap charge state directly affect the Coulomb scattering rate for carriers, thus producing jumps in electrical current. For small-size devices at low temperatures, there is often only one defect within $k_B T$ of the Fermi level. Therefore, the electrical signal is insensitive to the other traps. The traps in a FET are normally very stable defects, as the measurements are reproducible over many thermal cycles from room temperature to cryogenic temperatures.

2.1 Statistical Measurements

In the rich literature of RTS, work has focused predominantly on the electrical properties of the trap in the absence of a magnetic field. The essential ingredient for detecting a single spin-flip is to convert the spin orientation of the trap to an electric charge. Here, by analyzing the change of statistics of the RTS in the magnetic field, we show that the RTS is an effective measurement to probe the spin state of the trap [9].

In the single-spin measurement experiments, the channel current can be recorded by a fast dynamic signal analyzer or by a high-frequency lockin amplifier. In Fig. 2a the channel current is recorded over a narrow gate voltage ramped from 720 mV to 760 mV, swept in a 10-ms time interval. Actually, 80 per cent of the transistors that we tested had no such trap states at all. In those cases, we can apply a high-voltage spike to the gate to induce a paramagnetic defect, with hot electrons, for study. Superimposed on the monotonically increasing background source/drain current is stochastic switching between two discrete values of channel current. This switching is the above-mentioned well-known RTS, which is a hallmark of the capture and emission of one electron by a single trap state. The well-defined RTS evolution demonstrates that over the 720 mV to 760 mV range, the trap is energetically well isolated from other traps. A filled trap implies electrostatic repulsion that diminishes the channel current. At high gate voltages (near point C in Fig. 2a) the Fermi level, E_F , is well above the trap level, E_T . Thus, the trap is almost always filled, repelling electrons and allowing less current to flow in the source/drain channel. In contrast, at low gate voltages (near point A in Fig. 2a), when E_F is well below E_T , the trap is empty most of the time and the high current state is more probable. At the midpoint, when $E_F = E_T$ (near point B in Fig. 2a), the probability for the trap filling is about 50 per cent. Thus, the source/drain current senses the two charge states of the trap.

In this experiment the FET channel is basically a very sensitive electrometer. A fast dynamic analyzer allows one to collect the data in real time with

¹ For a comprehensive review, see [7].

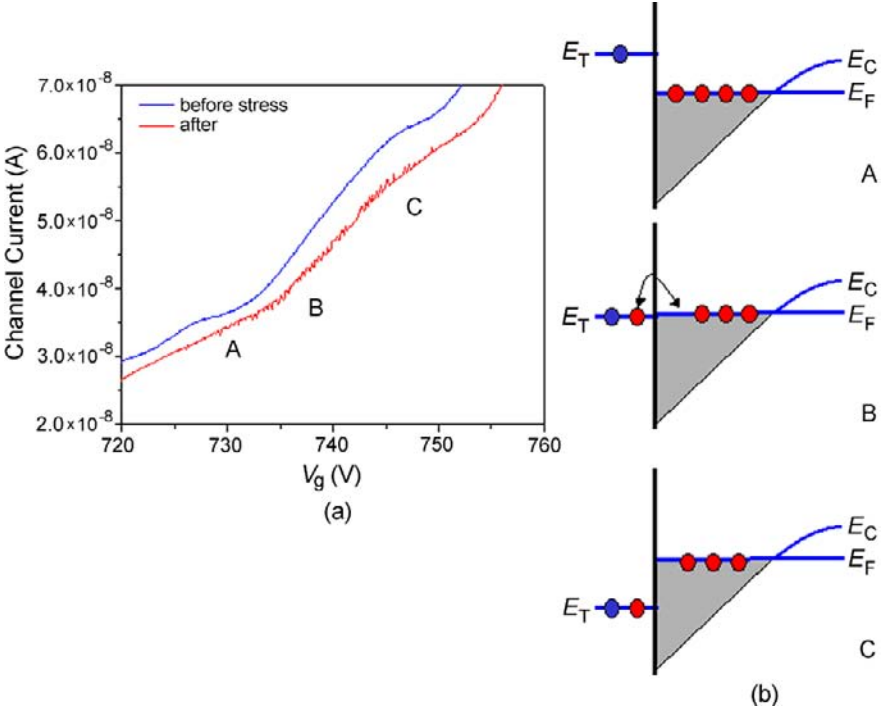


Fig. 2. (a) The channel current is measured as a function of the gate voltage with a constant scanning rate of about mV/ms, at 4.2 K before and after the electric stress. The evolution of the change in trap-filling probability can be seen after the stress. (b) The energy diagram of the single trap and FET channel bath for the points A, B, and C of curve displayed in (a). Here, the singly occupied state should actually be downshifted by the Coulomb correlation energy, U , not shown for simplicity

a maximum rate of several hundred kHz. The frequency of the tunneling from the channel to the trap for this particular sample is about 20 kHz. Thus, the charge sensitivity of the small FET channel is of the order of $10^{-4} e/(\text{Hz})^{1/2}$. The rapid tunneling rate also allows us to obtain excellent statistics of the trap-filling probability in a short period of time, which is necessary for detecting the small change in statistical distribution at ESR (discussed later).

Here, we would like to describe briefly how one can compute the RTS statistics through a simple and reliable method using histograms. Figure 3 shows the histograms for varying gate voltages. For each gate voltage, the histogram for the channel current shows two Gaussian distributions, corresponding to the two current levels. Without any noise, a histogram should consist of two discrete lines positioned at the two discrete levels. White noise spreads out the two lines to two overlapping Gaussian distributions. Figure 3 shows that the left peak grows while the right peak diminishes for increasing gate voltage. This is consistent with the fact that the defect is gradually charged. The

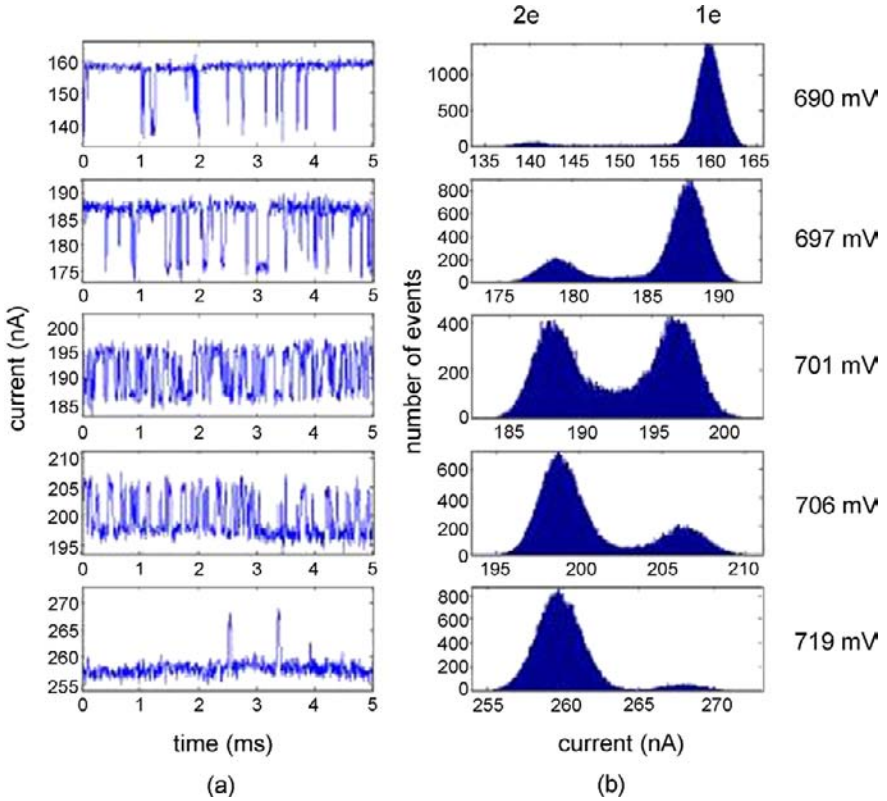


Fig. 3. (a) Channel current as a function of time for varying gate voltages at 4.2 K. The data is displayed only for 5 ms. From *top to bottom*, V_g is 690, 697, 701, 706 and 719 mV. (b) Histograms of RTS. Each histogram consists of two Gaussian distributions, corresponding to the two current levels. As V_g goes up, the peak for the low-current state dominates over the other one

ratio of the lifetimes on the high and low current states is the ratio of the area under the left peak to the area under the right peak. A routine can be used to automatically fit the histogram with two Gaussian distributions. Then, the area under each peak can be obtained easily.

The Zeeman shift of the single trap can be readily identified by studying the trap energy shift of the 50:50 trap-filling-probability point (where the Fermi Level E_F lines up with the trap energy E_T) as a function of magnetic field. Figure 4a shows the Zeeman shift of this 50:50 trap-filling energy as a function of an inplane magnetic field. The trap energy shift was inferred from the gate voltage shift [9].

Based on the sign of the Zeeman shift, we show that the charging transition transfers from a single-charge state, 1e, to a double-charge state, 2e; i.e., the charging is 1 to 2 rather than 0 to 1. In the energy diagram, Fig. 4b,

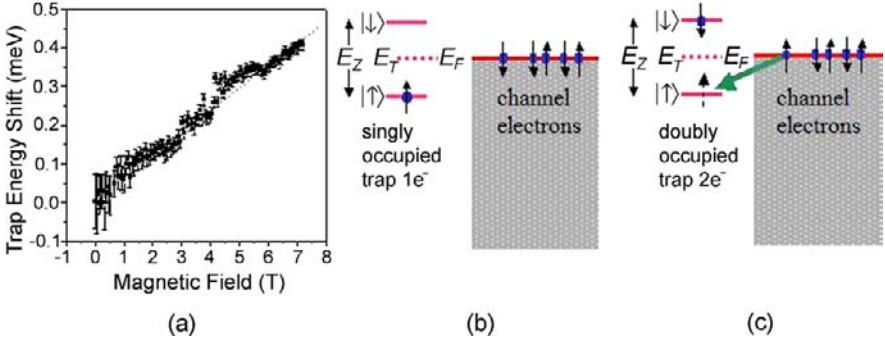


Fig. 4. (a) At the 50:50 trap-filling-probability point, the Fermi level matches the available defect energy level. The positive Zeeman shift of the trap energy versus magnetic field implies a $1e$ to $2e$ transition in the defect, rather than a $0e$ to $1e$ transition. (b) The Zeeman-split trap level relative to the FET channel Fermi level. The Fermi level would have to shift toward the upper Zeeman level to reach 50:50 occupation probability. (The singly occupied state should actually be downshifted by the Coulomb correlation energy, U , not shown.) (c) If the spin flips, the lower Zeeman level can become filled, producing the doubly occupied trap

the empty trap is modeled as an unpaired electron (e.g., a dangling bond) that occupies the level E_T (the central dashed line). In the presence of the magnetic field B , the single-electron state undergoes Zeeman splitting indicated by the two solid lines at energies $E_T \pm 1/2 E_Z$. At low temperatures and high fields, only the lower spin state is occupied. If the Fermi level is raised, an additional electron from the channel can tunnel into the upper spin state in Fig. 4b, forming a two-electron singlet state (e.g., a lone pair). Thus, the Fermi energy required for forming the two-electron state would increase when B is increased, as suggested by Fig. 4a. In contrast, an initially “spinless” empty trap would fill the lower Zeeman level, producing the opposite field dependence (i.e., the required Fermi energy decreases with increasing B), contrary to observation. Therefore, the initial empty trap begins in a $1e$ paramagnetic state ($S = 1/2$) (high current state) while the filled trap (lower current state) is a $2e$ singlet state ($S = 0$).

The same statistical measurement approach can also be used to study the $2e$ singlet to $2e$ triplet transition. In the case when there is more than one orbital available in the trap, there is also a possibility of forming a triplet two-particle state. For sufficiently strong magnetic fields, the triplet energy will become lower than the singlet discussed above. For a singlet state, the trapping probability increases as B increases. In contrast, for the triplet state, the trapping probability decreases as B increases. In fact, such a signature has been seen for a couple of devices when they were cooled to cryogenic temperatures rapidly. The consequence of such a transition has been realized recently at high magnetic fields in a similar MOSFET system [10].

2.2 Detection of Electron-Spin Resonance (ESR) of a Single Spin

To perform gate operations of spin rotations, many existing techniques for magnetic spin resonance can, in principle, be used. However, it has generally been accepted that qubits should be represented as individual spins. So in order to manipulate individual spin qubits, one has to be able to at least monitor the electron-spin resonance (ESR) of a single spin. In recent years, there have been several examples [11–14] of detection of magnetic resonance on single-electron spins in solids. Spin resonance of the nitrogen-vacancy defect center in diamond was detected optically [11, 12]. Spin precession of a localized electron spin on a surface has been detected by scanning tunneling microscopy [13, 14].

To create spin resonance of the paramagnetic trap, microwave radiation from 16 to 26 GHz, is delivered by semirigid coaxial cable, to a coaxial-to-waveguide converter, inside a cryostat. For higher frequencies, 26.5 to 50 GHz, a rectangular waveguide is used as the transmission line. In both cases, the sample is mounted on an endplate of the waveguide where the magnetic-field component is maximum while the electric-field component is nearly zero. Eliminating the electric component of the microwave is critical for the measurement. The photoconductivity of the sample is normally minimized to a few per cent. An excessive amount of microwave electric field can cause spurious effects [15, 16].

Our ESR detection scheme is based on the changing balance between the two source/drain current states of the transistor, when the Larmor precession frequency produces spin-flips. In effect, this is transistor-current-detected ESR. Following the paramagnetic trap model, described by the energy-band diagram in Fig. 4b, one can imagine that when the microwave frequency is E_z/h (i.e., at spin resonance), the spin state can be flipped, as in Fig. 4c. When the paramagnetic spin flips, the lower Zeeman level becomes available for trapping an additional electron. The trapping event increases the average source/drain current. A rate equation analysis of this trap/channel configuration can be used to calculate the ESR-induced change in trap-filling probability [17]. To detect the ESR microwave-induced change, we measure channel current at a fixed microwave frequency for 300 ms, during which there are about a few thousand RTS switching events, giving good statistics for the RTS.

Figure 5a represents a fragment of such a trace over a 10-ms time interval. To complete the current versus magnetic field dependence, full 300-ms traces are taken at 150–250 different magnetic fields. Since the signals are sometimes noisy, a systematic statistical procedure was used to measure the trap charge state, as described in the last section. A histogram of the source/drain current data versus time, as shown in Fig. 3 is used to measure the statistics of both the empty and filled trap states represented by the two peaks. For the perfect case of two discrete states, one expects two delta functions in the histogram. The broadening of the peaks in Fig. 3 is caused by noise.

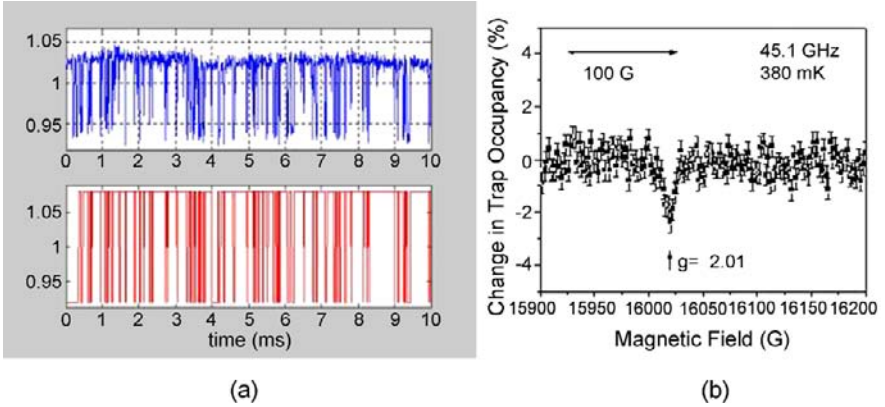


Fig. 5. (a) *Top*: the raw random telegraph data displayed for a time interval of 10 ms. *Bottom*: an algorithm for detection of abrupt changes is used on the raw data to reconstructed two-level RTS. This procedure reduces the statistical errors due to noise. (b) The change in trap-occupancy probability versus magnetic field for a fixed microwave frequency. The dip represents the electron-spin resonance

The charge-trapping probability ratio is proportional to the area ratio of the two peaks. For certain traps, whose charge produces only a small change in source/drain channel current, an additional step is taken to avoid noise errors. A more sophisticated algorithm [18], for detection of abrupt step changes, is executed numerically. As an example, the top of Fig. 5a is the raw random telegraph signal, containing noise. The bottom of Fig. 5a shows the noiseless two-state switching, reconstructed by the algorithm.

Figure 5b presents the ESR detection results for the single paramagnetic trap at a microwave frequency of 45.1 GHz. The error bars (about 1 per cent) in the figure indicate the standard deviation in a 300-ms dataset averaged over 4 adjacent magnetic fields. In Fig. 4a, an ESR peak in average current is centered around 16,025 G. Averaging blocks of 4 adjacent magnetic fields, the signal-to-noise ratio is greater than 4:1, and the ESR feature is reproducible in different runs, and for different traps, in different samples. The key to positively identify the single-trap ESR is from the change of RTS statistics rather than from device electrical conductance as it can drift with time and can be changed due to spurious effects [15, 16] induced by both electric and magnetic field components of the microwave. We find that the ESR signal is most pronounced in the range of gate voltages corresponding to a paramagnetic (nearly empty) trap (i.e., between points B and C in Fig. 2a). This is consistent with our assignment of filled and empty trap states. The ESR signature is only found at temperatures below about 1 K. At those temperatures, the electron magnetic moment is substantially polarized, and in any case, microwave heating limits the temperature. From the RTS Boltzmann occupation probability as a function of voltage, we find the effective tem-

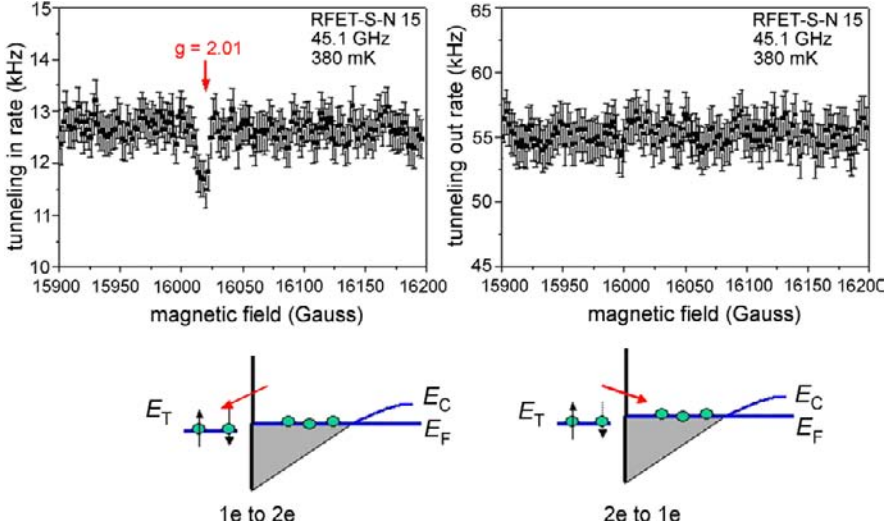


Fig. 6. The tunneling frequency is plotted as a function of magnetic field. While the rate of tunneling into the trap is substantially modified at ESR, the rate of tunneling out is unaffected by the ESR.

perature rises to about 1 K when a moderate microwave power of 0.1 mW is applied to the sample, even though the bath temperature still remains at about 0.4 K [9].

Similar runs have been carried out at other frequencies and in various samples [19]. A g -factor of 2.02 ± 0.015 is obtained. Since conduction electrons always have $g \leq 2$, and paramagnetic centers in SiO_2 always have $g \geq 2$, our results indicate a paramagnetic center in the oxide, or at the SiO_2/Si interface. Our observed g -value is somewhat larger than that for some known paramagnetic centers near the interface.² A P_b center is known to have a g -factor of 2.006 along the $\langle 100 \rangle$ direction, while the E' center is expected to have $g = 2.0005$. One possibility is that we are looking at a center that has a different local structure from these two typical examples. Another possibility is that the low-density conduction channel electrons might have slight ferromagnetic ordering, giving rise to a local field that slightly increases the apparent g -factor of the trap. We found that the large Rabi frequency produces nonlinear effects. At lower radio powers the trapping probability increases at ESR, and a peak is expected [17]. However, at higher powers, the ESR-induced signal inverts, leading to a decrease in trapping probability, as plotted in Fig. 5b.

We also see a nonlinear ESR response in the tunneling dynamics. In Fig. 6, the tunneling frequency is plotted as a function of field. While the rate of tunneling into the trap is substantially modified (about 10 per cent change) at

² See for example [20].

ESR, the rate of tunneling out is unaffected by the ESR. This observation is consistent with the fact that the $2e$ state is a singlet that should be insensitive to the spin-flip by ESR.

The detection of ESR of a single-spin trap was also reported by another group at a much higher temperature [21]. In their experiment, data was collected over a long period of time (\sim days) for a magnetic field scan at a fixed frequency.

2.3 Single-Shot Measurement

Although our group has been the first to electrically measure electron-spin resonance on a single semiconductor spin, due to the tiny difference in energy between the two spin states (limited by the low frequency in common commercial microwave generators) and the electronic heating generated by the continuous microwave radiation, the spin-orientation information was obtained by repeated measurements and thermal averaging. However, the method of spin orientation to charge conversion used for the ESR detection is completely compatible with single-shot read out (i.e., measuring two orthogonal spin states of the trap without repetition), required for quantum computation. The Fermi level can be adjusted so that it lies between the upper and lower Zeeman levels as illustrated in Fig. 4. At low temperatures and high B fields, if the lower Zeeman level is occupied by one electron, as in Fig. 4b, it cannot accept any additional electrons from the Fermi level. If only the upper Zeeman level is occupied, as in Fig. 4c, then an additional electron can be transferred from the Fermi sea to the lower Zeeman level. The distinction between two trapped charges, $2e$, versus one trapped charge, $1e$, can be sensed by the FET channel (i.e., the electrometer). For a practical quantum computer, the heating can be avoided by using microwave-free spin rotation for the single-qubit gates [1]. A similar spin-to-charge conversion scheme was, in fact, used to detect the spin orientation of a single spin in a GaAs quantum dot by a single tunneling event [22].

3 Fabrication and Characterization of Electrostatically Confined Quantum-Dot Structures in Si/SiGe Heterostructures

Although the single-spin measurements described in the previous section, were done on a structure that closely resembles nearly all proposed spin-based qubit architectures, the device uses a randomly positioned defect as its electron trap. It has been the goal of the community to fabricate similar devices in specially designed semiconductor structures that promise greater control over electron spin with the ability to entangle two spins, and to eventually build a scalable quantum processor.

Significant effort has been directed toward the development of electrostatically defined quantum dots as potential elements for quantum computation information. While a high level of control and sophistication has been achieved in current GaAs/AlGaAs-based structures [22–24], silicon-based heterostructures are expected to have the distinct advantage of possessing extremely long electron phase-coherence lifetimes, which can be attributed to the small spin-orbit interaction and the low natural abundance of isotopes with nuclear spin. Means of control in lateral quantum-dot devices is often exercised through the use of Schottky barrier top gates in which metal electrodes patterned on the semiconductor surface capacitively couple to the 2DEG. By applying a bias on the gates one can selectively deplete the charge carriers in the 2DEG directly below, and in the vicinity of the gates thereby controlling current flow.

Over the last several years attempts were made to create mesoscopic devices on strained Si/SiGe heterostructures by directly mimicking the existing geometries and fabrication processes that have been employed on GaAs/AlGaAs-based heterostructures. The success was often limited due to the high level of leakage current and/or the incomplete depletion of the 2DEG by Schottky gates on strained Si/SiGe. Several innovative approaches have recently been introduced as means of circumventing these obstacles. For example, Bo et al. [28] and Klein et al. [29] have fabricated quantum dots (QDs) by using atomic force microscope lithography and electron-beam lithography on Si/SiGe heterostructures, respectively. In their devices, trenches are created by the lithography, and the isolated two-dimensional electron regions are used as gates to control a QD surrounded by the trenches. Sakr et al. [30] of the UCLA group, has fabricated a laterally confined quantum-dot structure that is integrated with a charge readout channel using a strained Si layer on strain-relaxed SiGe buffer layers. In this structure, a new approach has been developed to embed leakage-secluded metallic side gates in etched groves that provide stronger gate to quantum-dot coupling. Devices with different sizes show reproducible single-electron charging effects and are stable over an extended period of time for dots of 30–150 electrons. The discrete electronic occupation of the quantum dots can be effectively detected using the adjacent quantum point-contact electrometer.

3.1 Demonstration of a One-Electron Quantum Dot

As a result of the continuous technical improvement of the nanofabrication techniques as well as the quality of epitaxial materials, the UCLA group has recently fabricated another generation of devices that show unprecedented high quality in terms of device stability and degree of gate control. The second generation of devices used a low-temperature thermal oxidation process to grow a very thin oxide layer (about 3 nm) making use of the cap layer of the epitaxial wafer. The incorporation of this unconventional insulating layer

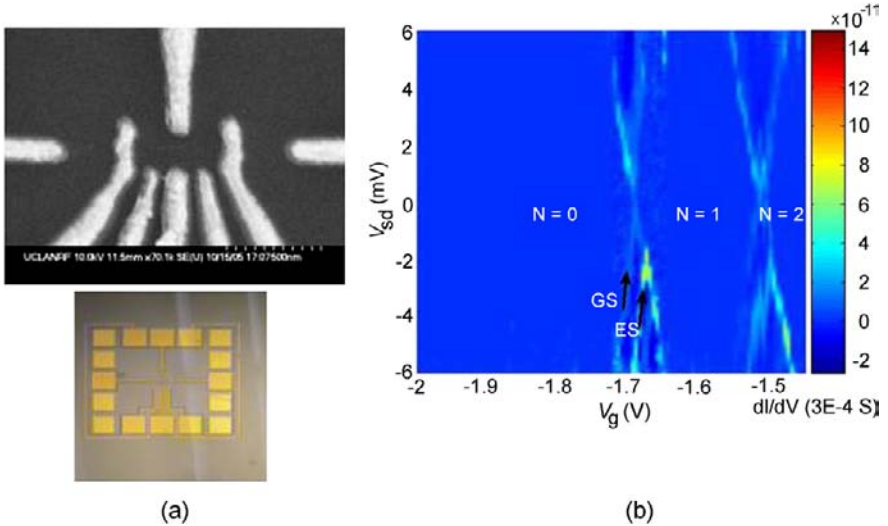


Fig. 7. (a) Scanning electron micrograph and electrode layout of the quantum-dot structure. (b) Stability plot of the differential conductance in a grayscale as a function of the source–drain voltage, V_{sd} , and the plunger gate voltage, V_g , at 0.4 K, completed in about 2 h

suppressed the gate leakage current to less than 0.1 pA at typical operation voltages.

Figure 7 shows two coupled quantum dots that are each defined by 4 gates. The layout of the device is adapted from what has been used successfully in GaAs/AlGaAs materials. As a result of the low leakage current the effective electron temperature is in equilibrium with the bath temperature and the conduction peaks are much narrower than that for the earlier-generation devices. Consequently, the stability diagram (i.e., dI/dV vs. V_{sd} vs. V_g shown in Fig. 7) reveals even the excited-state energy levels. More importantly, the insulating layer allowed us to pattern strongly coupled surface gates that were able to squeeze the number of electrons in the dot down to zero for the first time in SiGe-based quantum-dot devices. The complete absence of electrons in the dot at high gate voltages was verified by two well-established techniques. First, at high gate voltage there is no conductivity at sufficiently high source–drain bias. Second, the lowering of the tunneling barriers produced no additional conduction peaks. With the new generation of devices we can now vary the number of electrons in each dot precisely from 0 to 5 and change the effective interaction of the two dots. The stability plot measures the charging energy and the dot size. We found a charging energy of about 20 meV for the last observable Coulomb diamond. A dot diameter of about 20 nm can be deduced from this large charging energy.

With this new generation of structure, the spin splitting is also clearly visible in the stability diagram at high fields, as shown in Figs. 8a and b.

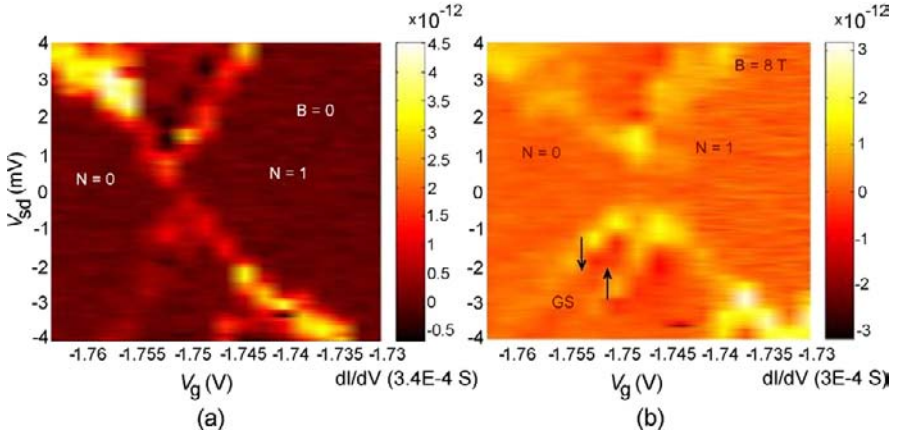


Fig. 8. The stability diagram at (a) $B = 0$ T and (b) at $B = 8$ T, the spin splitting is clearly visible as labeled by the two arrows

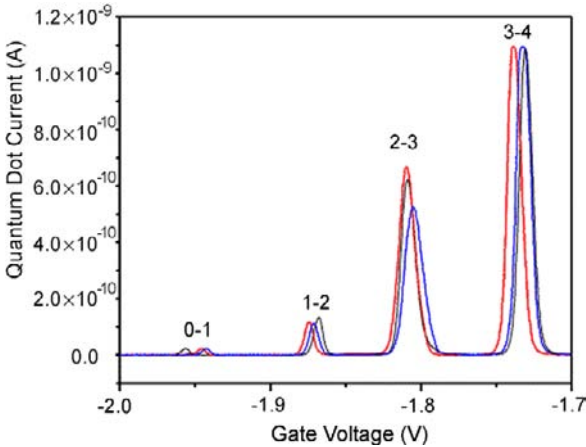


Fig. 9. Several successive traces of channel current as a function of gate voltage under the same conditions. Slight shifts in peak positions can be seen for different scans indicating long-term electric instability

Despite these encouraging developments, the surface gates on an oxide can often produce unexpected charges in the vicinity of the dots that alter the confinement potential and produce $1/f$ noise that affect the long-term electronic stability. For example, Fig. 9 shows several successive scans of channel current as a function of gate voltage under the same conditions. Slight shifts in peak positions can be seen for different scans. The fuzziness of the boundary lines in the stability diagram in Fig. 8 is another manifestation of the electric instability. This slight shift can make a pump/probe study, like that performed in GaAs systems, impossible. We also noticed that for the multiple gates, a couple of gates were dominant in the formation of the dot. We believe the un-ionized donor impurities can play important roles on small scales for the depletion-mode quantum dots.

In order to further utilize these Si devices for quantum information processing experiments including precise pulse-controlled spin logic and high-bandwidth readouts, the electrostatic environment has to be stable during the period of experiments. Towards this end, both Berer et al. [31] and Slinker et al. [32] have successfully used evaporated Pd on strained Si/SiGe as Schottky gates. Despite these hopeful results, it is recognized that further improvement of the effectiveness of the Schottky gates is needed to gain ultimate control in the few-electron regime.

In a more recent development, Scott et al. of the UCLA group came up with a new innovation that can produce high-quality Schottky gates for strained Si/SiGe heterojunctions, capable of depleting the high-mobility two-dimensional electrons locally, possessing superb leakage properties. We found that gold sputtered in Ar plasma forms an excellent Schottky gate. The surface gate depletes the underlying electrons at a small negative bias, which demonstrates that there are small numbers of surface states. The sputtered gold gates always showed dramatically less leakage current as compared to the evaporated gates [25]. In fact, the leakage current was at least five orders of magnitude lower compared to Au gates deposited by evaporation. We believe the surprisingly effective sputtered Au gates is a result of the interdiffusion of gold and SiGe atoms initiated by the energetic plasma gas. The Schottky barrier is likely a gold silicide compound, similar to the well-known platinum silicide, which is now used reliably with CCD camera production. To implement the sputtered Au process as surface gates at submicrometer scales, we have developed a so-called dual-layer process, which combines sputtering and evaporation and is compatible with standard electron-beam lithography. Because this technique is relatively simple and enables the formation of devices with conventional surface gates, it may be more readily incorporated into components for qubit applications.

3.2 Characterization of the Spin-Transition Sequence

With the MOSFET-like quantum-dot devices, we have performed an experiment to determine the spin transitions in the few-electron regime since the information is critical to design logic operations as well as readout steps. The energy of the conduction peaks (i.e., the Coulomb-blockade peaks) is measured as a function of the inplane magnetic field. The peak position depends on the magnetic field, B , through the Zeeman term, $-g\mu_B[S_z(N+1) - S_z(N)]$. The reason to apply an inplane field rather than a normal field is that we are interested mainly in the spin characteristics of the trap and would like to minimize the effects due to the orbital motion of electrons in the quantum dot. The field dependence gives information about the z -component of the quantum-dot spin. The negative slope of the line in the peak position vs. field curve indicates that the spin is added parallel to B . The energy shift can be readily calculated from the gate-voltage shift using the ratio of the horizontal to vertical scale in the stability diagram. We have discovered an unexpected

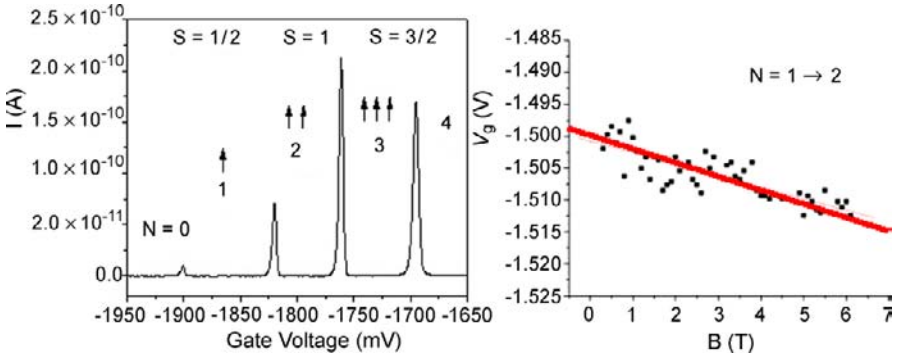


Fig. 10. (a) The channel current as a function of gate voltage at a fixed magnetic field. The transitions between different charge states have been labeled. (b) The Coulomb-blockade peak for the $1e$ to $2e$ transition as a function of the inplane magnetic field

spin-transition sequence as the number of electrons changed from 1 to 3. The total spins of the dot were found to be $S(N=1) = 1/2$, $S(N=2) = 1$, and $S(N=3) = 3/2$. This sequence is very different from that in a GaAs quantum dot, which was expected to have a $1/2$ to 0 to $1/2$ order. We believe the unusual configuration is most likely due to the electron–electron correlations in the dot [26]. Because of the large effective electron mass, the interaction energy becomes larger than that of the single-electron level spacing. So, the electrons prefer to occupy the high-energy levels to gain the exchange energy. Similar observations of high-spin states have been reported earlier in an etched Si dot fabricated from a Si-on-insulator wafer [27].

3.3 Single-Shot Measurement

As discussed earlier, for a practical operation of readout, one has to complete the measurement in a single attempt with high reliability. More specifically, one has to be able to measure two orthogonal spin states of the trap without repetition (i.e., single-shot). We would like to describe here schematically the procedures for such a measurement in the quantum-dot case.

The spin in the quantum dot is initially prepared in the “ground” (spin-up) state. This initialization can be done by first raising the Fermi level between the two spin states such that the spin-up state of the empty dot can be filled. The Fermi level is then raised slightly above the spin-down state. Since it takes a large charging energy to add the second electron, the down-spin state is guaranteed to be empty as shown in Fig. 11a. Instead of applying continuous microwave radiation, one can apply a short pulse that puts the trapped spin into a superposition of spin-up and spin-down states, as in Fig. 11b. This step is equivalent to a single qubit rotation. Next, one can apply a voltage to the gate to shift the Zeeman doublet to the config-

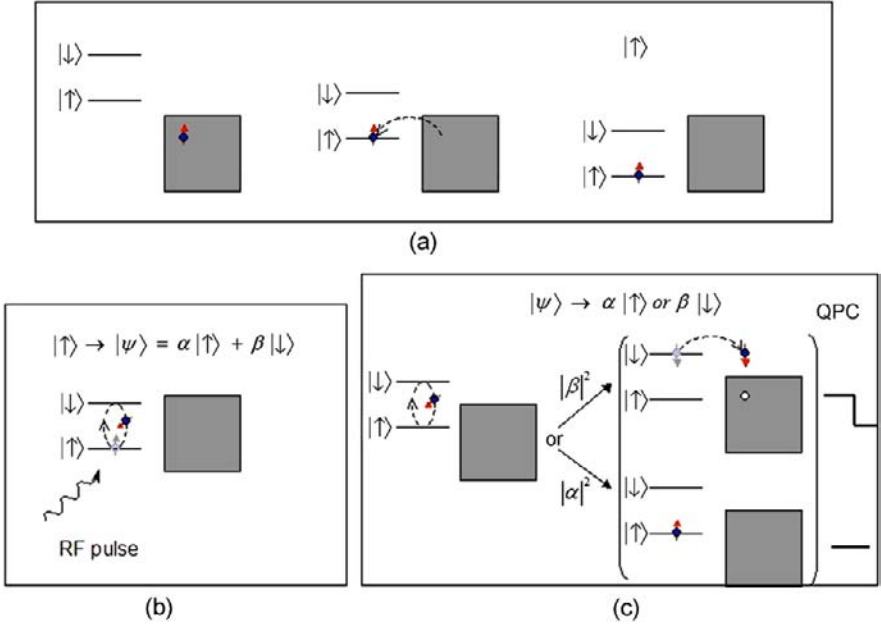


Fig. 11. Schematics for single-shot spin-state readout: (a) The spin-state initialization, (b) The spin state is prepared in a superposition by a microwave pulse, and (c) The state is then measured by detecting (or not detecting) the current jump in the QPC signal

uration shown in Fig. 11c. The spin-down state tunnels out (provided the spin-relaxation time T_1 exceeds the trapped-electron dwell time), while tunneling of the spin-up state is prohibited by the exclusion principle for a singlet state. Thus, the transport current will exhibit a jump, which can be associated with the spin-down state. What happens, if the electron is a superposition of spin-up and spin-down states? In this case, repetitive measurements using the same pulsewidth can obtain the superposition coefficients α and β . A systematic measurement as a function of the pulsewidth will provide one with the Rabi oscillation frequency that will precisely calibrate the gate operation timing. Inducement and control of coherent coupling between different qubits is a central issue in any architecture for quantum information processing. We would like to point out that the true quantum measurement described here is fundamentally different from the ensemble measurement that was already performed successfully in the GaAs quantum-dot system [33], where a probing current is passed through the dot. We believe that the capability to conduct the true quantum measurements of a single-spin state will be a major advancement in science and a significant step towards the physical implementation of spin-based quantum information processing.

4 Concluding Remarks

In conclusion, the research of individual-spin-based quantum information processing in Si materials has made remarkable progress in the last several years. The advancement can be summarized in two areas. First, manipulation and detection of an individual single-electron spin is now becoming reality by successfully implementing spin to charge conversion. Secondly, continuous effort and technological progress now allow us access to the few- and single-electron spin regimes in strained Si/SiGe epitaxial structures, which was not possible only a few years ago. The quality and stability of the engineered quantum-dot structures in strained SiGe are now catching up to the more mature GaAs-based quantum-dot structures. We believe that quantum information processing based on the individual electron spins in Si has distinct advantages over other competing physical systems, and will have a bright future through sustained research and development efforts.

Acknowledgements

We would like to express our gratitude to Dr. Ivar Martin of Los Alamos National Laboratory for theoretical support to the project, and Prof. Kang Wang for helping to secure the Si FET samples. The research at UCLA was supported by the Defense Advanced Research Projects Agency, and the Defense MicroElectronics Activity.

References

1. E. Yablonovitch, H.W. Jiang, H. Kosaka, H. Robinson, D. Sethu Rao, T. Szkopek, Proc. IEEE **91**, 727 (2003). Special Issue on Spintronics Technology 81, 91
2. B.E. Kane, Nature **393**, 133–137 (1998) 82
3. A.M. Tyryshkin, S.A. Lyon, A.V. Astashkin, A.M. Raitsimring, Phys. Rev. B **68**, 193207 (2003) 82
4. R. Vrijen, E. Yablonovitch, K. Wang, H.W. Jiang, A. Balandin, V. Roychowdhury, T. Mor, D. DiVincenzo, Phys. Rev. A **62**, 12306 (2000) 82
5. D. Loss, D.P. DiVincenzo, Phys. Rev. A **57**, 120 (1998) 82
6. M. Friesen, P. Rugheimer, D. Savage, M.G. Lagally, D.W. van der Weide, R. Joynt, M. Eriksson, Phys. Rev. B **67**, 121301 (2003) 82
7. M.J. Kirton, M.J. Uren, Adv. Phys. **38**, 367–408 (1989) 84
8. K.S. Ralls, W.J. Skocpol, L.D. Jackel, R.E. Howard, L.A. Fetter, R.W. Epworth, D.M. Tennant, Phys. Rev. Lett. **52**, 228–231 (1984) 84
9. M. Xiao, I. Martin, H.W. Jiang, Phys. Rev. Lett. **91**, 18301 (2003) 84, 86, 90
10. E. Prati, M. Fanciulli, G. Ferrari, M. Sampietro, Phys. Rev. B **74**, 033309 (2006) 87

11. J. Khler, J.A.J.M. Disselhorst, M.C.J.M. Donckers, E.J.J. Groenen, J. Schmidtand, W.E. Moerner, *Nature* **363**, 242–244 (1993) 88
12. F. Jelezko, T. Gaebel, I. Popa, A. Gruber, J. Wrachtrup, *Phys. Rev. Lett.* **92**, 076401 (2004) 88
13. Y. Manassen, R.J. Hames, J.E. Demuth, A.J. Castellano, *Phys. Rev. Lett.* **62**, 2531 (1989) 88
14. C. Durkan, M.E. Welland, *Appl. Phys. Lett.* **80**, 459 (2002) 88
15. E. Prati, M. Fanciulli, A. Calderoni, G. Ferrari, M. Sampietro, *Phys. Lett. A* **370**, 491–493 (2007) 88, 89
16. E. Prati, M. Fanciulli, A. Calderoni, G. Ferrari, M. Sampietro, *J. Appl. Phys.* **103**, 104503 (2008) 88, 89
17. I. Martin, D. Mozysky, H.W. Jiang, *Phys. Rev. Lett.* **90**, 018301 (2003) 88, 90
18. W. Liu, Z. Ji, L. Pfeiffer, K.W. West, A.J. Rimberg, *Nature* **423**, 422 (2003) 89
19. M. Xiao, I. Martin, E. Yablonovitch, H.W. Jiang, *Nature* **430**, 435 (2004) 90
20. E.H. Poindexter, in *Semiconductor Interfaces, Microstructure, and Devices* (Institute of Physics, Bristol, 1993) 90
21. M.S. Brandt, S.T.B. Goennenwein, T. Graf, H. Huebl, S. Lauterbach, M. Stutzmann, *Phys. Status Solidi* **8**, 2056 (2004) 91
22. J.M. Elzerman, R. Hanson, L.H. Willems van Beveren, B. Witkamp, L.M.K. Vandersypen, L.P. Kouwenhoven, *Nature* **430**, 431 (2004) 91, 92
23. N.J. Craig, J.M. Taylor, E.A. Lester, C.M. Marcus, M.P. Hanson, A.C. Gossard, *Science* **304**, 565 (2004) 92
24. J.R. Petta et al., *Science* **309**, 2180 (2005) 92
25. G.D. Scott, M. Xiao, E.T. Croke, E. Yablonovitch, H.W. Jiang, *Appl. Phys. Lett.* **90**, 032110 (2007) 95
26. Y. Hada, M. Eto, *Phys. Rev. B* **68**, 155322 (2003) 96
27. L.P. Rokhinson, L.J. Guo, S.Y. Chou, D.C. Tsui, *Phys. Rev. B* **63**, 035321 (2001) 96
28. X.Z. Bo, L.P. Rokhinson, H. Yin, D.C. Tsui, J.C. Sturm, *Appl. Phys. Lett.* **81**, 3263 (2002) 92
29. L.J. Klein, K.A. Slinker, J.L. Truitt, S. Goswami, K.L.M. Lewish, S.N. Coppersmith, D.W. van der Weide, M. Friesen, R.H. Blick, D.E. Savage, M.G. Lagally, C. Tahan, R. Joynt, M.A. Eriksson, J.O. Chu, J.A. Ott, P.M. Mooney, *Appl. Phys. Lett.* **84**, 4047 (2004) 92
30. M.R. Sakr, E. Yablonovitch, E.T. Croke, H.W. Jiang, *Appl. Phys. Lett.* **87**, 223104 (2005) 92
31. T. Berer, D. Pachinger, G. Pillwein, M. Muhlberger, H. Lichtenberger, G. Brunthaler, F. Schaffler, [arXiv:cond-mat/0508260](https://arxiv.org/abs/cond-mat/0508260) (2005) 95
32. K.A. Slinker, K.L.M. Lewis, C.C. Haselby, S. Goswami, L.J. Klein, J.O. Chu, S.N. Coppersmith, R. Joynt, R.H. Blick, M. Friesen, M.A. Eriksson, [arXiv/0508107](https://arxiv.org/abs/0508107) (2005) 95
33. F.H.L. Koppens et al., *Nature* **442**, 766 (2006) 97

Index

conversion, 91

pump/probe, 94

quantum information processing, 82, 97

quantum information processor, 81, 82

random telegraph signal, 83

readout channel, 92

Si/SiGe heterostructure, 92

single-shot read out, 91

spin resonance, 89

spin-to-charge, 91

Si/SiGe Quantum Devices, Quantum Wells, and Electron-Spin Coherence

J.L. Truitt¹, K.A. Slinker¹, K.L.M. Lewis¹, D.E. Savage¹, Charles Tahan², L.J. Klein¹, J.O. Chu³, P.M. Mooney⁴, A.M. Tyryshkin⁵, D.W. van der Weide⁶, Robert Joynt¹, S.N. Coppersmith¹, Mark Friesen¹, and M.A. Eriksson¹

¹ Department of Physics, University of Wisconsin, Madison, WI 53706, USA

² Cavendish Laboratory, Madingley Road, Cambridge CB3 0HE, UK

³ IBM Research Division, T.J. Watson Research Center, New York 10598, USA

⁴ Department of Physics, Simon Fraser University, Burnaby, BC V5A 1S6, Canada

⁵ Department of Electrical Engineering, Princeton University, Princeton, NJ 08544, USA

⁶ Department of Electrical and Computer Engineering, University of Wisconsin, Madison, WI 53706, USA

Abstract. Silicon quantum devices have progressed rapidly over the past decade, driven by recent interest in spintronics and quantum computing. Spin coherence has emerged as a leading indicator of suitable devices for quantum applications. In particular, the technique of electron-spin resonance (ESR) has proven powerful and flexible for probing both the magnitude and the nature of spin scattering, when compared to theoretical predictions. Here, we provide a short review of silicon quantum devices, focusing on silicon/silicon-germanium quantum wells. Our review touches on the fabrication and lithography of devices including quantum dots, and the development of Schottky top gates, which have recently enabled the formation of few-electron quantum dots with integrated charge sensors. We discuss recent proposals for quantum-dot quantum computing, as well as spin- and valley-scattering effects, which may limit device performance. Recent ESR studies suggest that spin scattering in high-mobility Si/SiGe two-dimensional electron gases may be dominated by the D'yakonov and Perel' mechanism arising from Bychkov–Rashba spin-orbit coupling. These results rely on theoretical predictions for the dependence of the coherence time T_2^* on the orientation of an external applied magnetic field. Here, we perform ESR experiments on a series of samples fabricated by different methods, including samples recently used to obtain few-electron quantum dots. While we observe some similarities with recent experiments, we find that for five out of six samples, the angular dependence of T_2^* was far larger than the theoretical predictions. We discuss possible causes for this discrepancy, but conclude that the theoretical understanding of these samples is not yet complete.

1 Introduction

Quantum devices are presently an area of intense activity. This is due in part to novel computing opportunities offered by quantum computing and quantum information more generally, and in part by the need to control quantum effects in classical devices. It also underscores a new era of technology, in which it has become possible to control the fundamental quantum degrees-of-freedom of microscopic objects, even within the confines of a solid-state matrix. Electron spins form an excellent basis for quantum devices, since they may be isolated in quantum dots, artificial or natural, and in principle they can be transported to distant locations through quantum channels. The spin variable can be controlled through either electric or magnetic fields [1].

The main challenge for spintronics applications is to manipulate and measure spins, while simultaneously isolating them from their environment. The degradation of spin information is known as decoherence. In the semiclassical spin field effect transistor (SFET) [2], decoherence leads to diminished functionality of the device, while for spin qubits, decoherence leads to computing errors [3]. Decoherence properties may depend on fundamental materials properties, growth conditions, temperature, or any number of environmental variables. The study of decoherence properties of spins has a long and venerable history in solid-state physics, and a number of powerful probe techniques have been established. Pre-eminent among these is spin resonance, for example electron-spin resonance (ESR) [4] or nuclear magnetic resonance (NMR) [5]. Many variations on these techniques have been developed. Quantum devices provide a challenge for such bulk techniques, since the number of active electrons may be very few. In this case, electrically detected ESR techniques (ED-ESR) play an important role [6]. In the limit of single-electron devices, completely new methods are required, based on single-spin manipulation and readout [7–14].

While many recent advances in quantum devices have occurred in the GaAs materials system, silicon occupies a unique position. On the one hand, the materials environment of silicon has the distinction of having the smallest spin-orbit coupling of any currently practical semiconducting material, due to its high position in the periodic table. Additionally, the predominant isotope of silicon is ^{28}Si , with nuclear spin zero. Modulation doping, isotopic purification, and clean heterostructures therefore hold the prospect of an environment with very low decoherence. On the other hand, Si quantum wells are clad by SiGe barriers, and therefore are intrinsically strained, leading to growth and fabrication challenges. Moreover, as an indirect-bandgap material, the conduction-band structure of silicon is fundamentally more complicated than that of direct-gap materials, leading to decoherence and spin manipulation challenges associated with multiple conduction valleys.

In this chapter, we review the decoherence properties of electron spins in silicon structures, with a focus on materials appropriate for few-electron quantum devices. While it is likely that single-electron measurements similar

to those in GaAs will be available in the near future, it is also urgent to understand the dominant decoherence sources in transport experiments involving many electrons. Below, we review the current status of silicon quantum devices, particularly those of importance for spin electronics (spintronics) and quantum computing. In addition to spin physics, we consider the special behavior of silicon devices related to valley physics. We also review the current status of ESR experiments in Si/SiGe quantum wells.

Many factors can affect transport in silicon devices, including variable germanium content in the quantum well and the barriers, use of oxide materials as barriers, proximity of modulation-doping layers and their impurity ions, presence of dopants in the quantum well, width of the quantum well, and roughness of the interfaces. It is therefore important to test current theories of scattering in a variety of devices and samples. In the second half of this chapter, we present preliminary data obtained from several different samples that have been recently used in the fabrication of quantum devices, including quantum point contacts and few-electron quantum dots. Based on transport data through these devices, we deduce that they are of very high quality. However, the samples are not of the same origin as those used in many recent ESR experiments. We find that while some of the samples show similar ESR behavior as previous experiments, others show differences that cannot be fully explained by existing theories. We conclude that the current understanding of Si structures, especially those of importance for quantum devices, is not yet complete.

2 Silicon Quantum Devices

Many high-performance devices in silicon, from microchips to qubits, are fabricated in two-dimensional structures, including inversion layers and quantum wells. Inversion layers have traditionally been of the greatest importance for commercial electronics, taking the form of metal oxide semiconductor field effect transistors (MOSFETs), with the active region an inversion layer at the silicon/silicon-dioxide interface. Because of their industrial importance, inversion layers have been extensively studied. A great wealth of knowledge about such structures and the devices formed on them can be found in the review paper of Ando, Fowler and Stern [15], and other texts [16].

Silicon quantum devices can be made using oxidation fabrication techniques, frequently in combination with silicon-on-insulator (SOI) structures. Much research in silicon single-electron transistors (SETs) has focused on high-temperature quantum dots [17–19]. However, a burst of activity on low-temperature quantum devices, with an emphasis on qubit development, has broadened the direction of recent fundamental research. This work covers a range of topics, including Coulomb-blockade effects [20], single-electron memories [21], control of electron density by top gates [22], and fine tuning of tunnel barrier resistances [23]. The resulting devices have attained a high

degree of sophistication, leading to quantum dots strongly coupled to charge sensors [24], triple dots [25], spin effects in coupled dots [26], and single-hole transfer devices [27].

Several variations on the MOSFET design have arisen, in some cases yielding better performance for quantum devices. Of particular interest is the doped SiO₂/Si/SiO₂ quantum well. Devices fabricated in such structures include double-dot charge qubits with strongly coupled charge sensors [28]. The quality of the quantum wells may be very high, enabling electrically detected electron-spin resonance with enough resolution to detect valley splitting [29]. (Further discussion is given below.) However, low-temperature mobilities in these structures are typically of the order of 10⁴ cm²/V s or lower [29]. Moreover, rough interfaces associated with oxide barriers may have a detrimental effect on electronic properties, especially in ultrathin quantum wells [30], and the electrostatic potentials from ionized dopants in the quantum well may interfere with device operation [31].

There are pros and cons in utilizing Si/SiO₂ interfaces for quantum devices. Silicon quantum dots created by oxidation may be extremely stable [32]. There has, nonetheless, been concern about ubiquitous defects at the interface between crystalline and noncrystalline materials [33–37]. In the very best oxide/silicon interfaces, defect densities can be very low indeed, suggesting that the challenges are not insurmountable. The preceding summary of Si/SiO₂ materials and devices is not meant to be exhaustive, since these structures are not the focus of the present work. For a more thorough treatment, we direct the reader elsewhere [15, 16, 38].

The Si/SiGe heterostructure is the main focus of this chapter. To form a two-dimensional electron gas (2DEG), a narrow silicon layer is clad within strain-relaxed SiGe barriers, causing tensile strain in the silicon [39]. Similarly, a hole gas is formed in a SiGe quantum well clad within silicon barriers. A review of growth issues in silicon/germanium materials is given in [40].

Highly doped Si/SiGe quantum wells have been successfully used to create quantum dots and double dots, both in p-type [41–43] and n-type [44, 45] materials. However, modulation doping can also be achieved in Si/SiGe heterostructures. The resulting structures are analogous to the epitaxial GaAs/AlGaAs structures, which have been utilized in a range of quantum devices of sufficient quality to form spin qubits [7–14]. One main difference between Si- and GaAs-based devices is strain, which occurs in the Si structures. Modulation-doped field effect transistors (MODFETs) or high electron mobility transistors (HEMTs) are expected to provide a factor of three improvement in mobilities over MOSFETs at room temperature [39], and even more improvement at low temperatures. Since the mid-1990s, silicon MODFETs have been optimized to provide mobilities in excess of 600,000 cm²/V s [39, 46–50]. For qubit devices, which do not utilize transport, there is no conclusive data that high mobilities correlate with desirable properties for quantum computing. However, existing qubits in GaAs utilize ultrahigh-mobility mate-

rials [7–9, 11], and it is anticipated that the same materials issues that reduce the mobility, such as remote impurities, or scattering centers in the quantum well or oxide interface, could also adversely affect qubit performance. In SiGe MODFETs, the primary scattering centers in ultrahigh-mobility materials are remote ionized impurities in the doping layer [39, 51, 52]. However, other scattering centers include rough interfaces in the quantum well, which arise from misfit dislocation formed during strained growth, even when no threading dislocations are present in the quantum well [40].

Quantum devices in silicon/silicon-germanium quantum wells have been reviewed in [53]. To form quantum dots in Si/SiGe quantum wells, lateral confinement can be produced by physical means, using lithographic and etching techniques to carve up the 2DEG [54, 55]. A more versatile technique uses nanoscale metallic gates to electrostatically deplete the 2DEG, analogous to techniques used in GaAs devices [56]. Optimally, these finger gates are fabricated on the surface of the heterostructure directly above the 2DEG, at a separation of about 50 nm. A primary challenge for creating top gates in silicon arises from the presence of leakage paths [57], which may result from threading dislocations, deep pits, or other morphological features associated with strained growth [58]. The leakage mechanisms may also vary for different growth methods [59]. Dislocations are generally harmful for electrical properties in the 2DEG. Fortunately, optimization of growth methods has shown that the number of defects can be minimized in the active layer. Since the absence of leakage is a prerequisite for good quantum devices, this area of research progressed rather slowly for several years, until the aforementioned difficulties were resolved.

One possibility for eliminating leakage is to avoid top gates altogether, by replacing them with side gates. The side gates are formed within the same 2DEG as the active device, but they are electrically isolated by means of reactive ion etching [60–62], in analogy with SOI-based devices. The etching provides confinement in one direction, allowing the formation of quantum wires [58, 63–65]. In combination with electrostatic gates, this technique enables electrical control of the tunnel barriers, which may be used to form quantum point contacts [66] and quantum dots [57, 62, 67, 68]. However, some drawbacks of side gating are large gate widths (compared with top gates), resulting in reduced gate density, and increased gate distance, which limits the fine tuning of gate-defined device features. A possible solution to this problem is to utilize metal gates fabricated within the etch trench [69]. This avoids the problem of leakage, while aligning the gates more closely with the quantum dot.

Difficulties in forming Schottky top gates have recently been overcome. Starting in the 1990s, it was shown that Schottky gates could modulate electron densities in 2DEGs [70, 71]. It is now possible to fabricate top-gated quantum dots by a number of different methods, including heterostructure

optimization [72, 73], etching the surface to remove near-surface highly doped regions [74].

Top-gated Si/SiGe quantum dots formed in 2DEGs have now been developed to the point that quantum effects such as Fano and Kondo resonances are now observed [73]. Top gates can also be used to create quantum point contacts [59, 66, 75–78]. Such point contacts have recently been used to enable spectroscopy of valley states in Si/SiGe 2DEGs [79].

An interesting recent approach to Si/SiGe heterostructure growth may provide an alternative route to forming robust Schottky gates. In [80] and [81], quantum wells were formed by strain-sharing growth methods, on top of an SOI substrate. In such structures, dislocations are entirely absent, since the structure is thinner than the critical thickness for dislocation formation. Strain sharing is accomplished by underetching the membrane, floating it off the substrate, and redepositing it on a new substrate. Transport measurements demonstrate the presence of a 2DEG. Such alternative growth methods may result in structures that are free of the types of roughness and defects that accompany conventional strained growths.

3 Spins and Valleys

Much of the recent interest in silicon quantum devices was initiated by the quantum-dot spin qubit proposal by Loss and Di Vincenzo [82]. (Recent progress is reviewed in [83].) Kane [84] has discussed the advantages of working in silicon, and further innovations of using donor nuclear-spin qubits have been presented [85–89]. A similar donor-bound approach can be extended to electron-spin qubits [90–93]. Vrijen et al. [94] have made a further extension to silicon-germanium heterostructures. Schemes have also been proposed for electron-spin-based quantum computation in silicon-germanium quantum dots [95, 96].

Spin-decoherence mechanisms are of fundamental importance for spin-based quantum devices, and more generally for spintronics [1]. Silicon is an excellent model system for studies of decoherence, and electron spins in silicon have long coherence times [97], making them particularly attractive for applications. When nuclear spins are present, the electron phase-relaxation time T_M for phosphorus-bound donor electrons is dominated by spectral diffusion due to flip-flops of the host nuclear spins [98]. However, the isotopic purification of silicon’s naturally abundant, spin-zero nuclear isotope ^{28}Si leads to orders of magnitude improvement. In the latter case, the electron-spin decoherence time T_2 has been measured to be as long as 14 ms at 7 K, and extrapolates to of the order of 60 ms for an isolated spin [99]. While it has so far been possible to detect spin resonance in specialized silicon structures [100], and while spin coherence has been observed in quantum dots [73], there have not yet been reports of spin qubits in silicon quantum devices.

An important distinction between silicon and GaAs quantum devices is the low-lying valley structure of their conduction bands. As an indirect-gap semiconductor, bulk silicon exhibits six degenerate valleys, which may compete with spin as a quantum variable for quantum computing applications [53, 101]. The valley degree-of-freedom is very important in low-temperature, quantum devices, leading to a recent resurgence of interest in the subject of valley splitting.

In a silicon inversion layer or quantum well, only two valleys will be populated [the $\pm z$ valleys, for silicon (001)]. The degeneracy of these valleys is broken in the presence of a sharp quantum-well interface. The value of this valley splitting, and its importance for experiments has been the subject of interest for many years, beginning with the surface scattering theory of Sham and Nakayama [102], the “electric breakthrough” theory of Ohkawa and Uemura [103–105], and other formulations [106–109]. More recently, tight-binding methods [110–113] and effective-mass theories [101, 113, 114] have provided new insights.

A crucial question is whether valley splitting is large enough to allow a workable spin-qubit Hilbert space. A number of experimental papers have measured valley splitting as a function of magnetic field [29, 115–122], finding surprisingly small values of the splitting, which would not enable spin qubits. However, the significance of atomic steps due to quantum wells grown on miscut substrates, or, more generally, in the presence of interfacial roughness has recently been shown to cause a large reduction of the valley splitting [79, 114, 123–125]. Lateral confinement lifts this suppression, allowing valley splitting to approach its theoretical upper bound [79]. Valley splitting is also found to approach the theoretical upper bound in SiO₂/Si/SiO₂ quantum wells [29, 30, 126]. In this case, because of the narrow quantum wells and the sharp potential barriers, the valley splitting reaches very large values, on the order of 20 meV. Because of the dependence of valley splitting on lateral confinement, quantum devices like quantum point contacts have become an important new tool in the study of valley splitting [75, 76, 79].

4 ESR in Silicon Quantum Wells

While for qubit applications one must be concerned with spin relaxation of localized spins, the transport of spin information over long distances is important for many spintronics applications. Interestingly, the mechanisms for spin relaxation of electrons with extended wavefunctions are quite different than those of localized electrons. Delocalized electrons undergo momentum scattering. D’yakonov and Perel’ (DP) pointed out in the early 1970s that such scattering of electrons gives rise to spin relaxation in the presence of spin-orbit coupling [127]. This DP mechanism dominates spin relaxation at low temperatures in two-dimensional electron gases in GaAs heterostructures

[128]. It also dominates the field-independent part of the relaxation at intermediate temperatures in bulk GaAs [129, 130]. In addition to the advantage of naturally abundant nuclear spin-zero isotopes, noted above, silicon also has much weaker spin-orbit coupling than GaAs, and the DP mechanism is therefore not as significant. Nevertheless, it is expected to dominate the relaxation in two-dimensional electron gases in Si 2DEGs.

There have been a number of studies of electron-spin coherence in Si/SiGe 2DEGs over the last decade, as well as measurements on related X -valley systems [131, 132]. A principle measurement technique is ED-ESR [133], which is of importance because of the reduced number of spins in the 2DEG compared with bulk. The signal in this case is obtained from conductivity measurements, and arises mainly from the reduction of spin polarization, rather than electron heating [134]. ED-ESR can be extended to provide information on valley splitting as well, in which case it is known as EVR [79]. Sharp ESR resonances in Si/SiGe 2DEGs also allow for standard microwave absorption measurements of as few as 10^9 spins [135–137].

Early ESR measurements demonstrated the importance of potential fluctuations caused by ionized donors in the doping layer [135–137], which are also thought to play a leading role in limiting the mobility in these devices [39, 51, 52]. Indeed, mobility calculations, based on an ESR density of states analysis of the potential fluctuations, provide good agreement with experimental values [138].

The ESR data exhibit anisotropy with respect to the magnetic-field direction in both the linewidth (dephasing time) and the electron g -factor [133, 139, 140]. This behavior suggests Bychkov–Rashba spin-orbit coupling as an origin for DP-mediated spin relaxation. Wilamowski and coworkers have proposed an additional modulation of the spin-orbit coupling and the ESR signal, originating from the motional narrowing due to cyclotron motion [141, 142]. The anisotropy is also affected by the germanium content in the quantum well [143, 144] and the electric current [145], providing a mechanism for g -factor tuning in these systems.

ESR measurements provide several crucial estimates of device parameters in the Si/SiGe quantum well. Wilamowski et al. obtain the Bychkov–Rashba spin-orbit coupling parameter $\alpha = 0.55 \times 10^{-12}$ eV cm [139, 140]. Graeff et al. obtain the anisotropic g -factors $g_{\parallel} = 2.0007$ and $g_{\perp} = 1.9999$ for the 2DEG charge density of $n = 4 \times 10^{11}$ cm $^{-2}$. Pulsed measurements suggest spin coherence (T_2) times up to 3 μ s [146]. The latter may be enhanced by confinement effects [144]. The longitudinal spin relaxation time is strongly enhanced by inplane magnetic fields, giving T_1 on the order of 1 ms in a 3.55 T field [134].

In the remainder of this chapter we revisit the issue of linewidth anisotropy. We specifically consider several of the same heterostructures that were used to fabricate quantum devices [57, 62, 72, 73, 79]. We provide a comprehensive treatment of six different samples, using transport measurements to extract

Table 1. Sample parameters and measurements of six $\text{Si}_{1-x}\text{Ge}_x/\text{Si}/\text{Si}_{1-x}\text{Ge}_x$ quantum wells. The first section of the table contains growth parameters: quantum-well width, germanium composition of the barriers (x), dopant offset distance, doping-layer thickness, spacer-layer thickness, and capping-layer thickness. The next section contains results from Hall transport measurements: 2DEG charge density (n_e), mobility (μ) and momentum relaxation time (τ_p). The last three columns contain ESR results: T_2^* is derived from (1), using $g = 2.00$ for all samples, $A(15^\circ)$ is the anisotropy parameter corresponding to the magnetic-field orientation $\theta = 15^\circ$, as described in (3), and b is the fitted quadratic coefficient of the anisotropy, from (4)

Sample	Well width (nm)	x	Offset (nm)	Dopants (nm)	Spacer (nm)	Cap (nm)	n_e (10^{11} cm^{-2})	μ ($\text{cm}^2/\text{V s}$)	τ_p (ps)	T_2^* (μs)	$A(15^\circ)$	b (rad^{-2})
ibm-01	8.0	0.30	14	1	14	3.5	4.0	37,300	4.3	0.6	1.0	1.6
uw-030827	10	0.35	15	22	35	10	4.8	90,000	9.7	0.1	4.7	38
uw-030903	10	0.25	13	17	35	10	4.3	86,700	9.4	0.2	2.1	13
uw-031121	10	0.30	20	6	60	20	5.4	38,000	5.0	0.1	2.0	25
uw-031124	10	0.30	20	26	40	20	4.7	63,200	6.9	0.1	2.0	18
uw-031203	10	0.30	60	6	60	20	2.6	17,100	1.8	0.5	2.3	10

the electron density and scattering time. We use ESR to measure T_2^* and to provide an indication of the spin-decoherence mechanism. A detailed study indicates that the dominant decoherence mechanism is strongly dependent on the orientation of the magnetic field – so much so that it is inconsistent with mechanisms described in the papers described above. Our main conclusions are presented in Table 1.

5 Samples

The Si/SiGe heterostructures were grown by ultrahigh-vacuum chemical vapor deposition at the University of Wisconsin-Madison and at IBM-Watson [48]. The 2DEG sits near the top of a strained Si layer grown on a strain-relaxed $\text{Si}_{1-x}\text{Ge}_x$ buffer layer, as shown in Fig. 1a of [57]. Above the 2DEG is a $\text{Si}_{1-x}\text{Ge}_x$ offset layer, followed by a phosphorus-doped dopant layer, and then a $\text{Si}_{1-x}\text{Ge}_x$ spacer layer capped with Si at the surface. Table 1 contains the heterostructure details for each sample.

Hall measurements were performed on each sample. The Hall bars were fabricated by etching and Ohmic contacts were made to the 2DEG by Au/Sb metal evaporation and annealing at 400°C for 10 min. The Hall data were

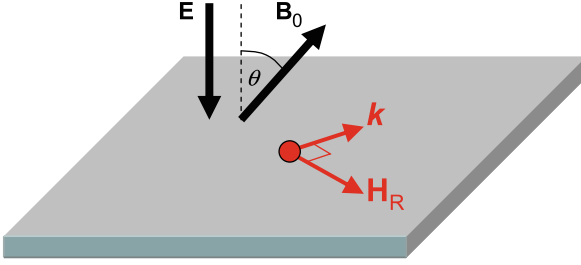


Fig. 1. Electrons in the quantum well move in the presence of a modulation-doping field. As a consequence of relativity, they then experience an effective inplane magnetic field H_R , known as the Rashba field, in addition to an external magnetic field B_0 , which is oriented at angle θ from the normal direction

used to extract the electron density and mobility. From the mobility we derived the momentum relaxation time $\tau_p = m_e^* \mu / e$, an important parameter in spin relaxation via spin-orbit and related interactions. The parameters reported in Table 1 have been corrected for a small parallel conduction path using the method of Kane et al.,¹ and in each case this correction was smaller than 1% [147].

6 ESR Measurements

Electron-spin resonance data were acquired with a Bruker ESP300E X-band spectrometer, using an Oxford Instruments ESR900 continuous-flow cryostat to maintain a sample temperature of 4.2 K. Magnetic-field calibration and tracking was done with an ER035M NMR Gaussmeter. The power dependence was checked to ensure the experiments were performed at low enough power that the peak width did not depend on the power level.

The ESR spectra for all samples were measured as a function of the orientation of the applied magnetic field, given by the angle θ between the magnetic field and the growth direction of the sample, as shown in Fig. 1. Figures 2a and c describe two-dimensional maps of the ESR intensity as a function of magnetic field and orientation angle for two selected samples. The peak-to-peak ESR linewidths ΔH_{pp} were extracted by fitting the lineshapes to the derivative of a Lorentzian, as shown in the insets of Figs. 2b and d. The linewidths exhibit a pronounced dependence on the orientation angle θ , as shown in Figs. 2b and d. The minimal ESR linewidths (at $\theta = 0$) and

¹ The unchanging slope of the transverse resistance shows that the conductivity of the parallel conduction path is much less than the conductivity of the 2DEG. This limit is consistent with Kane's analysis, allowing us to extract the 2DEG mobility and electron density as well as the conductivity of the parallel conduction path.

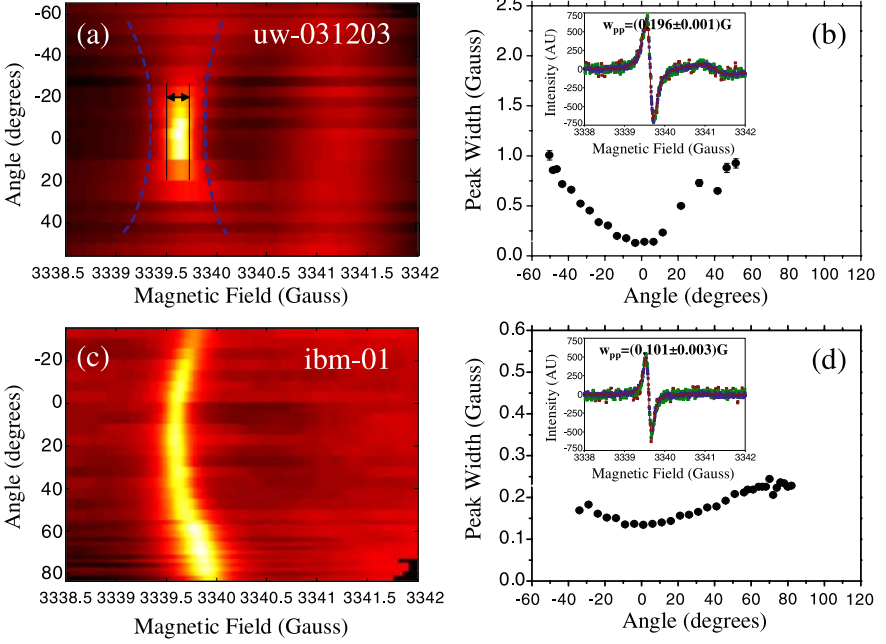


Fig. 2. Orientation map of the ESR signal from (a) sample uw-031203 and (c) sample ibm-01. The color scale describes the peak intensity. The angle on the vertical axis is explained in Fig. 1. Lorentzian fits to the peak width are shown in (b) and (d) for the same two samples (see *inset*), as a function of the field angle

the observed linewidth anisotropies are summarized in Table 1, based on the analysis described below.²

7 Decoherence Analysis

The ESR linewidth ΔH_{pp} is directly related to the coherence time T_2^* through the expression [4]

$$\Delta H_{\text{pp}} = \frac{2}{\sqrt{3}} \frac{\hbar}{g\mu_B} \left(\frac{1}{T_2^*} \right), \quad (1)$$

² In many ESR data sets, including the inset of Fig. 2b, there is a small peak near 3341 G, in the region of Landé g -factor, $g \approx 2.0$. The peak shows no orientational dependence, and it is wider than the 2DEG peak. Because the peak is almost perfectly equidistant between two 42 G split phosphorous peaks (not shown in the figure), we deduce that it arises from electrons in the dopant layer, which are shared among clusters of phosphorous nuclei. For example, see [148], especially Figs. 15 and 16.

where g is the Landé g -factor and μ_B is the Bohr magneton. It has been proposed [141] that the orientational dependence of T_2^* (and thus of ΔH_{pp}) in similar 2DEG structures results from a D'yakonov–Perel' spin relaxation mechanism due to fluctuating Rashba fields [127]. There is an electric field perpendicular to the plane of the 2DEG, due to ionized donors in the doping layer, or other interface effects. As a consequence of relativity, mobile electrons in the quantum well then experience an effective magnetic field in the plane of the 2DEG called the Rashba field H_R . (See Fig. 1.) Two-dimensional scattering processes therefore induce a fluctuating field ΔH_R in the 2DEG plane. When the external magnetic field \mathbf{B}_0 is perpendicular to the 2DEG ($\theta = 0$), the fluctuating ΔH_R is perpendicular to \mathbf{B}_0 . However, when \mathbf{B}_0 is tilted with respect to the 2DEG ($\theta \neq 0$), a component of the fluctuating field appears along \mathbf{B}_0 , resulting in an orientational dependence of T_2^* . In general, there may be other contributions to the linewidth, due to inhomogeneous broadening or other decoherence mechanisms, so that the spin-coherence time T_2^* may be written as

$$\frac{1}{T_2^*} = \frac{1}{T_{2R}} + \frac{1}{T_2'},$$

where $1/T_{2R}$ is the Rashba contribution, and $1/T_2'$ includes all other contributions.

Two groups have derived expressions for T_{2R} in the limit $\omega_c \tau_p \cos \theta \gg 1$. Both results can be written in similar fashion as

$$\frac{1}{T_{2R}} = \alpha^2 k_F^2 \tau_p \left[\frac{\eta}{1 + (\omega_c \cos \theta)^2 \tau_p^2} \sin^2 \theta + \frac{1/2}{1 + (\omega_L - \omega_c \cos \theta)^2 \tau_p^2} (\cos^2 \theta + 1) \right]. \quad (2)$$

The coefficient $\eta = 1/2$ was obtained in [141], while $\eta = 2$ was obtained in [149]. The Rashba coefficient α is defined in the Rashba Hamiltonian $\mathcal{H} = \alpha(\boldsymbol{\sigma} \times \mathbf{k}_F) \cdot \hat{\mathbf{n}}$, where $\boldsymbol{\sigma}$ are the Pauli spin matrices, \mathbf{k}_F is the Fermi wavevector of the electron, $\omega_c = eB/m_e^*$ is the cyclotron frequency, and $\omega_L = g\mu_B H/\hbar$ is the Larmor spin precession frequency [141]. The limit $\omega_c \tau_p \cos \theta \gg 1$ implies that (2) is valid only for small angles θ .

If $1/T_{2R}$ is the dominant term in $1/T_2^*$, then (2) can be normalized to give the anisotropy parameter $A(\theta)$, which depends on the momentum scattering time τ_p , but not the Rashba parameter α .³

³ The presumed origin of the Rashba field in these samples is from asymmetries occurring in the heterostructure, which lead to internal electric fields. There are four main types of asymmetries: (a) bulk inversion asymmetry (BIA) associated with the crystal lattice of the growth material [150], (b) structural inversion asymmetry (SIA) arising from explicit asymmetries in the heterostructure (e.g., dopants on the top, not the bottom) [150], (c) native interface asymmetry (NIA) arising from chemical bonds at the interface [151], and (d) fluctuations in the dopant con-

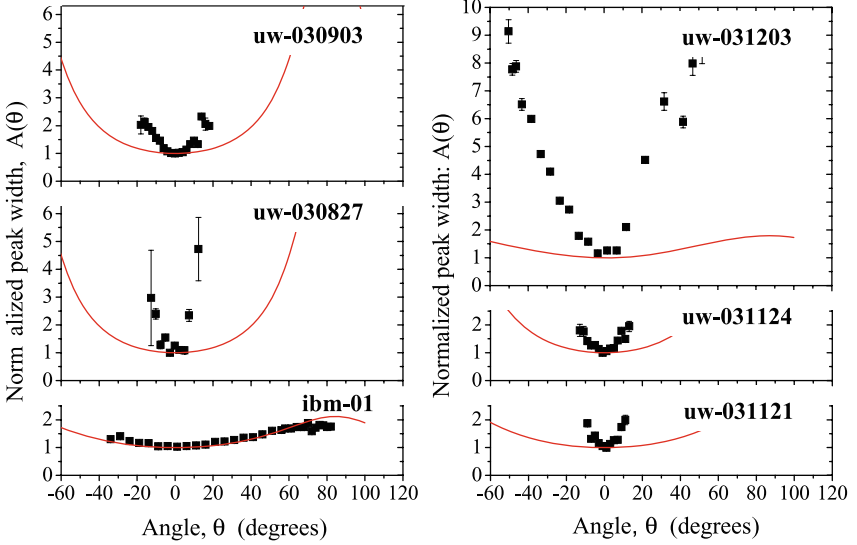


Fig. 3. Normalized experimental peak widths are presented as a function of the magnetic-field orientation θ , for all six samples. The corresponding theoretical predictions for the anisotropy parameter $A(\theta)$ in (3) are shown as lines, using $\eta = 1/2$

$$\begin{aligned}
 A(\theta) &\equiv \frac{\Delta H_{\text{pp}}(\theta)}{\Delta H_{\text{pp}}(0)} = \frac{1/T_2^*(\theta)}{1/T_2^*(0)} \\
 &= [1 + (\omega_L - \omega_c)^2 \tau_p^2] \\
 &\quad \times \left[\frac{\eta \sin^2 \theta}{1 + (\omega_c \cos \theta)^2 \tau_p^2} + \frac{(\cos^2 \theta + 1)/2}{1 + (\omega_L - \omega_c \cos \theta)^2 \tau_p^2} \right]. \quad (3)
 \end{aligned}$$

8 Results

In Fig. 3, we show the renormalized linewidths for all six samples, along with the theoretical results for $A(\theta)$. In five of these six cases, the experimental anisotropies at small angles clearly differ substantially from the theoretical predictions. We can quantify this difference as follows. Since (3) applies for small θ , we can perform a Taylor expansion to give

$$A(\theta) = 1 + b\theta^2 \quad (\theta \ll \pi/2), \quad (4)$$

where the quadratic coefficient b is a measure of how quickly the anisotropy increases with angle θ . For each sample, b can be determined experimentally centration [152]. Neither (a) nor (c) are present in Si/SiGe heterostructures [153], leaving (b) and (d) as the possible sources of perpendicular electric fields. It is most likely that SIA arises from modulation doping fields, which can also lead to local fluctuations in the charge density (d).

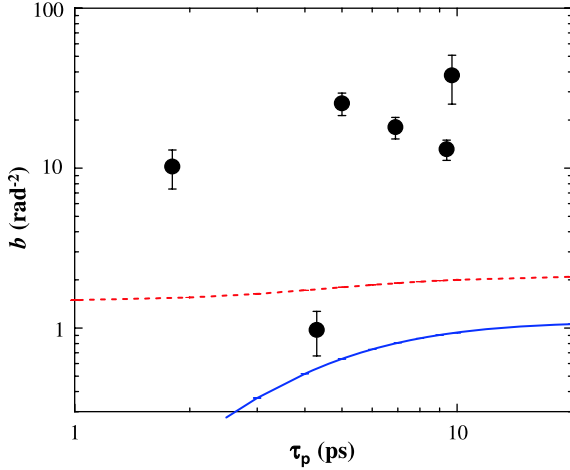


Fig. 4. The quadratic coefficient b of the anisotropy parameter $A(\theta)$, from (3) and (4), obtained by fitting to the experimental data near the origin, and expressed as a function of the momentum scattering time τ_p . The lines show the theoretical predictions for $\eta = 2$ (*dashed line*) and $\eta = 1/2$ (*solid line*)

by fitting the data. A plot of b as a function of the momentum relaxation time τ_p is given in Fig. 4, and the results are also listed in Table 1. For all six samples, the quadratic coefficients b differ substantially from the theoretical predictions, considering both proposed values of η . Even more striking, the maximum theoretical value of b for any value of τ_p is about 2 rad^{-2} . This value is nearly an order of magnitude smaller than the experimental observations for five of the six samples.

As Fig. 4 demonstrates, the semiclassical expression for $1/T_{2R}$ in (2) does not account for the observed behavior of $1/T_2^*$ in our samples. Various mechanisms could be contributing to the linewidth, through the component $1/T_2'$. In this case, $1/T_2'$ would necessarily contain an angular dependence, otherwise the functional form of the anisotropy would be unchanged, leaving b unaffected. The observed discrepancy must therefore involve an angular dependence. Since bulk silicon possesses a crystallographic inversion symmetry, orientationally dependent mechanisms [141, 154] originating from the anti-symmetric Dresselhaus term in the Hamiltonian [155], should not contribute to the linewidth.

There are several possible explanations for the observed anisotropy. In a recent paper, it was shown that in addition to the magnetic excitation mechanism, a microwave electric field may also excite ESR, as mediated by the spin-orbit coupling in a AlAs quantum well [132]. This contribution could provide an anomalous orientational dependence, since it depends only on the inplane component of the E -field. However, the same mechanism has not yet been observed in Si quantum wells, where the spin-orbit coupling is very

small. In our experiments, we were careful to place samples only at the zero-field nodes of the resonating cavity, so related effects would be minimized. Further, sample IBM-1 shows dramatically different orientational dependence from the other samples, yet the measurement procedure was the same for all samples. Thus, electric-field effects seem an unlikely explanation for the divergent examples of broadening observed here. It is also possible that the unexpected behavior arises from the angular dependence of the inhomogeneous broadening. One could test this hypothesis by means of pulsed EPR experiments, which measure T_2 instead of T_2^* , thus removing the sensitivity to inhomogeneous broadening. The latter can arise from static dipole-dipole interactions with ^{29}Si nuclei. Interactions with residual ^{29}Si nuclei can also be eliminated by growing quantum wells with isotopically purified ^{28}Si .

9 Conclusions

In this chapter, we have reviewed the current state of silicon quantum devices and silicon ESR in 2DEGs. We have also presented results of ESR and transport measurements in a number of 2DEGs used in recent quantum-device experiments. Specifically, we have analyzed the orientational dependence of the ESR linewidths. In one of our samples, we observed a dependence similar to recent observations in other groups. However, for five other samples, we observe an orientation-dependent spin decoherence with an anisotropy larger than the predictions of any current theory.

As discussed in the first half of this chapter, silicon quantum devices have advanced dramatically over the past decade, and are increasingly used in spintronics and related valley-based applications. Recent progress has demonstrated that quantum effects thought to be difficult to observe in silicon can in fact be realized, and one hopes that this will be a springboard for future work.

Acknowledgments

This work was supported by NSA/LPS under ARO contract number W911NF-04-1-0389, and by the National Science Foundation under Grant Numbers DMR-0325634, CCF-0523675, and DMR-0079983.

References

1. I. Žutić, J. Fabian, S. Das Sarma, Spintronics: Fundamentals and applications. *Rev. Mod. Phys.* **76**, 323–410 (2004) 102, 106
2. S. Datta, B. Das, Electronic analog of the electro-optic modulator. *Appl. Phys. Lett.* **56**, 665–667 (1990) 102

3. M.A. Nielsen, I.L. Chuang, *Quantum Computation and Quantum Information* (Cambridge University Press, Cambridge, 2000) 102
4. C. Poole, *Electron Spin Resonance*, 2nd edn. (Dover, Minneola, 1996) 102, 111
5. C.P. Slichter, *Principles of Magnetic Resonance*, 2nd edn. (Springer, Berlin, 1978) 102
6. D. Stein, K. von Klitzing, G. Weimann, Electron spin resonance on GaAs-Al_xGa_{1-x}As heterostructures. *Phys. Rev. Lett.* **51**, 130–133 (1983) 102
7. M. Ciorga, A.S. Sachrajda, P. Hawrylak, C. Gould, P. Zawadzki, S. Jullian, Y. Feng, Z. Wasilewski, Addition spectrum of a lateral dot from Coulomb and spin blockade spectroscopy. *Phys. Rev. B* **61**, R16315–R16318 (2000) 102, 104, 105
8. T. Fujisawa, D.G. Austing, Y. Tokura, Y. Hirayama, S. Tarucha, Allowed and forbidden transitions in artificial hydrogen and helium atoms. *Nature* **419**, 278–281 (2002) 102, 104, 105
9. J.M. Elzerman, R. Hanson, L.H. Willems van Beveren, B. Witkamp, L.M.K. Vandersypen, L.P. Kouwenhoven, Single-shot read-out of an individual electron spin in a quantum dot. *Nature* **430**, 431 (2004) 102, 104, 105
10. F.H.L. Koppens, J.A. Folk, J.M. Elzerman, R. Hanson, L.H. Willems van Beveren, I.T. Vink, H.P. Tranitz, W. Wegscheider, L.P. Kouwenhoven, L.M.K. Vandersypen, Control and detection of singlet-triplet mixing in a random nuclear field. *Science* **309**, 1346–1350 (2005) 102, 104
11. J.R. Petta, A.C. Johnson, J.M. Taylor, E.A. Laird, A. Yacoby, M.D. Lukin, C.M. Marcus, M.P. Hanson, A.C. Gossard, Coherent manipulation of coupled electron spins in semiconductor quantum dots. *Science* **309**, 2180–2184 (2005) 102, 104, 105
12. A.C. Johnson, J.R. Petta, J.M. Taylor, A. Yacoby, M.D. Lukin, C.M. Marcus, M.P. Hanson, A.C. Gossard, Triplet-singlet spin relaxation via nuclei in a double quantum dot. *Nature* **435**, 925–928 (2005) 102, 104
13. R. Hanson, L.H. Willems van Beveren, I.T. Vink, J.M. Elzerman, W.J.M. Naber, F.H.L. Koppens, L.P. Kouwenhoven, L.M.K. Vandersypen, Single-shot readout of electron spin states in a quantum dot using spin-dependent tunnel rates. *Phys. Rev. Lett.* **94**, 196802 (2005) 102, 104
14. F.H.L. Koppens, C. Buizert, K.J. Tielrooij, I.T. Vink, K.C. Nowack, T. Meunier, L.P. Kouwenhoven, L.M.K. Vandersypen, Driven coherent oscillations of a single electron spin in a quantum dot. *Nature* **442**, 766–771 (2006) 102, 104
15. T. Ando, A.B. Fowler, F. Stern, Electronic properties of two-dimensional systems. *Rev. Mod. Phys.* **54**, 437–672 (1982) 103, 104

16. S.M. Sze, *Physics of Semiconductor Devices*, 2nd edn. (Wiley, New York, 1981) 103, 104
17. Y. Takahashi, M. Nagase, H. Namatsu, K. Kurihara, K. Iwdate, Y. Nakajima, S. Horiguchi, K. Murase, M. Tabe, Fabrication technique for Si single-electron transistor operating at room temperature. *Electron. Lett.* **31**, 136–137 (1995) 103
18. L. Guo, E. Leobandung, L. Zhuang, S.Y. Chou, Fabrication and characterization of room temperature silicon single electron memory. *J. Vac. Sci. Technol. B* **15**, 2840–2843 (1997) 103
19. S.K. Ray, L.K. Bera, C.K. Maiti, S. John, S.K. Banerjee, Electrical characteristics of plasma oxidized $\text{Si}_{1-x-y}\text{Ge}_x\text{C}_y$ metal–oxide–semiconductor capacitors. *Appl. Phys. Lett.* **72**, 1250–1252 (1998) 103
20. D. Ali, H. Ahmed, Coulomb blockade in a silicon tunnel junction device. *Appl. Phys. Lett.* **64**, 2119–2120 (1994) 103
21. L. Guo, E. Leobandung, S.Y. Chou, A silicon single-electron transistor memory operating at room temperature. *Science* **275**, 649–651 (1997) 103
22. M. Khoury, M.J. Rack, A. Gunther, D.K. Ferry, Spectroscopy of a silicon quantum dot. *Appl. Phys. Lett.* **74**, 1576–1578 (1999) 103
23. K.-S. Park, S.-J. Kim, I.-B. Baek, W.-H. Lee, J.-S. Kang, Y.-B. Jo, S.D. Lee, C.-K. Lee, J.-B. Choi, J.-H. Kim, K.-H. Park, W.-J. Cho, M.-G. Jang, S.-J. Lee, SOI single-electron transistor with low RC delay for logic cells and SET/FET hybrid ICs. *IEEE Trans. Nanotechnol.* **4**, 242–248 (2005) 103
24. E.G. Emiroglu, D.G. Hasko, D.A. Williams, Isolated double quantum dot capacitively coupled to a single quantum dot single-electron transistor in silicon. *Appl. Phys. Lett.* **83**, 3942–3944 (2003) 104
25. S.D. Lee, K.S. Park, J.W. Park, J.B. Choi, S.-R.E. Yang, K.-H. Yoo, J. Kim, S.I. Park, K.T. Kim, Single-electron spectroscopy in a coupled triple-dot system: Role of interdot electron-electron interactions. *Phys. Rev. B* **62**, R7735–R7738 (2000) 104
26. S.D. Lee, S.J. Shin, S.J. Choi, J.J. Lee, J.B. Choi, S. Park, S.-R.E. Yang, S.J. Lee, T.H. Zyung, Si-based Coulomb blockade device for spin qubit logic gate. *Appl. Phys. Lett.* **89**, 023111 (2006) 104
27. A. Fujiwara, Y. Takahashi, Manipulation of elementary charge in a silicon charge-coupled device. *Nature* **410**, 560–562 (2001) 104
28. J. Gorman, D.G. Hasko, D.A. Williams, Charge-qubit operation of an isolated double quantum dot. *Appl. Phys. Lett.* **95**, 090502 (2005) 104
29. K. Takashina, Y. Ono, A. Fujiwara, Y. Takahashi, Y. Hirayama, Valley polarization in Si(100) at zero magnetic field. *Phys. Rev. Lett.* **96**, 236801 (2006) 104, 107
30. T. Ouisse, D.K. Maude, S. Horiguchi, Y. Ono, Y. Takahashi, K. Murase, S. Cristoloveanu, Subband structure and anomalous valley splitting in ultra-thin silicon-on-insulator MOSFET's. *Physica B* **249–251**, 731–734 (1998) 104, 107

31. R. Augke, W. Eberhardt, C. Single, F.E. Prins, D.A. Wharam, D.P. Kern, Doped silicon single electron transistors with single island characteristics. *Appl. Phys. Lett.* **76**, 2065–2067 (2000) 104
32. N.M. Zimmerman, W.H. Huber, A. Fujiwara, Y. Takahashi, Excellent charge offset stability in a Si-based single-electron tunneling transistor. *Appl. Phys. Lett.* **79**, 3188–3190 (2001) 104
33. J.H.F. Scott-Thomas, S.B. Field, M.A. Kastner, H.I. Smith, D.A. Antoniadis, Conductance oscillations periodic in the density of a one-dimensional electron gas. *Phys. Rev. Lett.* **62**, 583–586 (1989) 104
34. R.A. Smith, H. Ahmed, Gate controlled Coulomb blockade effects in the conduction of a silicon quantum wire. *J. Appl. Phys.* **81**, 2699–2703 (1997) 104
35. L.P. Rokhinson, L.J. Guo, S.Y. Chou, D.C. Tsui, Double-dot charge transport in Si single-electron/hole transistors. *Appl. Phys. Lett.* **76**, 1591–1593 (2000) 104
36. B.H. Choi, Y.S. Yu, D.H. Kim, S.H. Son, K.H. Cho, S.W. Hwang, D. Ahn, B.-G. Park, Double-dot-like charge transport through a small size silicon single electron transistor. *Physica E* **13**, 946–949 (2002) 104
37. K.H. Cho, B.H. Choi, S.H. Son, S.W. Hwang, D. Ahn, B.-G. Park, B. Naser, J.-F. Lin, J.P. Bird, Evidence of double layer quantum dot formation in a silicon-on-insulator nanowire transistor. *Appl. Phys. Lett.* **86**, 043101 (2005) 104
38. Y. Ono, A. Fujiwara, K. Nishiguchi, H. Inokawa, Y. Takahashi, Manipulation and detection of single electrons for future information processing. *J. Appl. Phys.* **97**, 031101 (2005) 104
39. F. Schäffler, High-mobility Si and Ge structures. *Semicond. Sci. Technol.* **12**, 1515–1549 (1997) 104, 105, 108
40. B.S. Meyerson, UHV/CVD growth of Si and Si:Ge alloys: chemistry, physics, and device applications. *Proc. IEEE* **80**, 1592–1608 (1992) 104, 105
41. P.A. Cain, H. Ahmed, D.A. Williams, J.M. Bonar, Hole transport through single and double SiGe quantum dots. *Appl. Phys. Lett.* **77**, 3415–3417 (2000) 104
42. P.A. Cain, H. Ahmed, D.A. Williams, Conductance peak splitting in hole transport through a SiGe double quantum dot. *Appl. Phys. Lett.* **78**, 3624–3626 (2001) 104
43. P.A. Cain, H. Ahmed, D.A. Williams, Hole transport in coupled SiGe quantum dots for quantum computation. *J. Appl. Phys.* **92**, 346–350 (2002) 104
44. H. Qin, S. Yasin, D.A. Williams, Fabrication and characterization of a SiGe double quantum dot structure. *J. Vac. Sci. Technol. B* **21**, 2852–2855 (2003) 104
45. D.S. Gandolfo, D.A. Williams, H. Qin, Characterization of a silicon–germanium quantum dot structure at 4.2K and 40 mK. *J. Appl. Phys.* **97**, 063710 (2005) 104

46. S.F. Nelson, K. Ismail, J.J. Nocera, F.F. Fang, E.E. Mendez, J.O. Chu, B.S. Meyerson, Observation of the fractional quantum Hall effect in Si/SiGe heterostructures. *Appl. Phys. Lett.* **61**, 64–66 (1992) 104
47. K. Ismail, J.O. Chu, K.L. Saenger, B.S. Meyerson, W. Rausch, Modulation-doped n-type Si/SiGe with inverted interface. *Appl. Phys. Lett.* **65**, 1248–1250 (1994) 104
48. K. Ismail, M. Arafa, K.L. Saenger, J.O. Chu, B.S. Meyerson, Extremely high electron mobility in Si/SiGe modulation-doped heterostructures. *Appl. Phys. Lett.* **66**, 1077–1079 (1995) 104, 109
49. L. Di Gaspare, K. Alfaramawi, F. Evangelisti, E. Palange, G. Barucca, G. Majni, Si/SiGe modulation-doped heterostructures grown on silicon-on-insulator substrates for high-mobility two-dimensional electron gases. *Appl. Phys. Lett.* **79**, 2031–2033 (2001) 104
50. T. Okamoto, M. Ooya, K. Hosoya, S. Kawaji, Spin polarization and metallic behavior in a silicon two-dimensional electron system. *Phys. Rev. B* **69**, 041202 (2004) 104
51. F. Stern, S.E. Laux, Charge transfer and low-temperature electron mobility in a strained Si layer in relaxed $\text{Si}_{1-x}\text{Ge}_x$. *Appl. Phys. Lett.* **61**, 1110–1112 (1992) 105, 108
52. D. Monroe, Y.H. Xie, E.A. Fitzgerald, P.J. Silverman, G.P. Watson, Comparison of mobility-limiting mechanisms in high-mobility $\text{Si}_{1-x}\text{Ge}_x$ heterostructures. *J. Vac. Sci. Technol.* **11**, 1731–1737 (1993) 105, 108
53. M.A. Eriksson, M. Friesen, S.N. Coppersmith, R. Joynt, L.J. Klein, K. Slinker, C. Tahan, P.M. Mooney, J.O. Chu, S.J. Koester, Spin-based quantum dot quantum computing in silicon. *Quantum. Inf. Process.* **3**, 133–146 (2004) 105, 107
54. W.X. Gao, K. Ismail, K.Y. Lee, J.O. Chu, S. Washburn, Observation of ballistic conductance and Aharonov–Bohm oscillations in Si/SiGe heterostructures. *Appl. Phys. Lett.* **65**, 3114–3116 (1994) 105
55. S.J. Koester, K. Ismail, K.Y. Lee, J.O. Chu, Negative differential conductance in strained Si point contacts and wires. *Appl. Phys. Lett.* **71**, 1528–1530 (1997) 105
56. L.P. Kouwenhoven, C.M. Marcus, P.L. McEuen, S. Tarucha, R.M. Westervelt, N.S. Wingreen, Electron transport in quantum dots, in *Mesoscopic Electron Transport*, ed. by L.L. Sohn, L.P. Kouwenhoven, G. Schön (Kluwer, Dordrecht, 1997), pp. 105–214 105
57. L.J. Klein, K.A. Slinker, J.L. Truitt, S. Goswami, K.L.M. Lewis, S.N. Coppersmith, D.W. van der Weide, M. Friesen, R.H. Blick, D.E. Savage, M.G. Lagally, C. Tahan, R. Joynt, M.A. Eriksson, J.O. Chu, J.A. Ott, P.M. Mooney, Coulomb blockade in a silicon/silicon–germanium two-dimensional electron gas quantum dot. *Appl. Phys. Lett.* **84**, 4047–4049 (2004) 105, 108, 109
58. S. Kanjanachuchai, T.J. Thornton, J.M. Fernández, H. Ahmed, Coulomb blockade in strained-Si nanowires on leaky virtual substrates. *Semicond. Sci. Technol.* **16**, 72–76 (2001) 105

59. T. Berer, D. Pachinger, G. Pillwein, M. Mühlberger, H. Lichtenberger, G. Brunthaler, F. Schäffler, Lateral quantum dots in Si/SiGe realized by a Schottky split-gate technique. *Appl. Phys. Lett.* **88**, 162112 (2006) 105, 106
60. S.J. Koester, K. Ismail, K.Y. Lee, J.O. Chu, Weak localization in back-gated Si/Si_{0.7}Ge_{0.3} quantum-well wires fabricated by reactive ion etching. *Phys. Rev. B* **54**, 10604–10608 (1996) 105
61. K.Y. Lee, S.J. Koester, K. Ismail, J.O. Chu, Electrical characterization of Si/Si_{0.7}Ge_{0.3} quantum well wires fabricated by low damage CF₄ reactive ion etching. *Microelectron. Eng.* **35**, 33–36 (1997) 105
62. L.J. Klein, K.L.M. Lewis, K.A. Slinker, S. Goswami, D.W. van der Weide, R.H. Blick, P.M. Mooney, J.O. Chu, S.N. Coppersmith, M. Friesen, M.A. Eriksson, Quantum dots and etch-induced depletion of a silicon two-dimensional electron gas. *J. Appl. Phys.* **99**, 023509 (2006) 105, 108
63. M. Holzmann, D. Többen, G. Abstreiter, M. Wendel, H. Lorenz, J.P. Kotthaus, F. Schäffler, One-dimensional transport of electrons in Si/Si_{0.7}Ge_{0.3} heterostructures. *Appl. Phys. Lett.* **66**, 833–835 (1995) 105
64. R.G. Van Veen, A.H. Verbruggen, E. van der Drift, F. Schäffler, S. Radelhaar, Experimental study on magnetoresistance phenomena in n-type Si/SiGe quantum wires. *Semicond. Sci. Technol.* **14**, 508–516 (1999) 105
65. E. Giovine, A. Notargiacomo, L. Di Gaspare, E. Palange, F. Evangelisti, R. Leoni, G. Castellano, G. Torrioli, V. Foglietti, Investigation of SiGe-heterostructure nanowires. *Nanotechnology* **12**, 132–135 (2001) 105
66. U. Wieser, U. Kunze, K. Ismail, J.O. Chu, Fabrication of Si/SiGe quantum point contacts by electron-beam lithography and shallow wet-chemical etching. *Physica E* **13**, 1047–1050 (2002) 105, 106
67. U. Dötsch, U. Gennser, C. David, G. Dehlinger, D. Grützmacher, T. Heinzel, S. Lüscher, K. Ensslin, Single-hole transistor in a *p*-Si:SiGe quantum well. *Appl. Phys. Lett.* **78**, 341–343 (2001) 105
68. A. Notargiacomo, L. Di Gaspare, G. Scappucci, G. Mariottini, F. Evangelisti, E. Giovine, R. Leoni, Single-electron transistor based on modulation-doped SiGe heterostructures. *Appl. Phys. Lett.* **83**, 302–304 (2003) 105
69. M.R. Sakr, H.W. Jiang, E. Yablonovitch, E.T. Croke, Fabrication and characterization of electrostatic Si/SiGe quantum dots with an integrated read-out channel. *Appl. Phys. Lett.* **87**, 223104 (2005) 105
70. M. Holzmann, D. Többen, G. Abstreiter, F. Schäffler, Field-effect induced electron channels in a Si/Si_{0.7}Ge_{0.3} heterostructure. *J. Appl. Phys.* **76**, 3917–3919 (1994) 105
71. R.B. Dunford, N. Griffin, D.J. Paul, M. Pepper, D.J. Robbins, A.C. Churchill, W.Y. Leong, Schottky gating high mobility Si/Si_{1-x}Ge_x 2D electron systems. *Thin Solid Films* **369**, 316–319 (2000) 105

72. K.A. Slinker, K.L.M. Lewis, C.C. Haselby, S. Goswami, L.J. Klein, J.O. Chu, S.N. Coppersmith, R. Joynt, R.H. Blick, M. Friesen, M.A. Eriksson, Quantum dots in Si/SiGe 2DEGs with Schottky top-gated leads. *New J. Phys.* **7**, 246 (2005) 106, 108
73. L.J. Klein, D.E. Savage, M.A. Eriksson, Coulomb blockade and Kondo effect in a few-electron silicon/silicon-germanium quantum dot. *Appl. Phys. Lett.* **90**, 033103 (2007) 106, 108
74. T. Berer, D. Pachinger, G. Pillwein, M. Mühlberger, H. Lichtenberger, G. Brunthaler, F. Schäffler, Single-electron transistor in strained Si/SiGe heterostructures. *Physica E* **34**, 456–459 (2006) 106
75. D. Többen, D.A. Wharam, G. Abstreiter, J.P. Kotthaus, F. Schäffler, Transport properties of a Si/SiGe quantum point contact in the presence of impurities. *Phys. Rev. B* **52**, 4704–4707 (1995) 106, 107
76. D. Többen, D.A. Wharam, G. Abstreiter, J.P. Kotthaus, F. Schäffler, Ballistic electron transport through a quantum point contact defined in a Si/Si_{0.7}Ge_{0.3} heterostructure. *Semicond. Sci. Technol.* **10**, 711–714 (1995) 106, 107
77. G. Scappucci, L. Di Gaspare, E. Giovine, A. Notargiacomo, R. Leoni, F. Evangelisti, Conductance quantization in etched Si/SiGe quantum point contacts. *Phys. Rev. B* **74**, 035321 (2006) 106
78. G.D. Scott, M. Xiao, H.W. Jiang, E.T. Croke, E. Yablonovitch, Sputtered gold as an effective Schottky gate for strained Si/SiGe nanostructures. *Appl. Phys. Lett.* **90**, 032110 (2007) 106
79. S. Goswami, K.A. Slinker, M. Friesen, L.M. McGuire, J.L. Truitt, C. Tahan, L.J. Klein, J.O. Chu, P.M. Mooney, D.W. van der Weide, R. Joynt, S.N. Coppersmith, M.A. Eriksson, Controllable valley splitting in silicon quantum devices. *Nat. Phys.* **3**, 41–45 (2007) 106, 107, 108
80. M.M. Roberts, L.J. Klein, D.E. Savage, K.A. Slinker, M. Friesen, G. Celler, M.A. Eriksson, M.G. Lagally, Elastically relaxed free-standing strained-silicon nanomembranes. *Nat. Mater.* **5**, 388–393 (2006) 106
81. P. Zhang, E.P. Nordberg, B.-N. Park, G.K. Celler, I. Knezevic, P.G. Evans, M.A. Eriksson, M.G. Lagally, Electrical conductivity in silicon nanomembranes. *New J. Phys.* **8**, 200 (2006) 106
82. D. Loss, D.P. DiVincenzo, Quantum computation with quantum dots. *Phys. Rev. A* **57**, 120–126 (1998) 106
83. V. Cerletti, W.A. Coish, O. Gywat, D. Loss, Recipes for spin-based quantum computing. *Nanotechnology* **16**, R27–R49 (2005) 106
84. B.E. Kane, A silicon-based nuclear spin quantum computer. *Nature* **393**, 133–137 (1998) 106
85. J.L. O’Brien, S.R. Schofield, M.Y. Simmons, R.G. Clark, A.S. Dzurak, N.J. Curson, B.E. Kane, N.S. McAlpine, M.E. Hawley, G.W. Brown, Towards the fabrication of phosphorus qubits for a silicon quantum computer. *Phys. Rev. B* **64**, 161401 (2001) 106

86. G. Berman, G.W. Brown, M.E. Hawley, V.I. Tsifrinovich, Solid-state quantum computer based on scanning tunneling microscopy. *Phys. Rev. Lett.* **87**, 097902 (2001) 106
87. T.D. Ladd, J.R. Goldman, F. Yamaguchi, Y. Yamamoto, E. Abe, K.M. Itoh, All-silicon quantum computer. *Phys. Rev. Lett.* **89**, 017901 (2002) 106
88. T. Schenkel, A. Persaud, S.J. Park, J. Nilsson, J. Bokor, J.A. Liddle, R. Keller, D.H. Schneider, D.W. Cheng, D.E. Humphries, Solid state quantum computer development in silicon with single ion implantation. *J. Appl. Phys.* **94**, 7017–7024 (2003) 106
89. R.G. Clark, R. Brenner, T.M. Buehler, V. Chan, N.J. Curson, A.S. Dzurak, E. Gauja, H.S. Goan, A.D. Greentree, T. Hallam, A.R. Hamilton, L.C.L. Hollenberg, D.N. Jamieson, J.C. McCallum, G.J. Milburn, J.L. O'Brien, L. Oberbeck, C.I. Pakes, S.D. Prawer, D.J. Reilly, F.J. Ruess, S.R. Schofield, M.Y. Simmons, F.E. Stanley, R.P. Starrett, C. Wellard, C. Yang, Progress in silicon-based quantum computing. *Philos. Trans. R. Soc. Lond., Ser. A* **361**, 1451–1471 (2003) 106
90. A.J. Skinner, M.E. Davenport, B.E. Kane, Hydrogenic spin quantum computing in silicon: A digital approach. *Phys. Rev. Lett.* **90**, 087901 (2003) 106
91. A.M. Stoneham, A.J. Fisher, P.T. Greenland, Optically driven silicon-based quantum gates with potential for high-temperature operation. *J. Phys., Condens. Matter* **15**, L447–L451 (2003) 106
92. C.D. Hill, L.C.L. Hollenberg, A.G. Fowler, C.J. Wellard, A.D. Greentree, H.-S. Goan, Global control and fast solid-state donor electron spin quantum computing. *Phys. Rev. B* **72**, 045350 (2005) 106
93. T.M. Buehler, V. Chan, A.J. Ferguson, A.S. Dzurak, F.E. Hudson, D.J. Reilly, A.R. Hamilton, R.G. Clark, D.N. Jamieson, C. Yang, C.I. Pakes, S. Prawer, Controlled single electron transfer between Si:P dots. *Appl. Phys. Lett.* **88**, 192101 (2006) 106
94. R. Vrijen, E. Yablonovitch, K. Wang, H.W. Jiang, A. Balandin, V. Roychowdhury, T. Mor, D. DiVincenzo, Electron-spin-resonance transistors for quantum computing in silicon-germanium heterostructures. *Phys. Rev. A* **62**, 012306 (2000) 106
95. J. Levy, Quantum-information processing with ferroelectrically coupled quantum dots. *Phys. Rev. A* **64**, 052306 (2001) 106
96. M. Friesen, P. Rugheimer, D.E. Savage, M.G. Lagally, D.W. van der Weide, R. Joynt, M.A. Eriksson, Practical design and simulation of silicon-based quantum-dot qubits. *Phys. Rev. B* **67**, 121301(R) (2003) 106
97. J.P. Gordon, K.D. Bowers, Microwave spin echoes from donor electrons in silicon. *Phys. Rev. Lett.* **1**, 368–370 (1958) 106
98. E. Abe, K.M. Itoh, J. Isoya, S. Yamasaki, Electron-spin phase relaxation of phosphorus donors in nuclear-spin-enriched silicon. *Phys. Rev. B* **70**, 033204 (2004) 106

99. A.M. Tyryshkin, S.A. Lyon, A.V. Astashkin, A.M. Raitsimring, Electron spin relaxation times of phosphorus donors in silicon. *Phys. Rev. B* **68**, 193207 (2003) 106
100. M. Xiao, I. Martin, E. Yablonovitch, H.W. Jiang, Electrical detection of the spin resonance of a single electron in a silicon field-effect transistor. *Nature* **430**, 435–439 (2004) 106
101. M. Friesen, S. Chutia, C. Tahan, S.N. Coppersmith, Valley Splitting Theory of SiGe/Si/SiGe Quantum Wells. *Phys. Rev. B*, to appear. condmat/0608229 (unpublished) 107
102. L.J. Sham, M. Nakayama, Effective-mass approximation in the presence of an interface. *Phys. Rev. B* **20**, 734–747 (1979) 107
103. F.J. Ohkawa, Y. Uemura, Theory of valley splitting in an N -Channel (100) inversion layer of Si: I. Formulation by extended zone effective mass theory. *J. Phys. Soc. Jpn.* **43**, 907–916 (1977) 107
104. F.J. Ohkawa, Y. Uemura, Theory of valley splitting in an N -Channel (100) Inversion Layer of Si: II. Electric Break Through. *J. Phys. Soc. Jpn.* **43**, 917–924 (1977) 107
105. F.J. Ohkawa, Electric break-through in an inversion layer: Exactly solvable model. *Solid State Commun.* **26**, 69–71 (1978) 107
106. H. Fritzsche, Effect of stress on the donor wave functions in germanium. *Phys. Rev.* **125**, 1560–1567 (1962) 107
107. W.D. Twose, in the Appendix of [106] 107
108. M. Nakayama, L.J. Sham, Surface-induced valley-splitting in n -channel (001) silicon-MOS charge layer. *Solid State Commun.* **28**, 393–396 (1978) 107
109. F.J. Ohkawa, Multi-valley effective mass theory. *J. Phys. Soc. Jpn.* **46**, 736–743 (1979) 107
110. T.B. Boykin, G. Klimeck, M.A. Eriksson, M. Friesen, S.N. Coppersmith, P. von Allmen, F. Oyafuso, S. Lee, Valley splitting in strained silicon quantum wells. *Appl. Phys. Lett.* **84**, 115–117 (2004) 107
111. T.B. Boykin, G. Klimeck, M. Friesen, S.N. Coppersmith, P. von Allmen, F. Oyafuso, S. Lee, Valley splitting in low-density quantum-confined heterostructures studied using tight-binding models. *Phys. Rev. B* **70**, 165325 (2004) 107
112. T.B. Boykin, G. Klimeck, P. von Allmen, S. Lee, F. Oyafuso, Valley splitting in V-shaped quantum wells. *J. Appl. Phys.* **97**, 113702 (2005) 107
113. M.O. Nestoklon, L.E. Golub, E.L. Ivchenko, Spin and valley-orbit splittings in SiGe/Si heterostructures. *Phys. Rev. B* **73**, 235334 (2006) 107
114. M. Friesen, M.A. Eriksson, S.N. Coppersmith, Magnetic field dependence of valley splitting in realistic Si/SiGe quantum wells. *Appl. Phys. Lett.* **89**, 202106 (2006) 107
115. P. Weitz, R.J. Haug, K. von Klitzing, F. Schäffler, Tilted magnetic field studies of spin- and valley-splittings in Si/Si_{1-x}Ge_x heterostructures. *Surf. Sci.* **361–362**, 542–546 (1996) 107

116. S.J. Koester, K. Ismail, J.O. Chu, Determination of spin- and valley-split energy levels in strained Si quantum wells. *Semicond. Sci. Technol.* **12**, 384–388 (1997) 107
117. H.W. Schumacher, A. Nauen, U. Zeitler, R.J. Haug, P. Weitz, A.G.M. Jansen, F. Schäffler, Anomalous coincidences between valley split Landau levels in a Si/SiGe heterostructure. *Physica B* **256–258**, 260–263 (1998) 107
118. V.S. Khrapai, A.A. Shashkin, V.P. Dolgoplov, Strong enhancement of the valley splitting in a two-dimensional electron system in silicon. *Phys. Rev. B* **67**, 113305 (2003) 107
119. K. Lai, W. Pan, D.C. Tsui, S. Lyon, M. Mühlberger, F. Schäffler, Two-flux composite fermion series of the fractional quantum hall states in strained Si. *Phys. Rev. Lett.* **93**, 156805 (2004) 107
120. M.A. Wilde, M. Rhode, C. Heyn, D. Heitmann, D. Grundler, U. Zeitler, F. Schäffler, R.J. Haug, Direct measurements of the spin and valley splittings in the magnetization of a Si/SiGe quantum well in tilted magnetic fields. *Phys. Rev. B* **72**, 165429 (2005) 107
121. K. Lai, W. Pan, D.C. Tsui, S. Lyon, M. Mühlberger, F. Schäffler, Intervalley gap anomaly of two-dimensional electrons in silicon. *Phys. Rev. Lett.* **96**, 076805 (2006) 107
122. K. Lai, T.M. Lu, W. Pan, D.C. Tsui, S. Lyon, J. Liu, Y.H. Xie, M. Mühlberger, F. Schäffler, Valley splitting of Si/Si_{1-x}Ge_x heterostructures in tilted magnetic fields. *Phys. Rev. B* **73**, 161301 (2006) 107
123. T. Ando, Valley splitting in the silicon inversion layer: Misorientation effects. *Phys. Rev. B* **19**, 3089–3095 (1979) 107
124. S. Lee, P. von Allmen, Magnetic-field dependence of valley splitting in Si quantum wells grown on tilted SiGe substrates. *Phys. Rev. B* **74**, 245302 (2006) 107
125. P. von Allmen, S. Lee, Zero valley splitting at zero magnetic field for strained Si/SiGe quantum wells grown on tilted substrates. *condmat/0606395* (unpublished) 107
126. K. Takashina, A. Fujiwara, S. Horiguchi, Y. Takahashi, Y. Hirayama, Valley splitting control in SiO₂/Si/SiO₂ quantum wells in the quantum Hall regime. *Phys. Rev. B* **69**, 161304(R) (2004) 107
127. M. D'yakonov, V. Perel', Spin relaxation of conduction electrons in non-centrosymmetric semiconductors. *Sov. Phys. Solid State* **13**, 3023–3026 (1972) 107, 112
128. F. Meier, B.P. Zakharchenya (eds.), *Optical Orientation*, Modern Problems in Condensed Matter Physics, vol. 8 (North-Holland, Amsterdam, 1984) 108
129. J.M. Kikkawa, D.D. Awschalom, Resonant spin amplification in n-type GaAs. *Phys. Rev. Lett.* **80**, 4313–4316 (1998) 108
130. W.O. Putikka, R. Joynt, Theory of optical orientation in n-type semiconductors. *Phys. Rev. B* **70**, 113201 (2004) 108

131. N. Nestle, G. Denninger, M. Vidal, C. Weinzierl, K. Brunner, K. Eberl, K. von Klitzing, Electron spin resonance on a two-dimensional electron gas. *Phys. Rev. B* **56**, R4359–R4362 (1997) 108
132. M. Schulte, J.G.S. Lok, G. Denninger, W. Dietsche, Electron spin resonance on a two-dimensional electron gas in a single AlAs quantum well. *Phys. Rev. Lett.* **94**, 137601 (2005) 108, 114
133. C.F.O. Graeff, M.S. Brandt, M. Stutzmann, M. Holzmann, G. Arbreiter, F. Schäffler, Electrically detected magnetic resonance of two-dimensional electron gases in Si/SiGe heterostructures. *Phys. Rev. B* **59**, 13242–13250 (1999) 108
134. J. Matsunami, M. Ooya, T. Okamoto, Electrically detected electron spin resonance in a high-mobility silicon quantum well. *Phys. Rev. Lett.* **97**, 066602 (2006) 108
135. W. Jantsch, Z. Wilamowski, N. Sandersfeld, F. Schäffler, ESR investigations of modulation-doped Si/SiGe quantum wells. *Phys. Status Solidi* **210**, 643–648 (1999) 108
136. W. Jantsch, Z. Wilamowski, N. Sandersfeld, F. Schäffler, Electric and magnetic field fluctuations in modulation doped Si/Ge quantum wells. *Physica E* **6**, 218–221 (2000) 108
137. N. Sandersfeld, W. Jantsch, Z. Wilamowski, F. Schäffler, ESR investigation of modulation-doped Si/SiGe quantum wells. *Thin Solid Films* **369**, 312–315 (2000) 108
138. Z. Wilamowski, N. Sandersfeld, W. Jantsch, D. Többen, F. Schäffler, Screening breakdown on the route toward the metal-insulator transition in modulation doped Si/SiGe quantum wells. *Phys. Rev. Lett.* **87**, 026401 (2001) 108
139. Z. Wilamowski, W. Jantsch, H. Malissa, U. Rössler, Evidence and evaluation of the Bychkov–Rashba effect in SiGe/Si/SiGe quantum wells. *Phys. Rev. B* **66**, 195315 (2002) 108
140. Z. Wilamowski, W. Jantsch, ESR studies of the Bychkov–Rashba field in modulation doped Si/SiGe quantum wells. *Physica E* **12**, 439–442 (2002) 108
141. Z. Wilamowski, W. Jantsch, Suppression of spin relaxation of conduction electrons by cyclotron motion. *Phys. Rev. B* **69**, 035328 (2004) 108, 112, 114
142. Z. Wilamowski, W. Jantsch, Spin relaxation of 2D electron in Si/SiGe quantum well suppressed by applied magnetic field. *Semicond. Sci. Technol.* **19**, S390–S391 (2004) 108
143. H. Malissa, W. Jantsch, M. Mühlberger, F. Schäffler, Z. Wilamowski, M. Draxler, P. Bauer, Anisotropy of g-factor and electron spin resonance linewidth in modulation doped SiGe quantum wells. *Appl. Phys. Lett.* **85**, 1739–1741 (2004) 108
144. W. Jantsch, H. Malissa, Z. Wilamowski, H. Lichtenberger, G. Chen, F. Schäffler, G. Bauer, Spin properties of electrons in low-dimensional SiGe structures. *J. Supercond.* **18**, 145–149 (2005) 108

145. Z. Wilamowski, H. Malissa, F. Schäffler, W. Jantsch, *g*-factor tuning and manipulation of spins by an electric current. cond-mat/0610046 (unpublished) 108
146. A.M. Tyryshkin, S.A. Lyon, W. Jantsch, F. Schäffler, Spin manipulation of free two-dimensional electrons in Si/SiGe quantum wells. Phys. Rev. Lett. **94**, 126802 (2005) 108
147. M.J. Kane, N. Apsley, D.A. Anderson, L.L. Taylor, T. Kerr, Parallel conduction in GaAs/Al_xGa_{1-x}As modulation doped heterojunctions. J. Phys. C **18**, 5629–5636 (1985) 110
148. G. Feher, Electron spin resonance experiments on donors in silicon. I. Electronic structure of donors by the electron nuclear double resonance technique. Phys. Rev. **114**, 1219–1244 (1959) 111
149. C. Tahan, R. Joynt, Rashba spin-orbit coupling and spin relaxation in silicon quantum wells. Phys. Rev. B **71**, 075315 (2005) 112
150. P. Pfeffer, W. Zawadzki, Spin splitting of conduction subbands in III–V heterostructures due to inversion asymmetry. Phys. Rev. B **59**, R5312–R5315 (1999) 112
151. J.T. Olesberg, W.H. Lau, M.E. Flatté, C. Yu, E. Altunkaya, E.M. Shaw, T.C. Hasenberg, T.F. Boggess, Interface contributions to spin relaxation in a short-period InAs/GaSb superlattice. Phys. Rev. B **64**, 201301(R) (2001) 112
152. E.Y. Sherman, Random spin-orbit coupling and spin relaxation in symmetric quantum wells. Appl. Phys. Lett. **82**, 209–211 (2003) 113
153. E.Y. Sherman, Minimum of spin-orbit coupling in two-dimensional structures. Phys. Rev. B **67**, 161303(R) (2003) 113
154. E.L. Ivchenko, Spin relaxation of free carriers in a noncentrosymmetric semiconductor in a longitudinal magnetic field. Sov. Phys. Solid State **15**, 1048–1050 (1973) 114
155. G. Dresselhaus, Spin-orbit coupling effects in zinc blende structures. Phys. Rev. **100**, 580–586 (1955) 114

Index

T_2^* , 111	electron-spin coherence, 108
ΔH_{pp} , 111	electron-spin resonance (ESR), 101, 102
²⁸ Si, 115	ESR, 101, 102, 111
²⁹ Si nuclei, 115	ESR linewidth, 111
coherence time, 111	few-electron, 101
D'yakonov and Perel' (DP), 107	Hall measurements, 109
decoherence, 106	inversion layers, 103
electrically detected electron-spin resonance (ESR), 102	quantum dots, 101, 102, 106

quantum wells, 102, 107, 110
Rashba parameter, 112
silicon-on-insulator (SOI), 103
silicon/silicon-germanium quantum wells, 101, 105
single-electron transistors (SETs), 103
SiO₂/Si/SiO₂, 104
spin coherence, 106, 108
spin-decoherence mechanisms, 106
ultrahigh-vacuum chemical vapor deposition, 109
valley splitting, 104, 107

“This page left intentionally blank.”

Electrical Detection of Electron-Spin Resonance in Two-Dimensional Systems

Junya Matsunami and Tohru Okamoto

Department of Physics, University of Tokyo, 7-3-1 Hongo, Bunkyo-ku,
Tokyo 113-0033, Japan

Abstract. We report electrically detected electron-spin resonance (ESR) measurements in a high-mobility two-dimensional electron system formed in a Si/SiGe heterostructure. Firstly, we clarify the origin of the ESR-induced resistivity change by optimizing the configuration among the Landau levels and the chemical potential. The observed decrease in the longitudinal resistivity shows that the primary cause is a change in the chemical potential, not a rise in the electron temperature. Heat flow in steady state under resonance conditions is also discussed. Secondly, we demonstrate a novel analysis of the resistivity change to deduce the spin-relaxation times. The longitudinal spin-relaxation time T_1 is obtained to be of the order of 1 ms in an inplane magnetic field of 3.55 T. The suppression of the effect of the Rashba fields due to high-frequency spin precession qualitatively explains the very long T_1 .

1 Mechanism of Electrical Detection

Detection of electron-spin resonance (ESR) can be broadly classified into two categories: (1) spectroscopic detection and (2) electrical detection. Electrical detection is preferable especially for measurements in low-dimensional systems because the magnitude of the resistivity change does not scale with the size of the system. Electrical detection has further advantages of its applicability to wide frequency and temperature ranges. Moreover, electrically detected ESR can be a novel tool to probe the relation between the spin polarization and electrical conduction.

For electrical detection of ESR, the resistivity must be sensitive to the spin-flip. Stein et al. demonstrated that electrical detection is indeed possible in quantum Hall systems [1]. They performed measurements at the odd Landau level (LL) filling factors ν , and observed the ESR signal as a positive change $\Delta\rho_{xx}$ in the longitudinal resistivity ρ_{xx} . Following the pioneering work, electrically detected ESR measurements have been performed intensively in quantum Hall systems formed in GaAs/AlGaAs heterostructures. The measurements have so far revealed, for example, the electron g-factor from the resonance field [2, 3] and the dynamic nuclear-spin polarization from the shift of the resonance field [4, 5]. However, for all its importance,

the mechanism of electrical detection remained unclear. In this section, we determine it from measurements in a “specific” LL configuration [6].

We performed electrically detected ESR measurements in a high-mobility Si/SiGe heterostructure sample. Four-probe ac resistivity measurements were performed for a Hall bar sample. The ESR signal $\Delta\rho_{xx}$ was observed during the magnetic field sweep in the presence of continuous 100 GHz millimeter-wave radiation. The sample was mounted inside an oversized waveguide inserted into a pumped ^3He refrigerator. By rotating the waveguide in a Helmholtz magnet, we changed the angle of the two-dimensional (2D) plane with respect to the magnetic field without changing the millimeter-wave configuration in the waveguide.

We first describe the “standard” LL configuration used in previous studies. In 2D systems subject to a strong perpendicular magnetic field, the kinetic energy of carriers is quantized into discrete LLs separated by the cyclotron gap $\hbar\omega_c$ ($\omega_c = eB_{\perp}/m^*$). Each LL is further split by the Zeeman splitting energy $E_Z = |g^*|\mu_B B_{\text{tot}}$. Here, B_{tot} and B_{\perp} are the total and perpendicular magnetic field, and m^* and g^* are electron effective mass and g-factor, respectively. When $E_Z > \hbar\omega_c$ and $\nu = \text{odd}$, the equilibrium chemical potential μ is located between spin-split LLs with the same orbital index as illustrated in Fig. 1a. Electrons and holes cause dissipation when they are thermally activated between the spin-split LLs. For low enough temperature, ρ_{xx} increases with the number of thermally activated carriers and shows an Arrhenius temperature dependence;

$$\rho_{xx} \simeq R_0 \exp\{-(E_{\downarrow,n} - \mu_{\downarrow})/k_B T_e\} + R_1 \exp\{-(\mu_{\uparrow} - E_{\uparrow,n})/k_B T_e\}. \quad (1)$$

Here, LLs and their energy are labeled by their spin index (\uparrow, \downarrow) and orbital index n . As can be seen from (1), ρ_{xx} is very sensitive to the chemical potential μ_{\downarrow} (μ_{\uparrow}) for spin-down (spin-up) electrons as well as the electron temperature T_e .

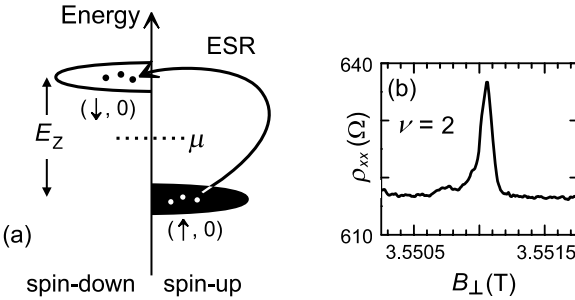


Fig. 1. (a) ESR excitation process and (b) the observed ESR signal in the standard LL configuration [6]

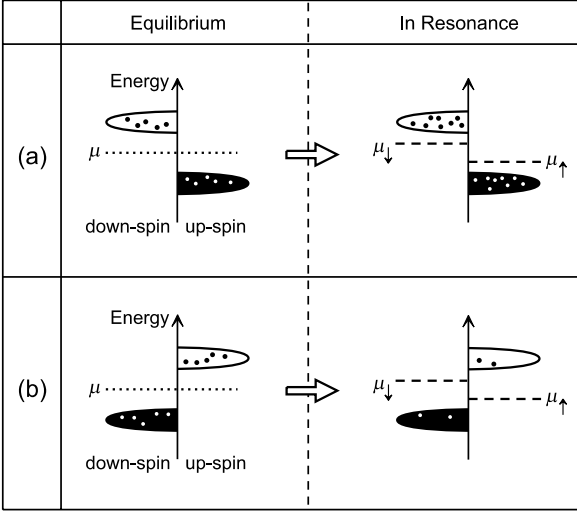


Fig. 2. Effect of the chemical-potential shift (a) for the standard LL configuration and (b) the specific LL configuration

Figure 1b shows positive $\Delta\rho_{xx}$ observed in the Si/SiGe heterostructure sample at $E_Z < \hbar\omega_c$ and $\nu = 2^1$ [6]. As illustrated in Fig. 1a, in this situation ESR excitation occurs from the filled LL($\uparrow, 0$) to the empty LL($\downarrow, 0$). There are two effects that can cause positive $\Delta\rho_{xx}$. First, since the spin population is changed by the spin-flip, μ_{\downarrow} increases while μ_{\uparrow} decreases from their equilibrium value μ , as illustrated in Fig. 2a. Since μ_{\downarrow} and μ_{\uparrow} get closer to $E_{\downarrow,0}$ and $E_{\uparrow,0}$, respectively, ρ_{xx} increases. Secondly, T_e increases by the resonant-energy absorption of the 2D electron system (2DES). This can also be the cause of the positive $\Delta\rho_{xx}$. Indeed, positive $\Delta\rho_{xx}$ observed in GaAs/AlGaAs heterostructures have been discussed in terms of electron heating [7]. Since these two effects can both cause positive $\Delta\rho_{xx}$, it has been difficult to determine the origin in the standard LL configuration.

To overcome the difficulty, we located μ below a spin-down LL and above a spin-up LL as illustrated in Fig. 2b. In this case, by their upward and downward shift from μ , μ_{\downarrow} and μ_{\uparrow} get away from their nearest LLs and ρ_{xx} decreases. Hence, the effect of the shift in μ_{\downarrow} and μ_{\uparrow} can be distinguished from the electron heating effect, in contrast to the case of the standard LL configuration.

Figure 3a illustrates the “specific” LL configuration adopted in our measurements [6]. Thermally excited holes in LL($\downarrow, 0$) and electrons in LL($\uparrow, 2$) cause finite ρ_{xx} . For the ESR excitation to occur, there must be more spin-up LLs than spin-down LLs below μ . To meet this requirement, we located not only LL($\uparrow, 0$) but also LL($\uparrow, 1$) below LL($\downarrow, 0$) by increasing $E_Z/\hbar\omega_c$. Since

¹ Note that the twofold valley degeneracy $g_v = 2$ remains in 2DESs formed in Si (001) quantum wells. At $\nu = 2$, μ lies between the spin-split LLs with $n = 0$ as in the case of $\nu = 1$ in GaAs/AlGaAs heterostructures.

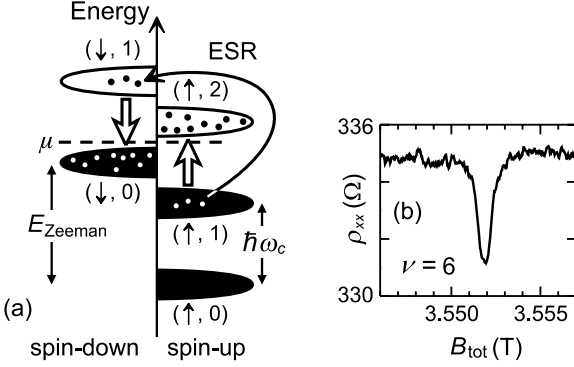


Fig. 3. (a) ESR-induced carrier dynamics and (b) the observed ESR signal in the specific LL configuration [6]

E_Z and $\hbar\omega_c$ are proportional to B_{tot} and B_{\perp} , respectively, we can control the ratio $E_Z/\hbar\omega_c = (|g^*|m^*/2m_0)(B_{\text{tot}}/B_{\perp})$ by tilting the sample in a magnetic field. Although $E_Z < \hbar\omega_c$ for $B_{\text{tot}}/B_{\perp} = 1$, the hierarchy between E_Z and $\hbar\omega_c$ can be inverted by increasing B_{tot}/B_{\perp} if we choose a host material with relatively large $|g^*|m^*$ such as Si. The realization of the specific LL configuration was confirmed by the B_{tot}/B_{\perp} dependence of Shubnikov–de Haas oscillations.

As shown in Fig. 3b, the ESR signal was observed as negative $\Delta\rho_{xx}$ in the specific LL configuration. Negative $\Delta\rho_{xx}$ cannot be caused by electron heating because $\partial\rho_{xx}/\partial T$ is positive. To explain it, we discuss the ESR-induced carrier dynamics shown in Fig. 3a. Since the orbital index n does not change during the spin-flip, the photoexcitation occurs mainly from the filled LL($\uparrow, 1$) to the empty LL($\downarrow, 1$). When the longitudinal spin-relaxation time T_1 is much longer than the electron–lattice relaxation time τ_{e-1} , photoexcited electrons in LL($\downarrow, 1$) and holes in LL($\uparrow, 1$) relax to LL($\downarrow, 0$) and LL($\uparrow, 2$), respectively. The total number of conduction carriers is reduced by the recombination of photoexcited carriers with thermally activated carriers. The negative $\Delta\rho_{xx}$ can be understood as a consequence of the upward and downward shift of μ_{\downarrow} and μ_{\uparrow} . We consider that the effect of the chemical potential shift dominates in $\Delta\rho_{xx}$ as far as $T_1 \gg \tau_{e-1}$.

To discuss heat flow in the steady state, we show a generalized schematic diagram in Fig. 4. A similar heat-bath model has been proposed to understand the nuclear-spin relaxation in solid ^3He systems where exchange motion of atoms caused by the quantum effect dominates the nuclear magnetism.² We consider that the Zeeman energy can flow to the lattice mainly via the 2D orbital motion of electrons because T_1 of electrons bound to donors in bulk silicon is extremely long [9, 10]. As discussed in Sect. 2, the Rashba interaction couples the Zeeman system to the orbital system in a 2DES formed in an asymmetric potential well although it is not strong in silicon 2DESs [11]. The electron–electron interaction conserves the Zeeman energy, while it

² For a review, see [8].

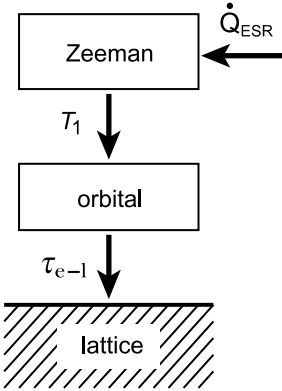


Fig. 4. Schematic heat-flow diagram

is expected to contribute to thermalization in the orbital system. Assuming that T_1 is much longer than τ_{e-1} , the ESR absorption increases the Zeeman energy without a significant increase in the temperature of the orbital system.

2 Determination of Spin-Relaxation Times

One of the most representative applications of ESR is the determination of spin-relaxation times. This has recently become increasingly important especially in the context of spintronics applications, to which long spin-relaxation times are critical [12].³ To attain long spin-relaxation times, Si appears to be a suitable host material. For its weak spin-orbit and electron–nuclear spin interactions, electron spin in Si is strongly isolated from the surroundings. Silicon has the further advantage that knowledge and resources accumulated in the traditional silicon electronics can be fully exploited. Recently, both T_1 and T_2 of the order of μs were reported in ESR measurements made on 2DESS formed in Si quantum wells [14–16]. The measurements were restricted to the frequency of 9.4 GHz (corresponding to the resonance field of $B \simeq 0.34$ T) because they were made with X-band ESR spectrometers. To present a clear guideline for device applications, methodological breakthroughs are highly desired to measure spin-relaxation times in a wide measurement environment. In this section we demonstrate a novel analysis of electrically detected ESR signals to obtain spin-relaxation times [6]. By applying it to the high-mobility Si/SiGe heterostructure sample in a strong magnetic field, we show that longitudinal spin relaxation is strongly suppressed by the combination of high-frequency spin precession and weak orbital scattering.

We begin by introducing the strong dependence of the resistivity ρ on the spin polarization P in silicon 2DESS, which here plays a key role. Since the

³ For a review, see [13].

first report of a metal–insulator transition at zero magnetic field in a high-mobility Si-MOSFET (metal oxide semiconductor field effect transistor) [17], transport properties of silicon 2DESs have been actively studied for the last decade.⁴ It is well known that strong positive inplane magnetoresistance is observed in silicon 2DESs [19–21]. Because the magnetic field B_{\parallel} applied parallel to the 2D plane does not directly affect the 2D orbital motion of electrons, the observed positive B_{\parallel} dependence of ρ is attributed to the spin polarization of 2DESs [22].

Figure 5a shows negative $\Delta\rho$ observed in the inplane magnetic field configuration. Electron heating cannot cause negative $\Delta\rho$ because $\partial\rho/\partial T$ is positive.⁵ As illustrated in Fig. 5b, the photoexcited carriers are expected to relax their energy immediately to the lattice without spin relaxation, as in the specific LL configuration discussed in Sect. 1. By the upward (downward) shift of μ_{\downarrow} (μ_{\uparrow}), the spin polarization P is reduced. The negative $\Delta\rho$ is understood as a consequence of the reduction ΔP of P because $\partial\rho/\partial P$ is positive.

We directly obtain ΔP from $\Delta\rho$ by $\Delta\rho = (\partial\rho/\partial P)\Delta P$. The relation between ρ and P can be calibrated by using the inplane magnetoresistance $\rho(B_{\parallel})$ in the absence of radiation. Figure 5c shows an example. Thanks to the constant density of states for the inplane magnetic-field configuration ($B_{\perp} = 0$), P is given as a function of B_{\parallel} and T . Calculations yield

$$P = \frac{k_{\text{B}}T_{\text{e}}}{E_{\text{F}}} \ln \left[\frac{1 + e^{(\mu + E_{\text{Z}})/k_{\text{B}}T_{\text{e}}}}{1 + e^{\mu/k_{\text{B}}T_{\text{e}}}} \right], \quad (2)$$

where

$$\mu = k_{\text{B}}T_{\text{e}} \ln \left[-1 - e^{-E_{\text{Z}}/k_{\text{B}}T_{\text{e}}} + \sqrt{(1 - e^{-E_{\text{Z}}/k_{\text{B}}T_{\text{e}}})^2 + 4e^{(E_{\text{F}} - E_{\text{Z}})/k_{\text{B}}T_{\text{e}}}} \right] \quad (3)$$

is the equilibrium chemical potential for spin-down electrons, $E_{\text{Z}} = g^* \mu_{\text{B}} B_{\parallel}$ is the Zeeman splitting energy, and $E_{\text{F}} = 2\pi\hbar^2 N_{\text{s}}/g_{\text{v}} m^*$ is the Fermi energy at the full spin polarization (N_{s} is the 2D electron concentration).⁶ The upper horizontal axis of Fig. 5c shows P calculated from (2) and (3) for $T_{\text{e}} = 0$. The magnetoresistance shows a sharp kink at the full spin polarization ($P = 1$), ensuring that the increase in ρ is caused mainly by the spin polarization. By using obtained $\partial\rho/\partial P$, $\Delta\rho$ is transformed into ΔP , as shown in the right vertical axis of Fig. 5a.

To derive T_1 and T_2 from the B_{\parallel} dependence of ΔP , we consider the balance between spin excitation and relaxation in the steady state under

⁴ For a review, see [18].

⁵ The metallic T dependence of ρ survives in a strong B_{\parallel} in 2DESs formed in high-mobility Si quantum wells, while it is suppressed by B_{\parallel} in 2DESs in Si-MOS structures and 2D hole systems in GaAs/AlGaAs heterostructures [21].

⁶ In the calculation, the enhancements of $|g^*|$ and m^* due to the carrier-correlation effect [22, 23] are taken into account. For $T_{\text{e}} = 0$, (2) and (3) give $P = E_{\text{Z}}/E_{\text{F}}$ and $\mu = (E_{\text{F}} - E_{\text{Z}})/2$.

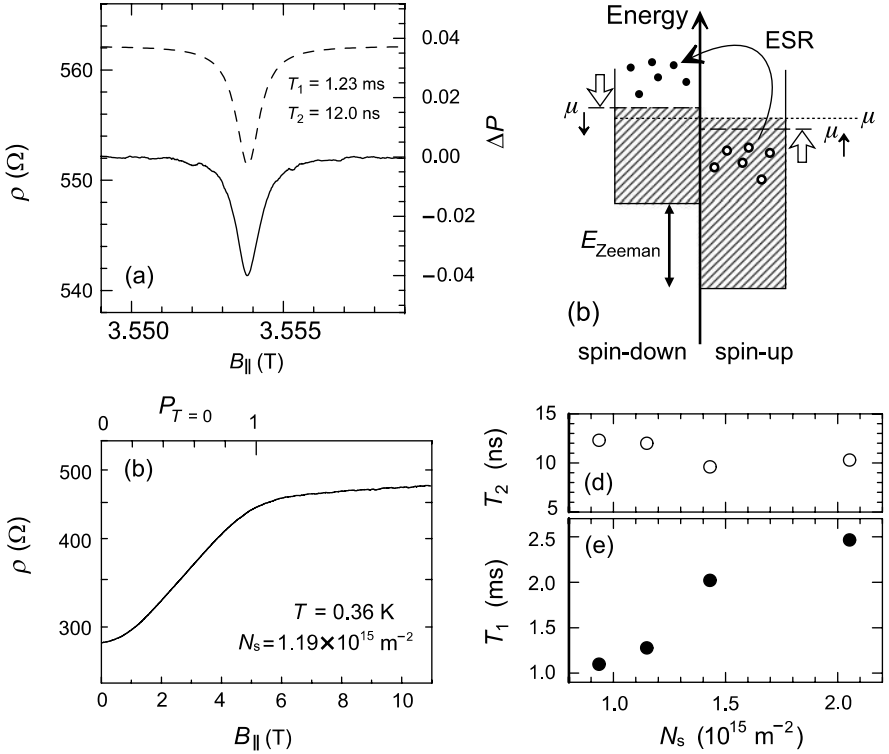


Fig. 5. (a) Observed ESR signal (*solid line*) and the result of fitting by (7) (*dashed line*, shifted in vertical direction for clarity) in the inplane magnetic-field configuration. *Right vertical axis* shows the transformation of $\Delta\rho$ into ΔP . (b) ESR-induced carrier dynamics in an inplane magnetic field [6]. (c) Inplane magnetoresistance observed in the Si/SiGe heterostructure sample. *Upper horizontal axis* shows P calculated from (2) and (3). (d), (e) Spin-relaxation times T_2 and T_1 vs. N_s obtained in the inplane magnetic field of 3.55 T [6]

continuous-wave excitation. For this purpose, it is convenient to define a coordinate system (x', y', z) rotating about the z -axis (taken along the external magnetic field B_{\parallel}) at the frequency ω of the oscillating magnetic field. In the rotating frame the oscillating magnetic field can be expressed as a static magnetic field B_1 along the x' -axis, and B_{\parallel} shrinks to $B_{\parallel} - \omega/\gamma$, where γ is the gyromagnetic ratio. The value of B_1 can be roughly estimated from its relationship $B_1 \sim E_1 n_{\text{Si}}/c$ to the amplitude of the oscillating electric field E_1 , where n_{Si} is the refractive index of silicon and c is the speed of light. We obtain E_1 from electron cyclotron resonance absorption measurements made in a perpendicular static magnetic field [24]. For example, $B_1 = 0.8 \mu\text{T}$ for a millimeter-wave output power of 19 mW. Assuming that spin relaxation can be simply characterized by two parameters T_1 and T_2 , the time evolution of

the magnetization \mathbf{M} is described by the Bloch equations as follows [25];

$$\frac{dM_{x'}}{dt} = (\gamma B_{\parallel} - \omega)M_{y'} - \frac{M_{x'}}{T_2}, \quad (4)$$

$$\frac{dM_{y'}}{dt} = \gamma B_{\perp} M_z - (\gamma B_{\parallel} - \omega)M_{x'} - \frac{M_{y'}}{T_2}, \quad (5)$$

$$\frac{dM_z}{dt} = -\gamma B_{\perp} M_{y'} - \frac{M_z - M_0}{T_1}. \quad (6)$$

Here, M_0 is the equilibrium value of M_z and $(M_z - M_0)/M_0$ is identified with $\Delta P/P$. By solving (4)–(6) for the steady state ($d\mathbf{M}/dt = 0$) under weak excitation ($(M_z - M_0)/M_0 \ll 1$), the B_{\parallel} dependence of ΔP is related to T_1 and T_2 as

$$\frac{\Delta P}{P} = \frac{M_z - M_0}{M_0} = -\frac{\gamma^2 B_{\perp}^2 T_1 T_2}{1 + (\omega - \gamma B_{\parallel})^2 T_2^2}. \quad (7)$$

The dashed line in Fig. 5a shows the result of fitting by (7). The observed ESR signals have Lorentzian lineshapes and are well fitted by (7). As can be seen from (7), T_1 and T_2 can be obtained from the amplitude and linewidth of the ESR signals, respectively. Figures 5d and e show the obtained T_1 and T_2 as a function of N_s . In the experimental range of T and N_s , T_1 was estimated to be of the order of 1 ms, whereas T_2 was about 10 ns. No significant T dependence was found in T_1 and T_2 in the range of 2 to 6 K.

The obtained values of T_1 and T_2 sharply contrast with those reported in earlier measurements on lower-mobility Si quantum wells in low magnetic fields ($B \simeq 0.34$ T), in which both T_1 and T_2 were found to be of the order of μs [14–16]. The values $T_1 \sim 1$ ms obtained here are by far the longest values ever reported for 2D systems as far as we know. The very long T_1 indicates that longitudinal spin relaxation is strongly suppressed in the high-mobility silicon 2DES under a strong magnetic field.

Spin relaxation in 2DESs formed in Si/SiGe heterostructures is considered to be caused chiefly by the Rashba fields, which arise from the asymmetry of quantum-well structures [15, 16, 26]. As illustrated in Fig. 6, the Si quantum well is sandwiched between positively charged Sb ions in the doped layer and negatively charged acceptors in the p-type substrate. Electrons feel an effective electric field \mathbf{E}_{eff} perpendicular to the 2D plane. In the coordinate system moving along with the electrons, the perpendicular electric field is transformed into effective magnetic fields $\mathbf{B}_{\text{R}} = \alpha \mathbf{k}_{\text{F}} \times \mathbf{E}_{\text{eff}}$ distributed isotropically in the 2D plane, which are the so-called Rashba fields [27]. Here, \mathbf{k}_{F} is the Fermi wavevector of electrons. In Si 2DESs, the Rashba parameter α is three orders of magnitude smaller than that in 2D systems based on III–V semiconductors [11].

Spin relaxation due to the Rashba fields can be treated by following the standard procedures given in a textbook [25]. The relaxation terms $M_{x'}/T_2$, $M_{y'}/T_2$, and $(M_z - M_0)/T_1$ in the Bloch equations (4)–(6) are reproduced

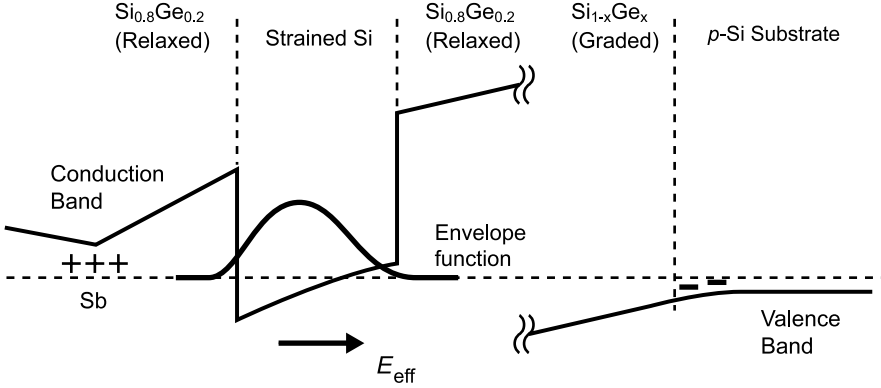


Fig. 6. Band diagram of the Si/SiGe heterostructure

by considering the Rashba perturbation Hamiltonian to second order. The spin-relaxation rates $1/T_1$ and $1/T_2$ are written as

$$\frac{1}{T_1} = \gamma^2 \int_{-\infty}^{\infty} G(t) \cos(\omega_L t) dt, \quad (8)$$

$$\frac{1}{T_2} = \gamma^2 \int_{-\infty}^{\infty} G(t) dt + \frac{1}{2T_1}, \quad (9)$$

where

$$G(t) = \overline{B_R^i(t) B_R^i(0)} \quad (i = x, z) \quad (10)$$

is the correlation function of the Rashba fields and $\omega_L = \gamma B_{\parallel}$ is the Larmor frequency (x -axis is taken in the 2D plane). We can see from (8) and (9) that $1/T_1$ and $1/T_2$ are given by the Fourier transform of $G(t)$ at frequencies ω_L and 0, respectively. This is because the static z -component of \mathbf{B}_R causes spin precession to be faster or slower, while the x -component oscillating at ω_L (static in the rotating frame) causes a change in the longitudinal spin component.

Since the Rashba fields change their direction as electrons are scattered, $G(t)$ decays monotonically with time. The decay time τ_c of $G(t)$ is roughly estimated⁷ from the momentum scattering time $\tau_m = m^*/N_s e^2 \rho$. The longitudinal spin-relaxation rate $1/T_1$, which is given by the Fourier transform of $G(t)$ at ω_L , decreases with increasing ω_L . Figure 7 depicts how longitudinal spin relaxation is suppressed by spin precession. When spin precession is slower than the decay of $G(t)$ ($\omega_L \tau_c \ll 1$), the suppression is weak. This is consistent with the fact that T_1 and T_2 of the same order have been reported in previous works on lower-mobility Si/SiGe samples in low magnetic fields where $\omega_L \tau_c \sim 1$ [14–16]. Under high-frequency spin precession $\omega_L \tau_c \gg 1$, on

⁷ For the accurate estimation of τ_c , e-e scattering, which does not contribute to the momentum scattering time, should also be considered [13].

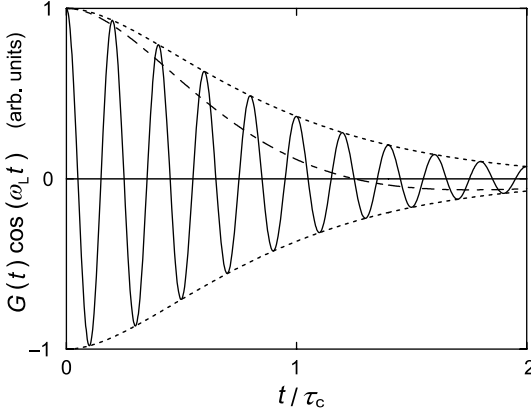


Fig. 7. $G(t) \cos(\omega_L t)$ as a function of time for $\omega_L \tau_c = 0.2$ (dashed line) and 5 (solid line)

the other hand, most of the contribution from the integrand in (8) canceled out by the oscillations of $\cos(\omega_L t)$, and longitudinal spin relaxation is strongly suppressed. This qualitatively explains the large $T_1/T_2 \sim 10^5$ obtained in the high-mobility sample located in a high magnetic field. We consider that high-frequency spin precession, together with weak orbital scattering, results in the extremely long T_1 of ~ 1 ms.

To derive explicit expressions for T_1 and T_2 , we need to assume an actual expression for $G(t)$. When B_R^i ($i = x, z$) randomly take two discrete values $\pm B_R$, $G(t)$ shows a single exponential decay $G(t) = G(0)\exp(-|t|/\tau_c)$. In this case the suppression is given by $T_1/T_2 = 1 + \omega_L^2 \tau_c^2$ [25, 26]. However, the above assumption cannot be a good approximation for high-mobility 2DESs, in which the dominant scattering mechanism is the small-angle scattering caused by remote ionized dopants. To discuss the issue quantitatively, further systematic studies are required both experimentally and theoretically.

In the presence of B_\perp , an additional term $\cos(\omega_c t)$ is multiplied to the integrands of (8) and (9) because \mathbf{B}_R change their direction periodically at frequency ω_c by the cyclotron motion of electrons. It is interesting to ask how spin relaxation is described in quantum Hall systems, in which the cyclotron motion is quantized by the strong B_\perp . Although there have been several theoretical works concerning this point [28–30], so far T_1 has not been measured in quantum Hall systems. Determination of T_1 in the quantum Hall regime is in principle possible by applying the analysis presented in this chapter. This is an issue for further studies.

References

1. D. Stein, K. v. Klitzing, G. Weimann, Phys. Rev. Lett. **51**, 130 (1983) 129

2. M. Dobers, K. v. Klitzing, G. Weimann, Phys. Rev. B **38**, 5453 (1988) 129
3. H.W. Jiang, E. Yablonovitch, Phys. Rev. B **64**, 041307(R) (2001) 129
4. M. Dobers, K. v. Klitzing, J. Schneider, G. Weimann, K. Ploog, Phys. Rev. Lett. **61**, 1650 (1988) 129
5. A. Berg, M. Dobers, R.R. Gerhardts, K. v. Klitzing, Phys. Rev. Lett. **64**, 2563 (1990) 129
6. J. Matsunami, M. Ooya, T. Okamoto, Phys. Rev. Lett. **97**, 066602 (2006) 130, 131, 132, 133, 135
7. R. Meisels, Semicond. Sci. Technol. **20**, R1 (2005) 131
8. R.A. Guyer, R.C. Richardson, L.I. Zane, Rev. Mod. Phys. **43**, 532 (1971) 132
9. H. Honig, E. Stupp, Phys. Rev. Lett. **1**, 275 (1958) 132
10. G. Feher, E.A. Gere, Phys. Rev. **114**, 1245 (1959) 132
11. Z. Wilamowski, W. Jantsch, H. Malissa, U. Rössler, Phys. Rev. B **66**, 195315 (2002) 132, 136
12. D.D. Awschalom, D. Loss, N. Samarth (eds.), *Semiconductor Spintronics and Quantum Computation* (Springer, Berlin, 2002) 133
13. I. Žutić, J. Fabian, S. Das Sarma, Rev. Mod. Phys. **76**, 323 (2004) 133, 137
14. C.F.O. Graeff, M.S. Brandt, M. Stutzmann, M. Holzmann, G. Abstreiter, F. Schäffler, Phys. Rev. B **59**, 213242 (1999) 133, 136, 137
15. Z. Wilamowski, W. Jantsch, Phys. Rev. B **69**, 035328 (2004) 133, 136, 137
16. A.M. Tyryshkin, S.A. Lyon, W. Jantsch, F. Schäffler, Phys. Rev. Lett. **94**, 126802 (2005) 133, 136, 137
17. S.V. Kravchenko, G.V. Kravchenko, J.E. Furneaux, V.M. Pudalov, M. D'Iorio, Phys. Rev. B **50**, 8039 (1994) 134
18. E. Abrahams, S.V. Kravchenko, M.P. Sarachik, Rev. Mod. Phys. **73**, 251 (2001) 134
19. T. Okamoto, S. Kawaji, J. Phys. Soc. Jpn. **65**, 3716 (1996) 134
20. T. Okamoto, S. Kawaji, Phys. Rev. B **57**, 9097 (1998) 134
21. T. Okamoto, M. Ooya, K. Hosoya, S. Kawaji, Phys. Rev. B **69**, 041202(R) (2004) 134
22. T. Okamoto, K. Hosoya, S. Kawaji, A. Yagi, Phys. Rev. Lett. **82**, 3875 (1999) 134
23. V.M. Pudalov, M.E. Gershenson, H. Kojima, N. Butch, E.M. Dizhur, G. Brunthaler, A. Prinz, G. Bauer, Phys. Rev. Lett. **88**, 196404 (2002) 134
24. M. Ooya, J. Matsunami, T. Okamoto (unpublished) 135
25. C.P. Slichter, *Principles of Magnetic Resonance*, 3rd edn. (Springer, Berlin, 1990) 136, 138
26. C. Tahan, R. Joynt, Phys. Rev. B **71**, 075315 (2005) 136, 138
27. Yu.A. Bychkov, E.I. Rashba, J. Phys. C **17**, 6039 (1984) 136
28. D.M. Frenkel, Phys. Rev. B **43**, 14228 (1991) 138

29. W. Apel, Yu.A. Bychkov, Phys. Rev. Lett. **82**, 3324 (1999) 138
30. A.A. Burkov, L. Balents, Phys. Rev. B **69**, 245312 (2004) 138

Index

- | | |
|---|--|
| 2D electron system (2DES), 131 | Rashba fields, 136 |
| electrically detected electron-spin
resonance (ESR), 129 | Si/SiGe heterostructure, 130
spin-flip, 131
spin-relaxation time, 133
spintronics applications, 133 |
| quantum Hall systems, 129 | |

Quantitative Treatment of Decoherence

Leonid Fedichkin and Vladimir Privman

Center for Quantum Device Technology, Department of Physics and Department of Electrical and Computer Engineering, Clarkson University, Potsdam, NY 13699-5721, USA

Abstract. We review several approaches to define and quantify decoherence. We find that a measure based on a norm of deviation of the density matrix is appropriate for quantifying decoherence for quantum registers. For a semiconductor double quantum-dot charge qubit, evaluation of this measure is presented. For a general class of decoherence processes, including those occurring in semiconductor qubits, we establish that this measure is additive: It scales linearly with the number of qubits in the quantum register.

1 Introduction

Decoherence [1–19] is an important physical phenomenon occurring inevitably in most experiments dealing with quantum objects. It is usually defined as a process whereby the physical system of interest interacts with the environment or other larger system with complex structure and, because of this interaction, changes its evolution from unperturbed, coherent internal dynamics. In some sense, the information about the initial and subsequent states of system undergoing decoherence is leaking into the outer world: The system is no longer described by a wavefunction, but rather by the statistical density matrix [20–24]. The quantum-wavefunction description only applies to the total system, including the environmental modes, which has many more degrees-of-freedom. Because of the importance of quantum coherence for quantum information processing [25–66], quantitative characterization of decoherence has become an active research field with many open problems.

Since quantum information processing requires maintaining high levels of coherence, emphasis has recently shifted from large-time system dynamics at experimentally better studied coherence-decay timescales to almost perfectly coherent dynamics at much shorter times. Many quantum systems proposed as candidates for qubits (quantum bits) for practical realizations of quantum computing require quantitative evaluation of their coherence. In other words, a single measure characterizing decoherence is desirable for comparison of different qubit designs and their optimization. Besides the evaluation of single-qubit performance one also has to analyze scaling of decoherence as the register size (the number of qubits involved) increases. Direct quantitative calculations of decoherence of even few-qubit quantum registers are

not feasible. Therefore, a practical approach has been to explore quantitative single-parameter measures of decoherence [67], develop techniques to calculate such measures at least approximately for realistic one- and two-qubit systems [68, 69], and then establish scaling (additivity [70, 71]) for multi-qubit quantum systems.

In Sect. 2, we outline different approaches to define and quantify decoherence. We argue that a measure based on a properly defined norm of deviation of the density matrix is appropriate for quantifying decoherence in quantum registers. For a semiconductor double quantum-dot qubit, evaluation of this measure is reviewed in Sect. 3. For a general class of decoherence processes, including those occurring in semiconductor qubits considered in Sect. 3, we argue, in Sect. 4, that this measure is additive. Thus, the level of quantum noise scales linearly with the number of qubits.

2 Measures of Decoherence

In this section, we consider briefly several approaches to quantifying the degree of decoherence due to interactions with the environment. In Sect. 2.1, we discuss the approach based on the asymptotic relaxation timescales. The entropy and idempotency-defect measures are reviewed in Sect. 2.2. The fidelity measure of decoherence is considered in Sect. 2.3. In Sect. 2.4, we review our results on the operator norm measures of decoherence. Section 2.5 discusses an approach to eliminate the initial-state dependence of the decoherence measures.

2.1 Relaxation Timescales

Decoherence of quantum systems is frequently characterized by the asymptotic rates at which they reach thermal equilibrium at temperature T . One of the reasons for focusing on relaxation rates is that long-time behavior is relatively easy to observe in ensemble experiments. Markovian approximation schemes typically yield an exponential approach to the limiting values of the density matrix elements for large times [21–23]. For a two-state system, this defines the timescales T_1 and T_2 , associated, respectively, with the approach by the diagonal (thermalization) and offdiagonal (dephasing, decoherence) density-matrix elements to their limiting values. More generally, for large times we approximate deviations from stationary values of diagonal and offdiagonal density matrix elements as

$$\begin{aligned}\rho_{kk}(t) - \rho_{kk}(\infty) &\propto e^{-t/T_{kk}}, & (1) \\ \rho_{jk}(t) &\propto e^{-t/T_{jk}} \quad (j \neq k). & (2)\end{aligned}$$

The shortest time among T_{kk} is often identified as T_1 . Similarly, T_2 can be defined as the shortest time among $T_{n \neq m}$. These definitions yield the characteristic times of thermalization and decoherence (dephasing).

For candidate systems for quantum computing realizations, noise effects are commonly reduced by working at very low temperatures and making their structure features nanosize for strong quantization. Then, for the decoherence and thermalization times we have, $T_2 \ll T_1$, e.g., [21]. Therefore, the decoherence time is a more crucial parameter for quantum computing considerations. The timescale T_2 is compared to the “clock” times of quantum control, i.e., the quantum gate functions, T_g , in order to ensure the fault-tolerant error correction criterion $T_g/T_2 \leq O(10^{-4})$, e.g., [66].

The disadvantages of this type of analysis are that the exponential behavior of the density matrix elements in the energy basis is applicable only for large times, whereas for quantum computing applications, the short-time behavior is usually relevant [18]. Moreover, while the energy basis is natural for large times, the choice of the preferred basis is not obvious for short and intermediate times [18, 72]. Therefore, the timescales T_1 and T_2 have limited applicability in evaluating quantum computing scalability.

2.2 Quantum Entropy

An alternative approach is to calculate the entropy [20] of the system,

$$S(t) = -\text{Tr}(\rho \ln \rho), \quad (3)$$

or the idempotency defect, also termed the first-order entropy [73–75],

$$s(t) = 1 - \text{Tr}(\rho^2). \quad (4)$$

Both expressions are basis independent, have a minimum at pure states and effectively describe the degree of the state’s “purity.” Any deviation from a pure state leads to the deviation from the minimal values, 0, for both measures,

$$S_{\text{pure state}}(t) = s_{\text{pure state}}(t) = 0. \quad (5)$$

2.3 Fidelity

Writing the total Hamiltonian as follows,

$$H = H_S + H_B + H_I, \quad (6)$$

where H_S is the term describing internal system dynamics, H_B governs the evolution of the environment, and H_I describes system–environment interaction, let us now define the fidelity [76, 77],

$$F(t) = \text{Tr}_S[\rho_{\text{ideal}}(t)\rho(t)]. \quad (7)$$

Here, the trace is over the system degrees-of-freedom, and $\rho_{\text{ideal}}(t)$ represents the pure-state evolution of the system under H_S only, without interaction with the environment ($H_I = 0$). In general, the Hamiltonian term H_S governing the system dynamics can be time dependent. For the sake of simplicity

throughout this review we restrict our analysis to constant H_S , since approximate evaluation of decoherence can be done [64] for qubits controlled by constant Hamiltonian. In this case

$$\rho_{\text{ideal}}(t) = e^{-iH_S t} \rho(0) e^{iH_S t}. \quad (8)$$

More sophisticated scenarios with qubits evolving under time-dependent H_S were considered in [78–80].

The fidelity provides a certain measure of decoherence in terms of the difference between the “real,” environmentally influenced, $\rho(t)$, evolution and the “free” evolution, $\rho_{\text{ideal}}(t)$. It will attain its maximal value, 1, only provided $\rho(t) = \rho_{\text{ideal}}(t)$. This property relies on the fact the $\rho_{\text{ideal}}(t)$ remains a projection operator (pure state) for all times $t \geq 0$.

As an illustrative example consider a two-level system decaying from the excited to the ground state, when there is no internal system dynamics,

$$\rho_{\text{ideal}}(t) = \begin{pmatrix} 0 & 0 \\ 0 & 1 \end{pmatrix}, \quad (9)$$

$$\rho(t) = \begin{pmatrix} 1 - e^{-\Gamma t} & 0 \\ 0 & e^{-\Gamma t} \end{pmatrix}, \quad (10)$$

and the fidelity is a monotonic function of time,

$$F(t) = e^{-\Gamma t}. \quad (11)$$

Note that the requirement that $\rho_{\text{ideal}}(t)$ is a pure-state (projection operator), excludes, in particular, any $T > 0$ thermalized state as the initial system state. For example, let us consider the application of the fidelity measure for the infinite-temperature initial state of our two-level system. We have

$$\rho(0) = \rho_{\text{ideal}}(t) = \begin{pmatrix} 1/2 & 0 \\ 0 & 1/2 \end{pmatrix}, \quad (12)$$

which is not a projection operator. The spontaneous-decay density matrix is then

$$\rho(t) = \begin{pmatrix} 1 - (e^{-\Gamma t}/2) & 0 \\ 0 & e^{-\Gamma t}/2 \end{pmatrix}. \quad (13)$$

The fidelity remains constant

$$F(t) = 1/2, \quad (14)$$

and it does not provide any information on the time dependence of the decay process.

2.4 Norm of Deviation

In this subsection we consider the operator norms [81] that measure the deviation of the system from the ideal state, to quantify the degree of decoherence as proposed in [67]. Such measures do not require the initial density matrix to be pure-state. We define the deviation according to

$$\sigma(t) \equiv \rho(t) - \rho_{\text{ideal}}(t). \quad (15)$$

We can use, for instance, the eigenvalue norm,

$$\|\sigma\|_{\lambda} = \max_i |\lambda_i|, \quad (16)$$

or the trace norm,

$$\|\sigma\|_{\text{Tr}} = \sum_i |\lambda_i|, \quad (17)$$

etc., where λ_i are the eigenvalues of the deviation operator (15). A more precise definition of the eigenvalue norm for a linear operator, A , is [81]

$$\|A\| = \sup_{\varphi \neq 0} \left[\frac{\langle \varphi | A^\dagger A | \varphi \rangle}{\langle \varphi | \varphi \rangle} \right]^{1/2}. \quad (18)$$

Since density operators are bounded, their norms, as well as the norm of the deviation, can always be evaluated. Furthermore, since the density operators are Hermitian, this definition obviously reduces to the eigenvalue norm (16). We also note that $\|A\| = 0$ implies that $A = 0$.

The calculation of these norms is sometimes simplified by the observation that $\sigma(t)$ is traceless. Specifically, for two-level systems, we get

$$\|\sigma\|_{\lambda} = \sqrt{|\sigma_{00}|^2 + |\sigma_{01}|^2} = \frac{1}{2} \|\sigma\|_{\text{Tr}}. \quad (19)$$

For our example of the two-level system undergoing spontaneous decay, the norm is

$$\|\sigma\|_{\lambda} = 1 - e^{-\Gamma t}. \quad (20)$$

2.5 Arbitrary Initial States

The measures considered in the preceding subsections quantify decoherence of a system provided its initial state is given. However, this is not always the case. In quantum computing, it is impractical to keep track of all the possible initial states for each quantum register, that might be needed for implementing a particular quantum algorithm. Furthermore, even the preparation of the initial state can introduce additional noise. Therefore, for evaluation of fault tolerance (scalability), it will be necessary to obtain an upper-bound estimate of decoherence for an arbitrary initial state.

To characterize decoherence for an arbitrary initial state, pure or mixed, we proposed [67] to use the maximal norm, D , which is determined as an

operator norm maximized over all initial density matrices. It is defined as the worst case scenario error,

$$D(t) = \sup_{\rho(0)} (\|\sigma(t, \rho(0))\|_{\lambda}). \quad (21)$$

For realistic two-level systems coupled to various types of environmental modes, the expressions of the maximal norm are surprisingly elegant and compact. They are usually monotonic and contain no oscillations due to the internal system dynamics, as, for example, are the results obtained for semiconductor quantum-dot qubits considered in the next section.

In summary, we have considered several approaches to quantifying decoherence: relaxation times, entropy and fidelity measures, and norms of deviation, and we defined the maximal measure that is not dependent on the initial state, and that will be later shown to be additive; see Sect. 4.

3 Decoherence of Double Quantum-Dot Charge Qubits

As a representative example, let us review evaluation of decoherence for semiconductor quantum dots. Quantum devices based on solid-state nanostructures have been among the major candidates for large-scale quantum computation because they can draw on existing advances in nanotechnology and materials processing [82]. Several designs of semiconductor quantum bits (qubits) were proposed [27, 28, 37, 41–44, 83–85]. In particular, the encoding of quantum information into spatial degrees of freedom of electrons placed in a quantum dot was considered in [41–44, 85]. A relatively fast decay of coherence of electron states in ordinary quantum dots, e.g., [26], can be partially suppressed by encoding quantum information in a subspace of electron states in specially designed arrays of quantum dots (artificial crystals), proposed in [86]. Actually, under certain conditions even double-dot systems in semiconductors can be relatively well protected against decoherence caused by their interactions with phonons and electromagnetic fields [38]. This observation was confirmed in recent experiments [45], which demonstrated coherent quantum oscillations of an electron in a double-dot structure.

Several designs of double-dot qubits have been explored in recent experiments [46–50] carried out at temperatures ranging from tens to hundreds of mK. The temperature dependence of relaxation rates in Si charge qubits was studied theoretically in [51, 52]. Recently, it has been pointed out [68] that in the zero-temperature limit and for conventional double-dot structures higher-order processes in electron–phonon interactions dominate decoherence.

In this section, we consider the acoustic phonon bath as the main source of decoherence for the considered type of qubit, which is supported by theoretical and experimental evidence, e.g., [38, 46]. Decoherence due to different sources, e.g., due to trapping center defects [87, 88], can play an important role in other situations.

In the next subsection, we outline the structure of double-dot qubits. Sections 3.2 and 3.3 are devoted to the consideration of the electron–phonon interaction for two realistic cases: In Sect. 3.2 we analyze the piezoacoustic interaction in crystals with zincblende lattice and with parabolic quantum dot confinement potential. Double dots with prevalence of piezointeraction have been fabricated [45] in gated GaAs/AlGaAs heterostructures. In Sect. 3.3 we study the deformation interaction with acoustic phonons in “quantum dots” formed by double impurities in semiconductors with inversion symmetry of elementary lattice cell. Experiments with the latter type of double-dot systems have been reported in [47, 48]. Finally, Sects. 3.4–3.7 present illustrative calculations of the noise level for selected quantum gates.

3.1 Model

We consider a double-dot structure sketched in Fig. 1. It consists of two quantum dots coupled to each other via a tunneling barrier and containing a single electron hopping between the dots. We limit our consideration to double-dot structures in which the energy required to transfer to the upper levels is much higher than the lattice temperature and energy spacing between the two lowest levels.

The electron is considered to be in a superposition of two basis states, $|0\rangle$ and $|1\rangle$,

$$\psi = \alpha\psi_0 + \beta\psi_1. \quad (22)$$

The states that define the “logical” basis are not the physical ground and first excited state of the double-dot system. Instead, ψ_0 (the “0” state of the qubit) is chosen to be localized at the first quantum dot and, to a zeroth-order approximation, be similar to the ground state of that dot if it were isolated. Similarly, ψ_1 (the “1” state) resembles the ground state of the second dot (if it were isolated). This assumes that the dots are sufficiently (but not necessarily exactly) symmetric. We denote the coordinates of the potential minima of the dots (dot centers) as vectors \mathbf{R}_0 and \mathbf{R}_1 , respectively. The distance between the dot centers is

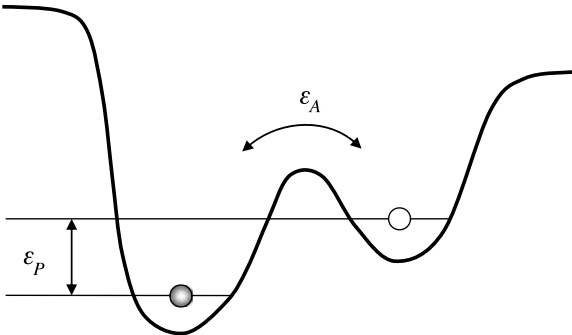


Fig. 1. Electron in a double-well potential

$$L \equiv |\mathbf{L}| \equiv |\mathbf{R}_1 - \mathbf{R}_0|. \quad (23)$$

The Hamiltonian of an electron within a phonon environment is given by

$$H = H_e + H_p + H_{ep}. \quad (24)$$

The electron term is

$$H_e = -\frac{1}{2}\varepsilon_A(t)\sigma_x - \frac{1}{2}\varepsilon_P(t)\sigma_z, \quad (25)$$

where σ_x and σ_z are Pauli matrices, whereas $\varepsilon_A(t)$ and $\varepsilon_P(t)$ can be time dependent, as determined by unitary single-qubit quantum gate functions that are carried out. They can be controlled externally by adjusting the potential on the control electrodes (gates) surrounding the double-dot system. For constant ε_A and ε_P , the energy splitting between the electron energy levels is

$$\varepsilon = \sqrt{\varepsilon_A^2 + \varepsilon_P^2}. \quad (26)$$

The Hamiltonian of the phonon bath is described by

$$H_p = \sum_{\mathbf{q},\lambda} \hbar\omega_q b_{\mathbf{q},\lambda}^\dagger b_{\mathbf{q},\lambda}, \quad (27)$$

where $b_{\mathbf{q},\lambda}^\dagger$ and $b_{\mathbf{q},\lambda}$ are, respectively, the creation and annihilation operators of phonons characterized by the wavevector \mathbf{q} and polarization λ . We approximately assume isotropic acoustic phonons, with a linear dispersion,

$$\omega_q = sq, \quad (28)$$

where s is the speed of sound in the semiconductor material. In the next subsection we show that the electron–phonon interaction can be derived in the form

$$H_{ep} = \sum_{\mathbf{q},\lambda} \sigma_z (g_{\mathbf{q},\lambda} b_{\mathbf{q},\lambda}^\dagger + g_{\mathbf{q},\lambda}^* b_{\mathbf{q},\lambda}), \quad (29)$$

with the coupling constants $g_{\mathbf{q},\lambda}$ determined by the architecture of the double dot and the properties of the material crystal structure.

3.2 Piezoelectric Interaction

The derivation in this subsection follows [68, 69]. The piezoacoustic electron–phonon interaction [89] is described by

$$H_{ep} = i \sum_{\mathbf{q},\lambda} \left(\frac{\hbar}{2\rho s q V} \right)^{1/2} M_\lambda(\mathbf{q}) F(\mathbf{q}) (b_{\mathbf{q}} + b_{-\mathbf{q}}^\dagger). \quad (30)$$

Here, ρ is the density of the semiconductor material, V is the volume of semiconductor, and for the matrix element $M_\lambda(\mathbf{q})$, one can derive

$$M_\lambda(\mathbf{q}) = \frac{1}{2q^2} \sum_{ijk} (\xi_i q_j + \xi_j q_i) q_k M_{ijk}. \quad (31)$$

In this expression, ξ_j are the polarization vector components for polarization λ , while M_{ijk} express the electric field as a linear response to the stress,

$$E_k = \sum_{ij} M_{ijk} S_{ij}. \quad (32)$$

For a crystal with a zincblende lattice, exemplified by GaAs, the tensor M_{ijk} has only those components nonzero for which all three indexes i, j, k are different; furthermore, all these components are equal $M_{ijk} = M$. Thus, we have

$$M_\lambda(\mathbf{q}) = \frac{M}{q^2} (\xi_1 q_2 q_3 + \xi_2 q_1 q_3 + \xi_3 q_1 q_2). \quad (33)$$

The form factor $F(\mathbf{q})$ accounting for the fact that the electrons in the quantum-dot geometry are not plane waves, is

$$F(\mathbf{q}) = \sum_{j,k} c_j^\dagger c_k \int d^3r \phi_j^*(\mathbf{r}) \phi_k(\mathbf{r}) e^{-i\mathbf{q}\cdot\mathbf{r}}, \quad (34)$$

where c_k, c_j^\dagger are annihilation and creation operators of the basis states $k, j = 0, 1$. For gate-engineered quantum dots, we consider the ground states in each dot to have an approximately Gaussian shape

$$\phi_j(\mathbf{r}) = \frac{1}{a^{3/2} \pi^{3/4}} e^{-|\mathbf{r} - \mathbf{R}_j|^2 / 2a^2}, \quad (35)$$

where $2a$ is a characteristic size of the dots.

We assume that the distance between the dots, L , is sufficiently large compared to a , to ensure that the different dot wavefunctions do not overlap significantly,

$$\left| \int d^3r \phi_j^*(\mathbf{r}) \phi_k(\mathbf{r}) e^{-i\mathbf{q}\cdot\mathbf{r}} \right| \ll 1, \quad \text{for } j \neq k. \quad (36)$$

This implies that the coupling leading to tunneling between the dots is small, as is the case for the recently studied experimental structures [45–48], where the splitting due to tunneling, measured by ε_A , was below $20 \mu\text{eV}$, while the electron quantization energy in each dot was at least several meV.

For $j = k$, we obtain

$$\begin{aligned} \int d^3r \phi_j^*(\mathbf{r}) \phi_j(\mathbf{r}) e^{-i\mathbf{q}\cdot\mathbf{r}} &= \frac{1}{a^3 \pi^{3/2}} \int d^3r e^{-|\mathbf{r} - \mathbf{R}_j|^2 / a^2} e^{-i\mathbf{q}\cdot\mathbf{r}} \\ &= e^{-i\mathbf{q}\cdot\mathbf{R}_j} e^{-a^2 q^2 / 4}. \end{aligned} \quad (37)$$

The resulting form factor is

$$F(q) = e^{-a^2 q^2 / 4} e^{-i\mathbf{q}\cdot\mathbf{R}} (c_0^\dagger c_0 e^{i\mathbf{q}\cdot\mathbf{L}/2} + c_1^\dagger c_1 e^{-i\mathbf{q}\cdot\mathbf{L}/2}), \quad (38)$$

where $\mathbf{R} = (\mathbf{R}_0 + \mathbf{R}_1)/2$. Finally, we get

$$F(\mathbf{q}) = e^{-a^2 q^2/4} e^{-i\mathbf{q}\cdot\mathbf{R}} [\cos(\mathbf{q}\cdot\mathbf{L}/2)I + i \sin(\mathbf{q}\cdot\mathbf{L}/2)\sigma_z], \quad (39)$$

where I is the identity operator. Only the second term in (39), which is not proportional to I , represents an interaction affecting the qubit states. It leads to a Hamiltonian term of the form (29), with coupling constants

$$g_{\mathbf{q},\lambda} = - \left(\frac{\hbar}{2\rho q s V} \right)^{1/2} M e^{-a^2 q^2/4 - i\mathbf{q}\cdot\mathbf{R}} \times (\xi_1 e_2 e_3 + \xi_2 e_1 e_3 + \xi_3 e_1 e_2) \sin(\mathbf{q}\cdot\mathbf{L}/2), \quad (40)$$

where $e_k = q_k/q$.

3.3 Deformation Interaction

Deformation coupling with acoustic phonons [89] is described by

$$H_{\text{ep}} = \Xi \sum_{\mathbf{q},\lambda} \left(\frac{\hbar}{2\rho q s V} \right)^{1/2} q F(\mathbf{q}) (b_{\mathbf{q},\lambda}^\dagger + b_{-\mathbf{q},\lambda}), \quad (41)$$

where Ξ is a material-dependent constant termed the ‘‘deformation potential.’’

Here, we consider a particular double-dot-like nanostructure that has been the focus of recent experiments, due to advances in its fabrication [47, 48] by controlled single-ion implantation: A double-impurity Si structure with hydrogen-like electron confinement potentials at both impurities (P atoms). We consider a hydrogen-like impurity state,

$$\phi_i(r) = \frac{1}{a^{3/2} \pi^{1/2}} e^{-|r - \mathbf{R}_i|/a}, \quad (42)$$

where a is the effective Bohr radius. The form factor in this case is given by the following formula,

$$F(\mathbf{q}) = \frac{e^{-i\mathbf{q}\cdot\mathbf{R}}}{[1 + (a^2 q^2)/4]^2} [\cos(\mathbf{q}\cdot\mathbf{L}/2)I + i \sin(\mathbf{q}\cdot\mathbf{L}/2)\sigma_z]. \quad (43)$$

The interaction can then be expressed in the form (29), but with different coupling constants,

$$g_{\mathbf{q}} = i\Xi q \left(\frac{\hbar}{2\rho q s V} \right)^{1/2} \frac{e^{-i\mathbf{q}\cdot\mathbf{R}}}{[1 + (a^2 q^2)/4]^2} \sin(\mathbf{q}\cdot\mathbf{L}/2). \quad (44)$$

We note that (40) and (44) were obtained within the framework of the effective-mass approximation, which is well justified for the group III–V semiconductors, e.g., GaAs. For semiconductors with conduction-band degeneracies near the band minima, including the group IV semiconductor Si, the expression (44) can be viewed as representing the averaged behavior of a rapidly oscillating coupling constant vs. the phonon wavevector, as shown in

[90] in other contexts. These oscillations result from intervalley interference effects, but in our case they can be ignored. Indeed, in all our later calculations, specifically, (53) and (70) below, the squares of the intermediate expressions for the coupling constants enter in integrals over all the spectrum of the three-dimensional phonon modes. Therefore, we do not expect the results to be significantly modified by rapid oscillations introduced by the band-structure degeneracies.

3.4 Error Estimates During Gate Functions

In general, the ideal qubit evolution governed by the Hamiltonian term (25) is time dependent. Decoherence estimates for some solid-state systems with certain shapes of time dependence of the system Hamiltonian were reported recently [78–80]. However, such calculations are rather complicated. Actually, there is no need to consider all possible time-dependent controls of a qubit to evaluate its performance. All single-qubit rotations that are required for quantum algorithms can be successfully implemented by using two constant-Hamiltonian gates, e.g., amplitude rotation and phase shift [64]. To perform both of these gates one can keep the Hamiltonian term (25) constant during the implementation of each gate, adjusting the parameters ε_A and ε_P as appropriate for each gate and for the idling qubit in between gate functions.

In the following subsections we give specific examples: In Sect. 3.5, we will consider decoherence during the implementation of the NOT gate (an amplitude gate). A π -phase shift gate is considered in Sect. 3.6. Then, in Sect. 3.7 we discuss the overall noise level estimate for a qubit subject to gate control.

3.5 Relaxation During the NOT Gate

The quantum NOT gate is a unitary operator that transforms the states $|0\rangle$ and $|1\rangle$ into each other. Any superposition of $|0\rangle$ and $|1\rangle$ transforms accordingly,

$$\text{NOT}(x|0\rangle + y|1\rangle) = y|0\rangle + x|1\rangle. \quad (45)$$

The NOT gate can be implemented by properly choosing ε_A and ε_P in the Hamiltonian term (25). Specifically, with constant

$$\varepsilon_A = \varepsilon \quad (46)$$

and

$$\varepsilon_P = 0, \quad (47)$$

the “ideal” NOT gate function is carried out, with these interaction parameters, over the time interval $T_g = \tau$,

$$\tau = \frac{\pi\hbar}{\varepsilon}. \quad (48)$$

The dominant source of quantum noise for the double-dot qubit subject to the NOT-gate type coupling, is relaxation involving energy exchange with the phonon bath (i.e., emission and absorption of phonons). In this case it is more convenient to study the evolution of the density matrix in the energy basis, $\{|+\rangle, |-\rangle\}$, which for this symmetric case is

$$|\pm\rangle = (|0\rangle \pm |1\rangle)/\sqrt{2}. \quad (49)$$

Then, assuming that the time interval of interest is $[0, \tau]$, the qubit density matrix can be expressed [22] as follows (with “th” for thermal),

$$\rho(t) = \begin{pmatrix} \rho_{++}^{\text{th}} + [\rho_{++}(0) - \rho_{++}^{\text{th}}] e^{-\Gamma t} & \rho_{+-}(0) e^{-(\Gamma/2 - i\varepsilon/\hbar)t} \\ \rho_{-+}(0) e^{-(\Gamma/2 + i\varepsilon/\hbar)t} & \rho_{--}^{\text{th}} + [\rho_{--}(0) - \rho_{--}^{\text{th}}] e^{-\Gamma t} \end{pmatrix}. \quad (50)$$

This is the standard Markovian approximation for the evolution of the density matrix. For large times, this evolution would result in the thermal state, with the offdiagonal density matrix elements decaying to zero, while the diagonal ones approach the thermal values proportional to the Boltzmann factors corresponding to the energies $\pm\varepsilon/2$. However, we are only interested in such evolution for a short time interval, τ , of a NOT gate. The rate parameter Γ is the sum [22] of the phonon emission rate, W^e , and absorption rate, W^a ,

$$\Gamma = W^e + W^a. \quad (51)$$

The probability for the absorption of a phonon due to excitation from the ground state to the upper level is

$$w^\lambda = \frac{2\pi}{\hbar} |\langle f | H_{\text{ep}} | i \rangle|^2 \delta(\varepsilon - \hbar s q), \quad (52)$$

where $|i\rangle$ is the initial state with the extra phonon with energy $\hbar s q$ and $|f\rangle$ is the final state, \mathbf{q} is the wavevector, and λ is the phonon polarization. Thus, we have to calculate

$$W^a = \sum_{\mathbf{q}, \lambda} w^\lambda = \frac{V}{(2\pi)^3} \sum_{\lambda} \int d^3q w^\lambda. \quad (53)$$

For the interaction (29) one can derive

$$w^\lambda = \frac{2\pi}{\hbar} |g_{\mathbf{q}, \lambda}|^2 N^{\text{th}} \delta(\varepsilon - \hbar s q), \quad (54)$$

where

$$N^{\text{th}} = \frac{1}{\exp(\hbar s q / k_B T) - 1} \quad (55)$$

is the phonon occupation number at temperature T , and k_B is the Boltzmann constant.

For the piezoacoustic interaction, the coupling constant in (40) depends on the polarization. For longitudinal phonons, the polarization vector has Cartesian components, expressed in terms of the spherical-coordinate angles,

$$\xi_1^{\parallel} = e_1 = \sin \theta \cos \phi, \quad \xi_2^{\parallel} = e_2 = \sin \theta \sin \phi, \quad \xi_3^{\parallel} = e_3 = \cos \theta, \quad (56)$$

where $e_j = q_j/q$. For transverse phonons, it is convenient to define the two polarization vectors $\xi_i^{\perp 1}$ and $\xi_i^{\perp 2}$ to have

$$\xi_1^{\perp 1} = \sin \phi, \quad \xi_2^{\perp 1} = -\cos \phi, \quad \xi_3^{\perp 1} = 0, \quad (57)$$

$$\xi_1^{\perp 2} = -\cos \theta \cos \phi, \quad \xi_2^{\perp 2} = -\cos \theta \sin \phi, \quad \xi_3^{\perp 2} = \sin \theta. \quad (58)$$

Then, for longitudinal phonons, one obtains [69]

$$w^{\parallel} = \frac{\pi}{\rho s V q} M^2 e^{-a^2 q^2/4} \times 9 \sin^4 \theta \cos^2 \theta \sin^2 \phi \cos^2 \phi \sin^2(qL \cos \theta/2). \quad (59)$$

For transverse phonons, one gets

$$w^{\perp 1} = \frac{\pi}{\rho s V q} M^2 e^{-a^2 q^2/4} (-2 \sin \theta \cos^2 \theta \sin \phi \cos \phi + \sin^3 \theta \cos \phi \sin \phi)^2 \sin^2(qL \cos \theta/2), \quad (60)$$

$$w^{\perp 2} = \frac{\pi}{\rho s V q} M^2 e^{-a^2 q^2/4} (-2 \sin \theta \cos \theta \cos^2 \phi + \sin \theta \cos \theta \sin^2 \phi)^2 \sin^2(qL \cos \theta/2). \quad (61)$$

By combining these contributions and substituting them in (53), we get the probability of absorption of a phonon for all polarizations,

$$W_{\text{piezo}}^{\text{a}} = \frac{M^2}{20\pi\rho s^2\hbar L^5 k^4} \frac{\exp\left(-\frac{a^2 k^2}{2}\right)}{\exp\left(\frac{\hbar s k}{k_{\text{B}} T}\right) - 1} \times \left\{ (kL)^5 + 5kL[2(kL)^2 - 21] \cos(kL) + 15[7 - 3(kL)^2] \sin(kL) \right\}, \quad (62)$$

where

$$k = \frac{\varepsilon}{\hbar s} \quad (63)$$

is the wavevector of the absorbed phonon.

For the deformation interaction (44), one can obtain the following result,

$$w = \frac{\pi \Xi^2}{\rho s V} \frac{q}{[1 + (a^2 q^2)/4]^4} \sin^2(\mathbf{q} \cdot \mathbf{L}/2) \delta(\varepsilon - \hbar s q). \quad (64)$$

The total probability for a phonon absorption is

$$W_{\text{deform}}^{\text{a}} = \frac{\Xi^2}{4\pi\rho s^2\hbar} \frac{k^3}{(1 + a^2 k^2/4)^4} \frac{1 - \sin(kL)/(kL)}{\exp\left(\frac{\hbar s k}{k_{\text{B}} T}\right) - 1}. \quad (65)$$

Finally, the expressions for the phonon emission rates, W^{e} , can be obtained by multiplying the above expressions, (62) and (65), by $(N_{\text{th}} + 1)/N_{\text{th}}$.

3.6 Dephasing During a Phase Gate

The π gate is a unitary operator that does not change the absolute values of the probability amplitudes of a qubit in the superposition of the $|0\rangle$ and $|1\rangle$ basis states. It changes the relative phase between the probability amplitudes. Specifically, any superposition of $|0\rangle$ and $|1\rangle$ transforms according to

$$H(x|0\rangle + y|1\rangle) = x|0\rangle - y|1\rangle. \quad (66)$$

Over a time interval τ , the π gate can be carried out with constant interaction parameters,

$$\varepsilon_A = 0 \quad (67)$$

and

$$\varepsilon_P = \varepsilon = \frac{\pi\hbar}{\tau}. \quad (68)$$

In [68], double-dot qubit dynamics during implementation of phase gates was considered. The relaxation dynamics is suppressed during the π gate, because there is no tunneling between the dots. Quantum noise then results due to pure dephasing, i.e., via the decay of the offdiagonal qubit density matrix elements, while the diagonal density matrix elements remain constant. In the regime of pure dephasing, the qubit density matrix can be represented as [72, 91]

$$\rho(t) = \begin{pmatrix} \rho_{00}(0) & \rho_{01}(0)e^{-B^2(t)+i\varepsilon t/\hbar} \\ \rho_{10}(0)e^{-B^2(t)-i\varepsilon t/\hbar} & \rho_{11}(0) \end{pmatrix}, \quad (69)$$

with the spectral function,

$$\begin{aligned} B^2(t) &= \frac{8}{\hbar^2} \sum_{\mathbf{q}, \lambda} \frac{|g_{\mathbf{q}, \lambda}|^2}{\omega_q^2} \sin^2 \frac{\omega_q t}{2} \coth \frac{\hbar\omega_q}{2k_B T} \\ &= \frac{V}{\hbar^2 \pi^3} \int d^3 q \sum_{\lambda} \frac{|g_{\mathbf{q}, \lambda}|^2}{q^2 s^2} \sin^2 \frac{qst}{2} \coth \frac{\hbar qs}{2k_B T}. \end{aligned} \quad (70)$$

For the piezoelectric interaction, the coupling constant $g_{\mathbf{q}, \lambda}$ was obtained in (40), and the expression for the spectral function takes the form

$$\begin{aligned} B_{\text{piezo}}^2(t) &= \frac{M^2}{2\pi^3 \hbar \rho s^3} \int_0^\infty q^2 dq \int_0^\pi \sin \theta d\theta \int_0^{2\pi} d\varphi \\ &\quad \times \sum_{\lambda} \frac{(\xi_1^\lambda e_2 e_3 + \xi_2^\lambda e_1 e_3 + \xi_3^\lambda e_1 e_2)^2}{q^3} \exp(-a^2 q^2/2) \\ &\quad \times \sin^2(qL \cos \theta) \sin^2 \frac{qst}{2} \coth \frac{\hbar qs}{2k_B T}, \end{aligned} \quad (71)$$

see (56)–(58). For the deformation interaction, we have the coupling constant (44), and the expression for the spectral function is given by

$$B_{\text{deform}}^2(t) = \frac{\Xi^2}{\pi^2 \hbar \rho s^3} \int_0^\infty q^2 dq \int_0^\pi \sin \theta d\theta \times \frac{\sin^2(qL \cos \theta)}{q(1 + (a^2 q^2)/4)^4} \sin^2 \frac{qst}{2} \coth \frac{\hbar qs}{2k_B T}. \quad (72)$$

3.7 Qubit Error Estimates

The qubit error measure, D , is obtained from the density matrix deviation from the “ideal” evolution by using the operator norm approach [67] reviewed in Sect. 2.5. After lengthy intermediate calculations one gets [68] relatively simple expressions for the error during the NOT gate,

$$D_{\text{NOT}} = \frac{1 - e^{-\Gamma\tau}}{1 + e^{-\varepsilon/k_B T}}, \quad (73)$$

and the π gate,

$$D_\pi = \frac{1}{2} [1 - e^{-B^2(\tau)}]. \quad (74)$$

A realistic noise estimate could be taken as the worst-case scenario, i.e., the maximum of these two expressions for error per gate cycle. The expressions (73) and (74) were used to calculate the error rate for the double-dot qubit in GaAs and double-impurity qubit in Si. The parameters used were chosen to correspond to the experimentally realized structures, [45–48], and are summarized in Table 1. The calculated error measures are presented in Figs. 2 and 3. The gate time τ selected for the reported calculations, 6×10^{-11} s, is a representative value consistent with typical experimental conditions. In fact, decreasing the gating time does not lead to smaller quantum noise in this case because the energy gap of the driven qubit is $\sim 1/\tau$. If the gap is made too large, other excitations will play a role in decoherence, for instance, optical phonons. The timescale chosen here is within an optimal range, as discussed in [68].

Table 1. Qubit parameters

Parameter	GaAs double-dot qubit	Si double-impurity qubit
ρ , kg/m ³	5.31×10^3	2.33×10^3
s , m/s	5.14×10^3	9.0×10^3
Ξ , eV	3.3	–
e_{14} , C/m ²	–	0.16
κ	–	12.8
M , eV/m	–	$ee_{14}/(\varepsilon_0 \kappa)$
L , nm	50	50
a , nm	25	3

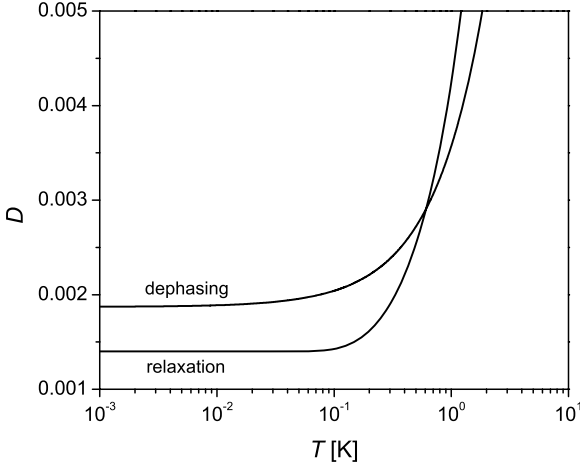


Fig. 2. Estimates of the error measure per cycle, D , due to the piezoelectric interaction in GaAs double dot, shown as a function of the temperature, T . The cycle time τ was 6×10^{-11} s

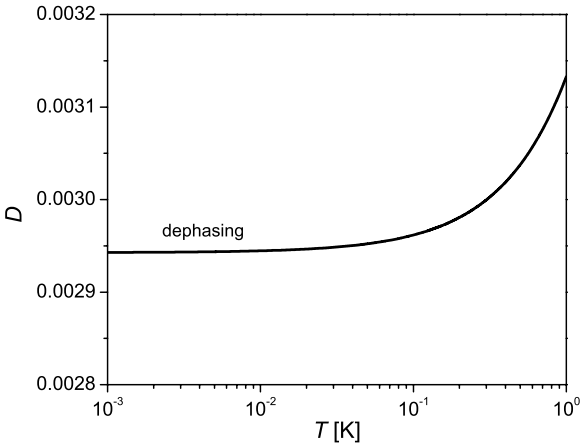


Fig. 3. Estimate of error rate per cycle, D , due to deformation phonon interaction for a double phosphorus impurity in Si, shown as a function of the temperature, T . The cycle time τ was 6×10^{-11} s. The relaxation rate for this range of the parameter values is negligibly small and respective values of D are not shown

In summary, we derived expressions for the error measure for double-dot and double-impurity qubits. The results, presented in Figs. 2 and 3, suggest that pure dephasing dominates at low temperatures. As the temperature increases beyond about 1 K, the effect of relaxation becomes comparable and ultimately dominant.

The error measure values found, are 1.5 or more orders of magnitude larger than the “traditional” fault-tolerance thresholds for multiqubit quantum computation, which range from $O(10^{-4})$ down to $O(10^{-6})$ [53, 54, 62, 65, 92, 93]. However, recent developments have yielded less strict requirements for the error rate [94–96], optimistically, as large as $O(10^{-2})$. Furthermore, there are several approaches to decrease decoherence effects by pulsed control [97–106], some recently tested experimentally in multispin NMR [107, 108]. Other ideas rely on the fact that instead of the bulk material, the qubit could

be manufactured in a one- or two-dimensional nanostructure [109, 110], the latter being already available experimentally [111], which would affect the phonon spectrum and lower decoherence effects.

4 Additivity of Decoherence Measures

In the study of decoherence of several-qubit systems, additional physical effects should be taken into account. Specifically, one has to consider the degree to which noisy environments of different qubits are correlated [91, 112]. In addition to acting as a source of the quantum noise, the correlated bath can induce an effective interaction, namely, create entanglement, between the qubits immersed in it [110, 113–115]. Furthermore, if all constituent qubits are effectively immersed in the same bath, then there are ways to reduce decoherence for this group of qubits without error-correction algorithms, by encoding the state of one logical qubit in a decoherence-free subspace of the states of several physical qubits [86, 91, 116–118]. In this section, we will consider several-qubit quantum registers and, as the “worst-case scenario” assume that the qubits experience uncorrelated noise, i.e., each is coupled to a separate bath. Since analytical calculations for several qubits are not feasible, we seek “additivity” properties that will allow us to estimate the error measure for the register from the error measures of the constituent qubits.

It is important to emphasize that loss of quantum coherence results in a loss of various two- and several-qubit entanglements in the system. The highest order (multiqubit) entanglements are “encoded” in the far-offdiagonal elements of the multiqubit register density matrix, and therefore these quantum correlations will decay at least as fast as the products of the decay factors for the qubits involved, as exemplified by several explicit calculations [119–122]. This observation leads to the conclusion that, for large times, the *rates* of decay of coherence of the qubits will be additive.

However, here we seek a different result: one valid not in the regime of the asymptotic large-time decay of quantum coherence, but for relatively short times, τ , of quantum gate functions, when the noise level, namely the value of the measure $D(\tau)$ for each qubit, is relatively small. In this regime, we will establish [70] in this section, that, even for strongly entangled qubits – which is important for the utilization of the power of quantum computation – the error measures D of the individual qubits in a quantum register are additive. Thus, the error measure for a register made of similar qubits, scales up linearly with their number, consistent with other theoretical and experimental observations [76, 107, 108].

In Sect. 4.1, we revisit the noise measure via the maximal deviation norm and discuss some of its properties. In Sect. 4.2, we introduce the diamond norm that is used as an auxiliary tool in the proof of additivity. We then establish an approximate upper bound for $D(t)$ for a register of several weakly

interacting but possibly strongly entangled qubits, and cite work that further refines the additivity properties for typical qubit realizations.

4.1 The Maximal Deviation Norm

To characterize decoherence for an arbitrary initial state, pure or mixed, we use the maximal norm, D , which was defined (21) in Sect. 2.5 as an operator norm maximized over all the possible initial density matrices. One can show that $0 \leq D(t) \leq 1$. This measure of decoherence will typically increase monotonically from zero at $t = 0$, saturating at large times at a value $D(\infty) \leq 1$. The definition of the maximal decoherence measure $D(t)$ looks rather complicated for a general multiqubit system. However, it can be evaluated in closed form for short times, appropriate for quantum computing, for a single-qubit (two-state) system. We then establish an approximate additivity that allows us to estimate $D(t)$ for several-qubit systems as well.

In the superoperator notation the evolution of the reduced density operator of the system (7) and the one for the ideal density matrix (8) can be formally expressed [62–64] in the following way

$$\rho(t) = T(t)\rho(0), \quad (75)$$

$$\rho^{(i)}(t) = T^{(i)}(t)\rho(0), \quad (76)$$

where $T, T^{(i)}$ are linear superoperators. In this notation the deviation can be expressed as

$$\sigma(t) = [T(t) - T^{(i)}(t)]\rho(0). \quad (77)$$

The initial density matrix can always be written in the following form,

$$\rho(0) = \sum_j p_j |\psi_j\rangle\langle\psi_j|, \quad (78)$$

where $\sum_j p_j = 1$ and $0 \leq p_j \leq 1$. Here, the set of the wavefunctions $|\psi_j\rangle$ is not assumed to have any orthogonality properties. Then, we get

$$\sigma(t, \rho(0)) = \sum_j p_j [T(t) - T^{(i)}(t)] |\psi_j\rangle\langle\psi_j|. \quad (79)$$

The deviation norm can thus be bounded,

$$\|\sigma(t, \rho(0))\|_\lambda \leq \|[T(t) - T^{(i)}(t)]|\phi\rangle\langle\phi|\|_\lambda. \quad (80)$$

Here, $|\phi\rangle$ is defined according to

$$\|[T - T^{(i)}]|\phi\rangle\langle\phi|\|_\lambda = \max_j \|[T - T^{(i)}]|\psi_j\rangle\langle\psi_j|\|_\lambda. \quad (81)$$

It transpires that for any initial density operator that is a statistical mixture, one can always find a density operator that is pure-state, $|\phi\rangle\langle\phi|$, such that $\|\sigma(t, \rho(0))\|_\lambda \leq \|\sigma(t, |\phi\rangle\langle\phi|)\|_\lambda$. Therefore, evaluation of the supremum over

the initial density operators in order to find $D(t)$, see (21), can be done over only pure-state density operators, $\rho(0)$.

Let us consider strategies of evaluating $D(t)$ for a single qubit. We can parameterize $\rho(0)$ as

$$\rho(0) = U \begin{pmatrix} P & 0 \\ 0 & 1 - P \end{pmatrix} U^\dagger, \quad (82)$$

where $0 \leq P \leq 1$, and U is an arbitrary 2×2 unitary matrix,

$$U = \begin{pmatrix} e^{i(\alpha+\gamma)} \cos \theta & e^{i(\alpha-\gamma)} \sin \theta \\ -e^{i(\gamma-\alpha)} \sin \theta & e^{-i(\alpha+\gamma)} \cos \theta \end{pmatrix}. \quad (83)$$

Then, one should find a supremum of the norm of deviation (16) over all the possible real parameters P , α , γ and θ . As shown above, it suffices to consider the density operator in the form of a projector and put $P = 1$. Thus, one should search for the maximum over the remaining three real parameters α , γ and θ .

Another parametrization of the pure-state density operators, $\rho(0) = |\phi\rangle\langle\phi|$, is to express an arbitrary wavefunction $|\phi\rangle = \sum_j (a_j + ib_j)|j\rangle$ in some convenient orthonormal basis $|j\rangle$, where $j = 1, \dots, N$. For a two-level system,

$$\rho(0) = \begin{pmatrix} a_1^2 + b_1^2 & (a_1 + ib_1)(a_2 - ib_2) \\ (a_1 - ib_1)(a_2 + ib_2) & a_2^2 + b_2^2 \end{pmatrix}, \quad (84)$$

where the four real parameters $a_{1,2}, b_{1,2}$ satisfy $a_1^2 + b_1^2 + a_2^2 + b_2^2 = 1$, so that the maximization is again over three independent real numbers. The final expressions (73) and (74) for $D(t)$, for our selected single-qubit systems considered in Sect. 3, are actually quite compact and tractable.

In quantum computing, the error rates can be significantly reduced by using several physical qubits to encode each logical qubit [86, 116, 117]. Therefore, even before active quantum error correction is incorporated [53–61], evaluation of decoherence of several qubits is an important, but formidable task. Thus, our aim is to prove the approximate additivity of $D_q(t)$, including the case of the initially strongly *entangled* qubits, labeled by q , whose dynamics is governed by

$$H = \sum_q H_q = \sum_q (H_{S_q} + H_{B_q} + H_{I_q}), \quad (85)$$

where H_{S_q} is the Hamiltonian of the q th qubit itself, H_{B_q} is the Hamiltonian of the environment of the q th qubit, and H_{I_q} is the corresponding qubit–environment interaction. In the next subsection we consider a more complicated (for actual evaluation) diamond norm [62–64], $K(t)$, as an auxiliary quantity used to establish the additivity of the more easily calculable operator norm $D(t)$.

4.2 Upper Bound for Measure of Decoherence

The establishment of the upper-bound estimate for the maximal deviation norm of a multiqubit system, involves several steps. We derive a bound for this norm in terms of the recently introduced (in the context of quantum computing) [62–64] diamond norm, $K(t)$. Actually, for single qubits, in several models the diamond norm can be expressed via the corresponding maximal deviation norm. At the same time, the diamond norm for the whole quantum system is bounded by the sum of the norms of the constituent qubits by using a specific stability property of the diamond norm. The use of the diamond norm was proposed in [62–64],

$$K(t) = \|T - T^{(i)}\|_{\diamond} = \sup_{\varrho} \left\| \{ [T - T^{(i)}] \otimes I \} \varrho \right\|_{\text{Tr}}. \quad (86)$$

The superoperators T , $T^{(i)}$ characterize the actual and ideal evolutions according to (75) and (76). Here, I is the identity superoperator in a Hilbert space G whose dimension is the same as that of the corresponding space of the superoperators T and $T^{(i)}$, and ϱ is an arbitrary density operator in the product space of twice the number of qubits.

The diamond norm has an important stability property, proved in [62–64],

$$\|B_1 \otimes B_2\|_{\diamond} = \|B_1\|_{\diamond} \|B_2\|_{\diamond}. \quad (87)$$

Note that (87) is a property of the superoperators rather than that of the operators.

Consider a composite system consisting of the two subsystems S_1 , S_2 , with the noninteracting Hamiltonian

$$H_{S_1 S_2} = H_{S_1} + H_{S_2}. \quad (88)$$

The evolution superoperator of the system will be

$$T_{S_1 S_2} = T_{S_1} \otimes T_{S_2}, \quad (89)$$

and the ideal one

$$T_{S_1 S_2}^{(i)} = T_{S_1}^{(i)} \otimes T_{S_2}^{(i)}. \quad (90)$$

The diamond measure for the system can be expressed as

$$\begin{aligned} K_{S_1 S_2} &= \|T_{S_1 S_2} - T_{S_1 S_2}^{(i)}\|_{\diamond} = \|(T_{S_1} - T_{S_1}^{(i)})T_{S_2} + T_{S_1}^{(i)} \otimes (T_{S_2} - T_{S_2}^{(i)})\|_{\diamond} \\ &\leq \|(T_{S_1} - T_{S_1}^{(i)}) \otimes T_{S_2}\|_{\diamond} + \|T_{S_1}^{(i)} \otimes (T_{S_2} - T_{S_2}^{(i)})\|_{\diamond}. \end{aligned} \quad (91)$$

By using the stability property (87), we get

$$\begin{aligned} K_{S_1 S_2} &\leq \|(T_{S_1} - T_{S_1}^{(i)}) \otimes T_{S_2}\|_{\diamond} + \|T_{S_1}^{(i)} \otimes (T_{S_2} - T_{S_2}^{(i)})\|_{\diamond} \\ &= \|T_{S_1} - T_{S_1}^{(i)}\|_{\diamond} \|T_{S_2}\|_{\diamond} + \|T_{S_1}^{(i)}\|_{\diamond} \|T_{S_2} - T_{S_2}^{(i)}\|_{\diamond} \\ &= \|T_{S_1} - T_{S_1}^{(i)}\|_{\diamond} + \|T_{S_2} - T_{S_2}^{(i)}\|_{\diamond} = K_{S_1} + K_{S_2}. \end{aligned} \quad (92)$$

The inequality

$$K \leq \sum_q K_q, \tag{93}$$

for the diamond norm $K(t)$ has thus been obtained. Let us emphasize that the subsystems can be initially entangled. This property is particularly useful for quantum computing, the power of which is based on qubit entanglement. However, even in the simplest case of the diamond norm of one qubit, the calculations are extremely cumbersome. Therefore, the use of the measure $D(t)$ is preferable for actual calculations.

For short times, of quantum gate functions, we can use (93) as an approximate inequality for order-of-magnitude estimates of decoherence measures, even when the qubits are interacting. Indeed, for short times, the interaction effects will not modify the quantities entering both sides significantly. The key point is that while the interaction effects are small, this inequality can be used for *strongly entangled* qubits.

The two deviation-operator norms considered are related by the following inequality

$$\|\sigma\|_\lambda \leq \frac{1}{2} \|\sigma\|_{\text{Tr}} \leq 1. \tag{94}$$

Here, the left-hand side follows from

$$\text{Tr}\sigma = \sum_j \lambda_j = 0. \tag{95}$$

Therefore, the ℓ th eigenvalue of the deviation operator σ that has the maximum absolute value, $\lambda_\ell = \lambda_{\text{max}}$, can be expressed as

$$\lambda_\ell = - \sum_{j \neq \ell} \lambda_j. \tag{96}$$

Thus, we have

$$\|\sigma\|_\lambda = \frac{1}{2} (2|\lambda_\ell|) \leq \frac{1}{2} \left(|\lambda_\ell| + \sum_{j \neq \ell} |\lambda_j| \right) = \frac{1}{2} \left(\sum_j |\lambda_j| \right) = \frac{1}{2} \|\sigma\|_{\text{Tr}}. \tag{97}$$

The right-hand side of (94) then also follows, because any density matrix has trace norm 1,

$$\|\sigma\|_{\text{Tr}} = \|\rho - \rho^{(i)}\|_{\text{Tr}} \leq \|\rho\|_{\text{Tr}} + \|\rho^{(i)}\|_{\text{Tr}} = 2. \tag{98}$$

From the relation (98) it follows that

$$K(t) \leq 2. \tag{99}$$

By taking the supremum of both sides of the relation (97) we get

$$D(t) = \sup_{\rho(0)} \|\sigma\|_\lambda \leq \frac{1}{2} \sup_{\rho(0)} \|\sigma\|_{\text{Tr}} \leq \frac{1}{2} K(t), \tag{100}$$

where the last step involves technical derivation details [70] not reproduced here. In fact, for a single qubit, calculations for typical models [70] give

$$D_q(t) = \frac{1}{2}K_q(t). \quad (101)$$

Since D is generally bounded by (or equal to) $K/2$, it follows that the multiqubit norm D is approximately bounded from above by the sum of the single-qubit norms even for the *initially entangled* qubits,

$$D(t) \leq \frac{1}{2}K(t) \leq \frac{1}{2} \sum_q K_q(t) = \sum_q D_q(t), \quad (102)$$

where q labels the qubits.

For specific models of decoherence of the type encountered in Sect. 3, as well as those formulated for general studies of short-time decoherence [67], a stronger property has been demonstrated [70], namely that the noise measures are actually equal, for low levels of noise,

$$D(t) = \sum_q D_q(t) + o\left(\sum_q D_q(t)\right). \quad (103)$$

In summary, in this section we considered the maximal operator norm suitable for evaluation of decoherence for a quantum register consisting of qubits immersed in noisy environments. We established the additivity property of this measure of decoherence for multiqubit registers at short times, for which the level of quantum noise is low, and the qubit–qubit interaction effects are small, but without any limitation on the initial entanglement of the qubit register.

Acknowledgments

We are grateful to A. Fedorov, D. Mozyrsky, D. Solenov and D. Tolkunov for collaborations and instructive discussions. This research was supported by the National Science Foundation, grant DMR-0121146.

References

1. G.W. Ford, M. Kac, P. Mazur, J. Math. Phys. **6**, 504 (1965) 141
2. A.O. Caldeira, A.J. Leggett, Physica A **121**, 587 (1983) 141
3. S. Chakravarty, A.J. Leggett, Phys. Rev. Lett. **52**, 5 (1984) 141
4. H. Grabert, P. Schramm, G.-L. Ingold, Phys. Rep. **168**, 115 (1988) 141
5. N.G. van Kampen, J. Stat. Phys. **78**, 299 (1995) 141
6. K.M. Fonseca Romero, M.C. Nemes, Phys. Lett. A **235**, 432 (1997) 141
7. C. Anastopoulos, B.L. Hu, Phys. Rev. A **62**, 033821 (2000) 141
8. G.W. Ford, R.F. O’Connell, Phys. Rev. D **64**, 105020 (2001) 141

9. D. Braun, F. Haake, W.T. Strunz, Phys. Rev. Lett. **86**, 2913 (2001) 141
10. G.W. Ford, J.T. Lewis, R.F. O'Connell, Phys. Rev. A **64**, 032101 (2001) 141
11. J. Wang, H.E. Ruda, B. Qiao, Phys. Lett. A **294**, 6 (2002) 141
12. E. Lutz, Phys. Rev. A **67**, 022109 (2003) 141
13. A. Khaetskii, D. Loss, L. Glazman, Phys. Rev. B **67**, 195329 (2003) 141
14. R.F. O'Connell, J. Zuo, Phys. Rev. A **67**, 062107 (2003) 141
15. W.T. Strunz, F. Haake, D. Braun, Phys. Rev. A **67**, 022101 (2003) 141
16. W.T. Strunz, F. Haake, Phys. Rev. A **67**, 022102 (2003) 141
17. V. Privman, D. Mozyrsky, I.D. Vagner, Comput. Phys. Commun. **146**, 331 (2002) 141
18. V. Privman, J. Stat. Phys. **110**, 957 (2003) 141, 143
19. V. Privman, Mod. Phys. Lett. B **16**, 459 (2002) 141
20. J. von Neumann, *Mathematical Foundations of Quantum Mechanics* (Princeton University Press, Princeton, 1983) 141, 143
21. A. Abragam, *The Principles of Nuclear Magnetism* (Clarendon, Oxford, 1983) 141, 142, 143
22. K. Blum, *Density Matrix Theory and Applications* (Plenum, New York, 1996) 141, 142, 152
23. N.G. van Kampen, *Stochastic Processes in Physics and Chemistry* (North-Holland, Amsterdam, 1992) 141, 142
24. W.H. Louisell, *Quantum Statistical Properties of Radiation* (Wiley, New York, 1973) 141
25. A. Shnirman, G. Schön, in *Quantum Noise in Mesoscopic Physics*, ed. by Y.V. Nazarov. Proc. NATO ARW Quantum Noise in Mesoscopic Physics (Kluwer, Dordrecht, 2003), p. 357 141
26. A. Ekert, R. Jozsa, Rev. Mod. Phys. **68**, 733 (1996) 141, 146
27. V. Privman, I.D. Vagner, G. Kventsel, Phys. Lett. A **239**, 141 (1998) 141, 146
28. B.E. Kane, Nature **393**, 133 (1998) 141, 146
29. D. Loss, D.P. DiVincenzo, Phys. Rev. A **57**, 120 (1998) 141
30. A. Imamoglu, D.D. Awschalom, G. Burkard, D.P. DiVincenzo, D. Loss, M. Sherwin, A. Small, Phys. Rev. Lett. **83**, 4204 (1999) 141
31. P. Zanardi, F. Rossi, Phys. Rev. B **59**, 8170 (1999) 141
32. Y. Nakamura, Y.A. Pashkin, H.S. Tsai, Nature **398**, 786 (1999) 141
33. T. Tanamoto, Phys. Rev. A **61**, 022305 (2000) 141
34. P.M. Platzman, M.I. Dykman, Science **284**, 1967 (1999) 141
35. G.P. Sanders, K.W. Kim, W.C. Holton, Phys. Rev. A **60**, 4146 (1999) 141
36. G. Burkard, D. Loss, D.P. DiVincenzo, Phys. Rev. B **59**, 2070 (1999) 141
37. R. Vrijen, E. Yablonovitch, K. Wang, H.W. Jiang, A. Balandin, V. Roychowdhury, T. Mor, D.P. DiVincenzo, Phys. Rev. A **62**, 012306 (2000) 141, 146

38. L. Fedichkin, M. Yanchenko, K.A. Valiev, *Nanotechnology* **11**, 387 (2000) 141, 146
39. S. Bandyopadhyay, *Phys. Rev. B* **61**, 13813 (2000) 141
40. A.A. Larionov, L.E. Fedichkin, K.A. Valiev, *Nanotechnology* **12**, 536 (2001) 141
41. J.A. Brum, P. Hawrylak, *Superlattices Microstruct.* **22**, 431 (1997) 141, 146
42. S. Bandyopadhyay, A. Balandin, V.P. Roychowdhury, F. Vatan, *Superlattices Microstruct.* **23**, 445 (1998) 141, 146
43. A. Balandin, K.L. Wang, *Superlattices Microstruct.* **25**, 509 (1999) 141, 146
44. L.A. Openov, *Phys. Rev. B* **60**, 8798 (1999) 141, 146
45. T. Hayashi, T. Fujisawa, H.-D. Cheong, Y.-H. Jeong, Y. Hirayama, *Phys. Rev. Lett.* **91**, 226804 (2003) 141, 146, 147, 149, 155
46. T. Fujisawa, T.H. Oosterkamp, W.G. van der Wiel, B.W. Broer, R. Aguado, S. Tarucha, L.P. Kouwenhoven, *Science* **282**, 932 (1998) 141, 146, 149, 155
47. L.C.L. Hollenberg, A.S. Dzurak, C. Wellard, A.R. Hamilton, D.J. Reilly, G.J. Milburn, R.G. Clark, *Phys. Rev. B* **69**, 113301 (2004) 141, 146, 147, 149, 150, 155
48. T.M. Buehler, V. Chan, A.J. Ferguson, A.S. Dzurak, F.E. Hudson, D.J. Reilly, A.R. Hamilton, R.G. Clark, D.N. Jamieson, C. Yang, C.I. Pakes, S. Prawer, *Appl. Phys. Lett.* **88**, 192101 (2006) 141, 146, 147, 149, 150, 155
49. P.A. Cain, H. Ahmed, D.A. Williams, *J. Appl. Phys.* **92**, 346 (2002) 141, 146
50. C.G. Smith, S. Gardelis, J. Cooper, D.A. Ritchie, E.H. Linfield, Y. Jin, H. Launois, *Physica E* **12**, 830 (2002) 141, 146
51. S.D. Barrett, G.J. Milburn, *Phys. Rev. B* **68**, 155307 (2003) 141, 146
52. D. Ahn, *J. Appl. Phys.* **98**, 033709 (2005) 141, 146
53. D. Aharonov, M. Ben-Or, e-print quant-ph/9611025 at www.arxiv.org (1996) 141, 156, 159
54. D. Aharonov, M. Ben-Or, e-print quant-ph/9906129 at www.arxiv.org (1999) 141, 156, 159
55. P.W. Shor, *Phys. Rev. A* **52**, 2493 (1995) 141, 159
56. A.M. Steane, *Phys. Rev. Lett.* **77**, 793 (1996) 141, 159
57. C.H. Bennett, G. Brassard, S. Popescu, B. Schumacher, J.A. Smolin, W.K. Wootters, *Phys. Rev. Lett.* **76**, 722 (1996) 141, 159
58. A.R. Calderbank, P.W. Shor, *Phys. Rev. A* **54**, 1098 (1996) 141, 159
59. A.M. Steane, *Phys. Rev. A* **54**, 4741 (1996) 141, 159
60. D. Gottesman, *Phys. Rev. A* **54**, 1862 (1997) 141, 159
61. E. Knill, R. Laflamme, *Phys. Rev. A* **55**, 900 (1997) 141, 159
62. A.Y. Kitaev, *Russ. Math. Surv.* **52**, 1191 (1997) 141, 156, 158, 159, 160
63. D. Aharonov, A. Kitaev, N. Nisan, in *Proc. XXXth ACM Symp. Theor. Comp.*, Dallas, TX, USA (1998), p. 20 141, 158, 159, 160

64. A.Y. Kitaev, A.H. Shen, M.N. Vyalyi, *Classical and Quantum Computation* (AMS, Providence, 2002) 141, 144, 151, 158, 159, 160
65. J. Preskill, Proc. R. Soc. Lond. A **454**, 385 (1998) 141, 156
66. D.P. DiVincenzo, Fort. Phys. **48**, 771 (2000) 141, 143
67. L. Fedichkin, A. Fedorov, V. Privman, Proc. SPIE **5105**, 243 (2003) 142, 145, 155, 162
68. L. Fedichkin, A. Fedorov, Phys. Rev. A **69**, 032311 (2004) 142, 146, 148, 154, 155
69. L. Fedichkin, A. Fedorov, IEEE Trans. Nanotechnol. **4**, 65 (2005) 142, 148, 153
70. L. Fedichkin, A. Fedorov, V. Privman, Phys. Lett. A **328**, 87 (2004) 142, 157, 162
71. A. Fedorov, L. Fedichkin, V. Privman, J. Comput. Theor. Nanosci. **1**, 132 (2004) 142
72. D. Mozyrsky, V. Privman, J. Stat. Phys. **91**, 787 (1998) 143, 154
73. J.I. Kim, M.C. Nemes, A.F.R. de Toledo Piza, H.E. Borges, Phys. Rev. Lett. **77**, 207 (1996) 143
74. W.H. Zurek, Rev. Mod. Phys. **75**, 715 (2003) 143
75. J.C. Retamal, N. Zagury, Phys. Rev. A **63**, 032106 (2001) 143
76. B.J. Dalton, J. Mod. Opt. **50**, 951 (2003) 143, 157
77. L.-M. Duan, G.-C. Guo, Phys. Rev. A **56**, 4466 (1997) 143
78. T. Brandes, T. Vorrath, Phys. Rev. B **66**, 075341 (2002) 144, 151
79. T. Brandes, R. Aguado, G. Platero, Phys. Rev. B **69**, 205326 (2004) 144, 151
80. D. Solenov, V. Privman, Int. J. Mod. Phys. B **20**, 1476 (2006) 144, 151
81. T. Kato, *Perturbation Theory for Linear Operators* (Springer, New York, 1995) 145
82. *Quantum Information Science and Technology Roadmap*, maintained online at qist.lanl.gov 146
83. D. Loss, D.P. DiVincenzo, Phys. Rev. A **57**, 120 (1998) 146
84. A. Imamoglu, D.D. Awschalom, G. Burkard, D.P. DiVincenzo, D. Loss, M. Sherwin, A. Small, Phys. Rev. Lett. **83**, 4204 (1999) 146
85. A. Barenco, D. Deutsch, A. Ekert, R. Jozsa, Phys. Rev. Lett. **74**, 4083 (1995) 146
86. P. Zanardi, M. Rasetti, Phys. Rev. Lett. **79**, 3306 (1997) 146, 157, 159
87. Y. Nakamura, Y.A. Pashkin, T. Yamamoto, J.S. Tsai, Phys. Rev. Lett. **88**, 047901 (2002) 146
88. I. Martin, D. Mozyrsky, H.W. Jiang, Phys. Rev. Lett. **90**, 018301 (2003) 146
89. G.D. Mahan, *Many-Particle Physics* (Kluwer, Dordrecht, 2000) 148, 150
90. X. Hu, B. Koiller, S. Das Sarma, Phys. Rev. B **71**, 235332 (2005) 151
91. G.M. Palma, K.A. Suominen, A.K. Ekert, Proc. R. Soc. A **452**, 567 (1996) 154, 157

92. E. Knill, R. Laflamme, W.H. Zurek, Proc. R. Soc. A **454**, 365 (1998) 156
93. P. Aliferis, D. Gottesman, J. Preskill, Quant. Inf. Comput. **6**, 97 (2006) 156
94. E. Knill, Phys. Rev. A **71**, 042332 (2005) 156
95. E. Knill, e-print quant-ph/0404104 at www.arxiv.org (2004) 156
96. E. Knill, Nature **434**, 39 (2005) 156
97. L. Viola, E. Knill, S. Lloyd, Phys. Rev. Lett. **82**, 2417 (1999) 156
98. L. Viola, S. Lloyd, E. Knill, Phys. Rev. Lett. **83**, 4888 (1999) 156
99. L. Fedichkin, Quant. Comp. Comput. **1**, 84 (2000) 156
100. M.S. Byrd, D.A. Lidar, Phys. Rev. Lett. **89**, 012307 (2002) 156
101. L. Viola, Phys. Rev. A **66**, 012307 (2002) 156
102. K. Khodjasteh, D.A. Lidar, Phys. Rev. A **68**, 022322 (2003) 156
103. Y. Ozhigov, L. Fedichkin, JETP Lett. **77**, 328 (2003) 156
104. L. Viola, E. Knill, Phys. Rev. Lett. **90**, 037901 (2003) 156
105. K. Khodjasteh, D.A. Lidar, Phys. Rev. Lett. **95**, 180501 (2005) 156
106. L. Viola, E. Knill, Phys. Rev. Lett. **94**, 060502 (2005) 156
107. H.G. Krojanski, D. Suter, Phys. Rev. Lett. **93**, 090501 (2004) 156, 157
108. H.G. Krojanski, D. Suter, Phys. Rev. Lett. **97**, 150503 (2006) 156, 157
109. M.I. Dykman, P.M. Platzman, Fortsch. Phys. **48**, 1095 (2000) 157
110. D. Solenov, D. Tolkunov, V. Privman, Phys. Rev. B **75**, 035134 (2007) 157
111. M.M. Roberts, L.J. Klein, D.E. Savage, K.A. Slinker, M. Friesen, G. Celler, M.A. Eriksson, M.G. Lagally, Nat. Mater. **5**, 388 (2006) 157
112. A. Fedorov, L. Fedichkin, J. Phys., Condens. Matter **18**, 3217 (2006) 157
113. D. Mozyrsky, A. Dementsov, V. Privman, Phys. Rev. B **72**, 233103 (2005) 157
114. D. Solenov, D. Tolkunov, V. Privman, Phys. Lett. A **359**, 81 (2006) 157
115. V. Privman, D. Solenov, D. Tolkunov, in *Proc. Conf. ICSICT-2006, Part 2*, ed. by T.-A. Tang, G.-P. Ru, Y.-L. Jiang (IEEE Press, New York, 2006), p. 1054 157
116. L.-M. Duan, G.-C. Guo, Phys. Rev. Lett. **79**, 1953 (1997) 157, 159
117. D.A. Lidar, I.L. Chuang, K.B. Whaley, Phys. Rev. Lett. **81**, 2594 (1998) 157, 159
118. R. Doll, M. Wubs, P. Hänggi, S. Kohler, Europhys. Lett. **76**, 547 (2006) 157
119. T. Yu, J.H. Eberly, Phys. Rev. B **68**, 165322 (2003) 157
120. M.J. Storcz, F.K. Wilhelm, Phys. Rev. A **67**, 042319 (2003) 157
121. D. Tolkunov, V. Privman, P.K. Aravind, Phys. Rev. A **71**, 060308 (2005) 157
122. T. Yu, J.H. Eberly, Phys. Rev. Lett. **97**, 140403 (2006) 157

Index

- decoherence, 141–144, 151, 159
- deformation coupling with acoustic
 - phonons, 150
- dephasing, 142
- double quantum-dot, 141
- fidelity, 142–144
- maximal norm, 158
- NOT gate, 151
- operator norms, 145
- piezoacoustic interaction, 152
- piezoelectric interaction, 148
- quantum entropy, 143
- qubit error measure, 155
- relaxation rates, 142
- relaxation time, 146

“This page left intentionally blank.”

Measuring the Charge and Spin States of Electrons on Individual Dopant Atoms in Silicon

Søren E.S. Andresen^{1,5}, Dane R. McCamey^{1,6}, Rolf Brenner^{1,7}, Marc A. Ahrens¹, Mladen Mitic¹, Victor C. Chan¹, Eric Gauja¹, Fay E. Hudson¹, Andrew J. Ferguson^{1,8}, Tilo M. Buehler^{1,9}, David J. Reilly^{1,10}, Robert G. Clark¹, Andrew S. Dzurak¹, Alex R. Hamilton¹, Cameron J. Wellard², Changyi Yang², Toby Hopf², Jeff McCallum², David N. Jamieson², Lloyd C. L. Hollenberg², Wayne D. Hutchison³, Hans Huebl^{1,4}, and Martin S. Brandt⁴

¹ Centre for Quantum Computer Technology, School of Physics and Electrical Engineering, University of New South Wales, Sydney, NSW 2052, Australia

² Centre for Quantum Computer Technology, School of Physics, University of Melbourne, Melbourne, VIC 3010, Australia

³ Centre for Quantum Computer Technology, School of Physics, University of New South Wales, ADFA, Canberra, ACT 2600, Australia

⁴ Walter Schottky Institut, Technische Universität München, Am Coulombwall 3, 85748 Garching, Germany

⁵ Present address: Niels Bohr Institute, University of Copenhagen, Universitetsparken 5, 2100 Copenhagen, Denmark

⁶ Present address: Department of Physics, University of Utah, 115 S 1400 E, Salt Lake City, UT 84112-0830, USA

⁷ Present address: NXP Semiconductors Germany GmbH, General Application Discretes, Stresemannallee 101, 22529 Hamburg, Germany

⁸ Present address: Cavendish Laboratory, University of Cambridge, J J Thomson Avenue, Cambridge CB3 0HE, UK

⁹ Present address: ABB Switzerland Ltd. Corporate Research, Segelhofstrasse 1, 5405 Baden-Dättwil, Switzerland

¹⁰ Present address: Department of Physics, Harvard University, Cambridge, MA 02138, USA

Abstract. We review an ongoing effort to demonstrate technologies required for quantum computing with phosphorus donors in silicon. The main aspect of our research is to achieve control over charge and spin states of individual dopant atoms. This work has required the development of new techniques for engineering silicon nanodevices at the atomic level. We follow an approach for implanting single phosphorus ions into silicon substrates with integrated p-i-n detectors. Configuring our devices with radio-frequency single-electron transistors (RF-SETs) allows for charge sensing at low temperatures. In this context, we perform measurements of single-electron charge transfer between individual phosphorus donors. In a parallel effort, we employ nanoscale Schottky contacts for populating and depopulating individual dopant atoms. Of particular interest is coherent manipulation of single-electron charge and spin

states on individual dopant atoms. Charge manipulation between coupled donor states may be achieved by either external microwave pumping or intrinsic tunnel coupling. Spin manipulation, on the other hand, involves magnetic resonance. In this context, we pursue electrically detected spin resonance in phosphorus-doped devices with a decreasing number of dopant atoms.

1 Quantum Computing with Phosphorus in Silicon

The use of single dopant atoms for encoding quantum information in the solid state was pioneered by Kane in his original proposal for nuclear-spin-based quantum computing using single phosphorus donors in silicon [1]. The basic ingredient of the Kane proposal is to incorporate ^{31}P donors with nuclear spin $1/2$ into a ^{28}Si host with zero nuclear spin. As such, each ^{31}P nucleus forms a two-level spin system in a background of zero nuclear spin. However, each ^{31}P donor is associated with a localized electron, which is used both to tune the nuclear magnetic resonance through hyperfine splitting, mediate the coupling between neighboring nuclear spins through exchange interaction, and for readout of ^{31}P nuclear spins through the electronic charge state.

Since the original Kane scheme, a number of different donor-based qubit systems have been proposed. In particular, schemes that utilize the electronic spin states of single donors are attractive. Detailed scalable strategies for such electron-spin qubits have recently been put forward [4]. A less complicated

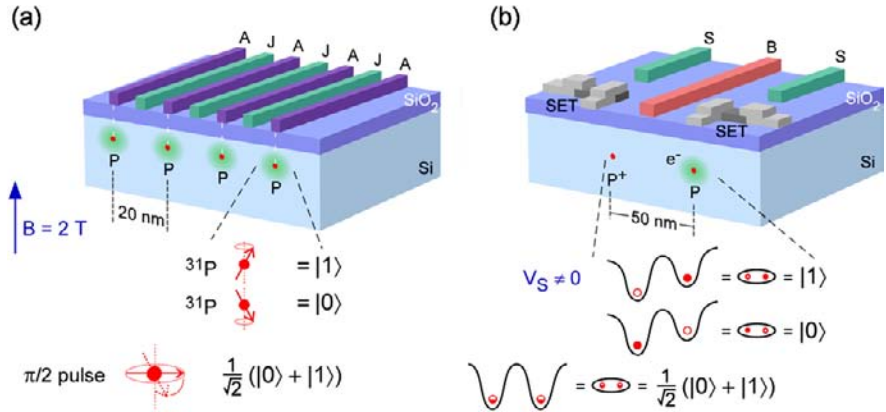


Fig. 1. (a) Original Kane proposal of encoding qubits on the nuclear spin of single phosphorus donors [1]. The concept features so-called A- and J-gates to electrically tune both hyperfine and exchange coupling. Coherent manipulation may be achieved through magnetic resonance. (b) Proposed scheme for charge-based single-donor quantum computing [2, 3]. Here, the qubit is encoded on the wavefunction of a single electron on a donor pair. Coherent behavior relies on the intrinsic tunnel coupling between the two donor states

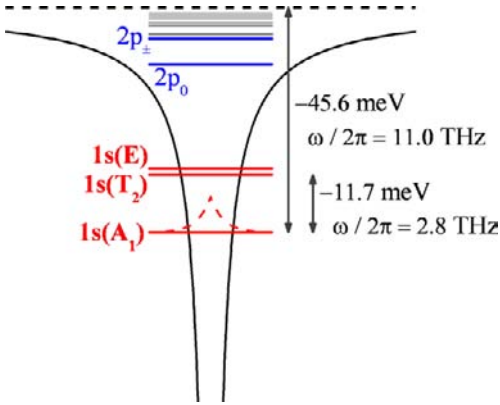


Fig. 2. Electronic levels of the phosphorus donor as observed by far-infrared spectroscopy [5]. Intervalley mixing gives rise to splitting of the 1s ground state into singlet (A_1), triplet (T_2), and doublet (E) superpositions of the six degenerate valleys

scheme that relies on electronic charge rather than spin states was previously proposed for quantum computing with single dopant atoms in silicon [2, 3]. This approach relies on the coherent tunnel coupling of a donor pair occupied by a single electron, where the qubit is encoded in the occupancy of each donor state.

1.1 Electronic Donor States of Phosphorus in Silicon

The basic properties of electronic donor states are of utmost importance for qubits based on individual dopant atoms. For phosphorus donors in silicon, a great deal is known from both experimental studies and different theoretical treatments pioneered by Kohn and Luttinger in the 1950s [5, 6]. Identifying the different levels is complicated by mixing of the six degenerate conduction band valleys in silicon due to the subatomic variation of the donor potential. This mixing gives rise to splitting of the hydrogen-like levels, lifting the six-fold valley degeneracy of the silicon conduction band. In the context of quantum computing, it is a big advantage that phosphorus donors have a nondegenerate ground-state with valley splitting of more than 10 meV to the degenerate triplet and doublet states. As such, it represents an ideal spin qubit in the sense that it has a nondegenerate orbital ground-state well separated from both the excited states as well as the conduction-band continuum.

1.2 Coupled Pairs of Phosphorus Donors as Charge Qubits

The proposed architecture for charge qubits based on single dopant atoms relies on the dynamics of a single electron on a pair of phosphorus donors in silicon, the so-called P_2^+ molecule [2, 3]. The concept of this system as a controllable two-level system relates to the so-called double quantum dots in gallium arsenide, recently reviewed by van der Wiel et al. [7]. In both systems, coherent behavior is achieved through tunnel coupling of two localized electronic states, tunable via an external electric field. In double quantum dots,

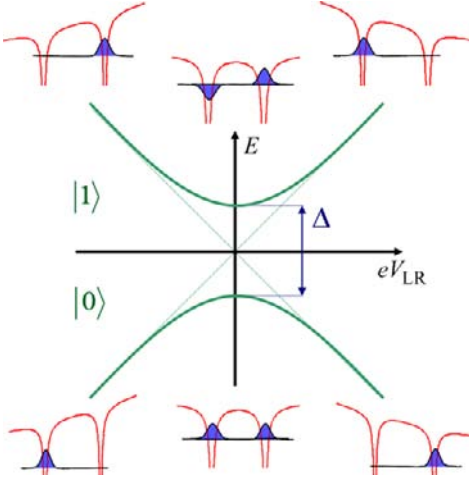


Fig. 3. Tuning of the single-electron ground and excited states with electric field for a tunnel coupled donor pair. The electric field works to localize the states on each donor, whereas the tunnel coupling gives rise to anticrossing with splitting into symmetric and antisymmetric states

these states are confined electrostatically, and until recently only as ground states of many-electron systems. The P_2^+ molecule on the other hand, represents a single-electron system governed by coherent tunnel coupling between the two donors. In the case of coupling much weaker than ionization and excitation energies, the ground and first excited states are simply superpositions of each single-donor ground state. The Hamiltonian of this two-level system in the basis of left and right donor states is given by

$$H = \begin{pmatrix} E_0 + eV_{LR} & -\Delta/2 \\ -\Delta/2 & E_0 - eV_{LR} \end{pmatrix}, \quad (1)$$

with single-donor ionization energy E_0 , electrostatic potential difference eV_{LR} , and coupling strength Δ . The eigenstates may be expressed in terms of a characteristic detuning angle $\theta = \tan^{-1}(\Delta/eV_{LR})$ as

$$\begin{aligned} |0\rangle &= \cos(\theta/2)|L\rangle + \sin(\theta/2)|R\rangle, \\ |1\rangle &= \sin(\theta/2)|L\rangle - \cos(\theta/2)|R\rangle, \end{aligned} \quad (2)$$

with corresponding energy eigenvalues $E = \mp\sqrt{\Delta^2 + (eV_{LR})^2}/2$. As indicated in Fig. 3, Δ describes the energy splitting between symmetric and antisymmetric states at the degeneracy point where the tunnel coupling gives rise to anticrossing behavior.

Coherent Manipulation

There are two basic schemes for coherent manipulation of charge qubits based on the P_2^+ molecule in silicon, both recently demonstrated for double quantum dots [8, 9]. The first approach relies on resonant pumping of the ground to excited state transition by a microwave field. Strong enough pumping will

lead to coherent evolution in terms of Rabi oscillations between the two P_2^+ eigenstates [10]. The second approach is to initialize the P_2^+ molecule in a localized donor state by an electric field, then move to the anticrossing where it no longer represents an eigenstate. Before decohering, the P_2^+ molecule will then undergo coherent Ramsey oscillations between the two localized states on each phosphorus donor [2].

The feasibility of achieving coherent manipulation of P_2^+ charge states depends mainly on the coupling strength in term of the Δ parameter compared to the dominating decoherence mechanisms, i.e., charge fluctuations and coupling to phonons. A crude estimate may be deduced as a hydrogenic approximation by scaling the result for H_2^+ in vacuum

$$\Delta = 2E_0 \left(1 + \frac{R}{a_B}\right) e^{-R/a_B} \quad (3)$$

for donor separation R and Bohr radius $a_B = 2.5$ nm for silicon. Much more accurate values are obtained for a full six-valley effective-mass treatment in the Kohn–Luttinger formalism [10, 11]. Such calculations show a strong dependence on the exact lattice configuration with a remarkable oscillatory behavior. Both approaches agree on an overall exponential dependence on donor separation with an order of magnitude scaling in approximately 5.8 nm. As a consequence, the exact lattice configuration has a huge impact on the coupling strength and hence on the dynamics of a given P_2^+ charge qubit.

2 Controlled Single-Ion Implantation

Our experimental work relies on a unique technology for single-ion implantation to configure MOS-based silicon nanodevices with a well-known number of dopant atoms. An active substrate allows for detection of low-energy phosphorus ions, and nanopatterned implantation masks enables us to position such atoms to within 20 nm.

2.1 Single-Ion Detection with Integrated p–i–n Diodes

In a recent report, we show how silicon substrates configured as p–i–n detectors may be used for single-ion implantation of shallow phosphorus atoms [12]. Our integrated p–i–n detectors are configured with on n-type backplane and two p-type frontside electrodes. The detectors are characterized to yield 100% charge-collection efficiency in a 10- μ m central region terminated by 5 nm of high-quality oxide. After optimizing our system in terms of signal-to-noise ratio, we have achieved detection of single 14 keV phosphorus ions with 98% confidence, meaning that 98% of all ion impacts will result in a signal well resolved over the noise threshold.

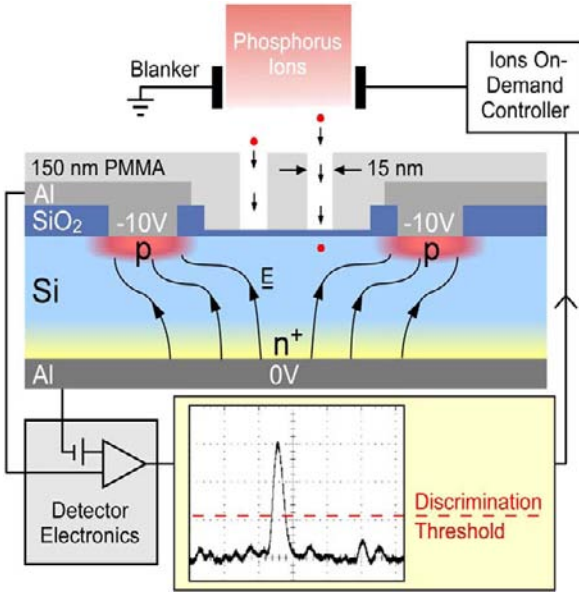


Fig. 4. Single-ion implantation scheme using integrated p-i-n detectors and a nanopatterned aperture mask. Electron-hole pairs generated by each ion impact are picked up by the detector electrodes under strong reverse biasing. The resulting microsecond charge transient is amplified in order to monitor each phosphorus ion impact

Integration with Nanofabrication

Some effort has gone into integrating our single-ion implantation technology with general nanofabrication based on electron-beam lithography [13]. For positioning, we make use of nanopatterned implantation masks with lithographically defined apertures of 15–20 nm diameter in 150-nm thick PMMA layers. The integrity of such masks is checked, both on detectors with no apertures and others with hundreds of apertures. The actual experimental devices are implanted through single apertures, or pairs of apertures separated by 50 nm. After implantation, a rapid thermal anneal at 1000°C is carried out in order to remove damage and activate the phosphorus donors. The resulting positional accuracy is estimated to be better than 20 nm, considering aperture size, straggle of the implanted ions, and diffusion during thermal treatment.

3 Charge Sensing with Superconducting RF-SETs

In order to perform measurements of single-electron charge and spin states in our atomically doped silicon devices, we make use of superconducting RF-SETs. The particular type of SET used in our experiments is based on a small island with overlapping tunnel junctions formed by aluminum double-angle evaporation with an intermediate oxidation step. Such RF-SETs have already been established as extremely sensitive and fast charge sensors approaching quantum-limited detection [14, 15].

3.1 Layout and Performance of RF-SET Measurements

The RF-SET measurements are performed as reflectometry on a resonant tank circuit consisting of a surface-mount inductor, the onchip parasitic capacitance, and the impedance represented by the SET itself. The tank circuit as well as bias-tees and several filters are mounted at millikelvin temperature in a dilution refrigerator with a 40-dB low-temperature HEMT preamplifier

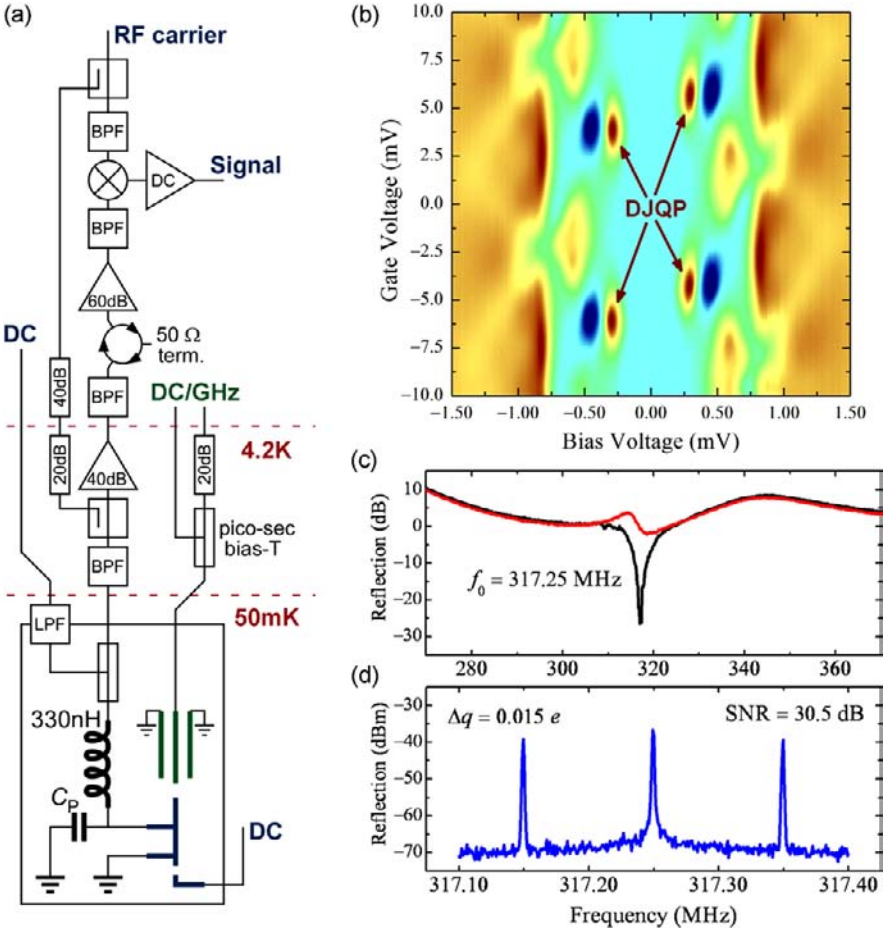


Fig. 5. (a) Experimental layout for RF reflectometry on resonant tank circuit formed by surface-mount inductor, onchip parasitic capacitance, and where the SET impedance represents a variable damping. (b) Reflected signal in color scale showing Coulomb diamonds of superconducting SET with extremely sensitive double Josephson quasiparticle peaks (DJQP). (c) Tuning of the tank circuit resonance from zero bias (*black*) to finite bias (*red*). (d) Signal-to-noise ratio of side bands under 100-kHz gate modulation yields a charge sensitivity of $10 \mu e / \sqrt{\text{Hz}}$

(300–400 MHz) at liquid helium temperature as illustrated in Fig. 5a. Reflectance measurements are performed by coupling in a carrier signal while amplifying the reflected signal and demodulating the response by mixing the two signals at room temperature.

The tank circuit works to match the 50–150 k Ω impedance of the SET to the 50- Ω impedance of the connected RF circuitry. The measured reflectance simply indicates how poorly the combined tank circuit is matched to 50 Ω , and is particularly sensitive at resonance. The resonance frequency of the tank circuit is determined by the inductance and parasitic capacitance alone as

$$\omega_0 = \frac{1}{\sqrt{LC_P}}, \quad (4)$$

while the impedance of the SET simply works to damp the resonance, thereby changing the Q-value of the resonator.

An example of Coulomb diamonds for one of our superconducting SETs is shown in Fig. 5b as reflected RF signal versus both gate and bias voltage. Figure 5c shows the corresponding change in the tank circuit resonance as the differential resistance of the SET changes from high to low. One feature of particular interest is the Josephson quasiparticle peak (DJQP) where the response is extremely sensitive in both gate and bias voltage [16]. This peak is due to a particular sequential tunneling process involving three quasiparticles, correlated through the Josephson coupling [17]. For charge sensing, the optimal sensitivity is achieved when operating at the edge of the DJQP in gate voltage. The charge sensitivity is measured by adding a gate modulation that induces fractions of an electron on the island as illustrated in Fig. 5d. Typical sensitivity values for our superconducting RF-SETs are in the range 5–15 $\mu\text{e}/\sqrt{\text{Hz}}$.

Charge Transfer in Atomically Doped Devices

Our ongoing research concentrates on RF-SET detected single-electron transfer in atomically doped silicon devices. A series of experiments is carried out to resolve some of the important energy- and timescales for qubits based on individual phosphorus donors. These experiments include both time-resolved measurements of single-electron transfer as well as spectroscopy by means of microwave-induced resonant transfer. Here, the spectroscopy may present new knowledge about the energy levels of such donor-based molecular structures, whereas the time-resolved studies may yield information about the relevant relaxation times for such quantum systems. Common for both types of experiment is that they are the first to address the relevant coupling strengths (coherent and incoherent) for charge qubits based on phosphorus donor pairs in silicon.

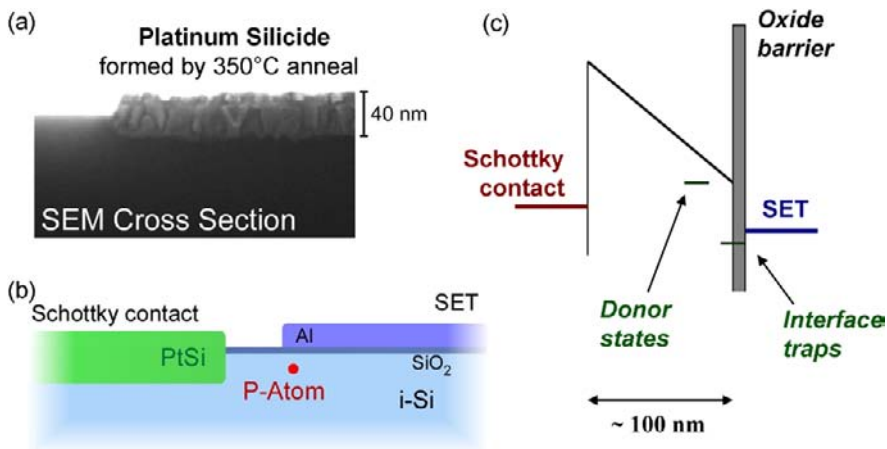


Fig. 6. (a) PtSi formed by thermal reaction of 25 nm Pt with a silicon substrate. (b) Device layout for studies of tunneling between nanoscale Schottky contacts and individual dopant atoms. (c) Simplified 1D potential landscape between the Schottky contact and SET with triangular Schottky barrier (0.6–0.8 eV) and possible localized states in terms of shallow donors and deep traps at the oxide interface

4 Initialization and Readout with Schottky Contacts

One challenging aspect of quantum computing with individual dopant atoms is the initialization of single-electron charge and spin states. For charge qubits based on phosphorus donor pairs, it is of particular importance to prepare the single-electron occupancy of the P_2^+ molecule. For this purpose, we employ a scheme for populating and depopulating individual dopant atoms by means of nanoscale Schottky contacts. Apart from charge initialization, there could also be scope for using such tunneling events for readout of single-electron spins on individual dopant atoms.

4.1 Contacting Atomically Doped Devices

Standard contacts achieved by heavy doping are not ideal for atomic devices, because of the random dopants that are introduced in the vicinity of the implanted regions [18]. Another scheme for contacting nanoscale silicon devices is the use of transition-metal silicide compounds. In particular, PtSi has been suggested in the context of Schottky barrier MOSFETs with nanoscale channel lengths [19]. In our devices PtSi Schottky contacts are used to populate and depopulate individual phosphorus donors.

We form our PtSi contacts by reaction of a 25-nm platinum layer deposited directly onto the silicon substrate after HF etching, where a lithographic pattern is used for both etching and metal lift-off. The silicide is formed during a 350°C forming-gas anneal, known to yield a stoichiometric compound with

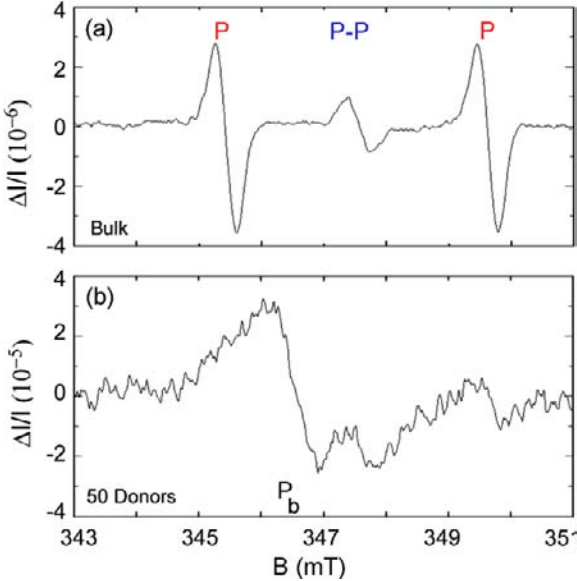


Fig. 7. Resonant change in photocurrent as a function of applied magnetic field for, (a) a bulk doped sample and, (b) a sample with 50 donors implanted. Microwaves in the X-band were applied. Visible in (a) are the two Si:P hyperfine split resonances as well as a central line arising from strongly exchange coupled donor pairs. Trace (b) shows an additional feature around 346 mT that is attributed to the P_b defect, a Si dangling bond near the interface

few defects [20]. The process takes place by diffusion of silicon into platinum rather than the other way around. Together with the high stability of the one-to-one stoichiometric silicide, this results in a noncritical process that introduces very few defects into the silicon substrate. By integrating this process with our single-ion implantation and aluminum SETs, we are able to study single-electron tunneling in atomically doped devices with nanoscale Schottky contacts (Fig. 6b).

In our experiments, we use the potential of the Schottky contact itself to induce single-electron transfer, as detected by a nearby RF-SET. The concept is illustrated by the potential landscape in Fig. 6c. A series of experiments are carried out to study the dynamical response of such single-electron transfer events. By resolving the relevant energy- and timescales, we wish to deduce the origin as either shallow donor states or interface-bound states.

5 Magnetic Resonance in Nanoscale Implanted Devices

To extend the above work to manipulation of a small number of electron spins, we have combined nanoscale devices with the electrical detection of magnetic resonance (EDMR). In EDMR, the electrical current through a semiconducting sample is monitored as electron-spin resonance (ESR) is induced. Due to spin-dependent transport processes, the current through the sample changes when the resonant conditions are satisfied, allowing sensitive detection of the magnetic resonance.

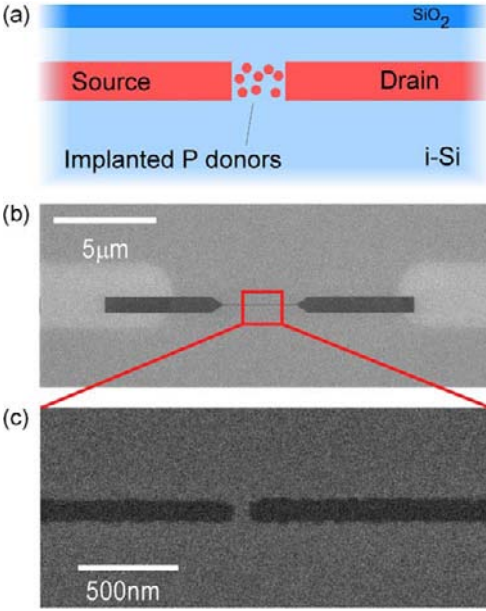


Fig. 8. (a) Schematic side view of the devices used for EDMR. Two degenerately doped leads connect to a sample region with ~ 50 implanted donors. (b) SEM top view of the device after implantation and before annealing, showing the diffused contacts (*light*) and the implanted extensions (*dark*). (c) SEM of the gap ($100 \times 100 \text{ nm}^2$) into which the dilute implant was performed

As an example, a bulk-doped wafer with phosphorus content 10^{17} cm^{-3} was contacted by degenerately doped ohmic contacts. Photoconductivity measurements were performed at 5 K by monitoring the current change with a lockin amplifier at magnetic field modulation ($\sim 1 \text{ kHz}$). Figure 7a shows the change in conductivity for the bulk-doped wafer as a function of applied magnetic field. Clearly visible are the two hyperfine phosphorus resonances, separated by 4.2 mT, as well as a central resonance associated with pairs of strongly exchange coupled phosphorus donors. The relative change in photocurrent for this sample was $\sim 3 \times 10^{-6}$ at resonance. In contrast to conventional ESR, where the signal intensity is directly proportional to the number of phosphorus atoms in the sample, the resonant current change observed here also depends on the recombination dynamics as well as on the sample geometry and cannot be used as easily to determine the number of donors involved.

To more quantitatively determine the influence of the smaller number of donors on the spin-dependent transport, we use a similar approach to that outlined above. For these studies, devices with a well-known number of phosphorus atoms were fabricated via ion implantation into highly resistive Si substrates. Highly doped source and drain leads were defined as small as 100 nm in width with a 100-nm gap. Into this gap 50 ± 7 phosphorus donors were implanted, as determined from the size of the PMMA aperture and the implant dose. A schematic of the device and SEM images of the implanted regions are shown in Fig. 8.

Figure 7b shows an example of the EDMR spectra obtained for these samples [21]. Here, the hyperfine-split phosphorus resonance is visible on the high magnetic field side. However, a large resonance obscures the low-field phosphorus resonance. This additional resonance can be identified from its g-factor as the P_b defect at the Si/SiO₂ interface [22]. The differences in relative intensities of the phosphorus and P_b resonances in Figs. 7a and b most likely arise from the stronger restriction of the current to the interface region in the ion-implanted device. Furthermore, different annealing procedures will lead to varying interface defect densities, manifested also as higher absolute photoconductivity in the bulk sample.

In the present samples, the current path is restricted only by the lower resistance through the implanted leads, and as a result a fraction of the photocurrent is able to flow around the gap region. To ensure that the signal observed was not due to the straggle at the edge of the implanted leads, additional devices were fabricated using arsenic as the donor for both the leads and ohmic contacts. These devices show that the maximum number of donors that we detect is less than 100.

To improve the signal, and reduce the effect of these shunt currents, geometrical restriction of the current paths would allow the current to be completely confined to the gap region, which should lead to larger relative current changes on resonance. This may be achieved for example by using silicon nanowires etched into SOI material.

Summary and Outlook

To summarize, nanoscale devices have been fabricated containing as few as 50 phosphorus donors in a nondegenerately doped region between degenerately doped source and drain leads. These donors were shown to influence the photocurrent flowing through the device when performing ESR.

Finally, it is important to note that EDMR also can be used as a tool to investigate the coherent manipulation of donor electrons. Recent work has demonstrated the ability to electrically detect coherent Rabi oscillations of an ensemble of phosphorus donors in silicon by pulsed EDMR [23, 24]. A combination of such pulsed magnetic resonance techniques with single-donor devices could be an interesting alternative route for experiments concerning detection of single-donor spin states.

Acknowledgements

Our work is funded by the Australian Research Council, the Australian Government and by the US National Security Agency and Army Research Office. The work at the Walter Schottky Institut was supported by Deutsche Forschungsgemeinschaft through SFB 631.

References

1. B.E. Kane, A silicon-based nuclear spin quantum computer. *Nature* **393**, 133–137 (1998) 170
2. L.C.L. Hollenberg, A.S. Dzurak, C. Wellard, A.R. Hamilton, D.J. Reilly, G.M. Milburn, R.G. Clark, Charge-based quantum computing using single donors in semiconductors. *Phys. Rev. B* **69**, 113301 (2004) 170, 171, 173
3. A.S. Dzurak et al., Charge-based silicon quantum computer architectures using controlled single-ion implantation, arXiv:cond-mat/0306265 (2003) 170, 171
4. L.C.L. Hollenberg, A.D. Greentree, A.G. Fowler, C.J. Wellard, Two-dimensional architectures for donor-based quantum computing. *Phys. Rev. B* **74**, 045311 (2006) 170
5. A.K. Ramdas, S. Rudriguez, Spectroscopy of the solid-state analogues of the hydrogen atom: donors and acceptors in semiconductors. *Rep. Prog. Phys.* **44**, 1297–1397 (1981) 171
6. W. Kohn, J.M. Luttinger, Theory of donor states in silicon. *Phys. Rev.* **98**, 915–922 (1955) 171
7. W.G. van der Wiel, S. De Franceschi, J.M. Elzerman, T. Fujisawa, S. Tarucha, L.P. Kouwenhoven, Electron transport through double quantum dots. *Rev. Mod. Phys.* **75**, 1–22 (2003) 171
8. T. Hayashi, T. Fujisawa, H.D. Cheong, Y.H. Jeong, Y. Hirayama, Coherent manipulation of electronic states in a double quantum dot. *Phys. Rev. Lett.* **91**, 226804 (2003) 172
9. J.R. Petta, A.C. Johnson, C.M. Marcus, M.P. Hanson, A.C. Gossard, Manipulation of a single charge in a double quantum dot. *Phys. Rev. Lett.* **93**, 186802 (2004) 172
10. C.J. Wellard, L.C.L. Hollenberg, S. Das Sarma, Theory of the microwave spectroscopy of a phosphorus-donor charge qubit in silicon: coherent control in the Si:P quantum-computer architecture. *Phys. Rev. B* **74**, 075306 (2006) 173
11. X. Hu, B. Koiller, S. Das Sarma, Charge qubits in semiconductor quantum computer architecture: tunnel coupling and decoherence. *Phys. Rev. B* **71**, 235332 (2005) 173
12. D.N. Jamieson et al., Controlled shallow single-ion implantation in silicon using an active substrate for sub-20-keV ions. *Appl. Phys. Lett.* **86**, 202101 (2005) 173
13. M. Mitic et al., Single atom Si nanoelectronics using controlled single-ion implantation. *Microelectron. Eng.* **78–79**, 279–286 (2005) 174
14. R.J. Schoelkopf, P. Wahlgren, A.A. Kozhevnikov, P. Delsing, D.E. Prober, The radio-frequency single-electron transistor (RF-SET): a fast and ultrasensitive electrometer. *Science* **280**, 1238–1242 (1998) 174

15. A. Aassime, D. Gunnarsson, K. Bladh, P. Delsing, Radio-frequency single-electron transistor: toward the shot-noise limit. *Appl. Phys. Lett.* **79**, 4031–4033 (2001) 174
16. A.A. Clerk, S.M. Girvin, A.K. Nguyen, A.D. Stone, Resonant Cooper-pair tunneling: quantum noise and measurement characteristics. *Phys. Rev. Lett.* **89**, 176804 (2002) 176
17. T.A. Fulton, P.L. Gammel, D.J. Bishop, L.N. Dunkleberger, G.J. Dolan, Observation of combined Josephson and charging effects in small tunnel junction circuits. *Phys. Rev. Lett.* **63**, 1307–1310 (1989) 176
18. D.N. Jamieson et al., Quantum effects in ion implanted devices. *Nucl. Instrum. Methods Phys. Res. B* **249**, 221–225 (2006) 177
19. C. Wang, J.P. Snyder, J.R. Tucker, Sub-40 nm PtSi Schottky source/drain metal-oxide-semiconductor field-effect transistors. *Appl. Phys. Lett.* **74**, 11741176 (1999) 177
20. G. Larrieu, E. Dubois, X. Wallart, X. Baie, J. Katcki, Formation of platinum-based silicide contacts: kinetics, stoichiometry, and current drive capabilities. *J. Appl. Phys.* **94**, 7801–7810 (2003) 178
21. D.R. McCamey, H. Huebl, M.S. Brandt, W.D. Hutchison, J.C. McCallum, R.G. Clark, A.R. Hamilton, Electrically-detected magnetic resonance in ion-implanted Si:P nanostructures. *Appl. Phys. Lett.* **89**, 182115 (2006) 180
22. A. Stesmans, V.V. Afanas'ev, Electron spin resonance features of interface defects in thermal (100)Si/SiO₂. *J. Appl. Phys.* **83**, 2449–2457 (1998) 180
23. C. Boehme, K. Lips, Electrical detection of spin coherence in silicon. *Phys. Rev. Lett.* **91**, 246603 (2003) 180
24. A.R. Stegner, C. Boehme, H. Huebl, M. Stutzmann, K. Lips, M.S. Brandt, Electrical detection of coherent ³¹P spin quantum states. *Nat. Phys.* **2**, 835–838 (2006) 180

Index

contacts, 177

EDMR, 178–180

electrical detection of magnetic resonance (EDMR), 178

electron-spin resonance (ESR), 178

electronic levels of the phosphorus donor, 171

ESR, 180

initialization, 177

ion implantation, 173

Kohn and Luttinger, 171

PtSi Schottky, 177

Rabi oscillations, 173, 180

radio-frequency single-electron transistors (RF-SETs), 169

readout, 170, 177

RF-SETs, 174

single-ion implantation, 173, 174

Electron Spin as a Spectrometer of Nuclear-Spin Noise and Other Fluctuations

Rogério de Sousa

Department of Physics, University of California, Berkeley, CA 94720, USA
rdesousa@uvic.ca*

Abstract. This chapter establishes the relationship between low-frequency noise and coherence decay of localized spins in semiconductors, as measured by a number of different pulse spin resonance sequences. A general relationship between an arbitrary noise spectral function and spin phase relaxation is derived, allowing microscopic calculations of electron spin-echo decay due to the magnetic noise produced by interacting nuclear spins. The electron–nuclear spin Hamiltonian is reviewed, including isotropic and anisotropic hyperfine interactions, internuclear dipolar interactions, and the effective nuclear–nuclear coupling mediated by the electron-spin hyperfine interaction. A microscopic calculation of the nuclear-spin noise spectrum arising due to nuclear–nuclear dipolar flip-flops is presented. We compare our explicit numerical results to electron spin-echo decay experiments of phosphorus impurities embedded in natural and in nuclear-spin-enriched silicon.

1 Introduction

Although the study of electron-spin dynamics using pulse electron-spin resonance is an established research field [1], many theoretical questions regarding the microscopic mechanisms for reversible and irreversible decay of spin coherence remain open. Recently, the quest toward scalable quantum computation using electron spins [2, 3] gave new impetus to pulse spin resonance, and sparked major experimental progress toward control and detection of individual electron spins in the solid-state environment [4–8].

The microscopic understanding of the mechanisms leading to electron-spin energy and phase relaxation, and the question of how to control these processes is central to the research effort in spin-based quantum computation. The goal of theory is to achieve microscopic understanding so that spin coherence can be controlled either from a materials perspective (i.e., choosing the best nanostructure for spin manipulation and dynamics) or from the design of efficient pulse sequences that reach substantial coherence enhancement without a high overhead in the number of pulses and energy deposition.

* Present address: Department of Physics and Astronomy, University of Victoria, Victoria, BC, Canada V8W 3P6

(The latter is particularly important in the context of low-temperature experiments where undesired heating from the microwave excitations must be avoided).

One has to be careful in order to distinguish the timescales characterizing electron-spin coherence. It is customary to introduce three timescales, T_1 , T_2^* , and T_2 . For localized electron spins, these timescales usually differ by many orders of magnitude, because each is dominated by a different physical process. T_1 is the $1/e$ decay time for the spin magnetization along the external magnetic-field direction. As an example, T_1 of a phosphorus donor impurity in silicon is of the order of a thousand seconds at low temperatures and moderate magnetic fields ($T = 4\text{ K}$ and $B = 0.3\text{ T}$) [9]. These long T_1 s are explained by noting that the spin-orbit interaction produces a small admixture of spin-up/down states; the electron-phonon interaction couples these admixtures leading to $\frac{1}{T_1} \propto B^5$ at low temperatures [10–12]. T_1 is generally long because a spin-flip in a magnetic field requires energy exchange with the lattice via phonon emission. The timescales T_2^* and T_2 are instead related to phase relaxation, and hence do not require transmission of energy to the lattice. Here, T_2^* is the $1/e$ decay time of the precessing magnetization in a free induction decay (FID) experiment ($\pi/2$ - t -measure, where $\pi/2$ denotes a spin rotation around the x -axis). Hence, T_2^* is the decay time of the total inplane magnetization of an ensemble of spins separated in space or time (e.g., a group of impurities separated in space, or the time-averaged magnetization of a single spin, as discussed in Sect. 2.3 below). For a phosphorus impurity in natural silicon, $T_2^* \approx 20\text{ ns}$ due to the distribution of frozen hyperfine fields, that are time independent within the measurement window of the experiment. The T_2^* decay is reversible, because the ensemble inplane magnetization is almost completely recovered by applying a spin-echo pulse sequence. In this review we define T_2 as the $1/e$ decay time of a Hahn echo ($\pi/2$ - τ - π - τ -echo). The irreversible decoherence time T_2 is caused by uncontrolled time-dependent fluctuations within each time interval τ . For a phosphorus impurity in natural silicon, we have $T_2 \approx 0.3\text{ ms}$ [13], four orders of magnitude longer than T_2^* .

The discussion above clearly indicates that the resulting coherence times are critically dependent on the particular pulse sequence chosen to probe spin dynamics. In Sect. 2 we show that spin coherence can be directly related to the spectrum of electron-spin phase fluctuations and a filter function appropriate for the particular pulse sequence. The phase of a precessing electron spin is a sensitive probe of magnetic fluctuations. This gives us the opportunity to turn the problem around and view pulse electron-spin resonance as a powerful tool enabling the study of low-frequency magnetic fluctuations arising from complex many-body spin dynamics in the environment surrounding the electron spin.

A particularly strong source of magnetic noise arises due to the presence of nuclear spins in the sample. It is in fact no surprise that the dominant mech-

anism for nuclear spin-echo [14] and electron spin-echo decay [15, 13] has long been related to the presence of nonresonant nuclear-spin species fluctuating nearby the resonant spin. Nevertheless, the theoretical understanding of these experiments was traditionally centered on phenomenological approaches [16–18], whereby the electron phase is described as a Markovian stochastic process with free parameters that can be fitted to experiment (this type of process has been traditionally denoted spectral diffusion, since the spin resonance frequency fluctuates along the resonance spectrum in a similar way to how a Brownian particle diffuses in real space).

Recently, we embarked on an effort aimed at understanding the mechanism of electron-spin decoherence due to nuclear spins from a fully microscopic point of view. In [19] we developed a semiclassical model for electron spin-echo decay based on the assumption that the relevant nuclear-spin dynamics results from pair “flip-flops”, where the spin of two nuclei located close to each other is exchanged due to their mutual dipolar interaction (Fig. 1). The flip-flop processes lead to fluctuations in the nuclear spin hyperfine field seen by the localized electron (e.g., a donor impurity or a quantum dot in a semiconductor). The semiclassical theory is based on the assumption that each flip-flop can be described by a random telegraph noise process (a phenomenological assumption), but with relaxation parameters that can be derived theoretically from a microscopic theory based on the nuclear-spin dipolar evolution. Therefore, this theory describes the irreversible decay of the effective hyperfine field produced by a pair of nuclear spins on the electron

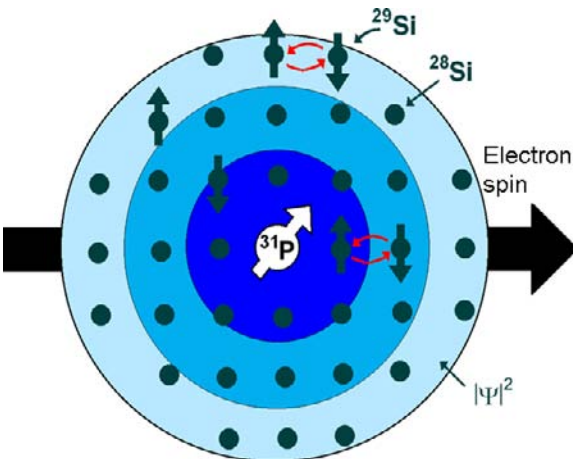


Fig. 1. The electron spin of a donor impurity in silicon is sensitive to the magnetic noise produced by nuclear spins within its wavefunction. When two ^{29}Si isotopes are close to each other, their nuclear-spin states may flip-flop due to their mutual dipolar interaction. These flip-flop events produce time-dependent fluctuations in the electron’s hyperfine field, leading to phase relaxation and spin-echo decay

spin. Comparison with experiment [13, 20–23] suggested reasonable order-of-magnitude agreement for the $1/e$ echo decay time (within a factor of 3) but poor qualitative agreement for the time dependence of the echo envelope. The next step was to develop a full quantum theory for the nuclear-spin dynamics affecting the electron spin. In [24] a cluster expansion method was developed to calculate echo decay due to the closed-system dynamics of a group of dipolar coupled nuclear spins, without any stochastic assumption about the nuclear-spin dynamics. At lowest order in this cluster expansion the qualitative and quantitative agreement with experimental data was quite good.

In Sect. 4 we develop a fully microscopic theory for the nuclear-spin noise spectrum arising due to pair flip-flops induced by the internuclear dipolar interaction. This allows us to give an elegant and simple derivation of the lowest-order cluster expansion results of [24] and to interpret these results from the point of view of nonequilibrium statistical mechanics. The full noise spectrum is expressed as a sum of delta-function contributions corresponding to isolated pair flip-flop transitions. We then show that irreversibility can be incorporated into the pair flip-flop processes by adding broadening to these sharp transitions, in a mean-field-like approach. Using the method of moments we are able to calculate these broadenings exactly (at infinite temperature). We show explicit numerical results for the noise spectrum affecting a donor impurity in silicon and compare the improved theory with echo-decay experiments in natural [21] and nuclear-spin-enriched samples [22].

2 Noise, Relaxation, and Decoherence

When the coupling between the spin qubit and the environment is weak, we may write a linearized effective Hamiltonian of the form

$$\mathcal{H}(t) = \frac{1}{2}\gamma B\sigma_z + \frac{1}{2} \sum_{q=x,y,z} \hat{\eta}_q(t)\sigma_q, \quad (1)$$

where $\mathbf{B} \parallel \hat{z}$ is a static (time-independent) magnetic field, γ is a gyromagnetic ratio in units of $(\text{sG})^{-1}$ (we set $\hbar = 1$ so that energy has units of frequency), σ_q for $q = x, y, z$ are the Pauli matrices describing qubit observables and $\hat{\eta}_q(t)$ represents the environmental (bath) degrees of freedom.

2.1 The Bloch–Wangsness–Redfield Master Equation

In order to describe the long-time dynamics we may take the limit $t \rightarrow \infty$. Such an approximation is appropriate provided $t \gg \tau_c$, where τ_c is a typical correlation time for bath fluctuations (later we will define τ_c properly and relax the long-time approximation). In this case, spin dynamics can be described by the Bloch–Wangsness–Redfield theory. The average values of

the Pauli operator satisfy a Master equation (for a derivation see Sect. 5.11 of [26])

$$\frac{d}{dt}\langle\boldsymbol{\sigma}\rangle = \gamma\mathbf{B} \times \langle\boldsymbol{\sigma}\rangle - \frac{1}{T_1}\langle\sigma_z\rangle\hat{\mathbf{z}} - \frac{1}{T_{2x}}\langle\sigma_x\rangle\hat{\mathbf{x}} - \frac{1}{T_{2y}}\langle\sigma_y\rangle\hat{\mathbf{y}}, \quad (2)$$

with

$$\frac{1}{T_1} = \frac{\pi}{2} \sum_{q=x,y} [\tilde{S}_q(+\gamma B) + \tilde{S}_q(-\gamma B)], \quad (3)$$

$$\frac{1}{T_{2x}} = \frac{\pi}{2} [\tilde{S}_y(+\gamma B) + \tilde{S}_y(-\gamma B)] + \pi\tilde{S}_z(0), \quad (4)$$

$$\frac{1}{T_{2y}} = \frac{\pi}{2} [\tilde{S}_x(+\gamma B) + \tilde{S}_x(-\gamma B)] + \pi\tilde{S}_z(0). \quad (5)$$

Here, the noise spectrum is defined as

$$\tilde{S}_q(\omega) = \frac{1}{2\pi} \int_{-\infty}^{\infty} e^{i\omega t} \langle \hat{\eta}_q(t) \hat{\eta}_q(0) \rangle dt. \quad (6)$$

In (3)–(5) we assume $\langle \hat{\eta}_q(t) \hat{\eta}_{q'}(0) \rangle = 0$ for $q \neq q'$. These equations are the generalization of Fermi's golden rule for coherent evolution. From (2) we may show that the coherence amplitude $|\langle \sigma_+ \rangle| = |\langle \sigma_x + i\sigma_y \rangle|/2$ in a FID experiment decays exponentially with a rate given by

$$\frac{1}{T_2^*} = \frac{1}{2} \left(\frac{1}{T_{2x}} + \frac{1}{T_{2y}} \right) = \frac{1}{2T_1} + \pi\tilde{S}_z(0). \quad (7)$$

In contrast, T_1 is the timescale for $\langle \sigma_z \rangle$ to approach equilibrium, i.e., T_1 is the energy relaxation time. According to (7) we have $T_2^* \leq 2T_1$. Note that T_1 depends on the noise spectrum only at frequencies $+\gamma B$ and $-\gamma B$, a statement of energy conservation. Positive frequency noise can be interpreted as processes where the qubit decays from \uparrow to \downarrow and the environment absorbs an energy quantum γB , while negative frequency noise refers to qubit excitation (from \downarrow to \uparrow) when the environment emits a quantum γB . The correlation time τ_c can be loosely defined as the inverse cutoff for $\tilde{S}_q(\omega)$, i.e., for $\omega \gg 1/\tau_c$ we may approximate $\tilde{S}_q(\omega) \approx 0$.

The Master equation [see (2)] leads to a simple exponential time dependence for all qubit observables. Actually this is not true in many cases of interest, including the case of a phosphorus impurity in silicon where this approximation fails completely (for Si:P the observed free induction decay is approximately $\exp[-(t/T_2^*)^2]$, while the echo can be fitted to $\exp[-(2\tau/T_2)^{2.3}]$). The problem lies in the fact that the $t \rightarrow \infty$ assumption averages out finite frequency fluctuations; note that T_2^* differs from T_1 only via static noise [$\tilde{S}_z(0)$ in (7)]. A large number of pulse spin-resonance experiments are sensitive to finite frequencies only, the most notable example being the spin echo, which is able to remove $\tilde{S}_z(0)$ completely. Therefore, one must develop a theory for coherent evolution that includes finite frequency fluctuations.

We may develop a theory for spin coherence that takes into account low-frequency fluctuations in the semiclassical regime $\hbar\omega \ll k_B T$, when $\tilde{S}_z(-\omega) = e^{-\hbar\omega/k_B T} \tilde{S}_z(\omega) \approx \tilde{S}_z(\omega)$. This is equivalent to assuming $S_z(t) = \langle \hat{\eta}_z(t) \hat{\eta}_z(0) \rangle \approx \langle \hat{\eta}_z(0) \hat{\eta}_z(t) \rangle = S_z(-t)$, or that $\hat{\eta}_z$ commutes at different times. In practice, the semiclassical approximation allows us to map $\hat{\eta}_z$ into a classical stochastic process.

To obtain analytical results we must further specialize to the pure dephasing limit $\hat{\eta}_q = 0$ for $q = x, y$ and we must assume $\hat{\eta}_z$ is distributed according to Gaussian statistics. For many realistic problems the pure dephasing limit turns out to be a good approximation to describe phase relaxation. A common situation is that the neglected components $\tilde{S}_{x,y}(\omega)$ are much smaller than $\tilde{S}_z(\omega)$ for positive frequencies much smaller than the qubit energy splitting. For example, in the case of a localized electron spin in a semiconductor, $\tilde{S}_{x,y}(\omega) \propto \omega^5$ due to the combination of the spin-orbit and electron-phonon interactions [12]. As a result, $\tilde{S}_{x,y}(\omega) \ll \tilde{S}_z(\omega)$ as $\omega \rightarrow 0$. The Gaussian approximation is described below.

2.2 Finite Frequency Phase Fluctuations and Coherence Decay in the Semiclassical-Gaussian Approximation

In many cases of interest, the environmental variable $\hat{\eta}_z$ is a sum over several dynamical degrees-of-freedom, and measurement outcomes for the operator $\hat{\eta}_z$ may assume a continuum of values between $-\infty$ and $+\infty$.¹ In those situations we can often resort to the central limit theorem that states that the statistics for outcomes η' follows a Gaussian distribution,

$$P[\hat{\eta}_z(t) = \eta'] = \frac{1}{\sqrt{2\pi\Delta^2}} \exp\left(-\frac{\eta'^2}{2\Delta^2}\right), \quad (8)$$

with a stationary (time-independent) variance given by $\Delta^2 = \langle \hat{\eta}_z^2(t) \rangle$. Here, $\langle A \rangle = \text{Tr}\{\hat{\rho}_B A\}$ is a thermal average taken over all bath degrees-of-freedom ($\hat{\rho}_B \propto e^{-\mathcal{H}_B/k_B T}$ is the canonical density matrix for the bath). We also assume $\langle \hat{\eta}_z(t) \rangle = 0$, since any constant drift in the noise can be incorporated in the effective B field.

Our problem is greatly simplified if we relate the operator $\hat{\eta}_z$ to a Gaussian stochastic process $\eta'(t)$ in the following way. For each time t , $\eta'(t)$ corresponds to a classical random variable, that can be interpreted as the *outcome of measurements performed by the qubit on the environment*. This allows us take averages over the bath states using (8). Note that the statement ‘‘Gaussian’’ noise refers specifically to the distribution of noise amplitudes, that is not necessarily related to the spectrum of fluctuations (see below).

¹ An important exception is the observation of individual random telegraph noise fluctuators in nanostructures (in this case $\hat{\eta} = \pm\eta'$ assumes only two discrete values). This results in important non-Gaussian features in qubit evolution.

Our simplified effective Hamiltonian leads to the following evolution operator [recall that we set $\hat{\eta}_{x,y} \equiv 0$ in (1)]

$$\mathcal{U}_\eta(t, 0) = e^{-i \int_0^t dt' \mathcal{H}(t')} = e^{-\frac{i}{2} \sigma_z [Bt + \int_0^t \eta'(t') dt']} = e^{-\frac{i}{2} \sigma_z [Bt + X_\eta(t)]}, \quad (9)$$

where we define

$$X_\eta(t) = \int_0^t \eta'(t') dt'. \quad (10)$$

Here, the subscript η emphasizes that this operator is a functional of the trajectory $\eta'(t')$. The effect of the distribution of trajectories η' can be described by assuming the qubit evolves according to the density matrix²

$$\rho(t) = \sum_\eta p_\eta \mathcal{U}_\eta(t, 0) \rho_0 \mathcal{U}_\eta^\dagger(t, 0), \quad (11)$$

where p_η denotes the appropriate weight probability for each environmental trajectory and ρ_0 is the $t = 0$ density matrix for the qubit. The coherence envelope at time t averaged over all possible noise trajectories is then

$$\begin{aligned} \langle\langle \sigma_+(t) \rangle\rangle &= \text{Tr}\{\sigma_+ \rho(t)\} \\ &= \sum_\eta p_\eta \text{Tr}\{\mathcal{U}_\eta^\dagger(t, 0) \sigma_+ \mathcal{U}_\eta(t, 0) \rho_0\} \\ &= e^{iBt} \sum_\eta p_\eta e^{iX_\eta(t)} \text{Tr}\{\sigma_+ \rho_0\} \\ &= \langle e^{iX_\eta(t)} \rangle e^{iBt} \text{Tr}\{\sigma_+ \rho_0\}, \end{aligned} \quad (12)$$

where we used the identity $e^{i\alpha\sigma_z} \sigma_+ e^{-i\alpha\sigma_z} = e^{2i\alpha} \sigma_+$. Here, the double average $\langle\langle \cdot \rangle\rangle$ denotes a quantum-mechanical average over the qubit basis plus an ensemble average over the noise trajectories $\eta'(t)$. We can evaluate the coherence amplitude explicitly by noting that the random variable $X(t) = \int_0^t \eta'(t') dt'$ is also described by a Gaussian distribution, but with a time-dependent variance given by $\sigma_t = \langle X^2(t) \rangle$. Therefore, we have

$$\langle e^{iX_\eta(t)} \rangle = \int_{-\infty}^{\infty} \frac{1}{\sqrt{2\pi\sigma_t}} e^{-\frac{X^2}{2\sigma_t^2}} e^{iX} = e^{-\frac{1}{2}\sigma_t^2}, \quad (13)$$

with σ_t given by

$$\begin{aligned} \sigma_t^2 &= \int_0^t dt_1 \int_0^t dt_2 \langle \eta'(t_1) \eta'(t_2) \rangle \\ &= 2 \int_0^t dt_1 \int_0^{t_1} dt_2 \langle \eta'(t_1) \eta'(t_2) \rangle \\ &= 2 \int_0^t dt' \int_{t'/2}^{t-t'/2} dT \langle \eta'(T + t'/2) \eta'(T - t'/2) \rangle \end{aligned}$$

² This assumption is equivalent to the Kraus representation in the theory of open quantum systems.

$$= 2 \int_0^t (t - t') S(t') dt'. \quad (14)$$

Here, we introduced the time-dependent correlation function $S(t') = \langle \eta'(T + t'/2) \eta'(T - t'/2) \rangle = \langle \eta(t') \eta(0) \rangle$, that is independent of a time translation T by virtue of the stationarity assumption.

It is straightforward to generalize (13) and (14) for echo decay. Instead of free evolution (denoted free induction decay in magnetic resonance), consider the Hahn echo given by the sequence $\pi/2 - \tau - \pi - \tau$ -echo. Here, the notation “ $\pi/2$ ” denotes a perfect, instantaneous 90° spin rotation around the x -axis (described by the operator $e^{-\frac{i}{4}\pi\sigma_x}$). The notation “ $-\tau$ ” means the spin is allowed to evolve freely for a time interval τ . “ π ” denotes a 180° spin rotation around the x -axis, also referred as a “ π -pulse” (this is described by the operator $e^{-\frac{i}{2}\pi\sigma_x} = -i\sigma_x$). The initial $\pi/2$ pulse prepares the qubit in the state $\rho_0 = |y+\rangle\langle y+|$, after which it is allowed to evolve freely for time τ , when the π -pulse is applied. After this pulse the qubit is allowed to evolve for a time interval τ again, after which the coherence echo is recorded. Hence, the evolution operator is given by

$$\mathcal{U}_{\text{Hahn}}(2\tau) = \mathcal{U}(2\tau, \tau)(-i\sigma_x)\mathcal{U}(\tau, 0). \quad (15)$$

The same procedure leading to (14) is now repeated in order to calculate the magnitude of the Hahn echo envelope at $t = 2\tau$. The quantum average is given by

$$\begin{aligned} \langle \sigma_+(2\tau) \rangle &= \text{Tr}\{\mathcal{U}^\dagger(\tau, 0)(i\sigma_x)\mathcal{U}^\dagger(2\tau, \tau)\sigma_+\mathcal{U}(2\tau, \tau)(-i\sigma_x)\mathcal{U}(\tau, 0)\rho_0\} \\ &= \text{Tr}\left\{\mathcal{U}^\dagger(\tau, 0)\sigma_x e^{i\int_\tau^{2\tau} dt'[B+\eta'(t')]} \sigma_+ \sigma_x \mathcal{U}(\tau, 0)\rho_0\right\} \\ &= \text{Tr}\left\{e^{i\int_\tau^{2\tau} dt'[B+\eta'(t')]} \mathcal{U}^\dagger(\tau, 0)\sigma_-\mathcal{U}(\tau, 0)\rho_0\right\} \\ &= e^{i\int_\tau^{2\tau} dt'[B+\eta'(t')]} e^{-i\int_0^\tau dt'[B+\eta'(t')]} \text{Tr}\{\sigma_-\rho_0\}. \end{aligned} \quad (16)$$

Therefore, the double average can be conveniently written as

$$\langle\langle \sigma_+(2\tau) \rangle\rangle = e^{-iB} \int_0^{2\tau} s(t') dt' \left\langle e^{-i\int_0^{2\tau} s(t') \eta'(t') dt'} \right\rangle \text{Tr}\{\sigma_-\rho_0\}, \quad (17)$$

with the introduction of an auxiliary echo function $s(t)$. For Hahn echo $s(t) = 1$ if $0 \leq t < \tau$ and $s(t) = -1$ if $t > \tau$. Note that the first term in (17) is exactly equal to one, because the Hahn echo is able to completely refocus a constant magnetic field. It is convenient to introduce the noise spectrum in (17) via $S(t) = \int e^{-i\omega t} \tilde{S}(\omega) d\omega$ in order to get the following expression for the coherence envelope

$$|\langle\langle \sigma_+(t) \rangle\rangle| = \exp\left[-\int_{-\infty}^{\infty} d\omega \tilde{S}(\omega) \mathcal{F}(t, \omega)\right]. \quad (18)$$

Here, we define a filter function that depends on the echo sequence $s(t')$,

$$\mathcal{F}(t, \omega) = \int_0^t dt' s(t') \int_0^{t'} dt'' s(t'') \cos [\omega(t' - t'')]. \quad (19)$$

For free induction decay [$s(t) \equiv 1$] we have

$$\mathcal{F}_{\text{FID}}(t, \omega) = \frac{1}{2} \frac{\sin^2(\omega t/2)}{(\omega/2)^2}. \quad (20)$$

Note that in the limit $t \rightarrow \infty$ (20) becomes $\pi\delta(\omega)t$, recovering the Bloch–Wangsness–Redfield result (7). The filter function for the Hahn echo becomes

$$\mathcal{F}_{\text{Hahn}}(2\tau, \omega) = \frac{1}{2} \frac{\sin^4(\omega\tau/2)}{(\omega/4)^2}. \quad (21)$$

Note that $\mathcal{F}_{\text{Hahn}}(2\tau, 0) = 0$. The Hahn echo filters out terms proportional to $\tilde{S}(0)$ in qubit evolution, this is equivalent to the well-known removal of inhomogeneous broadening by the echo. Any spin-resonance sequence containing instantaneous $\pi/2$ or π -pulses (not necessarily equally spaced) can be mapped into an appropriate filter function $\mathcal{F}(t, \omega)$. An important example is the class of Carr–Purcell sequences that can be used to enhance coherence.

General Results for the Short-Time Behavior

The short-time behavior can be derived quite generally when the time-dependent correlation function $S(t)$ is *analytic at $t = 0$* . In the semiclassical approximation $S(t) = S(-t)$, so an expansion about $t = 0$ leads to

$$\begin{aligned} S(t) &= \langle \eta'(t)\eta'(0) \rangle = \int_{-\infty}^{\infty} d\omega e^{-i\omega t} \tilde{S}(\omega) \\ &= \sum_{n=0}^{\infty} \frac{(-1)^n}{(2n)!} M_{2n} t^{2n}, \end{aligned} \quad (22)$$

with the $2n$ th moment of the noise spectrum defined as

$$M_{2n} = \int_{-\infty}^{\infty} d\omega \tilde{S}(\omega) \omega^{2n}. \quad (23)$$

Hence, if $S(t)$ is analytic at $t = 0$, we must have $M_{2n} < \infty$ for all n , i.e., the noise spectrum has a well-defined high-frequency cutoff [e.g., $S(\omega) \sim e^{-\omega/\Lambda}$ at high frequency]. It is important to keep in mind that the assumption of analyticity at $t = 0$ is actually quite restrictive. Physically, only $M_0 < \infty$ is required, so that $S(0) < \infty$ (this is the noise power or mean square deviation for η'). Important examples where $S(t)$ is not analytic at $t = 0$ include the Gauss–Markov model described below [see (26)].

If the $t = 0$ expansion exists we may immediately obtain the short-time behaviors for the free induction decay and Hahn echo:

$$\langle\langle \sigma_+(t) \rangle\rangle_{\text{FID}} = e^{-\int d\omega \tilde{S}(\omega) \frac{1}{2} \frac{\sin^2(\omega t/2)}{(\omega/2)^2}} \approx e^{-\frac{1}{2} M_0 t^2 + \frac{1}{24} M_2 t^4}, \quad (24)$$

$$\langle\langle\sigma_+(2\tau)\rangle\rangle_{\text{Hahn}} = e^{-\int d\omega \tilde{S}(\omega) \frac{1}{2} \frac{\sin^4(\omega\tau/2)}{(\omega/4)^2}} \approx e^{-\frac{1}{2}M_2\tau^4 + \frac{1}{12}M_4\tau^6}. \quad (25)$$

The short-time behavior described by (24) and (25) is *universal for noise spectra possessing a high-frequency cutoff*. Note the striking difference in time dependence: For free induction decay the coherence behaves as $\sim e^{-t^2}$, while for a Hahn echo we have $\sim e^{-\tau^4}$. This happens because the Hahn echo is independent of the mean square deviation $M_0 = S(0)$.

Example: The Gauss–Markov Model

The simplest model of Brownian motion assumes a phenomenological correlation function that decays exponentially in time,

$$S(t) = \Delta^2 \exp(-|t|/\tau_c), \quad (26)$$

where τ_c is a correlation time that describes the “memory” of the environmental noise.³ This model is useful, e.g., in liquid-state NMR in order to calculate the linewidths of a molecule diffusing across an inhomogeneous magnetic field. In that case, Δ becomes the typical field inhomogeneity, while the “speed” for diffusion is of the order of Δ/τ_c . The resulting environmental noise spectrum [Fourier transform of (26)] is a Lorentzian, given by

$$\tilde{S}(\omega) = \frac{\Delta^2 \tau_c}{\pi} \frac{1}{(\omega\tau_c)^2 + 1}. \quad (27)$$

We start by discussing free induction decay. Using (17) and (26) with $s(t') = 1$, we get

$$|\langle\langle\sigma_+(t)\rangle\rangle_{\text{FID}} = \exp\{-\Delta^2 \tau_c^2 [t/\tau_c + (e^{-t/\tau_c} - 1)]\}. \quad (28)$$

For $t \gg \tau_c$, (28) leads to

$$|\langle\langle\sigma_+(t)\rangle\rangle_{\text{FID}} \approx e^{-\Delta^2 \tau_c t}. \quad (29)$$

In this regime, the correlation function (26) can be approximated by a delta function, and the decay is a simple exponential signaling that a Master equation approach is appropriate [see (2)]. The coherence time is given by $T_2^* = 1/(\Delta^2 \tau_c)$. Interestingly, as $\tau_c \rightarrow 0$ with Δ finite, $T_2^* \rightarrow \infty$. This phenomenon is known as motional narrowing, inspired by the motion of molecules in a field gradient. The faster the molecule is diffusing, the narrower is its resonance line. Now, we look at the low-frequency noise limit, $t \ll \tau_c$. This leads to

$$|\langle\langle\sigma_+(t)\rangle\rangle_{\text{FID}} \approx e^{-\frac{1}{2}\Delta^2 t^2} \equiv e^{-(t/T_2^*)^2}. \quad (30)$$

³ Many authors use the terminology “Markovian dynamics” to denote evolution without memory, i.e., the limit $\tau_c \rightarrow 0$ in (26). This limit can be taken by setting $\Delta \rightarrow \infty$ with $\Gamma \equiv \Delta^2 \tau_c$ held finite. In that case we have $S(t) \rightarrow 2\Gamma\delta(t)$ resulting in a “white noise” spectrum and $\langle\sigma_+\rangle \propto e^{-\Gamma t}$.

In contrast to (29), the decay differs from a simple exponential and is independent of τ_c . This result is equivalent to an average over an ensemble of qubits at any specific time t (in other words, the linewidth $\Delta/\sqrt{2}$ and dephasing time $T_2^* = \sqrt{2}/\Delta$ are a consequence of inhomogeneous broadening). Therefore, the coherence decay is completely independent of the environmental kinetics. As we shall see below, this decay is to a large extent reversible by the Hahn echo.

The Hahn echo decay is calculated from (18), (21), and (27) leading to

$$\langle\langle\sigma_+(2\tau)\rangle\rangle_{\text{Hahn}} = \exp\{-\Delta^2\tau_c^2[2\tau/\tau_c - 3 + 4e^{-\tau/\tau_c} - e^{-2\tau/\tau_c}]\}. \quad (31)$$

For $\tau \gg \tau_c$ we again have motional narrowing, $\langle\langle\sigma_+(2\tau)\rangle\rangle_{\text{Hahn}} \approx e^{-\Delta^2\tau_c 2\tau}$, a result identical to FID [see (29)] if we set $t = 2\tau$. This occurs because the noise trajectories are completely uncorrelated before and after the π -pulse that plays no role in this limit. For $\tau \ll \tau_c$ we get

$$\langle\langle\sigma_+(2\tau)\rangle\rangle_{\text{Hahn}} \approx e^{-\frac{1}{24}(\Delta\tau_c)^2(\frac{2\tau}{\tau_c})^3} \approx e^{-\frac{2\tau}{T_2}^3}. \quad (32)$$

In drastic contrast to free induction decay, (32) depends crucially on the kinetic variable τ_c . The timescale T_2 for $1/e$ decay of Hahn echo⁴ is considerably longer than T_2^* when $\Delta \gg \tau_c$.

A Train of Hahn Echoes: The Carr–Purcell Sequence and Coherence Control

Consider the sequence $\pi/2$ – $[\tau$ – π – τ –echo]_{repeat}. It consists of the application of a π -pulse every odd multiple of τ , with the observation of an echo at even multiples of τ , i.e., at $t = 2n\tau$ for n integer.⁵ In the limit $\tau \ll \tau_c$ the n th echo envelope can be approximated by a product of n Hahn echoes,

$$\langle\langle\sigma_+(2n\tau)\rangle\rangle_{\text{CP}} \approx \langle\langle\sigma_+(2\tau)\rangle\rangle_{\text{Hahn}}^n \approx e^{-\frac{2n\tau}{T_2}(\frac{2\tau}{T_2})^2} \equiv e^{-\frac{2n\tau}{T_2^{\text{eff}}}}, \quad (33)$$

with $T_2^{\text{eff}} \equiv T_2[T_2/(2\tau)]^2$. As τ is decreased below T_2 the effective coherence time T_2^{eff} increases proportional to $1/\tau^2$. Therefore, a train of Hahn echoes can be used to control decoherence. Rewriting (33) with $t \equiv 2n\tau$ we get $T_2^{\text{eff}} = (2n)^{2/3}T_2$, showing that the scaling of the enhanced coherence time with the number of π -pulses is sublinear. The train of π -pulses spaced by $\tau \ll \tau_c$ effectively averages out the noise, because within τ much shorter than τ_c the noise appears to be time independent.

⁴ In the electron-spin resonance literature the $1/e$ decay time of a Hahn echo is often denoted T_M . Here, we follow the spintronics terminology and use T_2 for the $1/e$ decay of Hahn echo, and T_2^* for $1/e$ decay of FID in the low-frequency regime.

⁵ One can make the Carr–Purcell sequence robust against pulse errors by alternating the phase of the π -pulses, see, e.g., the Carr–Purcell–Meiboom–Gill sequence [26].

Loss of Visibility Due to High-Frequency Noise

In order to understand the role of high-frequency noise, consider the model Lorentzian noise spectrum peaked at frequency Ω with a broadening given by $1/\tau_d$,

$$\tilde{S}_L(\omega) = \frac{\Delta^2 \tau_d}{\pi} \frac{1}{(\omega - \Omega)^2 \tau_d^2 + 1}. \quad (34)$$

Using (18) and (20) and assuming $\Omega \gg 1/\tau_d$ we get

$$|\langle\langle \sigma_+(t) \rangle\rangle|_L \approx \exp \left[-2 \left(\frac{\Delta}{\Omega} \right)^2 (1 - e^{-t/\tau_d} \cos \Omega t) \right]. \quad (35)$$

Therefore, high-frequency noise leads to loss of visibility for the coherence oscillations. The loss of visibility is initially oscillatory, but decays exponentially to a fixed contrast for $t \gg \tau_d$. For comparison, consider a Gaussian noise spectrum,

$$\tilde{S}_G(\omega) = \frac{\Delta^2}{\sqrt{2\pi\sigma^2}} \exp \left[-\frac{(\omega - \Omega)^2}{2\sigma^2} \right]. \quad (36)$$

For $\Omega \gg \sigma$ we get

$$|\langle\langle \sigma_+(t) \rangle\rangle|_G \approx \exp \left[-2 \left(\frac{\Delta}{\Omega} \right)^2 (1 - e^{-\frac{1}{2}\sigma^2 t^2} \cos \Omega t) \right]. \quad (37)$$

Note that the difference between (35) and (37) lies in the time dependence of the approach to a fixed contrast. Deviations from Lorentzian behavior may be assigned to nonexponential decays of the coherence envelope. Although (35) and (37) were calculated for free induction decay, it is also a good approximation for Hahn echoes in the limit $\Omega \gg 1/\tau$.

2.3 Single-Spin Measurement Versus Ensemble Experiments: Different Coherence Times?

Recently, single-shot detection of the spin of a single electron in a GaAs quantum dot was demonstrated [5], and the Hahn echo decay of the singlet–triplet transition in a double quantum dot was measured [8]. Also, spin resonance of a single spin center in the Si/SiO₂ interface was detected through time-averaged current fluctuations [6]. These state-of-the-art experiments should be contrasted with the traditional spin-resonance measurements where the microwave excitation of a sample containing a large number of localized spins is probed. Naturally the following question arises: Are the coherence times extracted from ensemble experiments any different from those obtained in single-spin experiments?

The answer to this question is related to the *ergodicity* of the environment producing noise, i.e., whether time averages are equal to ensemble averages. Even when single-shot readout of a quantum degree of freedom is possible,

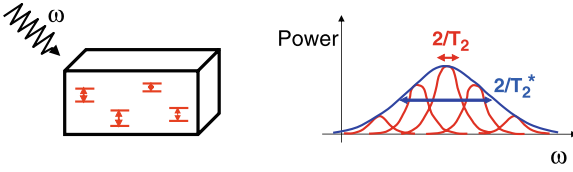
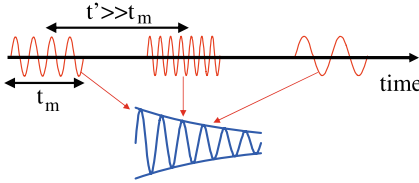
(a) Ensemble of spatially separated qubits

(b) Time average of a *single* qubit


Fig. 2. (a) A traditional spin-resonance experiment probes the coherent evolution of an ensemble of spatially separated spins. The spins can be separated into different “packets” with similar resonance frequencies, each packet with linewidth $2/T_2$. A free induction decay measurement is sensitive to the broadened linewidth $2/T_2^*$. A spin echo is needed in order to reveal the intrinsic linewidth $2/T_2$. (b) A similar situation applies to single-spin experiments subject to low-frequency noise, because each time ensemble may have a different resonance frequency

one must repeat each measurement several times, in order to obtain good average values for the observables. For example, measurements of the state of a single spin yields two possible outcomes and one must time average an ensemble of identical qubit evolutions in order to obtain an average value that reflects the correct outcome probabilities (in [5], each average value resulted from ~ 600 readout traces). The presence of phase fluctuation with correlation time τ_c smaller than the typical averaging time implies spin precession with distinct frequencies for readout traces separated in time. This may lead to strong free induction decay (low T_2^*) in a single-shot readout measurement, see Fig. 2. This was indeed observed in the double-dot experiments of Petta et al. [8].

The free induction decay time T_2^* in ensemble experiments may be quite different from single-spin experiments. This is because the spatial separation of spins adds several new contributions to zero-frequency noise. These include spatially inhomogeneous magnetic fields, g-factors, and strains. Nevertheless, the Hahn-echo decay time T_2 is not affected by zero-frequency noise. If the mechanisms for finite-frequency noise do not vary appreciably for spatially separated spins, and the environment affecting each individual spin is ergodic, the spin-echo decay time T_2 should be similar for a single spin or a collection of spatially separated spins.

The Gaussian theory of decoherence described here is appropriate for ergodic environments. It would be very interesting to explore model systems both experimentally and theoretically in order to search for detectable non-ergodic effects in coherent evolution.

3 Electron-Spin Evolution Due to Nuclear Spins: Isotropic and Anisotropic Hyperfine Interactions, Internuclear Couplings and the Secular Approximation

A localized electron spin coupled to a lattice of interacting nuclear spins provides a suitable model system for the microscopic description of environmental fluctuations affecting coherent evolution. Here, we describe a model Hamiltonian appropriate for localized electron spins in semiconductors, and discuss some truncations that can be made in a moderate magnetic field (typically larger than the inhomogeneous broadening linewidth, $B > 0.1$ T). We will discuss the secular approximation that allows an effective decoupling between electron- and nuclear-spin degrees-of-freedom, making the problem more tractable [the final result is summarized by (54) and (55) below].

3.1 The Electron–Nuclear Spin Hamiltonian

The full Hamiltonian for a single electron interacting with N nuclear spins is given by [26]

$$\mathcal{H} = \mathcal{H}_{eZ} + \mathcal{H}_{nZ} + \mathcal{H}_{en} + \mathcal{H}'_{en} + \mathcal{H}_{nn}. \quad (38)$$

Here, the Zeeman energies for electron and nuclear spins are, respectively,

$$\mathcal{H}_{eZ} = \frac{1}{2} \gamma_e B \sigma_z \quad (39)$$

$$\mathcal{H}_{nZ} = -\gamma_n B \sum_i I_{iz}, \quad (40)$$

where $\boldsymbol{\sigma} = (\sigma_x, \sigma_y, \sigma_z)$ is the Pauli matrix vector representing the electron spin, and $\mathbf{I}_i = (I_{ix}, I_{iy}, I_{iz})$ is the nuclear-spin operator for a nucleus located at position \mathbf{R}_i with respect to the center of the electron wavefunction. For $B = 1$ T we have $\gamma_e B \sim 10^{11}$ Hz and $\gamma_n B \sim 10^8$ Hz, note the drastic difference in Zeeman energy scale. The e–n coupling takes place due to isotropic and anisotropic hyperfine interactions. The isotropic hyperfine interaction is given by

$$\mathcal{H}_{en} = \frac{1}{2} \sum_i A_i^{\text{iso}} \mathbf{I}_i \cdot \boldsymbol{\sigma}, \quad (41)$$

with contact hyperfine interaction

$$A_i^{\text{iso}} = \frac{8\pi}{3} \gamma_{e0} \gamma_n \hbar |\Psi(\mathbf{R}_i)|^2, \quad (42)$$

where $\gamma_{e0} = e/(m_e c) = 1.76 \times 10^7 \text{ (sG)}^{-1}$ is the gyromagnetic ratio for a free electron and $\Psi(\mathbf{r})$ is the electron's wavefunction. Typical values of A_i^{iso} varies from $A_i^{\text{iso}} \sim 10^7 \text{ Hz}$ for $\mathbf{R}_i = 0$ (at the center of a donor impurity wavefunction) to $A_i^{\text{iso}} \sim 0$ for R_i much larger than the impurity Bohr radius. The anisotropic hyperfine interaction reads

$$\mathcal{H}'_{\text{en}} = \frac{1}{2} \sum_i \mathbf{I}_i \cdot \mathbf{A}'_i \cdot \boldsymbol{\sigma}, \quad (43)$$

with the anisotropic hyperfine tensor given by

$$(\mathbf{A}'_i)_{\text{lm}} = \gamma_{e0} \gamma_n \hbar \int d^3r |\Psi(\mathbf{r} - \mathbf{R}_i)|^2 \left(\frac{2r}{2r + r_0} \right) \left(\frac{3x_l x_m}{r^5} - \frac{\delta_{lm}}{r^3} \right), \quad (44)$$

where $r_0 = e^2/(m_e c^2)$ is the classical electron radius. Note that (41) and (43) are first-order perturbative corrections in the electron coordinate \mathbf{r} . Finally, the nuclear–nuclear dipolar coupling reads

$$\mathcal{H}_{\text{nn}} = \gamma_n^2 \hbar \sum_{i < j} \left[\frac{\mathbf{I}_i \cdot \mathbf{I}_j}{R_{ij}^3} - \frac{3(\mathbf{I}_i \cdot \mathbf{R}_{ij})(\mathbf{I}_j \cdot \mathbf{R}_{ij})}{R_{ij}^5} \right], \quad (45)$$

where $\mathbf{R}_{ij} = \mathbf{R}_i - \mathbf{R}_j$ is the distance between two nuclei. The typical energy scale for (45) is a few kHz for nearest neighbors in a crystal.

The full Hamiltonian equation (38) is a formidable many-body problem. It is particularly hard to study because of the lack of symmetry. In order to study theoretically the quantum dynamics of an electron subject to a large number of nuclear spins we need to truncate (38). Here, we discuss some simplifications appropriate for $B > 0.1 \text{ T}$, a condition typically satisfied in several experiments. The first approximation arises when we note that the electron Zeeman energy is typically 10^3 times larger than the nuclear Zeeman energy. For $B > 100 \text{ G}$ the former is much larger than A_i^{iso} , therefore the electron spin cannot be “flipped” by the action of the hyperfine interaction. In other words, “real” e–n flip-flop transitions get inhibited at these fields (however, virtual transitions induced by second-order processes such as $\mathcal{H}_{\text{en}}^2$ do produce visible effects, as discussed in Sect. 3.3). This consideration allows us to approximate the isotropic hyperfine interaction to a diagonal form (secular approximation),

$$\mathcal{H}_{\text{en}} \approx \frac{1}{2} \sigma_z \sum_i A_i^{\text{iso}} I_{iz}. \quad (46)$$

The anisotropic hyperfine interaction contains a similar diagonal contribution in addition to pseudosecular terms of the form $\sigma_z I_{i\pm}$. These terms lead to important echo modulations of the order of $\sim (A'_i/\gamma_n B)^2 \sim 0.1\text{--}1$ for moderate magnetic fields ($B \sim 0.1\text{--}1 \text{ T}$). To derive these terms, assume \hat{b} as the direction of the magnetic field and substitute $\boldsymbol{\sigma} \rightarrow \sigma_z \hat{b}$ in (43). The result is

$$\mathcal{H}'_{\text{en}} \approx \frac{1}{2} \sigma_z \sum_i (A'_{i\parallel} I_{iz} + A'_{i\perp} I_{i+} + A'^*_{i\perp} I_{i-}), \quad (47)$$

where

$$A'_{i\parallel} = \hat{z} \cdot \mathbf{A}'_i \cdot \hat{b}, \quad (48)$$

$$A'_{i\perp} = \frac{1}{2} [\hat{x} \cdot \mathbf{A}'_i \cdot \hat{b} + i \hat{y} \cdot \mathbf{A}'_i \cdot \hat{b}]. \quad (49)$$

For some lattice sites (closer to the center of the donor impurity) $A'_{i\perp}$ is a reasonable fraction of the nuclear-spin Zeeman energy (even for $B \sim 1$ Tesla), and as a consequence the precession axis of these nuclear spins will depend on the state of the electron, producing strong modulations in the nuclear-spin-echo signal [27, 28]. For the electron-spin equation (47) produces small modulations observed at the shortest timescales in the echo-decay envelope [22]. Finally, we may truncate (45) neglecting terms that do not conserve nuclear-spin Zeeman energy,

$$\mathcal{H}_{\text{nn}} \approx \sum_{i < j} b_{ij} (I_{i+} I_{j-} + I_{i-} I_{j+} - 4 I_{iz} I_{jz}), \quad (50)$$

with

$$b_{ij} = -\frac{1}{4} \gamma_n^2 \hbar \frac{1 - 3 \cos^2 \theta_{ij}}{R_{ij}^3}. \quad (51)$$

Here, θ_{ij} is the angle formed by the applied \mathbf{B} field and the vector \mathbf{R}_{ij} linking the two nuclear spins i, j . This leads to an important orientation dependence of coherence times.

3.2 Electron–Nuclear–Spin Evolution in the Secular Approximation

In the secular approximation [see (46)–(50)] the electron–nuclear-spin Hamiltonian is block-diagonal,

$$\mathcal{H} = \mathcal{H}_+ |\uparrow\rangle\langle\uparrow| + \mathcal{H}_- |\downarrow\rangle\langle\downarrow|, \quad (52)$$

where $|\uparrow\rangle\langle\uparrow|$ and $|\downarrow\rangle\langle\downarrow|$ are projectors in the electron spin-up and -down subspaces, respectively. Here, \mathcal{H}_{\pm} contains only nuclear-spin operators and is given by

$$\begin{aligned} \mathcal{H}_{\pm} &= \mathcal{H}_{\text{nn}} - \gamma_n B \sum_i I_{iz} \pm \frac{1}{2} \gamma_e B \\ &\quad \pm \frac{1}{2} \sum_i [A_i I_{iz} + A'_i I_{i+} + A'^*_{i\perp} I_{i-}], \end{aligned} \quad (53)$$

where $A_i \equiv A_i^{\text{iso}} + A'_{i\parallel}$ and $A'_i \equiv A'_{i\perp}$. Accordingly, the evolution operator becomes $\mathcal{U}(t) = \mathcal{U}_+(t) |\uparrow\rangle\langle\uparrow| + \mathcal{U}_-(t) |\downarrow\rangle\langle\downarrow|$, with $\mathcal{U}_{\pm}(t) = e^{-it\mathcal{H}_{\pm}}$. We can

write an explicit expression for the coherences as a function of the evolution operators $\mathcal{U}_{\pm}(t)$ provided the initial density matrix can be written in product form, $\rho_0 = \rho_{0e} \otimes \rho_{0n}$. The free induction decay is given by

$$\begin{aligned} \langle \sigma_+(t) \rangle_{\text{FID}} &= \text{Tr}_n \text{Tr}_e \{ \mathcal{U}^\dagger \sigma_+ \mathcal{U} \rho_{0e} \otimes \rho_{0n} \} \\ &= \text{Tr}_n \{ \mathcal{U}_+^\dagger \mathcal{U}_- \rho_{0n} \} \text{Tr}_e \{ \sigma_+ \rho_{0e} \}, \end{aligned} \quad (54)$$

where we used the fact that $\mathcal{U}^\dagger \sigma_+ \mathcal{U} = \mathcal{U}_+^\dagger \mathcal{U}_- \sigma_+$, and $\sigma_+ = |\uparrow\rangle\langle\downarrow|$. For the Hahn echo, we use $\mathcal{U}(\tau)\sigma_x\mathcal{U}(\tau)$ as our evolution operator, to get

$$\langle \sigma_+(2\tau) \rangle_{\text{Hahn}} = \text{Tr}_n \{ \mathcal{U}_-^\dagger \mathcal{U}_+^\dagger \mathcal{U}_- \mathcal{U}_+ \rho_{0n} \} \text{Tr}_e \{ \sigma_- \rho_{0e} \}. \quad (55)$$

Equations (54) and (55) are exact in the secular approximation, and make explicit the dependence of the electron's coherence envelope in the nuclear-spin Hamiltonian evolution.

Inhomogeneous Broadening Due to the Isotropic Hyperfine Interaction

The diagonal model

$$\mathcal{H}_{\pm} = -\gamma_n B \sum_i I_{iz} \pm \frac{1}{2} \gamma_e B \pm \frac{1}{2} \sum_i A_i I_{iz} \quad (56)$$

is easily solved exactly for nuclear spins initially in a product state. Assume the electron spin is pointing in the $+y$ direction, and the nuclear-spin states are distributed randomly, each nuclei with equal probability of pointing up or down. The free induction decay amplitude becomes

$$\begin{aligned} \langle \sigma_+(t) \rangle_{\text{FID}} &= \frac{i}{2} \text{Tr}_n \{ \mathcal{U}_+^\dagger \mathcal{U}_- \} \\ &= \frac{i}{2} e^{i\gamma_e B t} \prod_j \frac{1}{2} [e^{\frac{i}{2} A_j t} + e^{-\frac{i}{2} A_j t}] \\ &= \frac{i}{2} e^{i\gamma_e B t} \sum_{\xi_1 = \pm 1, \dots} \frac{1}{2^N} e^{\frac{i}{2} t \sum_j A_j \xi_j} \\ &\approx \frac{i}{2} e^{i\gamma_e B t} e^{-\frac{1}{8} t^2 \sum_j A_j^2}, \end{aligned} \quad (57)$$

where in the last line we assumed $N \rightarrow \infty$ with each individual $A_i \rightarrow 0$ so that the hyperfine field can be approximated by a continuous Gaussian distribution. The free induction decay rate or inhomogeneously broadened linewidth is given by $\frac{1}{T_2^*} \sim A_{\text{rms}} = \sqrt{\sum_j A_j^2}$. This fast decay rate should be compared to the Hahn echo: From (55) we see that $\langle \sigma_+(2\tau) \rangle_{\text{Hahn}} = -i/2$, the Hahn echo never decays. In fact, from (55) we can easily prove that the class of Hamiltonians of the form (52) satisfying $[\mathcal{H}_+, \mathcal{H}_-] = 0$ have time-independent Hahn echoes given by $\text{Tr}\{\sigma_- \rho_{0e}\}$ [29].

3.3 Beyond the Secular Approximation: Nuclear–Nuclear Interactions Mediated by the Electron-Spin Hyperfine Interaction

In the sections above we showed that the secular approximation allows us to decouple electron-spin dynamics from nuclear-spin dynamics completely. This approximation clearly does not hold at low magnetic fields, and the problem becomes considerably more complicated. The study of electron-spin evolution subject to the full isotropic hyperfine interaction has attracted a great deal of attention lately [29–32], particularly because of a series of free induction decay experiments probing electron-spin dynamics in quantum dots in the low magnetic field regime [33–38]. In the author’s opinion the most successful theoretical approach so far in the description of these experiments is to treat the collective nuclear spin field classically by taking averages over its direction and magnitude [30]. Here, we shall not discuss the interesting effects occurring at low fields. Instead, we will focus on the following question: What is the threshold field B_{th} for the secular approximation to hold? For intermediate $B > B_{\text{th}}$ (not satisfying $B \gg B_{\text{th}}$), how can the nonsecular terms be incorporated in a block-diagonal Hamiltonian of the form (52)?

In order to answer these questions, let’s consider the Hamiltonian

$$\mathcal{H} = \mathcal{H}_0 + \mathcal{V}, \quad (58)$$

$$\mathcal{H}_0 = \frac{1}{2}(\gamma_e + \gamma_n)B\sigma_z + \frac{1}{2}\sigma_z \sum_j A_j I_{jz}, \quad (59)$$

$$\mathcal{V} = \frac{1}{2} \sum_j A_j (\sigma_+ I_{j-} + \sigma_- I_{j+}), \quad (60)$$

where \mathcal{H}_0 and \mathcal{V} denote the secular and nonsecular contributions, respectively. Here, we remove the nuclear Zeeman energy by transforming to the rotating frame precessing at $\gamma_n B$. From (60) we may be tempted to assume that flip-flop processes involving an electron and a nuclear spin (e.g., $\uparrow\downarrow \rightarrow \downarrow\uparrow$) are forbidden by energy conservation at fields $\gamma_e B \gg A_i$. However, the situation is much more complex because higher-order “virtual” processes such as $\mathcal{V}^2 = A_i A_j I_{i+} I_{j-} \sigma_+ \sigma_- + \dots$ preserve the electron-spin polarization and hence may have a small energy cost (of the order of $A_i - A_j$ for $A_i \sim A_j$). As we show below, these processes actually lead to a long-range effective coupling between nuclear spins, similar to the RKKY interaction between nuclear spins in a metal. We will show this using the original self-consistent approach of Shenvi et al.

Let $|\psi^+\rangle$ be a “+” eigenstate of the Hamiltonian equation (58), i.e., $|\psi^+\rangle$ has primarily electron spin-up character. Without loss of generality, $|\psi^+\rangle$ can be written as

$$|\psi^+\rangle = |\uparrow, \psi_\uparrow^+\rangle + |\downarrow, \psi_\downarrow^+\rangle. \quad (61)$$

Because the perturbation \mathcal{V} flips the polarization of the electron, the action of \mathcal{H} on the electron spin-up and electron spin-down subspaces yields the two simultaneous equations,

$$\mathcal{H}_0|\uparrow, \psi_\uparrow^+\rangle + \mathcal{V}|\downarrow, \psi_\downarrow^+\rangle = E_+|\uparrow, \psi_\uparrow^+\rangle, \quad (62)$$

$$\mathcal{H}_0|\downarrow, \psi_\downarrow^+\rangle + \mathcal{V}|\uparrow, \psi_\uparrow^+\rangle = E_+|\downarrow, \psi_\downarrow^+\rangle. \quad (63)$$

Equation (63) can be solved for $|\downarrow, \psi_\downarrow^+\rangle$ and the resulting expression inserted into (62) yields

$$\mathcal{H}_0|\uparrow, \psi_\uparrow^+\rangle + \mathcal{V}\frac{1}{E_+ - \mathcal{H}_0}\mathcal{V}|\uparrow, \psi_\uparrow^+\rangle = E_+|\uparrow, \psi_\uparrow^+\rangle. \quad (64)$$

In the presence of an energy gap between the spin-up and spin-down states (this is certainly true at high magnetic fields satisfying $B > \sum A_j/\gamma_e$), the operator $1/(E_+ - \mathcal{H}_0)$ is always well defined [39]. Because the left-hand side of (64) depends on E_+ , it is not a true Schrödinger equation; to obtain E_+ exactly, (64) must be solved self-consistently. However, if we use $E_+ \approx (\gamma_e + \gamma_n)B/2$, then we can obtain an effective Hamiltonian from (64). The effective Hamiltonian in the electron spin-up subspace is

$$\mathcal{H}_{\text{eff}}^+ = \mathcal{H}_0 + \mathcal{V}_{\text{eff}}^+, \quad (65)$$

$$\mathcal{V}_{\text{eff}}^+ = \frac{1}{4} \sum_{j,k} A_j A_k I_{j-} \frac{1}{(\gamma_e + \gamma_n)B + \frac{1}{2} \sum_j A_j I_{jz}} I_{k+}. \quad (66)$$

We obtain a similar, but not identical, effective Hamiltonian for the spin-down subspace (note the transposition of the I_- and I_+ operators),

$$\mathcal{H}_{\text{eff}}^- = \mathcal{H}_0 + \mathcal{V}_{\text{eff}}^-, \quad (67)$$

$$\mathcal{V}_{\text{eff}}^- = -\frac{1}{4} \sum_{j,k} A_j A_k I_{j+} \frac{1}{(\gamma_e - \gamma_n)B + \frac{1}{2} \sum_j A_j I_{jz}} I_{k-}. \quad (68)$$

Equations (66) and (68) show that the overall coupling between nuclei does indeed decrease at high fields, because the operator $1/(E - \mathcal{H}_0)$ scales approximately as $1/B$. However, the energy cost for flip-flopping two nuclei j and k is proportional to $A_j - A_k$. Thus, if A_j and A_k are close in value, the nuclei can flip-flop even at high fields. Equations (66) and (68) were later derived using an alternative canonical transformation approach [40].

We may expand (66) and (68) in powers of $\sum_j A_j I_{jz}/(\gamma_e B)$, so that for the unpolarized case we have approximately

$$\mathcal{V}_{\text{eff}} \approx \frac{1}{2} \sigma_z \sum_{j,k} \frac{A_j A_k}{2(\gamma_e + \gamma_n)B} I_{j+} I_{k-}. \quad (69)$$

This effective Hamiltonian is of the secular type (52), and satisfies the symmetry condition $[\mathcal{H}_+, \mathcal{H}_-] = 0$. Therefore, a Hahn echo is able to refocus this interaction completely: *The effective interaction for hyperfine-mediated coupling alone [see (69)] does not lead to Hahn-echo decay.*

Shenvi et al. performed exact numerical calculations of electron spin-echo dynamics in clusters of $N = 13$ nuclear spins, including the full isotropic hyperfine interaction [29]. The Hahn-echo envelope was found to decay abruptly to a loss of contrast given by

$$|\langle \sigma_+(2\tau) \rangle| \approx \frac{1}{2} - \frac{\sum_j A_j^2}{[(\gamma_e + \gamma_n)B]^2}. \quad (70)$$

This shows that the threshold field for neglecting the nonsecular isotropic hyperfine interaction in the Hahn echo is given by the inhomogeneously broadened linewidth, $B_{\text{th}} = \sqrt{\sum_j A_j^2}/\gamma_e \sim 10\text{--}100$ G (for a donor impurity in silicon, B_{th} is ≈ 1 G for natural samples and ≈ 10 G for ^{29}Si -enriched samples).

Recently, Yao et al. [40] and Deng et al. [32] showed that the electron-mediated internuclear coupling may be observed as a magnetic-field dependence of the free induction decay time in small quantum dots. There is currently an interesting debate on the correct form of the time dependence for FID decay. Yao et al. derived the FID decay from (69) and obtained $\langle \sigma_+(t) \rangle \sim e^{-t^2}$, while Deng et al. carried out a full many-body calculation to argue that FID scales as a power law according to $\langle \sigma_+(t) \rangle \sim 1/t^2$.

4 Microscopic Calculation of the Nuclear-Spin Noise Spectrum and Electron-Spin Decoherence

In this section we discuss low-frequency noise due to interacting nuclear spins. For simplicity, we assume only isotropic hyperfine interaction. The inclusion of anisotropic hyperfine interaction is considerably more complicated, but can be seen to lead to echo modulations (at frequencies close to $\gamma_n B \sim 10^8 \text{ s}^{-1}$ per Tesla). In the next section we provide explicit numerical calculations for the case of a phosphorus impurity in silicon and compare our results to experiments.

We only consider the dipolar interaction between nuclear spins, neglecting other contributions to internuclear coupling such as the electron-mediated interaction (69). For calculations of Hahn echo at large B fields ($B > 0.1$ T), this is perfectly appropriate because, as discussed above, the neglected nonsecular contributions lead only to a small loss of visibility. It is important to emphasize that the nonsecular contributions result in a nuclear-spin noise spectrum that is dependent on the electron-spin state (back action), hence (18) can not be used.

4.1 Nuclear-Spin Noise

Using the approximations (46) and (50) we can write the electron–nuclear Hamiltonian in a form similar to (1). In the electron-spin Hilbert space, we assume an effective time-dependent Hamiltonian of the form

$$\mathcal{H}_{\text{eff}}^e = \frac{1}{2}\gamma_e B\sigma_z + \frac{1}{2}\sigma_z \sum_i A_i I_{iz}(t), \quad (71)$$

with $A_i \equiv A_i^{\text{iso}}$. Nuclear-spin noise is in turn determined by the effective Hamiltonian

$$\mathcal{H}_{\text{eff}}^n = \sum_{i<j} \mathcal{H}_{ij}^n, \quad (72)$$

$$\begin{aligned} \mathcal{H}_{ij} &= \gamma_n B(I_{iz} + I_{jz}) + b_{ij}(I_{i+}I_{j-} + I_{i-}I_{j+} - 4I_{iz}I_{jz}) \\ &\quad + \frac{1}{2}(A_i I_{iz} + A_j I_{jz}), \end{aligned} \quad (73)$$

where we decoupled the electron spin from the nuclear spins by assuming the nuclear-spin wavefunction evolves in the electron spin-up subspace ($\sigma_z \rightarrow 1$). An equally valid choice is to assume $\sigma_z \rightarrow -1$. It turns out that this choice does not matter within the pair approximation described below. We will check this by noting that the final answer is unchanged under the operation $A_i \rightarrow -A_i$ for all i .⁶

For now we assume the nuclear spins are unpolarized ($T = \infty$) so that $\langle \sum_i A_i I_{iz} \rangle = 0$. This approximation will be relaxed below. The time-dependent correlation function for nuclear spins is given by

$$\begin{aligned} S(t) &= \left\langle \sum_i A_i I_{iz}(t) \sum_j A_j I_{jz}(0) \right\rangle \\ &= \sum_i A_i^2 \langle I_{iz}(t) I_{iz}(0) \rangle + \sum_{i,j(\neq i)} A_i A_j \langle I_{iz}(t) I_{jz}(0) \rangle. \end{aligned} \quad (74)$$

We now invoke a “pair approximation” by assuming

$$\langle I_{iz}(t) I_{iz}(0) \rangle \approx \sum_{j(\neq i)} \langle I_{iz}(t) I_{iz}(0) \rangle_{ij}, \quad (75)$$

$$\langle I_{iz}(t) I_{jz}(0) \rangle \approx \langle I_{iz}(t) I_{jz}(0) \rangle_{ij}, \quad (76)$$

where $\langle \cdot \rangle_{ij}$ denotes a thermal average restricted to the ij Hilbert space. The operator $I_{iz}(t)$ is in the Heisenberg representation defined by the two-particle

⁶ As we shall see below, this approximation leads to identical results as the lowest-order cluster expansion developed in [24]. However, interesting interference effects arise when this approximation is not valid. The cluster-expansion method beyond lowest order [25] takes account of the full electron–nuclear evolution, therefore it can be used to study these effects.

Hamiltonian equation (73). Plugging (75) and (76) in (74) and reordering terms we get

$$S(t) \approx \sum_{i < j} \langle \hat{\eta}_{ij}(t) \hat{\eta}_{ij}(0) \rangle_{ij}, \quad (77)$$

with

$$\hat{\eta}_{ij} = A_i I_{iz} + A_j I_{jz}. \quad (78)$$

The same derivation could be given for finite temperature, when the thermal average of the hyperfine field is nonzero. The result is identical to (77) except for the substitution $\hat{\eta}_{ij} \rightarrow \delta \hat{\eta}_{ij} = \hat{\eta}_{ij} - \langle \hat{\eta}_{ij} \rangle$. Using the definition of the noise spectrum [see (6)] and expanding the correlator in the energy eigenstates of the pair Hamiltonian (73) we get

$$\tilde{S}_{ij}(\omega) = \sum_{\alpha, \beta} p_\alpha |\langle \alpha | \delta \hat{\eta}_{ij} | \beta \rangle|^2 \delta(\omega - E_{\beta\alpha}), \quad (79)$$

with $E_{\beta\alpha} = E_\beta - E_\alpha$ the energy difference between the energy eigenstates $|\alpha\rangle, |\beta\rangle$, and p_α the (thermal) occupation of state α . Therefore, the noise spectrum is a sum over all possible transition frequencies induced by the operator $\hat{\eta}_{ij}$. For nuclear spin 1/2 the ij Hamiltonian has the following eigenenergies and eigenstates (see Fig. 3)

$$E_{\uparrow\uparrow} = \gamma_n B - b_{ij} + a_{ij}, \quad (80)$$

$$E_+ = b_{ij} + \sqrt{b_{ij}^2 + \Delta_{ij}^2}, \quad (81)$$

$$E_- = b_{ij} - \sqrt{b_{ij}^2 + \Delta_{ij}^2}, \quad (82)$$

$$E_{\downarrow\downarrow} = -\gamma_n B - b_{ij} - a_{ij}, \quad (83)$$

$$|+\rangle = \cos \frac{\theta}{2} |\uparrow\downarrow\rangle + \sin \frac{\theta}{2} |\downarrow\uparrow\rangle, \quad (84)$$

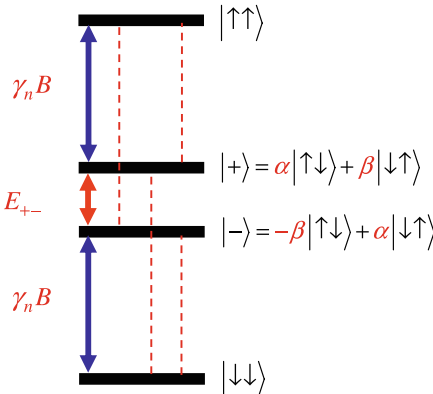


Fig. 3. Energy levels for two nuclear spins coupled through the dipolar interaction. The flip-flop mechanism corresponds to transitions between the states $|+\rangle$ and $|-\rangle$, which are admixtures of $|\uparrow\downarrow\rangle$ and $|\downarrow\uparrow\rangle$ states. The anisotropic hyperfine interaction couples states differing by $\sim \gamma_n B$ in energy

$$|-\rangle = -\sin\frac{\theta}{2}|\uparrow\downarrow\rangle + \cos\frac{\theta}{2}|\downarrow\uparrow\rangle, \quad (85)$$

with

$$a_{ij} = \frac{1}{4}(A_i + A_j), \quad (86)$$

$$\Delta_{ij} = \frac{1}{4}(A_i - A_j), \quad (87)$$

$$\cos\theta = \frac{\Delta_{ij}}{\sqrt{b_{ij}^2 + \Delta_{ij}^2}}, \quad (88)$$

$$\sin\theta = \frac{b_{ij}}{\sqrt{b_{ij}^2 + \Delta_{ij}^2}}. \quad (89)$$

Using (84) and (85) the transition matrix element is easily found to be

$$\langle -|\hat{\eta}_{ij}|+\rangle = -4\Delta_{ij}\sin\frac{\theta}{2}\cos\frac{\theta}{2} = -2\Delta_{ij}\sin\theta. \quad (90)$$

The transition frequency is simply the difference between (81) and (82),

$$E_{+-} = 2\sqrt{b_{ij}^2 + \Delta_{ij}^2}. \quad (91)$$

The resulting noise spectrum is therefore

$$\begin{aligned} \tilde{S}_{ij}(\omega) &= (A_{ij}^{\text{rms}})^2 \delta(\omega) \\ &\quad + 4\frac{b_{ij}^2 \Delta_{ij}^2}{b_{ij}^2 + \Delta_{ij}^2} [p_+ \delta(\omega + E_{+-}) + p_- \delta(\omega - E_{+-})], \end{aligned} \quad (92)$$

with a static contribution given by

$$\begin{aligned} (A_{ij}^{\text{rms}})^2 &= 4 \left[(p_{\uparrow\uparrow} + p_{\downarrow\downarrow}) a_{ij}^2 + (p_+ + p_-) \frac{\Delta_{ij}^4}{b_{ij}^2 + \Delta_{ij}^2} \right] \\ &\quad - 4 \left[(p_{\uparrow\uparrow} - p_{\downarrow\downarrow}) a_{ij} + (p_+ - p_-) \frac{\Delta_{ij}^2}{\sqrt{b_{ij}^2 + \Delta_{ij}^2}} \right]^2. \end{aligned} \quad (93)$$

The free induction decay due to this noise spectrum can be easily calculated using (18) and the filter function (20),

$$\begin{aligned} \langle\langle \sigma_+(t) \rangle\rangle &= \exp \left[-\frac{1}{2} \sum_{i < j} (A_{ij}^{\text{rms}})^2 t^2 \right] \\ &\quad \times \exp \left[-2 \sum_{i < j} (p_+ + p_-) \frac{b_{ij}^2 \Delta_{ij}^2}{b_{ij}^2 + \Delta_{ij}^2} t^2 \text{sinc}^2(\sqrt{b_{ij}^2 + \Delta_{ij}^2} t) \right], \end{aligned} \quad (94)$$

where $\text{sinc}(x) = \sin(x)/x$. As expected, the FID decay is usually dominated by the zero-frequency noise amplitude A_{ij}^{rms} [see (93)]. The dipolar-induced

decay may be visible provided A_{ij}^{rms} is much smaller than the finite-frequency noise amplitudes. For example, this is the case if the nuclear spins are polarized, since we have $A_{ij}^{\text{rms}} = 0$ exactly when $p_{\downarrow\downarrow} = 1$ in (93).

The Hahn-echo decay envelope is derived after integration with the filter function (21),

$$\langle\langle\sigma_+(2\tau)\rangle\rangle = \exp\left[-8\sum_{i<j}(p_+ + p_-)b_{ij}^2\Delta_{ij}^2\tau^4\text{sinc}^4\left(\sqrt{b_{ij}^2 + \Delta_{ij}^2}\tau\right)\right]. \quad (95)$$

At $T \rightarrow \infty$ ($p_+ = p_- = 1/4$) (95) is identical to the echo decay obtained by two completely different methods, viz. the lowest-order cluster expansion [see (20) in [24]] and the quasiparticle excitation model [see (18) in [40]]. As expected, (95) is independent of zero-frequency noise, and is exactly equal to 1 when either $b_{ij} = 0$ or $\Delta_{ij} = 0$, or when the nuclear spins are polarized ($p_+ = p_- = 0$).

By expanding the exponent in (94) and (95) in powers of time, we find that only even powers are present. The short-time behavior for FID is $\sim e^{-t^2}$, while for Hahn echo $\sim e^{-\tau^4}$ [this is a manifestation of the general result (24) and (25)]. This short-time approximation is valid for times much smaller than the inverse cutoff of the noise spectrum. It was found that the short-time expression $e^{-\tau^4}$ is a good approximation for GaAs quantum dots [40] but not for Si:P impurities [24].

4.2 Mean Field Theory of Noise Broadening: Quasiparticle Lifetimes

We showed that the noise spectrum due to flip-flop transitions in the Hilbert space formed by two nuclear spins i, j is a linear combination of delta functions. We may extend this pair approximation to clusters larger than two, and the number of delta functions will grow exponentially with cluster size [This can be done by systematically increasing the size of the Hilbert space beyond a single pair i, j in (75) and (76).] These delta functions can be interpreted as well-defined transitions between nuclear-spin excitations with infinite lifetime.⁷ The delta functions for transitions involving more than two nuclear spins do not necessarily occur at frequencies close to the pair flip-flop frequency E_{+-} . But on top of adding additional delta function peaks, the many-body interactions are expected to produce lifetime broadening for these sharp transitions, see Fig. 4. Below, we develop a simple mean field theory whose purpose is to estimate the magnitude of this broadening.

We can add broadening to the delta functions in a mean-field fashion by using the method of moments, which is applicable at infinite temperature (no

⁷ In [40] Yao et al. derive a similar quasiparticle picture via direct calculation of the time-dependent correlation function for the electron spin. However, the authors did not calculate the quasiparticle lifetimes. The noise spectrum is a natural starting point for developing a theory for quasiparticle lifetime broadening, as we show here.

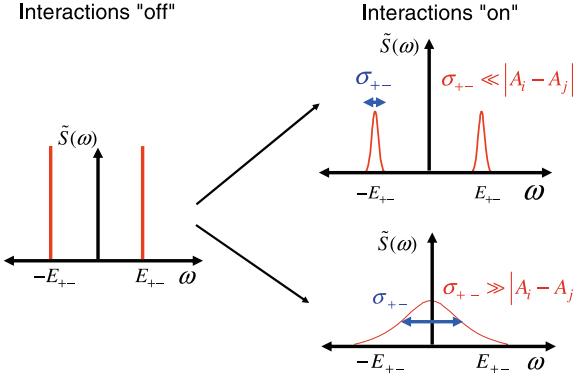


Fig. 4. An isolated pair of nuclear spins with infinite lifetime will produce a sharp peak in the noise spectrum. The role of the many-body interactions with other nuclear spins is to broaden this peak and smooth out the noise spectrum for the collective nuclear-spin excitations. Here, we calculate the line broadening for each pair flip-flop transition using a procedure similar to van Vleck's method of moments

nuclear-spin polarization, i.e., $k_B T \gg \gamma_n B$). In this limit, the noise spectrum is written as

$$\tilde{S}_{ij}(\omega) = \sum_{\alpha, \beta} \frac{1}{2^N} |\langle \alpha | \hat{\eta}_{ij} | \beta \rangle|^2 \delta(\omega - E_{\beta\alpha}), \quad (96)$$

where here α, β denote exact many-body eigenstates of the system of N -coupled nuclear spins. The n th moment $\int \omega^n \tilde{S}(\omega) d\omega$ can be calculated exactly using the invariance of the trace.⁸ Consider the zeroth moment,

$$\begin{aligned} \int_{-\infty}^{\infty} \tilde{S}_{ij}(\omega) d\omega &= \frac{1}{2^N} \sum_{\alpha, \beta} \langle \alpha | \hat{\eta}_{ij} | \beta \rangle \langle \beta | \hat{\eta}_{ij} | \alpha \rangle \\ &= \frac{1}{2^N} \text{Tr} \{ \hat{\eta}_{ij}^2 \} = \frac{1}{4} (A_i^2 + A_j^2). \end{aligned} \quad (97)$$

Accordingly, the second moment is given by

$$\begin{aligned} \int_{-\infty}^{\infty} \omega^2 \tilde{S}_{ij}(\omega) d\omega &= -\frac{1}{2^N} \text{Tr} \{ [\mathcal{H}_{\text{eff}}^n, \hat{\eta}_{ij}]^2 \} \\ &= \frac{1}{2} A_i^2 \sum_{k \neq i} b_{ik}^2 - b_{ij}^2 A_i A_j + \frac{1}{2} A_j^2 \sum_{k \neq j} b_{jk}^2. \end{aligned} \quad (98)$$

Note that (97) and (98) are exact at infinite temperature.

⁸ A similar method was used in the semiclassical theory of spectral diffusion in order to calculate the flip-flop rates for pairs of nuclear spins [19].

The mean field approximation employed here assumes each delta function in the noise spectrum is represented by a Gaussian function normalized to one.⁹ The noise spectrum becomes

$$\tilde{S}_{ij}(\omega) \approx \sum_{\alpha,\beta} \frac{1}{4} |\langle \alpha | \hat{\eta}_{ij} | \beta \rangle|^2 \frac{1}{\sqrt{2\pi\sigma_{\alpha\beta}^2}} \exp\left[-\frac{(\omega - E_{\alpha\beta})^2}{2\sigma_{\alpha\beta}^2}\right], \quad (99)$$

and the second moment is

$$\int_{-\infty}^{\infty} \omega^2 \tilde{S}_{ij}(\omega) d\omega \approx \sum_{\alpha,\beta} \frac{1}{4} |\langle \alpha | \hat{\eta}_{ij} | \beta \rangle|^2 (\sigma_{\alpha\beta}^2 + E_{\alpha\beta}^2). \quad (100)$$

We now calculate the broadenings $\sigma_{\alpha\beta}$ by equating (100) with (98). This procedure can be carried out exactly, since the noise spectrum has two identical peaks (Fig. 4) at frequencies $\pm E_{+-}$. The broadening is found to be

$$\sigma_{+-}^2 = \frac{b_{ij}^2 + \Delta_{ij}^2}{4\Delta_{ij}^2 b_{ij}^2} \sum_{k \neq i,j} (b_{ik}^2 A_i^2 + b_{jk}^2 A_j^2). \quad (101)$$

When $\Delta_{ij} < \sim b_{ij}$, the broadening becomes of the same order of magnitude as van Vleck's second moment for the dipolar interaction (equal to $9 \sum_k b_{ik}^2$ [26]). For $\Delta_{ij} \gg b_{ij}$ we have $\sigma_{+-} \sim \Delta_{ij}$, and $\sigma_{+-}/E_{+-} \sim 1$. This type of excitation is of high frequency and short lifetime, showing fast decay to a small loss of contrast as described by (37). Physically, the broadenings describe the diffusion of localized nuclear-spin excitations (deviations from thermal equilibrium) over length scales greater than the pair distance.

By adding broadenings to the delta functions in (92) we are able to plot a smooth noise spectrum, and study the relative contributions of a large number of nuclear spins as a function of a continuous frequency. The modified equation (92) summed over all nuclear pair contributions reads

$$\begin{aligned} \tilde{S}(\omega) = 4 \sum_{i < j} \frac{b_{ij}^2 \Delta_{ij}^2}{b_{ij}^2 + \Delta_{ij}^2} & \left\{ p_+ \frac{e^{-\frac{(\omega - E_{+-})^2}{2\sigma_{+-}^2}}}{\sqrt{2\pi\sigma_{+-}^2}} + p_- \frac{e^{-\frac{(\omega + E_{+-})^2}{2\sigma_{+-}^2}}}{\sqrt{2\pi\sigma_{+-}^2}} \right\} \\ & + \sum_{i < j} (A_{ij}^{\text{rms}})^2 \delta(\omega). \end{aligned} \quad (102)$$

⁹ We can verify this assumption by calculating the skewness (fourth moment divided by three times the second moment squared). For a perfect Gaussian the skewness is exactly one. We carried out this calculation and showed that for $\Delta_{ij} < \sim b_{ij}$ the skewness is very close to one. On the other hand, for $\Delta_{ij} \gg b_{ij}$ the skewness becomes large, and a better approximation is a Lorentzian with a cutoff at the wings. Nevertheless, by inspecting (95) we note that nuclear-spin pairs with $\Delta_{ij} \gg b_{ij}$ give a much weaker contribution to echo decay than pairs with $\Delta_{ij} \sim b_{ij}$. Therefore, this Gaussian fit is precisely valid for most important pairs. As discussed in (35) and (37) the difference between a Gaussian and a Lorentzian fit lies in the time dependence of the decay of coherence modulations; This is $\sim e^{-\sigma^2 t^2/2}$ for a Gaussian and $\sim e^{-t/\tau_d}$ for a Lorentzian.

For studies of echo decay we may drop the delta function contribution at zero frequency. Note that the first part of (102) gives an additional zero-frequency contribution that is the limit $\omega \rightarrow 0$ of the broadened spectrum. We emphasize that lifetime broadening was introduced to describe the effective irreversibility of an infinite nuclear-spin bath. But we should keep in mind that another important effect of the many-body interactions is to add additional peaks to the noise spectrum. Each of these peaks will have their own finite lifetime.

5 Electron Spin-Echo Decay of a Phosphorus Impurity in Silicon: Comparison with Experiment

In this section we apply our theory to a phosphorus donor impurity in bulk silicon. We consider both natural samples ($f = 4.67\%$ ^{29}Si nuclear spins) and isotopically enriched samples ($f = 99.23\%$ ^{29}Si nuclear spins). We show explicit numerical calculations of the nuclear-spin noise spectrum resulting from dipolar nuclear–nuclear couplings, predict the Hahn-echo envelope and compare our results with the experimental data of Tyryshkin et al. [21] and Abe et al. [22].

5.1 Effective-Mass Model for a Phosphorus Impurity in Silicon

Here, the donor impurity is described within effective-mass theory by a Kohn–Luttinger wavefunction [41],

$$\Psi(\mathbf{r}) = \frac{1}{\sqrt{6}} \sum_{j=1}^6 F_j(\mathbf{r}) u_j(\mathbf{r}) e^{i\mathbf{k}_j \cdot \mathbf{r}}, \quad (103)$$

$$\mathbf{k}_j = 0.85 \frac{2\pi}{a_{\text{Si}}} \hat{k}_j, \quad \hat{k}_j \in \{\hat{x}, -\hat{x}, \hat{y}, -\hat{y}, \hat{z}, -\hat{z}\}, \quad (104)$$

$$F_{1,2}(\mathbf{r}) = \frac{\exp\left[-\sqrt{\frac{x^2}{(nb)^2} + \frac{y^2+z^2}{(na)^2}}\right]}{\sqrt{\pi(na)^2(nb)}}, \quad (105)$$

with envelope functions F_j describing the effective-mass anisotropies. Here, $n = (0.029 \text{ eV}/E_i)^{1/2}$ with E_i being the ionization energy of the impurity ($E_i = 0.044 \text{ eV}$ for the phosphorus impurity, hence $n = 0.81$ in our case), $a_{\text{Si}} = 5.43 \text{ \AA}$ the lattice parameter for Si, $a = 25.09 \text{ \AA}$ and $b = 14.43 \text{ \AA}$ characteristic lengths for Si hydrogenic impurities [42]. Moreover, we will use experimentally measured values for the charge density on each Si lattice site $|u(\mathbf{R}_i)|^2 = \eta \approx 186$ [41]. Hence, the isotropic hyperfine interaction is given by

$$A_i^{\text{iso}} = \frac{16\pi}{9} \gamma_{e0} \gamma_n \eta [F_1(\mathbf{R}_i) \cos(k_0 X_i) + F_3(\mathbf{R}_i) \cos(k_0 Y_i) + F_5(\mathbf{R}_i) \cos(k_0 Z_i)]^2, \quad (106)$$

with the Si conduction-band minimum at $k_0 = (0.85)2\pi/a_{\text{Si}}$, gyromagnetic ratios for ^{29}Si nuclear spins $\gamma_n = 5.31 \times 10^3 (\text{sG})^{-1}$, and the free electron $\gamma_{e0} = 1.76 \times 10^7 (\text{sG})^{-1}$. It is instructive to check the experimental validity of (106) by calculating the inhomogeneous linewidth $\sim 1/(\gamma_{e0} T_2^*)$. A simple statistical theory [see (57)] leads to

$$\langle (\omega/\gamma_{e0} - B)^2 \rangle = \frac{f}{(2\gamma_{e0})^2} \sum_{\mathbf{R}_i \neq 0} (A_i^{\text{iso}})^2. \quad (107)$$

For natural silicon (nuclear-spin fraction $f = 0.0467$) our calculated root mean square linewidth is equal to 0.89 G. On the other hand, a simple spin-resonance scan leads to $2.5 \text{ G}/2\sqrt{2 \ln 2} = 1.06 \text{ G}$ [42]. Therefore, the simple model employed here is able to explain 84% of the experimental hyperfine linewidth. This is the level of agreement that we should expect when comparing our theory for echo decay with experiment.

5.2 Explicit Calculations of the Nuclear-Spin Noise Spectrum and Electron Spin-Echo Decay of a Phosphorus Impurity in Silicon

The nuclear-spin noise spectrum is calculated from (102) by excluding the $\delta(\omega)$ contribution. For each pair i, j we calculate the transition frequency (91) and broadening (101) using the derived microscopic values of the hyperfine interaction [see (106)] and the dipolar interaction

$$b_{ij} = -\frac{1}{4} \gamma_n^2 \hbar \frac{1 - 3 \cos^2 \theta_{ij}}{R_{ij}^3}. \quad (108)$$

For silicon, the sites i, j lie in a diamond lattice with parameter $a_{\text{Si}} = 5.43 \text{ \AA}$. We wrote a computer program that sums over lattice sites \mathbf{R}_i within r_0 of the center of the donor. Each site \mathbf{R}_i is then summed with all sites \mathbf{R}_j within r'_0 of \mathbf{R}_i (excluding double counting). After numerical tests we concluded that the values $r_0 = 200 \text{ \AA}$ and $r'_0 = 10 \text{ \AA}$ were high enough to guarantee convergence (increasing r_0 and r'_0 changes the calculations by a negligible amount). Our explicit numerical calculations for the echo decay without broadening [see (95)] reproduced the equivalent calculation of Witzel et al. [24] with no visible deviation. For $k_B T \gg \gamma_n B$ we may assume that the nuclear spins are completely unpolarized (the experimental data was taken at $T = 4 \text{ K}$ and $B = 0.3 \text{ T}$ [21]). We account for the isotopic fraction f (ratio of sites containing nuclear spin 1/2) using a simple averaging method. For example, the pair populations are set as $p_+ = p_- = f^2/4$, and the broadening $\sigma_{+-}^2 \propto f$ [note $\sum_k b_{ij}^2$ in (101)].

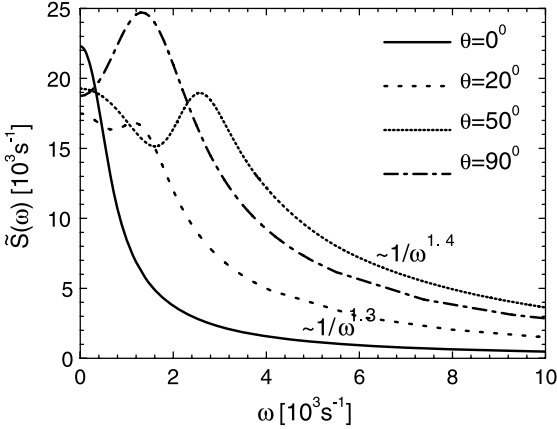


Fig. 5. Nuclear-spin noise affecting the electron-spin phase. We show the noise spectrum for several magnetic-field orientation angles θ with respect to the (001) direction. As θ is increased from zero, a broad peak develops at a frequency close to the dipolar splitting between nearest neighbors in the lattice. In this case, the noise spectrum is clearly nonmonotonous, and cannot be described by a Markovian model. The spin-echo envelope is a frequency integral of the noise spectrum weighted by a filter function

Figure 5 shows the nuclear-spin noise spectrum for natural Si at four different magnetic-field orientation angles θ with respect to the crystal direction (001). Here, $\theta = 0^\circ$ corresponds to $\mathbf{B} \parallel (001)$, while $\theta = 90^\circ$ corresponds to $\mathbf{B} \parallel (110)$. For θ away from zero the noise spectrum is characterized by a broad peak at which the flip-flop transition frequencies E_{+-} accumulate. The fact that the spectrum is nonmonotonic implies important *non-Markovian* behavior for electron-spin dynamics (recall that a Markovian noise spectrum is defined as a sum of Lorentzians, hence it is always monotonic). Interestingly, for θ close to zero and at low frequencies ($\omega < 5 \times 10^3 \text{ s}^{-1}$), the spectrum appears to be similar to a Lorentzian peaked at $\omega = 0$. However, one can not fit a Lorentzian up to high frequencies because the asymptotic behavior deviates significantly from $1/\omega^2$.

The Hahn echo is obtained by integrating the noise spectrum multiplied by the filter function (21) up to a frequency cutoff Λ (we used $\Lambda = 10^6\text{--}10^7 \text{ s}^{-1}$, and $df \sim 1\text{--}10 \text{ s}^{-1}$ in our numerical calculations). The result is shown in Fig. 6 for two different orientations. We show calculations of the echo without broadening [see (95), identical to the result shown in [24]] and for the echo with broadening, that is obtained through direct integration of the noise spectrum shown in Fig. 5. Note that the two theories are in close agreement here because for low nuclear-spin density ($f = 0.0467$) the broadenings are generally much smaller than the transition frequencies E_{+-} , at least for the important pairs causing spectral diffusion. Recall that our theory does not account for the anisotropic hyperfine interactions. Therefore, our theoretical

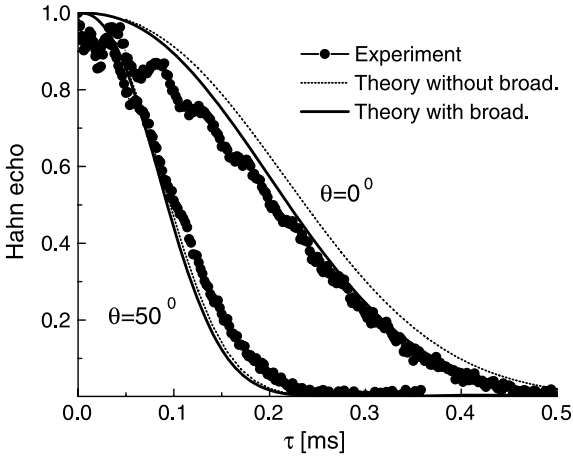


Fig. 6. Electron-spin echo decay of a phosphorus impurity in natural silicon (4.67% ^{29}Si nuclear spins) for two different magnetic-field orientations. We show experimental data from [21] together with theoretical calculations without flip-flop broadening (identical to [24]) and with flip-flop broadening. The latter is calculated by directly integrating the noise spectrum shown in Fig. 5 with the appropriate filter function

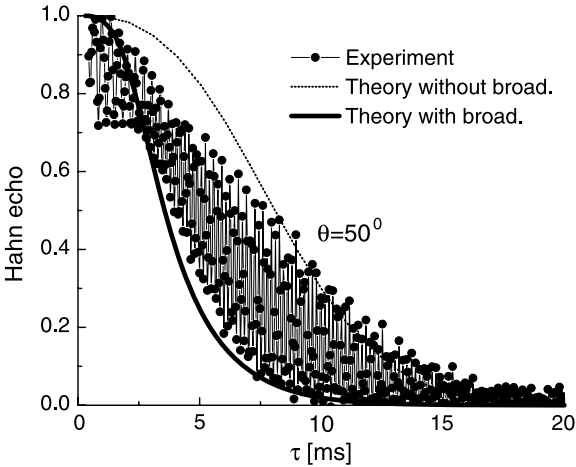


Fig. 7. Electron-spin-echo decay of a phosphorus impurity in isotopically enriched silicon (99.23% of ^{29}Si). Experimental data from [22]

results should be compared to the monotonic envelope enclosing the experimental data points.¹⁰ The echo modulations due to the anisotropic hyperfine interaction is clearly visible at short times in the experimental data shown in Fig. 6. These oscillations produce a loss of contrast of about 10% in the short-time regime. Apart from this effect, the agreement between theory and experiment is quite good.

¹⁰ We thank Dr. A.M. Tyryshkin for pointing this out to us.

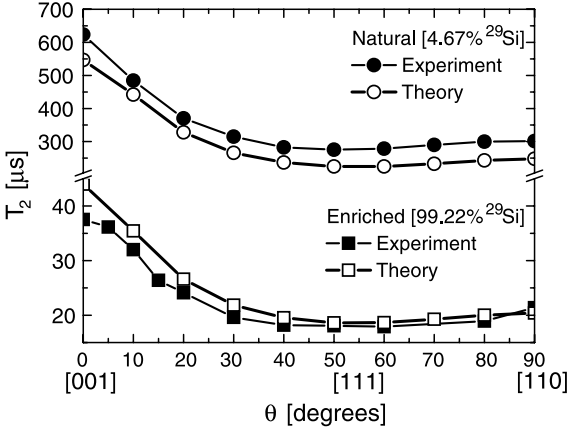


Fig. 8. Orientation dependence of the $1/e$ echo-decay time T_2 . θ is the angle between the applied magnetic field and the crystallographic (001) direction, so that $\theta = 90^\circ$ is along the (110) direction. We show experimental data for natural Si [21] and for isotopically enriched Si [22]. The theoretical calculations shown are without broadening. For natural Si, the experimental data was corrected for a θ -independent instantaneous diffusion decay, see [21]. Because of this the theoretical T_2 s are lower than the experimental T_2 s reported in [21], in contrast to what is observed in Fig. 6

Figure 7 shows echo-decay results for isotopically enriched samples ($f = 99.23\%$). The experimental data is from Abe et al. [22]. Note that here the echo modulations are very evident, the loss of contrast reaches $\sim 100\%$. The monotonic envelope on top of the experimental data is in reasonable agreement with the theory without broadening. However, the theory with broadening decays significantly faster. The difference between both theories increases for increasing f . This suggests that the mean-field theory proposed in Sect. 4.2 overestimates the broadening. We expect that a more sophisticated many-body calculation may account for this discrepancy.

Figure 8 shows the dependence of the $1/e$ echo decay time (T_2) with the magnetic-field angle. The shortest value of T_2 is obtained when \mathbf{B} is along the (111) direction ($\theta = 54.74^\circ$). In this case, none of the nearest-neighbor pairs have zero dipolar couplings. Only pairs i, j with \mathbf{R}_{ij} parallel to the (100), (010), and (001) directions have their dipolar interaction turned off by the magic angle [$\theta_{ij} = 54.74^\circ$ implies $\cos\theta_{ij} = 1/\sqrt{3}$ and $b_{ij} = 0$, see (108)]. On the other hand, for $\mathbf{B} \parallel (001)$, T_2 is longer by a factor of three. This occurs because the nearest-neighbor pairs, that usually give the strongest contribution to echo decay, are forming a magic angle with respect to $\mathbf{B} \parallel (001)$.¹¹

¹¹ The nearest neighbors for each site i are located at $\mathbf{R}_{ij} = \frac{1}{4}a_{\text{Si}}(1, 1, 1)$, $\frac{1}{4}a_{\text{Si}}(-1, -1, 1)$, $\frac{1}{4}a_{\text{Si}}(-1, 1, -1)$, and $\frac{1}{4}a_{\text{Si}}(1, -1, -1)$.

We now discuss the time dependence of the echo envelope. The echo decay without broadening fits well to the expression

$$\langle \sigma_+(2\tau) \rangle = e^{-(\frac{2\tau}{T_2})^{2.3}} \quad (109)$$

for a wide range of 2τ centered around T_2 and for all values of f (for a log–log plot, see Fig. 9 of [25]). Tyryshkin et al. [21] studied the time dependence of the natural-silicon experimental data by fitting the expression $v_E(2\tau) = e^{-2\tau/T'_2} e^{-(2\tau/T_2)^n}$. Here, T'_2 was interpreted as arising from a combination of spin-flip processes and the instantaneous diffusion mechanism, due to the finite concentration of donors. Tyryshkin et al. reported $T'_2 = 1.1$ ms and exponent $n = 2.4 \pm 0.1$ for all sample orientation angles between $20^\circ \leq \theta \leq 90^\circ$. For $\theta = 10^\circ$ they found $n = 2.6 \pm 0.1$, while for $\theta = 0^\circ$ $n = 3.0 \pm 0.2$. The time dependence at angles close to the (001) direction is yet to be explained theoretically. At natural abundance ($f = 0.0467$) the theory with broadening and the theory without broadening have similar time dependences. However, as f increases the time dependence of the broadened theory deviates significantly from the theory without broadening. As an example, for $f = 0.9923$ and $\theta = 50^\circ$ the broadened theory shows a crossover from $e^{-\tau^{3.3}}$ at short $\tau < 3 \mu\text{s}$ to $e^{-\tau^{1.7}}$ for $\tau > 3 \mu\text{s}$. This indicates that adding broadening to the nuclear-spin excitations leads to observable effects in the time dependence of electron-spin coherence. Unfortunately, the echo modulations are too strong in isotopically enriched samples (Fig. 7). This makes the precise experimental determination of the time dependence of the echo envelope quite difficult.

Equation (109) allows us to extract scaling of the $1/e$ decay time T_2 with the nuclear-spin fraction f . Note that in the theory without broadening f appears as a prefactor in the exponent due to $p_+ + p_- = f^2/4$. Therefore, we have simply

$$T_2 \propto f^{-2/2.3} = f^{-0.87}. \quad (110)$$

Abe et al. [43] measured T_2 for seven isotopically engineered samples with f ranging from 0.2–100%. Their study shows that T_2 must scale between $f^{-0.86}$ and $f^{-0.89}$, in good agreement with (110).

It is interesting to study the number and location of nuclear spins contributing to the noise spectrum. Figure 9 shows the contribution due to pairs inside shells concentric at the donor center (for natural silicon and $\theta = 50^\circ$). The contribution for $r_0 < 50 \text{ \AA}$ is quite small, but extends over a wide frequency spectrum. These nuclear spins are said to form a “frozen core”, because their noise amplitude is suppressed due to the strong difference in hyperfine fields affecting sites i, j . The frozen core of a Si:P donor has about 3×10^4 nuclear spins. This frozen-core effect plays an important role in other contexts as well such as optical spectroscopy experiments [44]. The nuclear-spin noise theory developed here allows a quantitative description of this

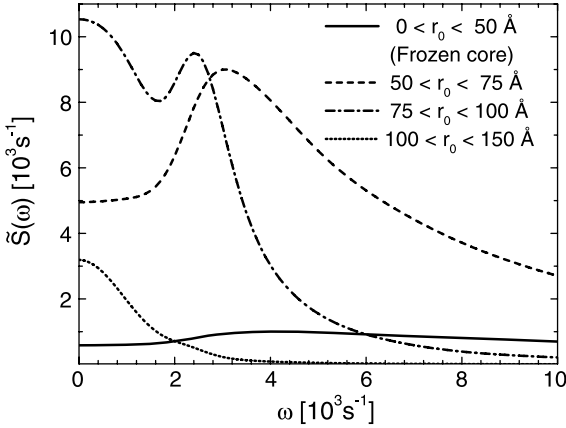


Fig. 9. Contribution of nuclear spins located at concentric shells around the donor (natural Si, $\theta = 50^\circ$). Nuclear pairs closer to the center ($r_0 < 50 \text{ \AA}$) have their fluctuation amplitude suppressed by the strong hyperfine field difference between sites i, j , forming a frozen core. The largest contribution is due to pairs located at $50 \text{ \AA} < r_0 < 100 \text{ \AA}$

effect.¹² From Fig. 9 it is evident that a significant fraction of the finite-frequency noise power comes from the large number of nuclear spins located between 50 \AA and 100 \AA off the donor center (about $\sim 2 \times 10^5$ nuclear spins). These pairs are satisfying a quasiresonance condition $\Delta_{ij} \sim b_{ij}$.

6 Conclusions and Outlook for the Future

In this chapter we describe a general theory for coherent evolution of an electron spin subject to time-dependent fluctuations along its quantization axis. Within the Gaussian approximation the electron-spin transverse magnetization can be expressed as a frequency integral over the magnetic noise spectrum multiplied by an appropriate filter function. The filter function depends on the particular pulse sequence used to probe spin coherence, differing substantially at low frequencies for free induction decay (FID) and Hahn echo.

We described a model Hamiltonian for a single-electron spin coupled to a lattice of interacting nuclear spins. For moderate magnetic fields ($B > 0.1 \text{ T}$) the model may be truncated to a secular Hamiltonian, with nonsecular effects incorporated into an effective indirect interaction between nuclear spins.

¹² In order to understand the frozen-core effect from our analytical expression for the noise spectrum, assume $A_i \gg A_j$ and $\Delta_{ij} \gg b_{ij}$ in (101). In this case we have $\sigma_{+-} \sim A_i$. From (102) the noise amplitude becomes $\sim b_{ij}^2/A_i$, which is much smaller than b_{ij} .

The latter is completely refocused by a Hahn echo, with higher-order effects leading to a small loss of visibility for the echo envelope.

We applied the general relationship between noise and decoherence to the case of a localized electron spin in isotopically engineered silicon, where the magnetic noise is mainly due to the dipolar fluctuation of spin-1/2 lattice nuclei. The nuclear-spin noise spectrum was calculated from a pair flip-flop model, resulting in a linear combination of sharp transitions (delta functions). The echo decay due to these sharp transitions is identical to the one derived by the lowest-order cluster expansion [24]. Next, we showed how to obtain a smooth noise spectrum by adding broadening to these transitions using a mean-field approach. The resulting noise spectrum was found to be strongly nonmonotonic, hence qualitatively different from the usual Lorentzian spectrum of a Gauss–Markov model. This structured noise spectrum is able to explain the non-Markovian dynamics ($\sim e^{-\tau^{2.3}}$) observed in electron spin-echo experiments for phosphorus-doped silicon. We compared the theories with and without broadening to two sets of experimental data, for natural and isotopically enriched silicon. The agreement was quite good for natural silicon, but not as good for ^{29}Si -enriched samples.

It is interesting to compare our results to the family of non-Gaussian phenomenological theories proposed a long time ago by Klauder and Anderson [16]. These authors classified spectral diffusion behavior in two groups, depending on the nature of the interactions causing magnetic noise. In “ T_1 samples” the magnetic noise is caused by nonresonant spins fluctuating individually (e.g., due to phonon emission). Magnetic noise in “ T_2 samples” is instead caused by the mutual interaction of the nonresonant spins. (For example, a nuclear-spin bath weakly coupled to the lattice is a “ T_2 sample” because the longitudinal nuclear-spin relaxation time is much longer than the transverse relaxation time.) Klauder and Anderson showed that echo-decay behavior in a variety of T_1 samples could be described by a Markovian theory by making assumptions about the general shape of the distribution of fluctuations at any given time. While a Gauss–Markov model leads to echo decay of the form $\sim e^{-\tau^3}$, a Lorentz–Markov model leads to $e^{-\tau^2}$ behavior, and intermediate non-Gaussian distributions result in $e^{-\tau^n}$ with n between two and three. Later, Zhidomirov and Salikhov [45] showed that similar behavior can be obtained in T_1 samples composed of a dilute distribution of magnetic impurities fluctuating according to a random telegraph noise model (Markovian with a non-Gaussian distribution).

Nevertheless, the problem of echo-decay behavior in “ T_2 samples” remained open. It was found empirically by many authors (see [13] and references therein) that echo-decay behavior in “ T_2 samples” is usually well fitted to the expression $\sim e^{-\tau^2}$, and the Lorentz–Markov model of Klauder and Anderson was often invoked as a phenomenological explanation. Here, we show that this behavior can be derived microscopically from a Gaussian model that takes into account the non-Markovian evolution of the coupled nuclear-spin

bath. The resulting behavior found by us [$e^{-\tau^{2.3}}$] is not due to a short-time approximation [the short-time behavior for each pair is actually given by $e^{-\tau^4}$, see (95)]. In order to explain these experiments we must consider the collective long-time evolution of a large number of nuclear spins [note that the characteristic frequency of fluctuation for a pair flip-flop $E_{+-} = 2\sqrt{b_{ij}^2 + \Delta_{ij}^2}$ gets renormalized to values much larger than the dipolar interaction b_{ij} when the nuclear spins are subject to strong hyperfine inhomogeneities $\Delta_{ij} = (A_i - A_j)/4$].

This theoretical explanation opens the way to novel microscopic interpretations of pulse electron-spin resonance experiments, where the electron spin may be viewed as a spectrometer of low-frequency magnetic noise due to a large number of nuclear spins or other magnetic moments. For example, a recent experiment [46] demonstrated that the silicon/silicon-oxide interface plays a major role in determining the spin-echo decay of antimony impurities implanted close to the interface. Recently, an interpretation of these results based on a model of magnetic $1/f$ noise due to dangling bonds at the amorphous interface was proposed [47]. Fitting this model to the experimental data established that the density of paramagnetic dangling bonds causing magnetic noise (10^{14} cm^{-2}) is much larger than previously anticipated on the basis of experiments probing dangling-bond spin resonance directly.

There are many open questions that deserve further investigation. First, what is the contribution of higher-order nuclear-spin transitions to the noise spectrum? This question may be answered by going beyond the simple pair flip-flop model assumed here, in a similar fashion as the cluster expansion developed in [24], or using an alternative linked cluster expansion for the spin Green's function [48]. Another interesting open question is the design of optimal sequences for suppressing the effects of nuclear-spin noise in electron-spin evolution, as was done for the random telegraph noise model in [49]. This is particularly important in the context of spin-based quantum computation. The efficiency of a Carr–Purcell sequence in suppressing the electron-spin coherence decay due to a nuclear-spin bath was considered in the framework of a semiclassical model (see [50], where the role of nuclear spins greater than $1/2$ was also considered) as well as using a cluster-expansion approach [51]. Recently, it was shown that the conditional evolution of the nuclear-spin bath driven by different electron-spin states can be used to control nuclear-spin dynamics for recovering part of the electron-spin coherence [52]. The reversal of the electron-mediated internuclear coupling [see (69)] by a Hahn echo is the simplest example of this back-action effect. We will certainly see many other interesting developments in the near future.

Acknowledgments

This research project began in 2001 under the supervision of Prof. Sankar Das Sarma, my Ph.D. advisor. I am grateful for and appreciate his guidance

and support. The collaboration continued with Wayne Witzel, another Ph.D. student in S. Das Sarma's group. This part of the work was supported by ARDA, US-ARO, US-ONR, and NSA-LPS. My postdoctoral work on this problem was in collaboration with Prof. K. Birgitta Whaley and Neil Shenvi. Neil also dedicated part of his Ph.D. thesis to problems related to electron-spin dynamics due to nuclear spins. This part of the work was supported by the DARPA SPINS program and the US-ONR. My long, energetic and prolific collaboration with Neil and Wayne cannot be overstated. I acknowledge great discussions with J. Fabian, X. Hu, A. Khaetskii, D. Loss, L.J. Sham, L.M.K. Vandersypen, and I. Zutíc. The role of experimentalists in the development of this theory was also very important. I wish to thank Stephen Lyon, Alexei Tyryshkin, Thomas Schenkel, Kohei Itoh, and Eisuke Abe for discussions and for providing their experimental data before it was published. Finally, I wish to acknowledge an enlightening conversation with Professor Erwin Hahn, who kindly shared his astonishing intuition on the problems that he pioneered a long time ago.

References

1. A. Schweiger, G. Jeschke, *Principles of Pulse Electron Paramagnetic Resonance* (Oxford University Press, Oxford, 2001) 183
2. X. Hu, in *Lecture Notes in Physics*, vol. 689, ed. by W. Pötz, U. Hohenester, J. Fabian (Springer, Berlin, 2006) 183
3. S. Das Sarma, R. de Sousa, X. Hu, B. Koiller, *Solid State Commun.* **133**, 737 (2005) 183
4. F. Jelezko et al., *Phys. Rev. Lett.* **92**, 0764401 (2004) 183
5. J.M. Elzerman et al., *Nature* **430**, 431 (2004) 183, 194, 195
6. M. Xiao et al., *Nature* **430**, 435 (2004) 183, 194
7. D. Rugar et al., *Nature* **430**, 329 (2004) 183
8. J.R. Petta et al., *Science* **309**, 2180 (2005) 183, 194, 195
9. G. Feher, E.A. Gere, *Phys. Rev.* **114**, 1245 (1959) 184
10. H. Hasegawa, *Phys. Rev.* **118**, 1523 (1960) 184
11. L.M. Roth, *Phys. Rev.* **118**, 1534 (1960) 184
12. R. de Sousa, S. Das Sarma, *Phys. Rev. B* **68**, 155330 (2003) 184, 188
13. M. Chiba, A. Hirai, *J. Phys. Soc. Jpn.* **33**, 730 (1972) 184, 185, 186, 216
14. B. Herzog, E.L. Hahn, *Phys. Rev.* **103**, 148 (1956) 185
15. J.P. Gordon, K.D. Bowers, *Phys. Rev. Lett.* **1**, 368 (1958) 185
16. J.R. Klauder, P.W. Anderson, *Phys. Rev.* **125**, 912 (1962) 185, 216
17. W.B. Mims, in *Electron Spin Resonance*, ed. by S. Geschwind (Plenum, New York, 1972) 185
18. K.M. Salikhov, Yu.D. Tsvetkov, in *Time Domain Electron Spin Resonance*, ed. by L. Kevan, R.N. Schwartz (Wiley, New York, 1979) 185
19. R. de Sousa, S. Das Sarma, *Phys. Rev. B* **68**, 115322 (2003) 185, 207

20. A.M. Tyryshkin, S.A. Lyon, A.V. Astashkin, A.M. Raitsimring, Phys. Rev. B **68**, 193207 (2003) 186
21. A.M. Tyryshkin, J.J.L. Morton, S.C. Benjamin, A. Ardavan, G.A.D. Briggs, J.W. Ager, S.A. Lyon, J. Phys. Condens. Matter **18**, S783 (2006) 186, 209, 210, 212, 213, 214
22. E. Abe, K.M. Itoh, J. Isoya, S. Yamasaki, Phys. Rev. B **70**, 033204 (2004) 186, 198, 209, 212, 213
23. A. Ferretti, M. Fanciulli, A. Ponti, A. Schweiger, Phys. Rev. **72**, 235201 (2005) 186
24. W.M. Witzel, R. de Sousa, S. Das Sarma, Phys. Rev. B **72**, 161306(R) (2005) 186, 203, 206, 210, 211, 212, 216, 217
25. W.M. Witzel, S. Das Sarma, Phys. Rev. B **74**, 035322 (2006) 203, 214
26. C.P. Slichter, *Principles of Magnetic Resonance*, 3rd edn. (Springer, Berlin, 1996) 187, 193, 196, 208
27. L.G. Rowan, E.L. Hahn, W.B. Mims, Phys. Rev. **137**, A61 (1965) 198
28. S. Saikin, L. Fedichkin, Phys. Rev. B **67**, 161302(R) (2003) 198
29. N. Shenvi, R. de Sousa, K.B. Whaley, Phys. Rev. B **71**, 224411 (2005) 199, 200, 202
30. I.A. Merkulov, Al.L. Efros, M. Rosen, Phys. Rev. B **65**, 205309 (2002) 200
31. A.V. Khaetskii, D. Loss, L. Glazman, Phys. Rev. Lett. **88**, 186802 (2002) 200
32. C. Deng, X. Hu, Phys. Rev. B **73**, 241303(R) (2006) 200, 202
33. D. Gammon et al., Phys. Rev. Lett. **86**, 5176 (2001) 200
34. K. Ono, S. Tarucha, Phys. Rev. Lett. **92**, 256803 (2004) 200
35. P.-F. Braun et al., Phys. Rev. Lett. **94**, 116601 (2005) 200
36. M.V.G. Dutt et al., Phys. Rev. Lett. **94**, 227403 (2005) 200
37. F.H.L. Koppens, Science **309**, 1346 (2005) 200
38. A.C. Johnson et al., Nature **435**, 925 (2005) 200
39. N. Shenvi, R. de Sousa, K.B. Whaley, Phys. Rev. B **71**, 144419 (2005) 201
40. W. Yao, R.-B. Liu, L.J. Sham, Phys. Rev. B **74**, 195301 (2006) 201, 202, 206
41. W. Kohn, in *Solid State Physics*, vol. 5, ed. by F. Seitz, D. Turnbull (Academic, New York, 1957), p. 257v 209
42. G. Feher, Phys. Rev. **114**, 1219 (1959) 209, 210
43. E. Abe, A. Fujimoto, J. Isoya, S. Yamasaki, K.M. Itoh, cond-mat/0512404 (unpublished) 214
44. R.G. DeVoe, A. Wokaun, S.C. Rand, R.G. Brewer, Phys. Rev. B **23**, 3125 (1981) 214
45. G.M. Zhidomirov, K.M. Salikhov, Sov. Phys. JETP **29**, 1037 (1969) 216
46. T. Schenkel et al., Appl. Phys. Lett. **88**, 112101 (2006) 217
47. R. de Sousa, Phys. Rev. B **76**, 245306 (2007) 217
48. S.K. Saikin, W. Yao, L.J. Sham, Phys. Rev. B **75**, 125314 (2007) 217

49. M. Möttönen, R. de Sousa, J. Zhang, K.B. Whaley, Phys. Rev. A **73**, 022332 (2006) 217
50. R. de Sousa, N. Shenvi, K.B. Whaley, Phys. Rev. B **72**, 045330 (2005) 217
51. W.M. Witzel, S. Das Sarma, Phys. Rev. Lett. **98**, 077601 (2007) 217
52. W. Yao, R.-B. Liu, L.J. Sham, Phys. Rev. Lett. **98**, 077602 (2007) 217

Index

- T_1 , 184
- T_2 , 184
- T_2^* , 184, 195
- Bloch–Wangsness–Redfield Master equation, 186
- Bloch–Wangsness–Redfield theory, 186
- Carr–Purcell sequence for coherence control, 193, 217
- Carr–Purcell sequences, 191
- decoherence, *see* spin coherence
- dipolar interaction, 197
- electron–nuclear-spin Hamiltonian, 198
- electron-spin coherence, 184, 217
- free induction decay (FID), 184, 191, 205
- frozen core of nuclear spins, 214
- Gauss–Markov model, 192
- Hahn echo, 190
 - decay due to nuclear spins, 206, 208
 - in isotopically enriched silicon, 212, 214
 - magnetic field orientation, 210, 213
 - noise filter function, 191
 - time dependence, 191, 213
- hyperfine interaction
 - anisotropic, 197
 - inhomogeneous broadening, 199
 - isotropic, 196
 - mediating nuclear–nuclear coupling, 200, 201
 - induction decay time, 195
 - isotropic and anisotropic hyperfine interactions, 183
 - isotropic hyperfine interaction, 196
- Markovian stochastic process, 185
- noise
 - high frequency, loss of visibility, 194
 - nuclear spin noise, 202, 210
 - relationship to decoherence, 186
 - surface effects, 217
- non-Markovian dynamics, 211, 216
- nuclear-spin noise, 203
- phosphorus impurity in silicon, 209
 - effective mass model, 209
 - electron spin decoherence, 209
 - inhomogeneous broadening, 210
- quantum computation, spin-based, 183
- relaxation time, 187
- secular approximation, 198
- spectral diffusion, 185
- spin coherence
 - Bloch–Wangsness–Redfield equation, 186
 - for a class of pulse sequences, 190
 - relationship to magnetic noise, 188
 - short time behavior, 191
 - single spin *vs.* many spins, 194
- spin echo, *see* Hahn echo
- spin-echo decay, 183, 195
- stochastic process, 188

A Robust and Fast Method to Compute Shallow States without Adjustable Parameters: Simulations for a Silicon-Based Qubit

Alberto Debernardi and Marco Fanciulli

MDM national lab, CNR-INFM, via Olivetti 2, 20041, Agrate Brianza, Italy
alberto.debernardi@mdm.infm.it
marco.fanciulli@mdm.infm.it

Abstract. Within the framework of the envelope function approximation we have computed – without adjustable parameters and with a reduced computational effort due to analytical expression of relevant Hamiltonian terms – the energy levels of the shallow P impurity in silicon and the hyperfine and superhyperfine splitting of the ground state. We have studied the dependence of these quantities on the applied external electric field along the [001] direction. Our results reproduce correctly the experimental splitting of the impurity ground states detected at zero electric field and provide reliable predictions for values of the field where experimental data are lacking. Further, we have studied the effect of confinement of a shallow state of a P atom at the center of a spherical Si-nanocrystal embedded in a SiO₂ matrix. In our simulations the valley–orbit interaction of a realistically screened Coulomb potential and of the core potential are included exactly, within the numerical accuracy due to the use of a finite basis set, while band-anisotropy effects are taken into account within the effective-mass approximation.

The building of a quantum computer, i.e., a computer where information processing obeys the laws of quantum mechanics, is one of the most intriguing and challenging task of 20th-century solid-state physics. The realization of this device will allow computations that, at present, exceed the capability of classical computers [1–4]: simulation of quantum systems, the prime factorization that has an important application in cryptography or efficient database access. An important factor, related to the evaluation of a technology leading to a device capable of quantum information processing, is the scalability. The year 1998 is an important date for quantum computing, since two milestone papers were published concerning the design of scalable solid-state devices that can be used for quantum computation. In fact, in this year, D. Loss and D.P. DiVincenzo [3] proposed to store a quantum bit in the spin of an electron confined in a quantum dot. In the same year B.E. Kane envisaged the scheme of a quantum computer [4] in which the quantum bits are nuclear spins of ³¹P impurities atoms at substitutional sites in silicon. In the latter scheme, the interaction between the nuclear spins at different

impurities sites is mediated by the electronic orbital of the impurity that, for shallow donors like P atoms in silicon (Si:P), extends for a few nanometers around the guest atom. Within this scheme simple quantum-bit manipulation as well as qubit–qubit interaction are achieved by an external electric field. An alternative scheme, exploiting the properties of impurities in silicon, has recently been proposed [5, 6]. In this scheme, the quantum information, embodied in electron spins bound to deep donors, is coupled via optically induced electronic excitation.

Kane’s proposal [4, 7] has driven increasing interest in the field of shallow impurities, and a number of theoretical studies that try to compute the properties of such a system were published in recent years [8–16]. Theoretical works are essentially divided into two categories: first-principles simulations, performed within the density functional theory, are allowed to study the effect of confinement in Si dots of small size, and numerical calculation by using the envelope function approximation to study extended systems where the use of *ab initio* techniques is prevented by the prohibitive computational cost (at least for the preset state-of-the-art classical computers). In the first category, we mention the calculation of electronic properties of clusters of small size [17], systematically investigated by Ossicini’s group [18–20], and the first-principles calculation of the hyperfine splitting in P-doped Si nanocrystal of small size (1 nm was the maximum radius considered) by Melnikov and Chelikowsky [14].

The computation of shallow impurity states can be conveniently performed by means of the envelope function approximation. However, to simulate in a realistic way the ground-state energy of the shallow states and its dependence on external field, it is necessary to include in the calculation the following quantities: I) band-structure effects of the host material, i.e., the band anisotropy of silicon near the conduction-band minima, II) the valley–orbit interaction (VO) [21], i.e., the fact that the impurity potential couples electronic states of different degenerate conduction-band minima (valleys) in crystalline silicon; III) the central cell correction, i.e., the difference between the “true” potential of the impurity and the screened Coulomb potential that is used to approximate the impurity potential. The latter is a hydrogen-like potential that is usually employed in the computation of shallow states since it exactly reproduces the “true” impurity Coulomb tail far from the impurity site. The difference between the true impurity potential and the hydrogen-like potential is expected to be significant only within the Wigner–Seitz cell surrounding the impurity and for this reason it is called the central-cell correction [22, 23].

An essential feature to realize the qubit as proposed by Kane’s quantum computer is the capability of tuning with an electric field the hyperfine splitting caused by the interaction between the P nuclear spin and the electron spin of the hydrogen-like impurity state. For shallow donors, the hyperfine splitting is mainly due to the isotropic contact or Fermi interaction, propor-

tional to the square modulus of the impurity wavefunction evaluated at the nuclear impurity site [24].

Kane proposed to manipulate via external electric fields the electronic wavefunction, therefore controlling the hyperfine splitting, and, for two qubits, the exchange interaction. In this context it is of paramount importance to determine what is the maximum electric field that can be applied to the system and that leaves the electron in the shallow state still bound to the donor atom. This critical electric field was recently determined theoretically for uniform electric field in bulk Si:P and found to be $E_{\text{cr}} \sim 2.5 \text{ MV/m}$ [25].

Within the envelope function approximation, different attempts have appeared in the literature [8–11] to compute P-impurity states in bulk Si or Si nanocrystals, the majority neglect valley–orbit interaction, while a few take it into account in an approximate [16] or a phenomenological way [15]. With the exception of [25, 26], we have not found in the literature any work that has taken into account in a reliable way valley–orbit interaction with central-cell correction to compute the electronic properties of shallow impurities in an external electric field. Following [25], we will show that to reproduce correctly the ground state of Si:P one has to include in the computation of the valley–orbit interaction, the central-cell corrections contribution due to impurity core electrons, a quantity that, to the best of our knowledge, nobody has taken into account before [25] in this type of calculations. By means of the envelope function of the conduction band and of a Gaussian basis set, we compute the electronic states of Si:P. In our calculation we take into account the band anisotropy within the effective-mass approximation, and we compute exactly, within the numerical accuracy due to the use of a finite basis set, the valley–orbit interaction of a realistically screened Coulomb potential, of the core potential, and of the electric field [25] or of the confinement potential approximated by a spherical well. In this chapter we present theoretical results for the energy levels of the shallow P impurity in silicon crystal as well as the hyperfine splitting of the ground state. We have studied the dependence of these quantities on the applied external electric field along the [001] direction. Our results reproduce correctly the experimental splitting of the impurity ground states detected at zero electric field. For increasing electric field, in contrast with what can be expected (on the basis of previous results) [15, 16] the main effect is not the spectrum narrowing of the 1s manifold, but the mixing of s- and p-like states. The mixing dominates the behavior of the impurity states energy at high electric field. The work is completed by a section where we applied our technique to compute the effect of confinement of a shallow electron in a spherical Si nanocrystal doped with one P atom.

1 Shallow Impurities in an External Field

In the limit of diluted concentration, the Hamiltonian, H , of a substitutional impurity in an external field $v_{\text{ext}}(\mathbf{r})$ reads

$$H \equiv H_0 + V_{\text{imp}} + v_{\text{ext}}(\mathbf{r}), \quad (1)$$

where V_{imp} is the donor-impurity potential and includes all the effects due to the presence of the guest atoms in the crystals, H_0 is the periodic Hamiltonian of the host crystal of which we are able to solve the Schrödinger equation $H_0\phi_{i,\mathbf{k}} = \varepsilon_i(\mathbf{k})\phi_{i,\mathbf{k}}$ and determine the Bloch eigenfunction $\phi_{i,\mathbf{k}}(\mathbf{r}) = e^{i\mathbf{k}\cdot\mathbf{r}}u_{i,\mathbf{k}}(\mathbf{r})$ and eigenvalues $\varepsilon_i(\mathbf{k})$. These data can be easily obtained, e.g., by the density function plane-wave pseudopotential technique, as was done in [25, 26] and in the present work. Our target is to find the eigenenergies and eigenfunction Ψ of H .

1.1 Envelope Function Approximation

For shallow states, where the extra electron is weakly bound to the impurity ion, it is convenient to solve the Schrödinger equation introducing the one-band approximation [22]

$$\Psi(\mathbf{r}) = \sum_{\mathbf{k}} F(\mathbf{k})e^{i\mathbf{k}\cdot\mathbf{r}}u_{\mathbf{k}}(\mathbf{r}), \quad (2)$$

where the summation is extended to all k -states of the conduction band (hereafter we will omit the conduction-band index since there is no possibility of confusion). F is called the envelope function and can be approximated by the summation of functions F_i highly localized in reciprocal space (since they are the Fourier transforms of highly delocalized shallow wavefunctions in real space) around the conduction-band minima (CBM) \mathbf{k}_i [22]

$$F(\mathbf{k}) \simeq \sum_{\mathbf{k}_i \in \text{CBM}} F_i(\mathbf{k} - \mathbf{k}_i). \quad (3)$$

This is equivalent to assuming that the eigenfunction of (1) (strictly an envelope function, the sum of the Fourier transform of $F_i(\mathbf{k})$) is so diffuse that one need only consider very close values of \mathbf{k} to the \mathbf{k}_i .¹ In reciprocal space, due to localization, the overlap between wavefunctions of two different minima can be usually safely neglected.

Within this approximation one assumes that only the wavefunctions $u_{\mathbf{k}}$ of the conduction band with energy close to the conduction-band minima contribute to the expansion of the impurity wavefunction (for which one can safely put $u_{\mathbf{k}} \simeq u_{\mathbf{k}_i}$). This assumption allows one to neglect the band structure and approximate the conduction band near the minimum by a quadratic form $\mathbf{p} \cdot \mathbf{M}_i^{-1} \cdot \mathbf{p}$ where \mathbf{p} is the momentum operator, and \mathbf{M}_i^{-1} is the inverse mass tensor at the i th conduction-band minima with wavevector \mathbf{k}_i .

By taking the expectation value of the Hamiltonian $\langle \Psi | H - E | \Psi \rangle = 0$, one obtains a Shindo–Nara-like equation [27]:

¹ This is one of the fundamental approximations of the effective-mass theory. This statement is the multivalley equivalent of approximation (2) as stated in [23], pp. 67.

$$\sum_{i,j} \int d\mathbf{r} F_i^*(\mathbf{r}) [(\mathbf{p} \cdot \mathbf{M}_i^{-1} \cdot \mathbf{p} - E) \delta_{i,j} + e^{-i(\mathbf{k}_i - \mathbf{k}_j) \cdot \mathbf{r}} u_{\mathbf{k}_i}^*(\mathbf{r}) (V_{\text{imp}}(\mathbf{r}) + v_{\text{ext}}(\mathbf{r})) u_{\mathbf{k}_j}(\mathbf{r})] F_j(\mathbf{r}) = 0, \quad (4)$$

where E is the energy computed relative to the conduction-band minima and $F_i(\mathbf{r})$ is the Fourier transform of $F_i(\mathbf{k})$. One can easily show that, with this definition, the wavefunction in real space can be written as

$$\Psi(\mathbf{r}) \simeq \sum_{i \in \text{CBM}} e^{i\mathbf{k}_i \cdot \mathbf{r}} u_{c,\mathbf{k}_i}(\mathbf{r}) F_i(\mathbf{r}), \quad (5)$$

where the summation index i labels all the equivalent conduction-band minima (CBM) and \mathbf{k}_i the corresponding wavevector (hereafter we will omit the conduction-band index since there is no possibility of confusion). The functions $u_{\mathbf{k}_i}$ have the periodicity of the host crystal. We expand their product in (4) in Fourier series

$$u_{\mathbf{k}_i}^*(\mathbf{r}) u_{\mathbf{k}_j}(\mathbf{r}) = \sum_{\mathbf{G}} C_{i,j}(\mathbf{G}) e^{i\mathbf{G} \cdot \mathbf{r}}, \quad (6)$$

where \mathbf{G} denote the reciprocal-lattice vectors.

For $i \neq j$, the second term in the square bracket in (4) gives the intervalley coupling due to the impurity potential (and to the external potential if it is present). It is convenient to divide this potential into two contributions

$$V_{\text{imp}}(\mathbf{r}) = -\epsilon^{-1} \frac{e^2}{r} + \Delta V_{\text{cell}}(\mathbf{r}). \quad (7)$$

The first term in the right-hand side is the Coulomb potential of a hydrogen-like impurity screened by the dielectric constant of the host crystal, ϵ , while the second term, $\Delta V_{\text{cell}}(\mathbf{r})$, represents the difference between the potential of the impurity (when the Coulomb tail is subtracted) and the potential of the bulk Si atom.

1.2 The Central-Cell Correction

In the present work, to compute ΔV_{cell} , we have neglected the difference of the valence density between Si:P and bulk Si, as well as the atomic relaxation of the neighbor shells surrounding the impurity, and we have approximated the central-cell correction

$$\Delta V_{\text{cell}}(\mathbf{r}) \simeq \Delta V_{\text{cc}}(\mathbf{r}) \equiv V_{\text{P}}^{\text{core}}(\mathbf{r}) - V_{\text{Si}}^{\text{core}}(\mathbf{r}), \quad (8)$$

with the difference between the (short-range) potential of (filled-shell) core electrons of Si and P atoms. The core correction potential, ΔV_{cc} , has spherical symmetry, and it vanishes rapidly outside the core radius as soon as the core density becomes negligible. No dielectric screening is necessary for this term since the potential is short range.

1.3 Numerical Basis Set

In our calculation we have expanded the envelope functions $F_i(\mathbf{r})$ on a Gaussian basis set:

$$e^{-\alpha r^2} r^l Y_{l,m}, \quad (9)$$

where the spherical harmonics $Y_{l,m}$ describe the angular dependence of the impurity wavefunction. The core correction term involves a radial integral that can be easily computed numerically with small computational effort due to the short range of the potential. However, this term can be computed analytically by fitting the core density with an appropriate function. With the exception of the short-range core term (see (8)) computationally inexpensive, by using the Gaussian basis set we can compute all matrix elements in an analytical form (i.e., in terms of elementary or special functions) with a considerable reduction of computational effort [28]. By using the Gaussian basis set, we can compute in real space the term involving the potential V_{imp} without assuming that the potential has no Fourier components outside the Brillouin zone, as is commonly done in standard effective-mass theory calculation.² In the expansion of the envelope function we include spherical harmonics up to f states ($l = 3$). The Gaussian parameters are chosen according to the formula: $\alpha = \alpha_0 \delta_\alpha^n$, where $n = -9, -8, \dots, 8, 9$; $\alpha_0 = 0.005 a_B^{-2}$; and $\delta_\alpha = 1.85$ (where a_B is the Bohr radius of hydrogen atom). In total, we use about ~ 1800 basis functions. This ensures an accurate convergence of our results at zero field and at nonvanishing fields for states that are localized at the impurity.

This basis set is particularly useful in the case when an uniform electric field is applied to the system. In fact, the use of a localized basis to expand the impurity wavefunction allows us to avoid the problem of computation of the matrix element of uniform electric field, that in the case of a plane-wave basis set can be solved only by recasting the Schrödinger equation in terms of a Berry phase [29, 30].

2 Phosphorous Impurity in Silicon

We applied the method presented in [25] to study the Stark effect of shallow states of diluted phosphorous impurities in silicon [25]. Our results are compared with experimental data, available at zero electric field. We will discuss the behavior of the shallow states as a function of a uniform electric field and in particular the physical mechanism responsible for the ionization of the ground states at a critical field E_{cr} , that according to the prediction of [25] is approximately 2.5 MV/m.

² See, e.g., approximation (1) in [23], pp. 67. We recommend this book to the reader interested in a clear and detailed discussion of the approximations used in standard envelope function theory.

2.1 Bulk Ingredients

The electronic band structure of a silicon crystal displays six conduction-band minima (valleys) located along the [001] and equivalent directions at a distance $k_0 \sim 0.84 \frac{2\pi}{a_L}$ from the Brillouin zone center (a_L denote the lattice parameter of Si). The expansion of the conduction-band energy of Si up to the quadratic term for the conduction-band minima along the e [001] direction reads (effective-mass approximation):

$$\varepsilon(\mathbf{k}) = \varepsilon(\mathbf{k}_1) + \frac{\hbar^2}{2m_T}(k_x^2 + k_y^2) + \frac{\hbar^2}{2m_L}(k_z - k_0)^2. \quad (10)$$

Similar expressions are used for the other conduction-band minima located at equivalent directions. At the conduction-band minima of silicon, the effective-mass tensor is highly anisotropic, i.e., the experimental value of the longitudinal effective mass $m_L = 0.916m_e$ differs significantly from the value of the transverse effective mass $m_T = 0.191m_e$.

In our calculation we use an ϵ that depends on the wavevector according to the parameterization given in [31], where the dependence of ϵ as a function of the wavevector is obtained by fitting first-principles calculation of bulk Si, while the only experimental parameter used is the high-frequency dielectric constant $\epsilon_\infty \equiv \epsilon(\mathbf{k} = \mathbf{0}) = 11.4$.

In our calculation we use the experimental values for the high-frequency dielectric constant, ϵ_∞ , and the effective masses of bulk silicon, m_T and m_L , because they are known with high precision. However, it is important to underline that, for the method described in [25] and used here, it is not necessary to use experimental data for the input of the calculation, since one can also use first-principles calculations to obtain the same parameters: in solids where ϵ_∞ , or \mathbf{M}_i^{-1} , or both parameters, are not measured (or the measured value is not accurate enough), these constants can be reliably computed by density functional theory.³

All other bulk Si quantities used to solve (4) are obtained by first principles. We compute ΔV_{cc} by the atomic density functional, $C_{i,j}$ and other Si bulk parameters by plane-wave pseudopotentials techniques [32]. In our calculation we include, as usual [33], only the $C_{i,j}(\mathbf{G})$ with $\mathbf{G} = \mathbf{0}$ terms. Obviously $C_{i,i}(\mathbf{0}) = 1$, the value of the other $\mathbf{G} = \mathbf{0}$ coefficients we computed are displayed in Table 1, and compared with previous values taken from literature.

3 Theoretical Results: Si:P

First, we assess the reliability of our results by comparing them with experimental data, available at zero field. If VO is neglected, the ground states

³ Note that, if all ingredients are computed by first principles, the method exposed here is parameter free.

Table 1. Coefficients of the Fourier expansion of different valleys of the periodic part of Block's states

$C_{\mathbf{k}_i, \mathbf{k}_j}$	This work	R. Resta [33]
$\mathbf{k}_x, -\mathbf{k}_x$	-0.2713	-0.181
$\mathbf{k}_x, \mathbf{k}_y$	0.3602	0.407

of a substitutional impurity in Si is six-fold degenerate. The VO interaction removes this degeneracy mixing of these six 1s states to obtain, according to the symmetry of the system, a singlet (A_1), a doublet (E), and a triplet (T_2) state. Our computed splitting of these states reproduce well the experimental data at zero electric field. The lower-energy modes (the 1s manifold) are (experimental data from [22] are in parenthesis): $A_1 = -41.7$ (-45.5) meV, $E = -30.1$ (-32.6) meV, $T_2 = -32.3$ (-33.8) meV. A result obtained without any adjustable parameters.

3.1 The Core-Correction Contribution

We stress the importance of including the core-correction term ΔV_{cc} , that gives the correct scattering of the shallow wavefunction with the core states of the impurity. In fact, neglecting the ΔV_{cc} contribution and considering the intervalley coupling due only to the screened Coulomb potential, we found that the A_1 ground state has an energy that is considerably lower (less than ~ -120 meV) than the core corrected one, while we find very similar results (with differences within ~ 2 meV) for E and T_2 states. The importance of including the ΔV_{cc} seems not to have been noticed before [25] despite the extensive published theoretical work on the energy of shallow states in Si:P. We attribute this rather surprising fact to three different causes. The first cause is that the intervalley coupling is frequently neglected: in this case the resulting ground-state energy is equal to 31.2 meV [34], it is sixfold degenerate (since the six valleys are not interacting), and the theoretical result does not reproduce the experimental splitting of s states, nor takes into account other physical phenomena such as the multivalley interferences that are of paramount importance for quantum computation. The second cause is that the intervalley coupling is included in an approximate or in a phenomenological way (i.e., by using experimental parameters), in the latter case an adjustable parameter is used to reproduce the energy of the ground state or the experimental splitting of the 1s-manifold, as was done, e.g., in [15]: in this case the use of an experimental constant gives no insight into the microscopic mechanisms responsible for the splitting of the 1s-manifold. The third cause is that the VO coupling, due to the Coulomb potential, was included in the Hamiltonian, but the ground-state energy was computed with a wavefunction with only a few variational parameters (as in [21] where two variational parameters were used, or [35] where the variational parameters are three):

in this case the agreement between theory and experiment must be considered fortuitous, on the basis of results of [25]. It is due to the cancelation of two independent and non-negligible effects: neglecting a significant part of the Hamiltonian (the contribution to valley-orbit interaction due to the central-cell correction) combined with the use of a few-parameter variational wavefunction that always gives an upper limit of the ground states and that produces in this case a considerable overestimation of the true ground-state energy associated to the approximated Hamiltonian.

3.2 Stark Effect

We applied the method of [25] to study the Stark effect of shallow states of diluted phosphorous impurities in silicon [25]. When a uniform electric field \mathcal{E} is applied the corresponding external potential reads (electron charge $-|e|$):

$$v_{\text{ext}}(\mathbf{r}) = -|e|\mathcal{E} \cdot \mathbf{r}. \quad (11)$$

Note that the potential associated to a uniform electric field tends to $-\infty$ when the electron moves in the direction of the electric field far away from the impurity nucleus. In this region of space, where the tail of the nucleus potential produces negligible effects the electron presents a free motion uniformly accelerated moving from the impurity into the direction of the electric field. In this free-electron region it is possible to find a solution of the Schrödinger equation with energy arbitrarily low due to the fact that the potential tends to $-\infty$. In the following, as is usual, the term “ground state” denotes the state of lower energy among all bounded states, i.e., those with wavefunction localized close to the impurity.

In the top panel of Fig. 1 we display our results for the computed lower 32 impurity levels (denoted with solid lines) as a function of a uniform electric field applied along the [001] direction. In the bottom panel of the figure we display the square modulus of ground-state wavefunctions (corresponding to the energy level of the top panel) computed at the impurity site ($\|\Psi(\mathbf{0})\|^2$), i.e., a quantity proportional to the hyperfine splitting. Following the common practice, we choose the crystal site of phosphorous atom as the origin of the Cartesian axis reference frame.

According to the results displayed in Fig. 1, the 1s-manifold, resulting from the coupling of 1s states by the intervalleys interaction, displays a small dependence on the electric field, at least up to 2–2.5 MV/m when the energy of this manifold becomes comparable with that of the p-like states. The energy of the ground state (A_1) decreases with increasing electric field, and the effect of the spectrum narrowing of the 1s manifold, resulting from the coupling of 1s states by the intervalleys interaction, is quite small at least up to 2–2.5 MV/m when the energy of this manifold becomes comparable with that of the p-like states. The electric field lifts the degeneracy of the doublet E state and (partially) of the triplet T_2 state; an effect that, on the energy scale of Fig. 1, becomes appreciable at 1.5–2 MV/m.

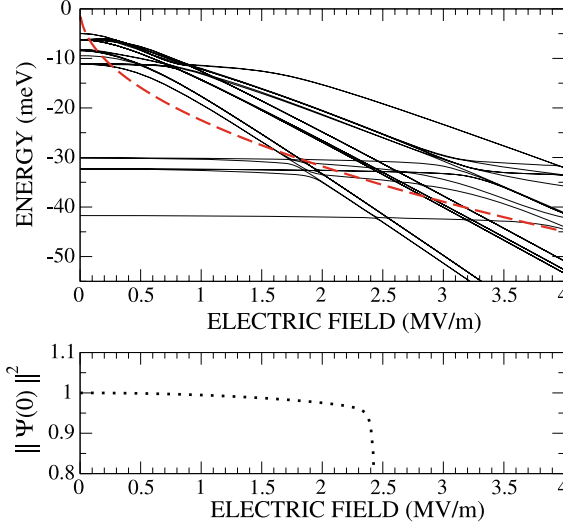


Fig. 1. *Top panel:* solid lines denote the lower energy levels of Si:P as a function of uniform electric field directed along (001); a dashed line denotes the minimum energy of the barrier surrounding the impurity. *Bottom panel:* the square modulus of the ground-state wavefunctions (dotted line) computed at the impurity site (and normalized to the zero-field result)

The mixing of s- p-like states dominates the behavior of impurity states at higher electric fields. When the electric field is increased, before the narrowing of the 1s spectrum becomes significant, the singlet energy level – s-like state, corresponding to the ground state up to $E_{cr} \sim 2.45$ MV/m – and a (almost) doublet energy level that originates from a zero-field $2p_0$ -like state, become almost degenerate. This gives a mixing of the two states and for fields larger than E_{cr} the ground state becomes a p-like state (almost) doubly degenerate. Since the 1s and $2p_0$ states have the same magnetic quantum number $m = 0$ their energy levels display anticrossing behavior [36] at \mathcal{E}_{cr} , as can be noticed by looking at the inset of Fig. 2.

To understand the physical mechanisms involved we have plotted in Fig. 2 the wavefunctions of these states along the z -axis (top and middle panel), and the energy barrier (bottom panel) separating the states localized near the impurity (located at the origin of the horizontal axis) from the free-electron region (in the right part of the figure). In the inset we display the states with lower energy at a value of the electric field near to \mathcal{E}_{cr} . The energy scale and the field scale are magnified with respect to the data of Fig. 1 to make visible to the reader the (anti)crossing behavior of the three lowest-energy levels. In Fig. 3 we show the two-dimensional contour plot of the square modulus of the ground-state wavefunction at zero field. From the figure, the reader can notice the sharp peak at the impurity site. The square modulus of the ground-state wavefunction displays a sharp peak at the impurity also for nonvanishing values of the electric field up to \mathcal{E}_{cr} (see top panel of Fig. 1). In the following discussion we refer to the field range of the inset in Fig. 1. At \mathcal{E}_{cr} the first excited state (in red) is a “pure” $2p_0$ -like state and it is mainly localized outside the barrier at $z \sim 18$ nm, a value that corresponds

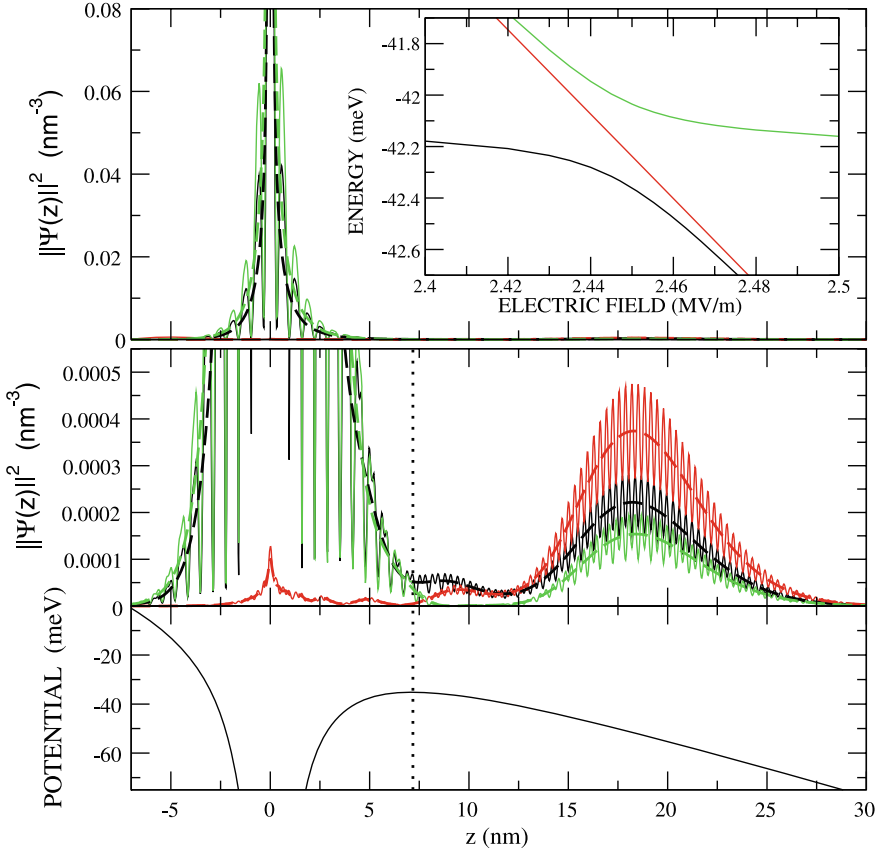


Fig. 2. Square modulus of the wavefunction (*solid lines*) and of the envelope function ($\sum_i \|F_i(z)\|^2$, *dashed lines*) of the three lowest-energy levels (in *black, red and green*) of Si:P (*top and middle panel* with different vertical scales) and the sum of electric field and screened Coulomb potential (*bottom panel*) as a function of the Cartesian coordinate z . The rapid oscillatory behaviors are fingerprints of multi-valley interference. $\mathcal{E} = (0, 0, 2.45)$ MV/m. *Vertical dotted line* correspond to (the saddle point at) the minimum of the energy barrier surrounding the impurity. *Inset*: the same as top panel of Fig. 1 on a magnified scale and on a selected range close to the critical field

approximately to the top of the red “hill”. Comparing the position of the wavefunction peak with the potential profile in the bottom of Fig. 2 one can easily understand that this state (red line) corresponds to an ionized state since it is in the space region of the free particles. For values of the electric field lower than \mathcal{E}_{cr} , the ground state is 1s-like and it is located at the impurity site within the potential barrier (bound state), while the second excited states (green line) shows a behavior similar to the first excited states. At \mathcal{E}_{cr} the two latter states mix and the states are localized partially either

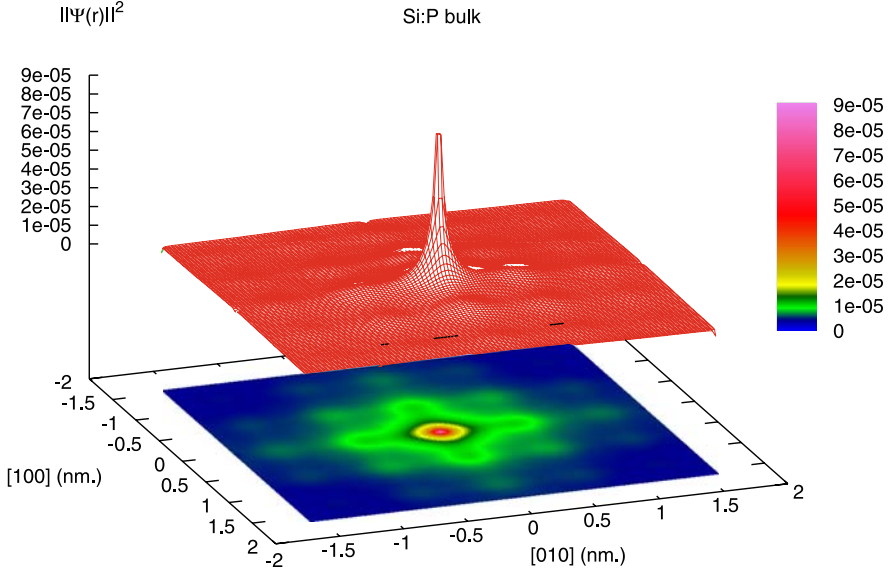


Fig. 3. Contour plot in the $[001]$ plane (passing through the origin) of the square modulus of the envelope function ($\sum_i \|F_i(z)\|^2$) of the ground state of Si:P (zero electric field)

within the potential barrier, or outside the potential barrier in the free-space region, as can be noticed by looking to the middle panel of Fig. 2. For values of the electric field larger than \mathcal{E}_{cr} , the ground (black line) state is $2p_0$ -like, and it is localized outside the energy barrier. Thus, the ground state at \mathcal{E}_{cr} becomes ionized by tunneling through the energy barrier, and the value of the hyperfine splitting decreases abruptly at $\mathcal{E} = \mathcal{E}_{\text{cr}}$. It is well known that the envelope function approximation can correctly predict only the magnitude of the hyperfine splitting [37], however, this fact would not affect the above results that are determined by the energies of the states, and we expect that the small discrepancies between the calculated A_1 state energy and the experimental value at zero field, will only shift \mathcal{E}_{cr} by a fraction of MV/m.

3.3 Electric-Field Dependence of Superhyperfine Constants

In Kane's proposal, the electric field is used not only to manipulate a single qubit, but also to allow the shallow wavefunction of an impurity to interact with another impurity nucleus located at a certain distance from the first. For this reason, it is important to know how the ground-state wavefunction is modified by an electric field not only at the impurity site, but also at other nuclear sites. To deal with a directly measurable quantity we consider the Fermi contact superhyperfine constant, obtained by electron–nuclear double resonance (ENDOR) measurements [38], and more recently by electron spin-

Table 2. SHF interaction of A-shell (in MHz) for Si:P at different value of (001) directed electric field (in MV/m)

Field	0	0.5	1	1.5	2
(0, 0, 4)	5.238	5.253	5.251	5.230	5.180
(0, 0, $\bar{4}$)	5.238	5.206	5.158	5.090	4.995
(4, 0, 0)	5.238	5.232	5.213	5.179	5.122

echo envelope modulation (ESEEM) [39], that is proportional to the square modulus of the envelope function computed at the impurity site or at sites of shell atoms surrounding the impurity.⁴

To study the dependence of the superhyperfine splitting (SHF) on the uniform electric field we consider here only the $A(0, 0, 4)$ shell that presents the larger SHF at zero field. This shell corresponds to the six Si atoms at $(\pm a_L, 0, 0)$, $(0, \pm a_L, 0)$ $(0, 0, \pm a_L)$. These atoms are equivalent at zero electric field and they present the same SHF, but this degeneracy is lifted when a uniform electric field is applied along the (001) direction.

Our results for the SHF interaction of the A-shell at zero field⁵ is $a = 5.238$ MHz to be compared with the experimental value $a = 5.962$ MHz [38]. Other theoretical results taken from the literature are: $a = 2.963$ MHz obtained by Overhof and Gerstmann [12] by first principles, $a = 5.848$ MHz obtained by Ivery and Mieher [41] by a multiband approach, and $a = 8.414$ MHz [41] that the same authors obtained by a traditional envelope function calculation.

In Table 2 we report our results for the SHF interaction of all nonequivalent positions of the A shell and for different values of an electric field along the [001] direction. The SHF interaction constants show both linear and quadratic field dependence and, more remarkably, the effect of the electric field can be detected already at low fields, around 0.5–1.0 MV/m, where a relative change of about 4% – within the accuracy of ENDOR measurements – has been predicted. From the table the reader can see that the SHF, at the atomic site of the shell with negative or null z , will have a reduction of the wave density as expected (the field is pointing to positive z). For small electric fields the wavefunction density increases for the atomic site of the shell placed along the [001] direction, while at higher electric fields there is a general reduction of the wavefunction density, also at the (004) site, due to an increased delocalization along the electric-field direction.⁶

⁴ At a Si^{29} nucleus (placed at \mathbf{r}_α), the wavefunction density is given by $|\psi(\mathbf{r}_\alpha)|^2 = -0.7615 \times 10^{-2} a_\alpha \text{ \AA}^{-3}$ where a_α is expressed in MHz [38].

⁵ Since, by definition, the pseudopotential technique does not reproduce the correct wavefunction density of bulk Si at the nucleus site, we use the experimental value $\|u_{\mathbf{k}_i}(\mathbf{0})\|^2 = 178$ (see [40]).

⁶ We found a similar effect of the electric field also for SHF interaction constants of other shells [28]. In general, our results agree with the experimental data and have

4 Confinement Effects

In the previous sections we have studied how it is possible to manipulate the wavefunction of shallow electron states by means of a uniform electric field. However, there are other ways to modify the wavefunction of the shallow state in bulk silicon. One of them is the confinement of the electron by means of a potential barrier. An example of a potential barrier that may be suitable for quantum computing applications is obtained by the conduction-band offset of the interface formed between bulk silicon and silicon dioxide (SiO_2). The bottom of the conduction band of SiO_2 is a few eV higher than the bottom of the conduction band of Si. Since the energy of shallow electrons is a few tens of meV, the shallow electron experiences a potential barrier at the Si/ SiO_2 interface that prevents it penetrating into the SiO_2 layer. This situation is experienced by those P atoms located close to the Si/ SiO_2 interface in MOSFETs (one-side confinement) or in FIN-FETs (three-side confinement). The influence of the barrier at the Si/ SiO_2 interface on the energy levels of P in silicon has been investigated previously in MOSFETs [42]. Here, we concentrate on the full confinement obtained in Si nanoclusters embedded in a SiO_2 matrix. Further, with the present technology it is possible to practically realize these devices, since Si nanostructures embedded in a SiO_2 matrix can be tailored (at least in principle) to the desired shape by oxidation of bulk Si.

To investigate the effect of confinement on the shallow levels we consider a phosphorous impurity placed at the center of a Si nanocrystal embedded in a SiO_2 matrix. We assume that the nanocrystal has a spherical shape with radius R . The shallow electron experiences the impurity potential V_{imp} and the confinement potential that can be approximated by a spherical well

$$v_{\text{ext}}(\mathbf{r}) = \begin{cases} 0, & \text{if } \mathbf{r} \leq R, \\ V_0, & \text{if } \mathbf{r} > R. \end{cases} \quad (12)$$

In our simulation we assume that \mathbf{M}_i^{-1} does not depend on the radius R , and we chose for the barrier height (i.e., for the confinement potential) the value $V_0 = 3.2$ eV, that corresponds to the experimental value of the conduction-band offset at the Si/ SiO_2 interface [43]. By inserting (12) into (4) we have computed the shallow states of Si nanocrystal doped with one P at the center. In Fig. 4 we have plotted our results for the lower-energy levels as a function of

an accuracy at least comparable with other theoretical results, with the exception of the first shell (denoted with $E(1, 1, 1)$). Compared to the first-principles approach of [12], our results overestimate the experimental data. We attribute this to the effect of relaxation of nearest-neighbor atoms to the impurity, neglected in the present calculation and expected to be important in this case. This would explain also the discrepancy of our results with the experimental hyperfine splitting (that, however, is far better than standard EMT). However, by the method of [25] one can easily compute the superhyperfine splitting of the shells far from the impurity atom, i.e., well above the range considered by Overhof and Gerstmann in their ab initio calculation [12].

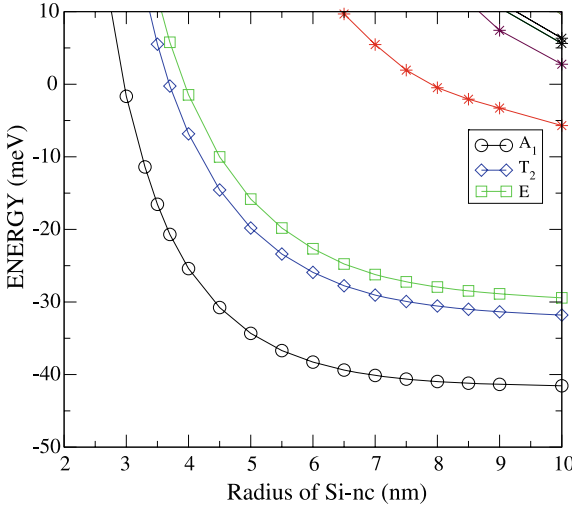


Fig. 4. Open circles, open diamonds, and open squares denote the calculated energy level of the 1s manifold for the A_1 (ground state), T_2 , and E states respectively, while stars denote the p levels. Continuous lines are a guide for the eye

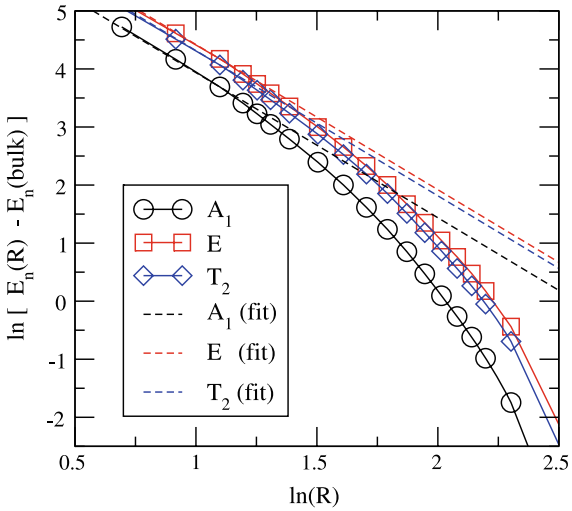


Fig. 5. Energy levels of the 1s manifold as a function of nanoparticle radius on logarithmic scales on both axis. Solid lines are the linear functions passing through the $R = 3$ nm data points (corresponding to ~ 1.1 of the horizontal scale) with slope determined by the value $\alpha = 2.5$

the nanoparticle radius. As expected, the confinement of the electron within the nanoparticle produces an increase of the energy of the shallow state, a fact that can be simply predicted on the basis of the indetermination principle: since $\Delta x \Delta p_x \sim \hbar$ the confinement of the electron in a nanostructure of size d in one dimension gives a kinetic energy increase of the order of $\frac{\hbar^2}{2m^*} \left(\frac{2\pi}{d}\right)^2$.

However, for nanoparticles of small size, when the radius of the nanocrystal becomes comparable to the donor Bohr radius, it is expected that the envelope function approximation breaks down: on the one hand the kinetic energy is so high that it exceeds the conduction-band minima, so that the electron is no longer bound to the P atom, but rather it can move in the

whole nanocrystal, and the effective mass is expected to approach the electron mass rather than to coincide with the bulk effective mass. On the other hand, if the electron is confined in a structure of linear dimension d in real space, the corresponding wavefunction in reciprocal space (i.e., the Fourier transform of the wavefunction in real space) is expected to be significant in a region of size $\frac{2\pi}{d}$. If we take $d = 3$ nm as the linear dimension of the confinement region where the shallow wavefunction is spread in real space, we obtain that the wavefunction in k -space is delocalized in a region that is about $\frac{1}{10}$ of the dimension of the reciprocal lattice vector of bulk Si. As a consequence, since the shallow wavefunction extends significantly in the first Brillouin zone, we do not expect that the shallow wavefunctions can be described by the superposition of localized functions in the reciprocal space around the conduction-band minima as assumed in (3).

We have investigated the dependence of the energy level E_n (where n labels the A_1 , T_2 and E states) of the 1s manifold as a function of the radius of the Si nanocrystal R ; we assume that $E_n(R)$ can be described by a simple power law of the type $\propto 1/R^\alpha$. Obviously $E_n(R)$ should approach the bulk value, $E_n(\text{bulk})$, in the limit $R \rightarrow \infty$. In Fig. 5 we display our results for the 1s manifold energy levels as a function of R on a logarithmic scale for both axis. With this choice of scale the parameter α is given by the slope of the data (i.e., α corresponds to minus the derivative of the function $\ln[E_n(R) - E_n(\text{bulk})]$ with respect to the variable $\ln(R)$). We can notice from Fig. 5 that the parameter α is not a constant in the range of radius investigated and a more complex functional dependence would be needed to fit our data, a result already pointed out in [26]. Since we are interested in the limit of small R , we have fitted the data points at $R = 3$ nm (that corresponds to ~ 1.1 in the abscissa) with straight lines (displayed in Fig. 5 as dashed lines), the slope of these lines corresponding to $\alpha = 2.5$. As can be noticed from the figure, the approximation $\alpha = 2.5$ can fit quite well the theoretical data, at least up to $R = 4$ nm.

The effect of confinement on the hyperfine splitting can be seen in Fig. 6 where we report our results for the hyperfine splitting as a function of nanocrystal size and compare the results with the experimental data taken from the work of Fujii et al. [44]. Our results are in good agreement with experimental data. The effect of confinement is clearly seen in the increase of the hyperfine splitting when the radius is reduced, thus suggesting that the confinements in nanostructures can be used to increase the hyperfine splitting. From the figure, it is evident that the effect of confinement on the hyperfine splitting can be well described by the theoretical approach outlined here, at least for nanocrystals with $R \geq 2$ –3 nm. For the reasons described above, we expect that this size corresponds to the smaller radius of the nanocrystal for which the envelope function approximation, adopted here, is still valid.

The dependence of the hyperfine splitting on the nanocrystal radius was studied in [14] by Melnikov and Chelikowsky who computed the hyperfine

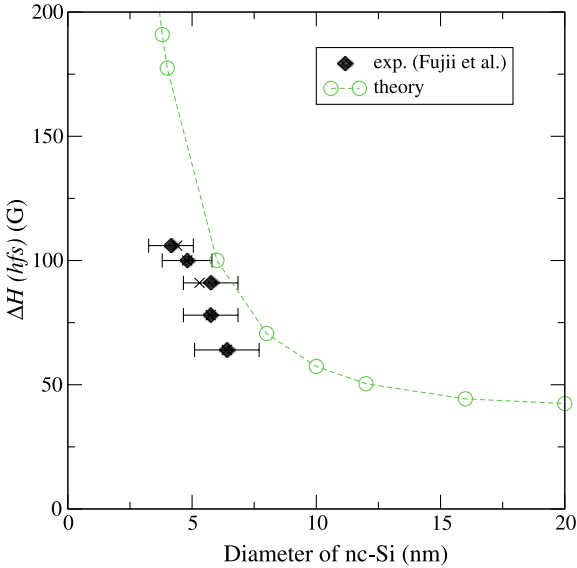


Fig. 6. Hyperfine splitting as a function of nanoparticle diameter. *Full diamonds* denote experimental values obtained by M. Fujii and coworkers [44], *open circles* theoretical results (*dashed line* is a guide for the eyes)

splitting of Si crystals of different size with one P at the center; the maximum radius considered in their work is about one nanometer. They found that the hyperfine splitting $\propto 1/R^\alpha$, with $\alpha = 1.5$. By using the theoretical data displayed in Fig. 6 we have obtained the value $\alpha = 2$, as reported in [26], where the technique previously described to study the dependence of the energy on R has been applied to compute the parameter α describing the dependence of hyperfine splitting on R (the interested reader can refer to the latter work for details of the fitting procedure).

5 Conclusions

We have developed a robust and fast⁷ method based on a Gaussian basis set for the computation of shallow states in semiconductors without adjustable parameters that includes, in a nonperturbative way, the valley–orbit coupling and the interaction with the core states of the impurity. Our results reproduce (within a few meV) the experimental splitting of the 1s manifold of Si:P at zero external electric field and provide reliable predictions of the properties of the system when a uniform electric field is present. We have computed the effect of confinement on shallow states of P dopant by computing the impurity energy level and the hyperfine splitting in spherical Si nanocrystals of different radii showing that our technique is capable of reproducing quantitatively the experimental trends.

⁷ All the calculations for this work were performed on a PC with a Pentium IV 2.80 GHz processor.

References

1. Awsvalhom et al. (eds.), *Semiconductor Spintronic and Quantum Computation* (Springer, Berlin, 2002) 221
2. M.A. Nielsen, I. Chuang, *Quantum Computation and Quantum Information* (Cambridge University Press, Cambridge, 2000) 221
3. D. Loss, D.P. DiVincenzo, Phys. Rev. A **57**, 120 (1998) 221
4. B.E. Kane, Nature **393**, 133 (1998) 221, 222
5. A.M. Stoneham, A.J. Fisher, P.T. Greenland, J. Phys., Condens. Matter **15**, L447 (2003) 222
6. A. Kerridge, A.H. Harker, A.M. Stoneham, J. Phys., Condens. Matter **19**, 282201 (2007) 222
7. A.J. Skinner, M.E. Davenport, B.E. Kane, Phys. Rev. Lett. **90**, 087901 (2003) 222
8. C.I. Pakes et al., Microelectron. J. **33**, 1053 (2002) 222, 223
9. L.M. Kettle et al., Phys. Rev. B **68**, 075317 (2003) 222, 223
10. G.D.J. Smit, S. Rogge, J. Caro, T.M. Klapwijk, Phys. Rev. B **68**, 193302 (2003) 222, 223
11. A.S. Martins, R.B. Capaz, B. Koiller, Phys. Rev. B **69**, 086320 (2004) 222, 223
12. H. Overhof, U. Gerstmann, Phys. Rev. Lett. **92**, 87602 (2004) 222, 233, 234
13. G.D.J. Smit, S. Rogge, J. Caro, T.M. Klapwijk, Phys. Rev. B **70**, 035206 (2004) 222
14. D.V. Melnikov, J.R. Chelikowsky, Phys. Rev. Lett. **92**, 046802 (2004) 222, 236
15. M. Friesen, Phys. Rev. Lett. **94**, 186403 (2005) 222, 223, 228
16. D. Ahn, J. Appl. Phys. **98**, 33709 (2005) 222, 223
17. I. Vasiliev, S. Ögüt, J.R. Chelikowsky, Phys. Rev. Lett. **79**, 1770 (1997) 222
18. S. Ossicini, E. Degoli, F. Iori, E. Luppi, R. Magri, G. Cantele, F. Trani, D. Ninno, Appl. Phys. Lett. **87**, 173120 (2005) 222
19. G. Cantele, E. Degoli, E. Luppi, R. Magri, D. Ninno, G. Iadonisi, S. Ossicini, Phys. Rev. B **72**, 113303 (2005) 222
20. M. Luppi, S. Ossicini, Phys. Rev. B **71**, 035340 (2005) 222
21. A. Baldereschi, Phys. Rev. B **1**, 4673 (1970) 222, 228
22. P.Y. Yu, M. Cardona, *Fundamentals of Semiconductors* (Springer, Berlin, 1996), and references therein 222, 224, 228
23. A.M. Stoneham, *Theory of Defects in Solids* (Oxford University Press, Oxford, 2001), and references therein 222, 224, 226
24. G. Feher, Phys. Rev. **114**, 1219 (1959) 223
25. A. Debernardi, A. Baldereschi, M. Fanciulli, Phys. Rev. B **74**, 035202 (2006) 223, 224, 226, 227, 228, 229, 234
26. A. Debernardi, M. Fanciulli, Solid State Sci., to be published 223, 224, 236, 237

27. K. Shindo, H. Nara, J. Phys. Soc. Jpn. **40**, 1640 (1976) 224
28. A. Debernardi, unpublished. A detailed account will be published elsewhere 226, 233
29. D. Vanderbilt, R.D. King-Smith, Phys. Rev. B **48**, 4442 (1993) 226
30. R. Resta, Rev. Mod. Phys. **66**, 899 (1994) 226
31. H. Nara, A. Morita, J. Phys. Soc. Jpn. **21**, 1852 (1966) 227
32. S. Baroni, A. Dal Corso, S. de Gironcoli, P. Giannozzi, <http://www.pwscf.org> 227
33. R. Resta, J. Phys. C, Solid State Phys. **10**, L179 (1977) 227, 228
34. R.A. Faulkner, Phys. Rev. **184**, 713 (1969) 228
35. S.T. Pantelides, C.T. Sah, Phys. Rev. B **10**, 621 (1974) 228
36. J. von Neumann et al., Phys. Z. **30**, 467 (1929) 230
37. W. Kohn, in *Solid State Physics*, vol. 5 (Academic, New York, 1957) 232
38. E.B. Hale, R.L. Mieher, Phys. Rev. **184**, 739 (1969) 232, 233
39. A. Ferretti, M. Fanciulli, A. Ponti, A. Schweiger, Phys. Rev. B **72**, 235201 (2005) 233
40. D.K. Wilson, Phys. Rev. **134**, A265 (1964) 233
41. J.L. Ivery, R.L. Mieher, Phys. Rev. B **11**, 822 (1975) 233
42. B.G. Martin, R.F. Wallis, Phys. Rev. B **18**, 5644 (1978) 234
43. R.J. Powell, J. Appl. Phys. **41**, 2424 (1970) 234
44. M. Fujii, A. Mimura, S. Hayashi, Y. Yamamoto, K. Murakami, Phys. Rev. Lett. **89**, 206805 (2002) 236, 237

Index

- | | |
|--|---|
| <ul style="list-style-type: none"> central cell correction, 222, 225, 229 confinement effects, 234 core correction, 225, 226, 228 electric field, 229 electron spin-echo envelope modulation (ESEEM), 233 envelope function, 221–224 Gaussian basis, 223, 226 | <ul style="list-style-type: none"> hyperfine splitting, 221, 222, 229, 236 Stark effect, 229 Stark effect of shallow states, 226 superhyperfine constants, 232 tunneling, 232 valley–orbit interaction, 221–223 |
|--|---|

“This page left intentionally blank.”

Photon-Assisted Tunneling in Quantum Dots

Enrico Prati, Rossella Latempa, and Marco Fanciulli

Laboratorio Nazionale Materiali e Dispositivi per la Microelettronica,
CNR-INFM, Via Olivetti 2, 20041 Agrate Brianza, Italy
enrico.prati@mdm.infm.it

Abstract. The manipulation and quantification of the effects produced by an rf field in a mesoscopic structure are fundamental issues in view of developing single-spin-based qubits. Here, we review the experiments on electron transport in quantum dots under microwave irradiation. The electromagnetic vector potential provides excitation of electrons in the leads and in the quantum dot, and an electromotive potential at the leads. The combinations of the two effects go under the name of photon-assisted tunneling. In the present review, the theory of photon-assisted tunneling, based on the Tien–Gordon model applied to the Coulomb-blockade regime of a quantum dot is outlined. An expression for the dc current flowing through the dot in response to a microwave signal is calculated. Then, a classification of different experiments, organized following the different processes adopted to create the dot is presented. Measurements of GaAs split-gate-defined single and double quantum dots as well as lithographically defined SET based on Si/SiGe technology are considered. Finally, recent experiments on a Si/SiO₂ commercial flash memory microwave irradiated up to 40 GHz are illustrated, without and with a static magnetic field up to 12 T.

1 Introduction

Quantum dots are fundamental components of several quantum information processing schemes [1, 2]. Their capability to confine electrons into nanometric volumes makes quantum dots natural candidates to host charge and spin qubits [3–5]. In quantum dots the energy spectrum is discrete [6] so the electronic states can be coupled by an electromagnetic field. Electron-spin qubits are based on Zeeman-state doublets, coupled by microwave irradiation at the resonance frequency. The microwave irradiation drives spin resonance and manipulation with pulses of appropriate duration [7]. It may also activate electron transport in the dot via *inelastic* tunneling due to exchanges of energy between electrons and microwave field (photon-assisted tunneling, PAT). An rf electromagnetic radiation coupled to a quantum dot induces several effects: temperature increasing of the electronic subsystem, resistivity fluctuations due to nonresonant background [9, 10], microwave frequency oscillations of the energy levels into the leads due to magnetic ac coupling

[11–15], photoionization of confined electrons [16], electron-state excitations in the leads due to single and multiple photon absorption [14, 15] and coupling of spin states with different angular momentum [7, 8]. Only the latter is relevant for quantum information processing, while the others have to be eliminated or minimized. Investigation and control of microwave-irradiated quantum dots should lead to an improvement of nanodevice architecture [17]. Photon-assisted tunneling in quantum dots, observed for the first time in 1994 by Kouwenhoven and coworkers in GaAs split-gate quantum-dot samples [14, 15] and later in double dots [18], is one of the most important effects. Analogous results have been obtained in GaAs samples by Von Klitzing et al. [19], and by Williams et al. [20] in 2004 in a lithographically defined single-electron transistor (SET) based on Si/SiGe technology. Recently, we observed photon-assisted tunneling in a commercial Si/SiO₂ flash memory, realized by STMicroelectronics, which behaves as a quantum dot at cryogenic temperature. The most complete literature refers to GaAs quantum dots, where the energy levels are split by applying a magnetic field of more than 0.5–1 T, which fully polarizes electron spins at milli-Kelvin temperatures. Here, we further develop the photon-assisted tunneling of spin-polarized electrons at 12 T in a standard technology ultrascaled flash memory that behaves as a 0D quantum dot embedded into a silicon nanowire. The present review is organized as follows: Sect. 2 illustrates the theory of photon-assisted tunneling (PAT) based on the Tien–Gordon model applied to the Coulomb-blockade regime of a (0D) quantum dot. The other sections review the experiments depending on the host semiconductor used to create the dot. Such a classification corresponds also to the different processes adopted to create the dot. Section 3 reports on the experiments performed on GaAs split-gate-defined quantum dots. Section 4 reports on the experiment on a lithographically defined SET in Si/SiGe technology. Finally, Sect. 5 illustrates the main results obtained using a Si/SiO₂ commercial flash memory where subthreshold discrete levels are provided by a single donor with energy levels below the conduction-band edge. In such a system the study of photon-assisted tunneling of unpolarized electrons has been extended to spin-polarized electrons through nondegenerate energy levels, by means of a 12 T static magnetic field.

2 Theory of Photon-Assisted Tunneling in Quantum Dots

Photon-assisted tunneling of quasiparticles was observed for the first time in a superconducting diode [21] and it was quantitatively modeled by Tien and Gordon [22]. There, the current through a barrier was examined under microwave irradiation. Tien and Gordon developed a general approach to predict the effect of a harmonic electric potential on the tunneling of single particles that has successfully been applied by Kouwenhoven and coworkers to tunneling of electrons through quantum dots [14, 15]. Indeed, the current

through a quantum dot is expressed as the balance of tunneling through its energy levels in the forward and backward directions. In the first section the Hamiltonian formalism of PAT is described. Such a formalism leads to the tunnel rate under microwave irradiation. The second section describes how the modified tunnel rates apply to the Coulomb blockade in quantum dots. The third describes the ratio between the quantities involved in the effect in realistic experimental conditions.

Hamiltonian Formalism of Tunneling under Microwave Irradiation

The model of Tien and Gordon assumes that the electric-field potential $V \cos \omega t$ due to the microwave field has to be linearly added to the generic single-electron unperturbed Hamiltonian H_0 of the system under investigation. The unperturbed Hamiltonian has eigenfunctions

$$\Psi(x, y, z, t) = f(x, y, z) e^{-iEt/\hbar}, \quad (1)$$

where E is the eigenvalue associated to Ψ . The new Hamiltonian

$$H = H_0 + eV \cos \omega t \quad (2)$$

has modified eigenfunctions

$$\Psi(x, y, z, t) = f(x, y, z) e^{-iEt/\hbar} \left(\sum_{-\infty}^{+\infty} B_n e^{-in\omega t} \right), \quad (3)$$

where B_n are generic coefficients to be determined, since the perturbation can not change the spatial distribution of the wavefunction. The substitution of the new generic eigenfunction into the time-dependent Schrodinger equation $i\hbar\dot{\psi} = H\psi$ imposes the relationship between the coefficients B_n [22]:

$$2nB_n = \alpha(B_{n+1} + B_{n-1}), \quad (4)$$

where $\alpha = eV/\hbar\omega$. The solution of such an equation is given in terms of the n th-order Bessel function of the first kind J_n

$$B_n = J_n(\alpha). \quad (5)$$

The eigenfunction is therefore

$$\Psi(x, y, z, t) = f(x, y, z) e^{-iEt/\hbar} \left(\sum_{-\infty}^{+\infty} J_n(\alpha) e^{-in\omega t} \right). \quad (6)$$

The tunnel rate in absence of applied field is

$$\Gamma(\Delta F) = (G/e^2) \Delta F / (1 - e^{-\beta \Delta F}), \quad (7)$$

where $\beta = 1/kT$, G is the characteristic conductance of the barrier, and F the Helmholtz free energy (thermodynamical potential at constant temperature $F = U - TS + \mu N$). The tunnel rate changes as a function of the photon energy as [14, 15]

$$\tilde{\Gamma}(\Delta F) = \sum_{-\infty}^{+\infty} J_n^2(\alpha) \Gamma(\Delta F \pm n\hbar\omega). \quad (8)$$

The generalized tunnel rate (8) must be used to calculate the current I_{DS} through quantum dots under microwave irradiation. The effect of the oscillating field on the tunnel rate directly reflects on the current through the dot. Following the generalized expression (7), the current will contain energy components at $E, E \pm \hbar\omega, E \pm 2\hbar\omega$, etc. These are called sidebands. The calculus of the current through the dot is presented in the next section.

Tunneling in Quantum Dots under Microwave Irradiation

Let's consider a single dot connected via tunnel barriers to two electrodes and capacitively coupled to the gate. Such a system can be modeled by an electrostatic equivalent circuit where the dot is connected to the leads A and B through the impedances Z_A and Z_B , and coupled to the gate through a capacitance C_G , as shown Fig. 1. Z_A and Z_B have ordinarily a very high real component (hundreds of $k\Omega$), while $C_{A,B}$ are comparable with C_G .

The total charge in the dot ne , where n is the number of electrons, is due to the positive charge Q_A at the barrier A, the negative charge $-Q_B$ at the barrier B, and the negative charge $-Q_G$ at the gate. The dot contains an integer number of electrons $ne = Q_A - Q_B - Q_G$ due to the capacitors C_A, C_B , and C_G . Kirchhoff's law gives:

$$Q_A = \frac{C_A}{C_\Sigma} (ne - (C_B + C_G)V_{DS} + C_G V_G), \quad (9)$$

$$Q_B = -\frac{C_B}{C_\Sigma} (ne + C_A V_{DS} + C_G V_G), \quad (10)$$

$$Q_G = -\frac{C_G}{C_\Sigma} (ne + C_A V_{DS} - (C_A + C_B)V_G), \quad (11)$$

where $C_\Sigma = C_A + C_B + C_G$, V_G is the gate voltage and V_{DS} is the drain-source voltage. The total drain-source current I_{DS} is the difference between the probability per unit time that one electron flows from A into the dot, and the probability that one electron flows back to the electrode in the opposite direction, times the unit charge. We call the first process $n_{\text{dot}} \rightarrow n_{\text{dot}} + 1$ to

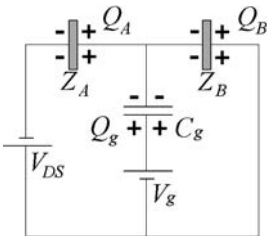


Fig. 1. Equivalent circuit of a single quantum dot

indicate that the total charge goes from Q_A to $Q_A - e$, and $n_{\text{dot}} \leftarrow n_{\text{dot}} - 1$ so the charge changes again from Q_A to $Q_A - e$. Each tunneling event of the kind $n_{\text{dot}} \rightarrow n_{\text{dot}} + 1$ causes a change of charge:

$$\Delta Q_A = -\frac{C_A}{C_\Sigma}e, \quad \Delta Q_B = \frac{C_B}{C_\Sigma}e, \quad \Delta Q_G = \frac{C_G}{C_\Sigma}e, \quad (12)$$

so the total change of the free energy ΔF is

$$\Delta F = \frac{(ne)^2}{2C_\Sigma} - \frac{((n+1)e)^2}{2C_\Sigma} - V_{\text{DS}}\Delta Q_A + V_G\Delta Q_G, \quad (13)$$

which gives

$$\Delta F = \frac{e}{C_\Sigma}((C_A - C_\Sigma)V_{\text{DS}} + C_G V_G - (n+1)e). \quad (14)$$

The current through the dot consists of the algebraic sum of the positive current due to the tunneling events in the forward direction that temporarily increases the electronic occupation of the dot by one unit, and the negative current that decreases the population by a unit. The tunnel rate is weighted by two factors: first, the Fermi distribution associated to the energy levels of the leads; second, the probability of the occupation of the energy levels of the dot, governed by the grand partition function. The tunneling probability is associated to a particular distribution of N electrons in k levels where $N > k$. The total number of distinct configurations of identical particles $\binom{N}{k}$. χ indicates the generic distribution of the electrons in the levels. In order to calculate the explicit expression of I_{DS} , we need to calculate the tunnel rates through the left and right barriers $\Gamma_{i,j}^{\text{in}}$ and $\Gamma_{i,j}^{\text{out}}$, where $i = l, r$ and j refers to the j th energy level E_j . They are

$$\Gamma_{i,j}^{\text{in}} = \Gamma_{i,j} \sum_n J_n^2(\alpha_i) f\left(E_j - \frac{C_G}{C_\Sigma}eV_g - nh\nu + eV_{\text{DSW}}, T_i\right), \quad (15)$$

$$\Gamma_{i,j}^{\text{out}} = \Gamma_{i,j} \sum_n J_n^2(\alpha_i) \left(1 - f\left(E_j - \frac{C_G}{C_\Sigma}eV_g - nh\nu + eV_{\text{DSW}}, T_i\right)\right), \quad (16)$$

where $f(E, T_i)$ is the Fermi distribution, $\Gamma_{i,j}$ is the tunnel rate through the barrier i at the energy E_j , and T_i is the temperature in the i th lead. The total current through the dot can be calculated through an arbitrary barrier. Here, we consider the left barrier.

$$I_{\text{DS}} = e \sum_{\chi} \sum_{\text{empty } j} P_{N,\chi} \Gamma_{l,j}^{\text{in}} - e \sum_{\chi} \sum_{\text{full } j} P_{N+1,\chi} \Gamma_{l,j}^{\text{out}}, \quad (17)$$

where the probabilities $P_{N,\chi}$ are calculated by using the master equation method.

Typical Regimes of Operation

The relevant quantities in the photon-assisted tunneling mechanisms are the energy separation ΔE of the levels in the dot, the charging energy ΔU_C , the energy fluctuation associated to the temperature kT , the voltage fluctuation due to the microwave field into the leads eV_{AC} , and finally the photon energy $h\nu$. The ratio between such quantities is made explicit throughout the text. Some experiments have been carried out in single dots and some in double dots, giving a richer number of possible bias conditions. Commonly, the energies involved are related as follows:

$$\Delta U_C \gg eV_{AC} \approx \Delta E \geq h\nu \gg kT. \quad (18)$$

In such conditions the two possible mechanisms that rule the photon-assisted tunneling in a dot with N electrons are presented in [23, 24] and sketched in Fig. 2. The first (top panel of Fig. 2) gives photon-assisted tunneling when the separation between the *ground state* of the dot at energy E_0 and the Fermi energy corresponds to $n h\nu$. The corresponding current peaks are called *sideband* peaks. The second mechanism occurs when the *excited state* E_1 is aligned with the Fermi energy of the leads (bottom panel of Fig. 2). E_1 is the first excited energy level of the dot (without the charging energy contribution). For such a mechanism it is sufficient that the photon energy $n h\nu$ exceeds, without necessarily matching, the energy $E_1 - E_0$. In analogy to photoionization, the electron at energy E_0 leaves the dot so the Coulomb blockade of the second electron is removed and the current through the energy level E_1 is allowed. At sufficiently high power the voltage fluctuation V_{AC} lets the current flow by the latter mechanism for a relevant fraction of time.

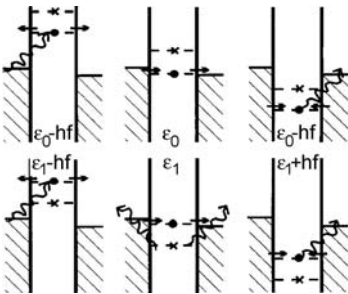


Fig. 2. Two principal tunneling mechanisms responsible for extra peaks due to PAT [24]. *Top panel:* formation of sideband peaks due to the matching of the ground-state E_0 and the Fermi energy of the leads with the photon energy. *Bottom panel:* tunneling through the excited state E_1 , allowed by PAT, provided the electron in the ground state absorbs a photon energy sufficient to leave the dot

3 Experimental Results in III–V Heterostructure Quantum Dots

Experimental Setup

In the literature several experiments related to III–V quantum dots have been reported in [14–18, 24, 25]. The experiments reported by [14, 15, 18, 24], were carried out in a dilution refrigerator. A coaxial cable allows the microwave field to reach the sample. The coaxial line was divided in three sections. From room temperature to the 1-K pot, a 0.085-in semirigid Be–Cu coaxial cable was used, while from the 1-K pot to the mixing chamber, a 0.085-in semirigid stainless-steel coaxial cable was used. From the mixing chamber to the sample, various types of low-attenuation semirigid or flexible coaxial cable were adapted. The coaxial cable was capacitively coupled (typically through a 10-pF capacitor) usually to the center gate, which is capacitively coupled to both dots. The incident power generates a microwave-frequency oscillating potential across the center barrier. The experiments reported by Fujisawa and Tarucha in [16] in both single and double dots were carried out in a ^3He refrigerator. The microwave was applied to the sample via the capacitive coupling of the coaxial cable to the center of the Schottky gate by a coplanar waveguide.

Single Dots

The first experiment on PAT in quantum dots was reported in [14, 15]. In such an experiment the energy $h\nu$ was about $80\ \mu\text{eV}$, while the charging energy was of the order of $450\ \mu\text{eV}$. The peak width Γ_{FWHM} was of the same order as the photon energy $h\nu$. Under such conditions, they measured the I_{DS} current versus the gate voltage V_{G} at zero bias and its change by applying a small bias. The zero-bias experiment is shown in Fig. 3, where a nonzero current due to the microwave field in the forward and reverse directions appears. The microwave irradiation, randomly distributed in the proximity of the device, causes two effects at the same time: one is the excitation of the electrons in the leads to higher-energy multiples of $h\nu$ from the Fermi energy of the reservoir; the second effect is the sinusoidal modulation of the energy levels in the device, which can be simplified in two different ac couplings to the two leads, namely $\alpha_{\text{S}}V_{\text{AC}}$ and $\alpha_{\text{D}}V_{\text{AC}}$. If the two couplings are equal, no current inversion is expected by sweeping the energy level of the dot. In their experiment such condition never applied. In particular, Fig. 3 shows the completely asymmetric case, i.e., an ac field coupled to only one barrier. Here, the dot acts as an electron pump. On one side of the peak, PAT leads to extra positive current and on the other side to extra negative current. This means that photons assist electron tunneling only through one barrier (that with $\alpha_i V_{\text{AC}} \neq 0$), while through the other one only normal tunneling occurs.

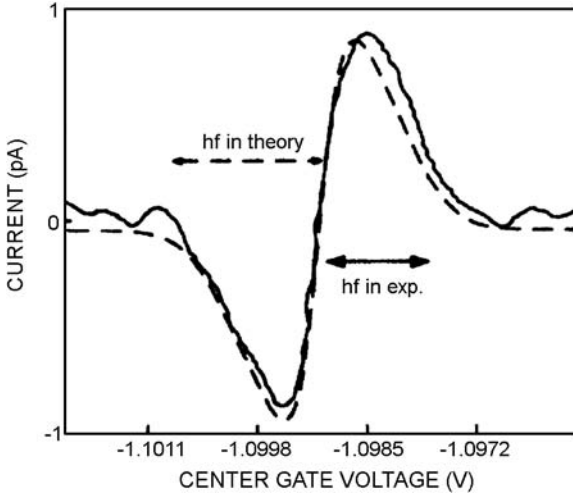


Fig. 3. Comparison between calculated (*dashed*) and measured (*solid*) currents in the dot at zero bias and for asymmetric coupling [14, 15]

The second experiment in single quantum dots was performed by the same group [24]. The major difference from the previous one is a different microwave coupling, induced symmetrically via the central gate. There, the two possible mechanisms studied by Bruder and Scholler [23] were experimentally realized. The first configuration refers to the PAT through the ground state of a dot, while the second is through the excited state. The excited state at energy E_1 is involved in transport after the removal of the electron that occupies the ground state of the dot at energy E_0 . In those experiments the photon energy $h\nu$ was $110\ \mu\text{eV}$, the thermal energy was $kT = 18\ \mu\text{eV}$, the energy level separation $\Delta E = 165\ \mu\text{eV}$ at a magnetic field of $B = 0.84\ \text{T}$, while the charging energy was $\Delta U = 1200\ \mu\text{eV}$. The effect is observed as a superposition of the two currents due to photon-assisted tunneling via the ground and the excited energy levels. Each energy level provides a peak when $E_i = E_F$, where the subscript i ranges over 0 (ground state) and 1 (excited state). In addition, two sidebands are present at the energies $E_i \pm h\nu$. Such an effect is shown in Fig. 4 ([24]).

Double Dots

The photon-assisted tunneling in double dots has been observed in three regimes. The first is when

$$\Delta E_i \gg h\nu \gg eV_{\text{DS}} \approx eV_{\text{AC}}, \quad (19)$$

where the index $i = 1, 2$ refers to the dot 1 and 2 separately; the second when

$$\Delta E_i \gg eV_{\text{DS}} \gg h\nu \gg eV_{\text{AC}}, \quad (20)$$

the third when

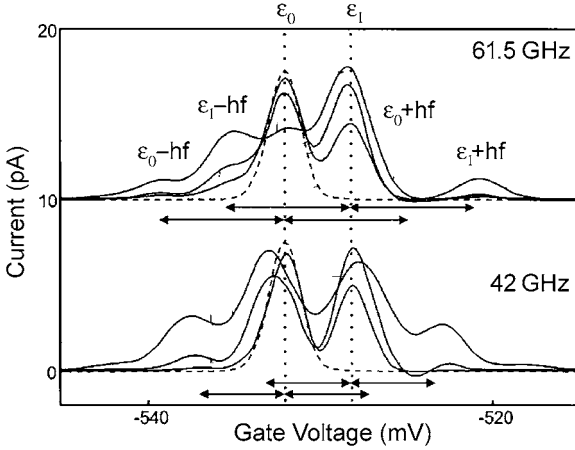


Fig. 4. Measured currents as a function of gate voltage for two different rf frequencies [24]. New resonances appear on the right and left side of the main one (sideband peaks), whose positions shift by an amount corresponding to the change of photon energy

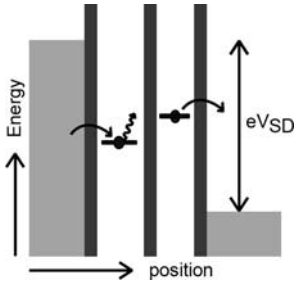


Fig. 5. Energy diagrams in a double-dot structure [18]. In order to contribute to the total current, an electron in the first dot needs to absorb a photon. Here, the voltage V_{SD} is applied between the source and drain contacts so the condition for the current to flow is that the $h\nu$ equals the difference between the energy levels of the two dots

$$\Delta E_i \gg eV_{DS} \gg eV_{AC} > h\nu. \quad (21)$$

The scheme of the second and the third cases is depicted in Fig. 5.

In the first configuration the Fermi energies of the two reservoirs are very close if compared to the energy spacing in each dot, and to the photon energy. In this case it is possible [16] to stop the current flowing by a misalignment between the energy levels of the two dots. Under microwave irradiation it is possible to tune the energy levels of the dots so that their energy difference corresponds to $h\nu$. The electron of the lowest-energy level is excited to the highest one in the other dot and it is replaced by an electron of the reservoir. Such a mechanism allows the current to flow.

In Fig. 6 is shown the effect when a small bias is applied. There, a satellite peak appears in the proximity of the main one caused by the alignment of the energy levels E_L and E_R of the two dots. The satellite peak consists of the current observed for those left and right gate voltages V_{GL} and V_{GR} such that

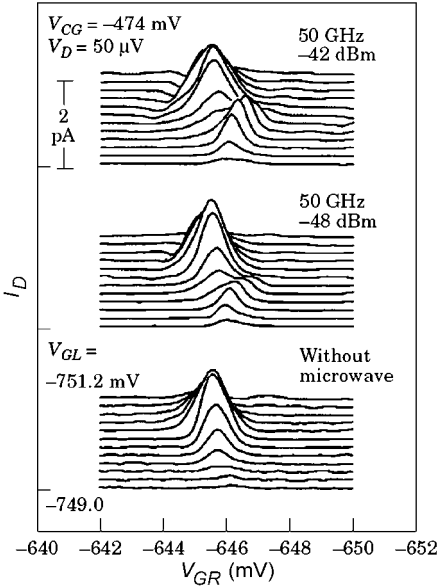


Fig. 6. Drain-current profiles in the so-called 0D–0D configuration with microwave (*first and second panel from the top*) and without microwave (*bottom panel*) [16]. The satellite peak appears as a consequence of microwave irradiation for left and right gate voltages V_{GL} and V_{GR} such that $E_L - E_R = h\nu$

$E_L - E_R = h\nu$. The same configuration has been exploited by Oosterkamp and coworkers [18] where the zero-bias condition has been applied, so the photon-induced current in the two directions is clearly observed (Fig. 7). A second configuration has been realized by exploiting the same interdot resonance but with a photon energy lower than the applied bias voltage eV_{DS} [18] and [25].

The experimental third condition where $eV_{AC} > h\nu$ has also been studied [25]. Under such strong coupling, multiple peaks appear corresponding to $nh\nu$, as shown in Fig. 8.

4 Group IV Heterostructure Quantum Dots

Experimental Setup

The transport in a lithographically defined Si:Ge single-electron transistor under microwave irradiation has been reported by Dovinos and Williams [20] of the Hitachi Cambridge Laboratories. The single-island SET was fabricated on a 30-nm $\text{Si}_{0.9}\text{Ge}_{0.1}$ layer that was phosphorus doped. The structure was defined by electron-beam lithography. The device was cooled in a 12-mK dilution refrigerator. The microwave signal was carried with a semirigid coaxial cable thermally anchored to several stages; a monopole 2 mm from the device was used as a microwave emitter. Both the antenna and the device were operated in vacuum.

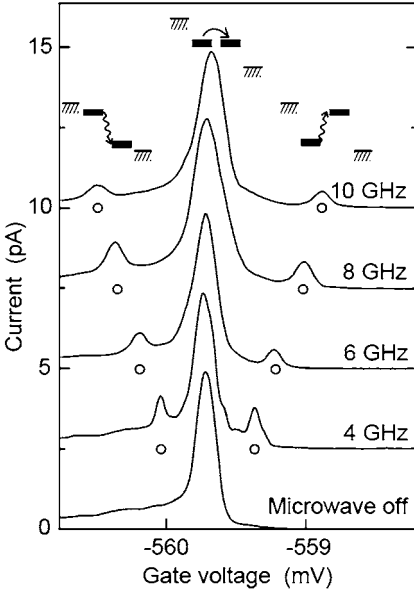


Fig. 7. Current in the double dot as a function of the first gate voltage, without (*lowest curve*) and with microwaves (*upper curves*) as a function of the microwave frequency [18]

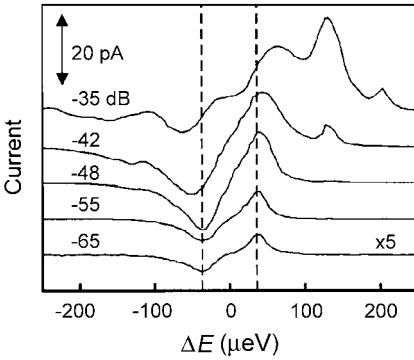


Fig. 8. Measured current in a strong coupled double dot as a function of ΔE for different microwave powers. At high powers, multiple-photon processes can take place, which result in extra current peaks [25]

Experimental Results

PAT is observed when the SET behaves as an island (by well-isolated conductance peaks). The zero-bias current is similar to that of [14, 15], as shown in Fig. 9. There, the authors report I_{DS} current fluctuations as a function of gate voltage V_{G} ($V_{\text{DS}} = 0$, $T = 20$ mK).

Current flows even with no bias, provided that there is an asymmetry in the radiation coupling at the leads. The authors study how the influence of both frequency and power of the external rf acts on PAT. The asymmetry of the oscillation increases with the rf frequency, while both the amplitude and width of the oscillations increase with power. Both the peak to peak height and the width of the oscillations are functions of the coupling factors

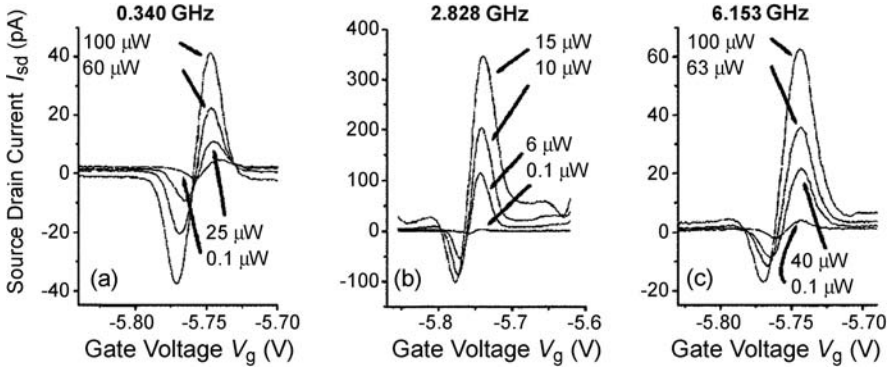


Fig. 9. Drain–source current for different microwave powers at zero bias as a function of gate voltage [20]. Plots refer to different frequencies

of the device $\alpha_i = eV_{DS}/\hbar\omega$, where $i = D, S$, which depend proportionally on the square root of the external power, P_{rf} . Both the oscillation width (depending on α_i maximum value) and amplitude (depending on the difference between α_i factors of the two tunnel barriers of the island) are enhanced by increasing P_{rf} . Nevertheless, the amount of power reaching the device strongly depends on the antenna impedance in the cryostat and cannot be controlled at all by the external source. The system setup, therefore, can hide some frequency effects on the shape of the oscillation and induce a large difference between photon-assisted currents (see, for example, Fig. 9, frequency 2.828 GHz where induced currents of about 400 pA at 15 μW were measured, while in the same figure, at a frequency of 6.153 GHz, values less than 70 pA at 100 μW have been detected). It was pointed out that some current oscillations at zero bias were observed even in the absence of microwave illumination. The authors attributed such effect to background blackbody radiation of the environment. Like in [14, 15], the dot acts in the electron–photon pump regime, due to the strong asymmetric coupling to the leads. Additional peaks have been observed by applying a dc bias $V_{DS} \neq 0$ (up to $-400 \mu\text{V}$) as shown in Fig. 10. The authors report I_{DS} current variations at 3 GHz as a function of gate voltage for different powers. As they show in Fig. 10 a second peak became visible, at sufficiently high microwave power, at a position that does not depend on the applied frequency. A new current peak is a signature of a new “tunnel channel” in the electronic transport of the device.

5 Si/SiO₂ nanoFET Quantum Dots

Experimental Setup

Photon-assisted tunneling in a decanano commercial flash memory based on Si/SiO₂ standard technology has been recently studied by the authors. Ex-

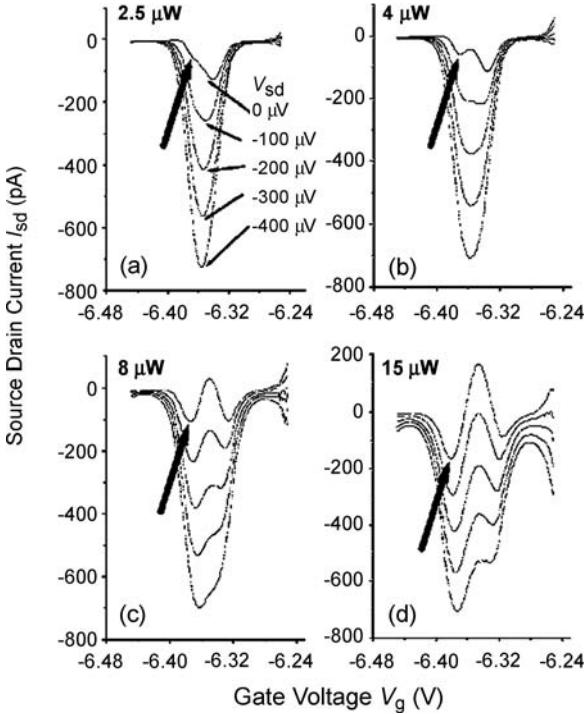


Fig. 10. Drain–source current as a function of gate voltage for different microwave powers and voltage bias [20] at a frequency of 3 GHz

perimental results are similar to those observed in devices based on the previously described technologies. The samples were commercial flash memories based on Si/SiO₂ technology provided by STMicroelectronics, with typical n-channel dimensions of 50 nm width and 136 nm length. The effective length was about 70 nm, as indicated by TEM analysis and simulations. In such samples, electronic transport occurs in 1D channels at the edges of the structure [26]. A systematic test of the whole bit line gave us the possibility to isolate samples with clearly separated current peaks, due to single dopants diffused from the contact region into the channel. These peaks are attributed to donors [26]. The sample was cooled in a 300-mK cryostat inserted into a 12 T superconducting magnet. The 1–40 GHz radiation was supplied by a coaxial line UT-141 beryllium in stainless steel, having a diameter of 3.5 mm. A dipole antenna was used at the end of the line to irradiate the sample, located at a distance of about 3 mm. Both the sample and the antenna were in liquid ³He.

Experimental Results

Drain–source currents (I_{DS}) revealed a typical single-dot Coulomb-blockade behavior at gate voltages below 3 V, where two well-resolved (about 40 mV

voltage-spaced) current peaks were measured. Each peak corresponds to electronic transport between the source and drain reservoirs, assisted by a localized state confined along the channel, associated to a single donor state [26]. At the temperature of 300 mK, transport is not thermally activated and it is completely ruled by elastic resonant tunneling. The flash memory, therefore, acts as a quantum dot, where conduction occurs through spatially localized states and electrons can be Coulomb blocked by a finite charging energy. In Fig. 11 the stability diagram of the first subthreshold peak is shown. Differential conductance is plotted in a color scale and arbitrary units versus gate and bias voltage, at 300 mK. Drain–source voltage V_{DS} is varied from -10 mV to 10 mV, while the control-gate polarization is swept into a 100 -mV voltage interval. Conductance variations develop triangular sectors evidenced by parallel black (continuous) lines. Extra lines are attributed to excited states (dashed-dot lines). Maximum values of differential conductance are evidenced in white, while dark zones refer to minimum ones. In our experiment, the electrochemical potential of only one of the reservoirs was changed. In particular, the source was grounded, so the vertical axis of Fig. 11 corresponds to the electrochemical potential of the drain, μ_D .

At zero bias, by tuning the gate voltage we found the first conduction peak at 2.39 V. Such a point corresponds to the alignment of the quantum-dot energy level E_0 with μ_D , when $V_{DS} = 0$. For other control gate voltages our dot is Coulomb blocked. For $V_{DS} \neq 0$, conduction occurs in a V-shaped region as outlined in the $(eV_{DS}, \Delta E_{CG})$ plane, whose edges have slopes (white lines) depending on the coupling capacitances between the dot and the external leads [6]. The coupling factor γ is 0.12 .

We studied the effect of radiation on the conductance of the device in the absence of bias at different frequencies and for rf powers ranging from

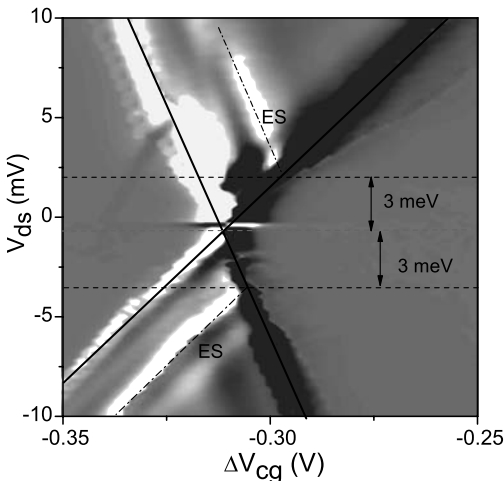


Fig. 11. Stability diagram of the first conduction peak. On the horizontal axis the gate voltage is expressed in terms of the barrier energy of the resonant state, E_0 , calculated on the basis of the coupling factor $\gamma = dE_0/dV_{CG}$ [19]. Throughout the text $\Delta E_{CG} = 0$ meV corresponds to 2.7 V. Excited-state lines (red) are also visible, at a distance of approximately 3 meV from the ground state

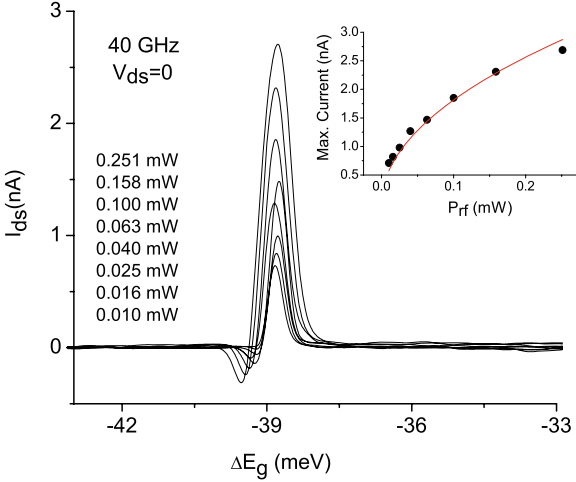


Fig. 12. Source-drain current dependence on microwave field power. As found by other authors [14, 15, 20] different couplings at the leads cause an asymmetric shape. The maximum currents follow a square-root trend (*inset*)

–20 dBm to –6 dBm. In Fig. 12 a set of experimental I_{DS} (V_{CG}) characteristics of the first conductance peak is shown. Measurements were performed at a base temperature of 300 mK. Assisted by the microwave field, current flows even if no bias is applied. The shape of current oscillations depends on the asymmetry of the coupling between source and drain reservoirs with the microwave field. Current peaks increase both in amplitude and width as a function of power P_{rf} , while they do not significantly depend on frequency. As in the cases discussed in the previous sections [20] the absolute power in the sample region is unknown and may change by several orders of magnitude as a function of frequency. Indeed, the electromagnetic environment of the sample depends strongly on the impedance load of the end of the coaxial line that terminates in the ^3He pot. In the inset of Fig. 12 a plot of the maximum peak current as a function of the microwave power is shown. Experimental data are well fitted by the function $c\sqrt{P_{rf}}$ (continuous red line) as measured also by Dovicos and Williams [20].

The same kind of experiment was performed when a static magnetic field was applied parallel to the conduction channel and its intensity was varied between 0 T and 12 T. In Fig. 13 the $I_{DS}(V_{CG})$ curves at rf powers ranging from 0.16 to 2.5 mW are compared at 0 T and 12 T. In the high microwave power regime ($eV_{AC} \geq \Delta E$), i.e. $P_{rf} \geq 0$ dBm new tunnel channels, associated to excited states are accessible, even with no bias applied. At 12 T we can assume complete spin polarization of both electrons in the leads and in the dot. In fact, at 300 mK the thermal broadening kT corresponds to about $75 \mu\text{eV}$, that is, at 12 T, $kT \ll \Delta E_{\text{Zeeman}}$. For a g-factor of 2 ΔE_{Zeeman} is equal to 1.375 meV. At such intense magnetic field the Zeeman splitting is comparable with the energy separation of the ground level E_0 and the excited level E_1 of the donor. Figure 13 shows two effects induced by strong magnetic field. The first consists of the current suppression due to the squeeze-

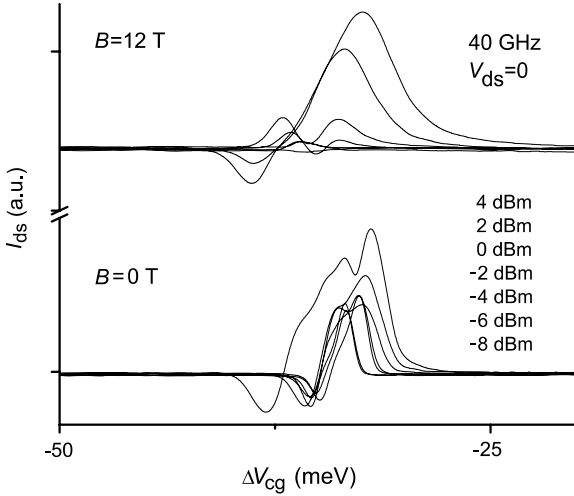


Fig. 13. Source–drain current dependence on microwave field power with and without a static magnetic field

ing of the localized electron wavefunction (see for example the I – V curves measured at rf powers below 0 dBm). The second one is the disappearance of multiple peaks visible without the field and ascribed to different donor excited states involved in tunneling. A spectroscopic quantitative analysis of the donor energy spectrum that takes into account the nature of the dopant site and the band structure of the gated silicon goes beyond the scope of this review. We observe that the application of an rf field of sufficiently high power may recover the tunneling current suppressed at 12 T (see the I – V at 4 dBm) and finally emphasize that electron transport at 12 T is fully spin polarized and that tunneling may occur only through Zeeman-resolved energy levels according to the spin orientation.

6 Conclusions

In the present review we have presented and discussed data and theoretical predictions for the photon-assisted tunneling of unpolarized and polarized electrons in GaAs, Si:SiGe and Si/SiO₂ quantum dots. The latter were obtained by the localized energy levels of a donor placed along the channel of a flash memory, in one of the edges of the sample, where the conductance occurs (nanowires) [26]. Photon-assisted tunneling is observed whenever a microwave field feeds a nanodevice where conduction occurs via elastic tunneling. Such a phenomenon can be exploited for fundamental studies in solid-state physics at the atomic scale, but it represents at the same time a problem for the development of quantum information processing devices. It is particularly clear that whenever single-spin manipulation is pursued, the photon-assisted current parallel to the ordinary elastic spin-dependent tunneling can overcome

and screen the latter. A possible solution is given by single-photon guns, capable of providing a small number of photons per unit time. On the other hand, such a mechanism can be an opportunity for technology, because of its capability of adding new degrees-of-freedom to the system. Spin is involved in the tunneling, as demonstrated by the experiments presented in Sect. 5.

References

1. B.E. Kane, *Nature* **393**, 133 (1998) 241
2. D. Loss, D.P. DiVincenzo, *Phys. Rev. A* **57**, 120 (1998) 241
3. R. Vrijen, E. Yablonovitch, K. Wang, H.W. Jiang, A. Balandin, V. Roychowdhury, T. Mor, D. DiVincenzo, *Phys. Rev. A* **62**, 12306 (2000) 241
4. M. Friesen, P. Rugheimer, D. Savage, M.G. Lagally, D.W. van der Weide, R. Joynt, M. Eriksson, *Phys. Rev. B* **67**, 121301 (2003) 241
5. R. Hanson et al., *Rev. Mod. Phys.* **79**, 1217 (2007) 241
6. C.W.J. Beenakker, *Phys. Rev. B* **44**, 1646 (1991) 241, 254
7. F.H.L. Koppens et al., *Nature* **442**, 766 (2006) 241, 242
8. M. Fanciulli, E. Prati, G. Ferrari, M. Sampietro, *AIP Conf. Proc.* **800**(1), 125–130 (2005) 242
9. R.G. Mani, V. Narayanamurti, K. von Klitzing, J.H. Smet, W.B. Johnson, V. Umansky, *Phys. Rev. B* **69**, 161306(R) (2004) 241
10. S.A. Studenikin, M. Potemski, A. Sachrajda, M. Hilke, L.N. Pfeiffer, K.W. West, *Phys. Rev. B* **71**, 245313 (2005) 241
11. G. Ferrari, L. Fumagalli, M. Sampietro, E. Prati, M. Fanciulli, *J. Appl. Phys.* **98**, 044505 (2005) 242
12. E. Prati, M. Fanciulli, A. Calderoni, G. Ferrari, M. Sampietro, *Phys. Lett. A* **370**, 491–493 (2007) 242
13. E. Prati, M. Fanciulli, A. Calderoni, G. Ferrari, M. Sampietro, *J. Appl. Phys.* **103**, 104503 (2008) 242
14. L.P. Kouwenhoven et al., *Phys. Rev. B* **50**, 2019 (1994) 242, 243, 247, 248, 251, 252, 255
15. L.P. Kouwenhoven et al., *Phys. Rev. Lett.* **73**, 3443 (1994) 242, 243, 247, 248, 251, 252, 255
16. T. Fujisawa, S. Tarucha, *Superlattices Microstruct.* **21**, 247 (1997) 242, 247, 249, 250
17. Obata et al., *Rev. Sci. Instrum.* **78**, 104704 (2007) 242, 247
18. T.H. Oosterkamp et al., *Nature* **395**, 873 (1998) 242, 247, 249, 250, 251
19. R.H. Blick, R.J. Haug, D.W. van der Weide, K. von Klitzing, K. Eberl, *Appl. Phys. Lett.* **67**, 3924–6 (1995) 242, 254
20. D. Dovinos, D. Williams, *Phys. Rev. B* **57**, 085313 (2005) 242, 250, 252, 253, 255
21. A.H. Dayem, R.J. Martin, *Phys. Rev. Lett.* **8**, 246 (1962) 242
22. P.K. Tien, J.R. Gordon, *Phys. Rev.* **129**, 647 (1963) 242, 243
23. C. Bruder, H. Scholler, *Phys. Rev. Lett.* **72**, 1076 (1994) 246, 248

24. T.H. Oosterkamp et al., Phys. Rev. Lett. **78**, 1536 (1997) 246, 247, 248, 249
25. Van Der Wiel et al., Physica B **272**, 31–35 (1999) 247, 250, 251
26. H. Sellier, G.P. Lansbergen, J. Caro, S. Rogge, N. Collaert, I. Ferain, M. Jurczak, S. Biesemans, Phys. Rev. Lett. **97**, 206805 (2006) 253, 254, 256

Index

Coulomb-blockade regime, 241

electron-spin qubits, 241

microwave irradiation, 241

photon-assisted tunneling (PAT), 241,
246

quantum information processing, 241

stability diagram, 254

Tien–Gordon model, 241

tunneling under microwave irradiation,
243

Index

- ^{28}Si , 115
- ^{29}Si nuclei, 115
- 2D electron system (2DES), 131
- ΔH_{pp} , 111
- AlAs/GaAs, 1
- Bloch–Wangsness–Redfield Master equation, 186
- Bloch–Wangsness–Redfield theory, 186
- Carr–Purcell sequence for coherence control, 193, 217
- Carr–Purcell sequences, 191
- central cell correction, 222, 225, 229
- coherence time, 111
- coherent optical manipulation, 53
- coherent single-spin manipulation, 15
- confinement effects, 234
- contacts, 177
- conversion, 91
- core correction, 225, 226, 228
- Coulomb oscillations, 27
- Coulomb-blockade regime, 241
- decoherence, 106, 141–144, 151, 159,
see spin coherence
- decoherence mechanisms, 73
- deformation coupling with acoustic phonons, 150
- dephasing, 142
- dipolar interaction, 197
- DNP, 6
- double quantum-dot, 141
- D’yakonov and Perel’ (DP), 107
- dynamic nuclear polarization, 2, 8
- EDMR, 178–180
 - electric field, 229
 - electric-dipole spin resonance, 16
 - electrical detection of magnetic resonance (EDMR), 178
 - electrically detected electron-spin resonance (ESR), 102, 129
 - electron g-factor, 54
 - electron spin-echo envelope modulation (ESEEM), 233
 - electron–nuclear-spin Hamiltonian, 198
 - electron-spin coherence, 56, 78, 108, 184, 217
 - electron-spin qubits, 241
 - electron-spin resonance (ESR), 101, 102, 178
 - electronic levels of the phosphorus donor, 171
 - ensemble spin dephasing time, 59
 - envelope function, 221–224
 - ESR, 1, 101, 102, 111, 180
 - ESR linewidth, 111
- Faraday-rotation spectroscopy, 56
- few-electron, 101
- fidelity, 142–144
- fractional quantum Hall effect, v
- free induction decay (FID), 184, 191, 205
- frozen core of nuclear spins, 214

- g-factor tensor, 51, 77
- GaAs, 38
- GaAs/AlAs, 1
- GaAs/AlGaAs, 35
- Gauss–Markov model, 192
- Gaussian basis, 223, 226
- Hahn echo, 190
 - decay due to nuclear spins, 206, 208
 - in isotopically enriched silicon, 212, 214
 - magnetic field orientation, 210, 213
 - noise filter function, 191
 - time dependence, 191, 213
- Hall measurements, 109
- hybrid double dots, 27
- hyperfine interaction
 - anisotropic, 197
 - inhomogeneous broadening, 199
 - isotropic, 196
 - mediating nuclear–nuclear coupling, 200, 201
- hyperfine splitting, 221, 222, 229, 236
- induction decay time, 195
- inductively detected NMR, 35
- initialization, 177
- inversion layers, 103
- ion implantation, 173
- isotropic and anisotropic hyperfine interactions, 183
- isotropic hyperfine interaction, 196
- Kohn and Luttinger, 171
- Kondo physics, vi
- Landau levels, 42
- local nuclear field, 10
- Markovian stochastic process, 185
- maximal norm, 158
- microwave irradiation, 241
- NMR, 37, 38, 40, 47
- noise
 - high frequency, loss of visibility, 194
 - nuclear spin noise, 202, 210
 - relationship to decoherence, 186
 - surface effects, 217
- non-Markovian dynamics, 211, 216
- NOT gate, 151
- nuclear-spin noise, 203
- nuclear-spin relaxation time, 8
- operator norms, 145
- parabolic quantum well, 1
- Pauli blocking, 60
- phase-synchronization condition, 68
- phosphorus impurity in silicon, 209
 - effective mass model, 209
 - electron spin decoherence, 209
 - inhomogeneous broadening, 210
- photon-assisted tunneling (PAT), 241, 246
- piezoacoustic interaction, 152
- piezoelectric interaction, 148
- PtSi Schottky, 177
- pump/probe, 94
- QHE, v
- QIP, vi
- quantonium device, 47
- quantum computation, spin-based, 183
- quantum dots, 101, 102, 106
- quantum entropy, 143
- quantum Hall effect, v
- quantum Hall systems, 129
- quantum information processing, 47, 76, 82, 97, 241
- quantum information processor, vi, 81, 82
- quantum wells, 40, 102, 107, 110
- qubit error measure, 155
- Rabi oscillations, 60, 173, 180
- radio-frequency single-electron

- transistors (RF-SETs), 169
- random telegraph signal, 83
- Rashba fields, 136
- Rashba parameter, 112
- RDENDOR, 1
- readout, 170, 177
- readout channel, 92
- relaxation rates, 142
- relaxation time, 146, 187
- resistively detected ESR, 1
- resistively detected nuclear magnetic resonance, 3
- RF-SETs, 174

- secular approximation, 198
- self-assembled (In,Ga)As/GaAs quantum dots, 53
- self-assembled quantum dots, 51, 52, 55
- semiconductor quantum dots, 47
- semiconductor quantum wells, 40
- Si/SiGe heterostructure, 92, 130
- silicon-on-insulator (SOI), 103
- silicon/silicon-germanium quantum wells, 101, 105
- single-electron transistors (SETs), 103
- single-ion implantation, 173, 174
- single-shot read out, 91
- single-spin manipulation, 16
- singly charged quantum dots, 62
- SiO₂/Si/SiO₂, 104
- Skyrme crystal, 44
- Skyrme Lagrangian, 42
- skyrmion excitations, v
- skyrmions, 42
- slanting Zeeman field, 15, 16, 19
- spectral diffusion, 185
- spin coherence, 51, 61, 106, 108
 - Bloch–Wangsness–Redfield equation, 186
 - for a class of pulse sequences, 190
 - relationship to magnetic noise, 188
 - short time behavior, 191
 - single spin *vs.* many spins, 194
- spin coherence times, 52
- spin echo, *see* Hahn echo
- spin Hall effect, v
- spin manipulation, 19, 20, 31
- spin resonance, 89
- spin synchronization, 68
- spin-decoherence mechanisms, 106
- spin-echo decay, 183, 195
- spin-flip, 131
- spin-lattice relaxation time T_1 , 43
- spin-relaxation time, 133
- spin-to-charge, 91
- spintronics applications, 133
- stability diagram, 254
- Stark effect, 229
- Stark effect of shallow states, 226
- stochastic process, 188
- strong Overhauser field, 38
- study, 1
- superhyperfine constants, 232

- T_1 , 184
- T_2 , 184
- T_2^* , 111, 184, 195
- Tien–Gordon model, 241
- time-resolved pump-probe
 - Faraday-rotation methods, 54
- tunneling, 232
- tunneling under microwave irradiation, 243
- two-level systems, 51

- ultrahigh-vacuum chemical vapor deposition, 109

- valley splitting, 104, 107
- valley–orbit interaction, 221–223
- vertical-lateral double quantum dot, 15, 16